

Effects of Background Synoptic Environment in Controlling the Tropical Cyclone Intensity and Size Changes in South China Sea in Pseudo-Global Warming Experiments

CHOW, Tsun Ngai

A Thesis Submitted in Partial Fulfilment
of the Requirements for the Degree of
Master of Philosophy
in
Earth and Atmospheric Sciences

The Chinese University of Hong Kong
August 2022

Thesis Assessment Committee

Professor LIU Lin (Chair)

Professor TAM Chi Yung Francis (Thesis Supervisor)

Professor TAI Pui Kuen Amos (Committee Member)

Professor CHAN Ting Fai Kelvin (External Examiner)

ABSTRACT

Tropical Cyclones (TCs), and the associated strong wind, rainfall and storm surges, are one of the most devastating natural hazards impacting coastal regions including the Peral River Delta. However, reasons for the differences in the TCs' intensity and size changes responding to the same Pseudo-Global Warming (PGW) signal remain unclear. In this project, PGW experiments were carried out by the Weather Research and Forecasting Model (WRF), with a 3 km grid inner domain, on 25 historical TCs superimposed with the projected 2036-2065 and the 2075-2099 PGW forcing from the CMIP5 RCP8.5 and RCP4.5 emission scenarios. Differences in azimuthally averaged maximum wind (V_{max}), radius of the azimuthally averaged maximum wind (RMW) and the radius of the azimuthally averaged gale-force wind (R17) across TCs in the South China Sea (SCS) were examined. It was found that the difference in TC's V_{max} percentage change under the same warming signal varies positively with historical sea surface temperature (SST) and negatively with historical vertical wind shear magnitude. Also, under the same warming, larger TCs' RMW decrease was associated with smaller historical mid-tropospheric relative humidity (RH), while larger R17 increase was associated with larger historical mid-tropospheric RH and larger historical outer wind speed, defined as the wind speed beyond R17 in the SCS. Here, Ertel potential vorticity (EPV) diagnostics were used to study the difference in the R17 percentage change with respect to the same forcing for TC Mary (1960) and Nuri (2008) associated with RCP8.5 far future climate. Results showed that a historically larger RH environment favors more diabatic EPV production, which is associated with an increase in the strength and the lateral extent of deep convection associated with the TC spiral rainbands, therefore causing a wider cyclonic EPV distribution and a larger R17 increase for TC Mary compared to TC Nuri in a warmed climate. Absolute angular momentum (AAM) budget was also used to diagnose the effects of outer wind speed on the difference in the response of TCs' R17 to the same warming signal. In general, a historically larger background AAM environment allows TCs to have stronger radial AAM influx in a warmed climate, which then enhances the radial AAM advection near the R17 and expanded the R17, while a historically weaker background AAM environment limits the AAM influx, therefore limiting the TCs' R17 expansion. Results in this work provide insights on explaining TCs' intensity and size projection uncertainties under naturally variating climate modes in different timescale in an anthropogenically warmed future climate background. Moreover, the environment that can cause even larger TCs risks in intraseasonal, interannual and interdecadal timescales in the future were identified.

摘要

颱風，並其帶來的強風，暴雨和風暴潮是其中一種對沿海地區，例如珠三角地區，造成極大破壞的自然災害。但是，科學家現時並不清楚為什麼颱風在一樣的 Pseudo-Global Warming (PGW) 影響下，會有不同的強度及大小變化。在本文章中，作者使用了最高解像度為 3 公里的 WRF 模型，去模擬二十五個過去的颱風在 CMIP5 RCP8.5 及 RCP45 排放情景下的 2036-2065 年，及 2075-2099 年在南海的改變。作者研究了這些颱風的最高風速(V_{max})，最高風速半徑(RMW)，以及強風圈半徑(R17)的變化。作者發現在同一個 PGW 實驗下，不同颱風的最高風速會隨著過去的海面溫度及垂直風切變而改變。同時，颱風的最高風速半徑會隨著過去的環境相對濕度而縮小。另外，颱風的強風圈半徑會隨著過去的環境相對濕度和外圍風速而增加。然後，作者使用了 Ertel Potential Vorticity (EPV) 去分析過去的環境相對濕度如何影響颱風瑪麗(1960)和颱風鸚鵡(2008)在 RCP8.5 排放情景下的 2075-2099 年強風圈的大小。作者發現，過去相對濕度較高的環境更適合螺旋雲帶的增強和擴大。因此，颱風製造更多透熱 EPV，導致範圍更廣的氣旋 EPV。所以，對比颱風鸚鵡(2008)，颱風瑪麗(1960)的強風圈半徑增加得更多。另外，作者使用了絕對角動量(AAM)預算，去分析過去的外圍風速如何影響不同颱風在同一個 PGW 訊號下的強風圈大小變化。在較強外圍風速背景下的颱風，在暖化後會有更強的向內絕對角動量通量，因而增加強風圈半徑附近的徑向絕對角動量移流，並使這些颱風變得更大。反之，較弱外圍風速背景限制了一些颱風的向內絕對角動量通量，令這些颱風的強風圈半徑在暖化背景下也沒有太大變化。這些結果可用作解釋颱風在暖化後，在不同自然氣候模式下的不確定性。同時，作者也發現了未來可能會引致更大颱風風險的環境。

Table of Contents

1.	Introduction	16
2.	Literature Review	18
2.1	TC structure	18
2.1.1	Typical Structure of a mature TC	18
2.1.2	Physics of the TC circulation	21
2.1.3	Physics of the spiral rainbands	23
2.2	Parameters quantifying a TC	26
2.2.1	Intensity	26
2.2.2	Size	28
2.3	Factors influencing the structure of a TC	30
2.3.1	Environmental influences on the intensity of a TC	31
2.3.2	Environmental influences on the outer core size of a TC	35
2.3.3	Environmental influences on the inner core size of a TC	39
2.3.4	Internal properties and processes influence on the intensity of a TC	40
2.3.5	Internal properties and processes influence on the outer core size of a TC	41
2.3.6	Internal properties and processes influence on the inner core size of a TC	42
2.4	Impact of global warming to the characteristics of TCs	42
2.4.1	Intensity changes	43
2.4.2	Size changes	44
3.	Data and Methodology	46
3.1	Model configuration	47
3.1.1	TC selected	47
3.1.2	WRF Model	48
3.1.3	Pseudo global warming method (PGW)	49
3.2	Regression Analysis	51
3.2.1	Multiple Linear Regression (MLR) analysis	51
3.2.2	Stepwise Regression Analysis	54

4.	TC Mean Intensity and Size Changes in the SCS in PGW Experiments.....	56
4.1	TC Selection based on the Comparison to the Best Track Data	56
4.2	Mean changes in the SCS.....	59
5.	Statistical Relationships between Differences in TC Intensity and Sizes Changes to the Historical Environment	65
5.1	Variations of TC intensity and size changes in each warming experiments	66
5.2	Relationship between historical environment to the variations of TC intensity and size changes in PGW experiments	69
5.2.1	Relationship Between Historical Environment to the Variations of Vmax Changes in PGW Experiments.....	71
5.2.2	Relationship Between Historical Environment to the Variations of RMW Changes in PGW Experiments.....	74
5.2.3	Relationship Between Historical Environment to the Variations of R17 Changes in PGW Experiments.....	77
6.	EPV Diagnostics of Relationship between Historical Environmental RH to R17 Change Variations in Future Climate for selected TCs.....	81
6.1	Model Verification and TC Mean Wind Field	82
6.2	Azimuthally Averaged EPV Diagnostics	83
6.3	Horizontal Structures.....	91
6.4	Volume Averaged EPV Diagnostics	94
6.5	Vertical cross-sections for TC Mary and TC Nuri at Selected Timesteps	100
7.	AAM Diagnostics of Relationship between Historical Outer Wind Speed to R17 Change Variations in Future Climate.....	105
7.1	Difference in Percentage Change of R17 in terms of AAM and Local AAM tendency ...	107
7.2	AAM Budget Analysis	109
7.2.1	Azimuthally Averaged AAM Budget Equation.....	109
7.2.2	Relative contribution of the change in radial wind and the radial gradient of AAM in the symmetric radial advection of AAM.....	111
7.3	AAMF Analysis	114
7.3.1	Difference in AAMF in warming runs and the control run	115

7.3.2	Relative contribution between the change in radial wind and the tangential wind to the SF in a warmed climate.....	117
7.4	Composites of R17 increasing TCs and R17 constant TCs.....	123
7.5	Synoptic Environment Associated with R17 Increasing TCs	127
7.6	Summary for AAM Budget Analysis.....	128
8.	Discussion and Limitations	131
8.1	Implications to future TC intensity and size projection	131
8.1.1	Variations and error estimation for mean TC intensity and size changes.....	131
8.1.2	Risk Assessment for Individual TC	134
8.1.3	Extreme Value Statistics	136
8.1.4	Statistical Forecast of Individual TC in the Future Climate	137
8.2	Projected RMW decrease in future climate.....	140
8.3	Relationship between variations of RMW percentage change in the future climate to the historical environment conditions	141
8.4	Relationship between variations of Vmax percentage change in the future climate to the historical environment conditions	143
8.5	Limitations.....	144
8.5.1	Experimental Design.....	144
8.5.2	Model Horizontal Resolution in Simulating the Responses of RMW	147
8.5.3	Sensitivity of the results to the choice of numerical model and the physics scheme	149
9.	Conclusion	150
10.	Reference.....	154
	APPENDIX I Selected CMIP5 Models	167
	APPENDIX II Superimposed PGW signals	169
	APPENDIX III Ertel Potential Vorticity (EPV) Diagnostics	171
	APPENDIX IV Absolute Angular Momentum (AAM) Budget Analysis	174
	APPENDIX V TCs Model Results Verification.....	176
	APPENDIX VI Statistical Significance on MLR Slope Map.....	183
	APPENDIX VII Difference in Volume Averaging of TC Mary and TC Nuri	188

List of Figure

Figure 2.1 Typical Structure of a tropical cyclone. Top photo is based on a satellite photo of the cloud structure of Hurricane Fran in 1996. Right-hand cut shows the vertical velocity from a numerical model and Left-hand cut shows the tangential wind from observation. Figure from Figure 3 of Emanuel, 2003	18
Figure 2.2 Schematic of the secondary circulation of a TC. (Figure from Figure 1 of Frank, 1977)	19
Figure 2.3 Model simulated Radar Reflectivity of top: composite, bottom: radial-vertical cross-section of a TC (Figure from Figure 1 in Wang, 2009)	20
Figure 2.4 Left: Temperature anomaly of a TC (shading), radial motion of the TC (contour). Right: Specific entropy, which can be translated to equivalent potential temperature. Contour: Absolute angular momentum. Vector denotes the secondary circulation (Figure from Figure 4 of Emanuel, 2003)	21
Figure 3.1 Historical Tracks of the TC selected from the Best Track data. Solid line showed the 14TC studied in the Multiple Linear Regression (MLR) analysis. Figure boundary (labeled as d01) showed the outer domain and black rectangle (labeled as d02) showed the inner domain of the WRF model.....	46
Figure 3.2 Procedures of the PGW Experiments. Changes in monthly mean SST, land surface temperature (surface T), atmospheric temperature profile ($T(z)$) and the specific humidity profile ($q(z)$) in the near future and the far future in the RCP8.5 and RCP4.5 emission scenarios were subtracted by the values in the historical climate, and then imposed to each of the selected TCs according to their month of occurrence in the past.	50
Figure 3.3 Illustration of the process of stepwise regression	54
Figure 4.1 Simulated TC tracks in (orange) control run, (green) RCP8.5 Far Future, (red) RCP8.5 Near Future, (purple) RCP4.5 Far Future, (brown) RCP4.5 Near Future compared to the (blue) best-tracked data. TCs were ordered in chronological order from top-left to lower-right.	57
Figure 4.2 Percentage changes of mean (a) Vmax, (b) RMW, (c) R17 in the SCS for 14 selected TC in 4 warming experiments, scaled to the change of mean SST in the SCS in (blue) RCP8.5 Far Future, (yellow) RCP8.5 Near Future, (green) RCP4.5 Far Future, (red) RCP4.5 Near Future. The percentage changes for each individual TC relative to the control were indicated by + symbol. * indicate the mean percentage change across all 14 TCs in that warming experiment. Black line indicates the linear regression of mean SST changes in the SCS to the mean percentage change across 14 TCs, which the slope for percentage change of mean Vmax and the mean R17 in the SCS is significantly different to 0 in 95% CI. Black dashed line showed the 95% prediction interval of the sample while grey dotted line showed the 95% confidence interval of the regression function. Details of the prediction interval and the confidence interval of the regression model were discussed in section 8.1	58
Figure 5.1 Box and whisker diagram of mean percentage change in (a) Vmax, (b) RMW, (c) R17 in each warming experiment relative to the control run for 14 TCs. See text for explanation for box and whisker diagram	66

Figure 5.2 10 m azimuthally averaged wind field in control and warming experiment for (a) TC Gordon (1989) and (b) TC Warren (1988) averaged across time in the SCS region. Black line denotes the 17 m s^{-1} , dashed line denoted the Vmax and the RMW while dash-dot line denotes the R17	67
Figure 5.3 MLR slope of normalized (a) detrended SST, (b) Atmospheric instability, (c) mid-tropospheric RH, (d) Vertical wind shear regressed to the percentage change of Vmax in each scenario and averaged across all warming experiments. Units of the colorbar were % of Vmax change per 1 unit of standardized environmental parameters. Overlayed were the TC tracks in the control run	70
Figure 5.4 Left column: (a,c,e,g) Step 1 and Right column: (b,d,f,h) step 2 of the stepwise regression map between the historical environmental variables of the 14 TCs to the variations of the Vmax percentage change of 14 TCs in (a,b) RCP8.5 Far Future, (c,d) RCP8.5 Near Future, (e,f) RCP4.5 Far Future and (g,h) RCP4.5 Near Future. color denotes (red) detrended SST, (blue) 1000 mb – 500 mb to 700 mb mean MSE, (green) vertical wind shear within 500 km from the TC center, (purple) 600 mb RH. Grey lines are the tracks of the 14TCs in control experiment.....	72
Figure 5.5 MLR slope of normalized (a) detrended SST, (b) Atmospheric instability, (c) mid-tropospheric RH, (d) Vertical wind shear regressed to the percentage change of RMW in each scenario, and averaged across all warming experiments. Units of the colorbar were % of RMW change per 1 unit of standardized environmental parameters. Overlayed were the TC tracks in the control run	74
Figure 5.6 Same as Figure 5.5b and 5.5c respectively, but for environmental variables extracted from the control run	75
Figure 5.7 Left column: (a,c,e,g) Step 1 and Right column: (b,d,f,h) step 2 of the stepwise regression map between the historical environmental variables extracted from the control run of the 14 TCs to the variations of the RMW percentage change of 14 TCs in (a,b) RCP8.5 Far Future, (c,d) RCP8.5 Near Future, (e,f) RCP4.5 Far Future and (g,h) RCP4.5 Near Future. color denotes (red) detrended SST, (blue) 1000 mb – 500 mb to 700 mb mean MSE, (green) vertical wind shear within 500 km from the TC center, (purple) 600 mb RH. Grey lines are the tracks of the 14TCs in control experiment.....	76
Figure 5.8 MLR slope of normalized (a) detrended SST, (b) Atmospheric instability, (c) mid-tropospheric RH, (d) Vertical wind shear , (e) 10m outer wind speed regressed to the percentage change of R17 in each scenario, and averaged across all warming experiments. Units of the colorbar were % of R17 change per 1 unit of standardized environmental parameters. Overlayed were the TC tracks in the control run	78
Figure 5.9 Left column: (a,c,e,g) Step 1 and Right column: (b,d,f,h) step 2 of the stepwise regression map between the historical environmental variables of the 14 TCs to the variations of the R17 percentage change of 14 TCs in (a,b) RCP8.5 Far Future, (c,d) RCP8.5 Near Future, (e,f) RCP4.5 Far Future and (g,h) RCP4.5 Near Future. color denotes (red) detrended SST, (blue) 1000 mb – 500 mb to 70 0mb mean MSE, (green) vertical wind shear within 500 km from the TC center, (purple) 600 mb RH, (wheat) 10 m outer wind speed (m s^{-1}). Grey lines are the tracks of the 14TCs in control experiment.....	79

Figure 6.1 Azimuthally averaged 10 m wind field of TC Mary (1960) and TC Nuri (2008) in the control run and the RCP8.5 Far Future run from H_DIA simulations. Black line denotes the 17 m s^{-1} wind speed, grey dashed line represented the Vmax and RMW while dash-dotted line showed the R17 of the TC. Also showed the Historical 600 mb RH for TC Mary and TC Nuri from the model output (green, right y-axis).....	82
Figure 6.2 Hovmöller diagrams of azimuthally averaged model outputted composite reflectivity difference between RCP8.5 Far Future run and control run (unit: dbz) (color), and historical environmental 600 mb RH (unit: %) (contour), each contour indicate 5% RH, for (a) TC Mary, (b) TC Nuri. lines denote (red) R17 in control run, (green) R17 in RCP8.5 Far Future run, (orange) RMW in RCP8.5 Far Future run. 2 black line indicate the time when the TC enters the SCS and landfall at the South China coast.....	83
Figure 6.3 Hovmöller diagrams of azimuthally averaged 700 mb to 850 mb mean EPV between RCP8.5 Far Future run and control run (unit: PVU) (color), and difference in model outputted composite reflectivity in RCP8.5 Far Future relative to the control run (unit: dBz) (contour), each contour indicate 5 dbz, for (a) TC Mary, (b) TC Nuri. lines denote (red) R17 in control run, (green) R17 in RCP8.5 Far Future run, (orange) RMW in RCP8.5 Far Future run. The black line denotes the time when the TC enters the SCS. End of y-axis is the time of landfalling at the South China coast. x-axis is from the TC center to 150 km radius	84
Figure 6.4 Hovmöller diagram of 500 mb to 700 mb mean model outputted diabatic heating rate (unit: K h^{-1}) (color) and 700 mb to 850 mb mean EPV (unit: PVU) (contour) for (a) Mary in control run, (b) Mary in RCP8.5 Far Future run, (c) Nuri in control run, (d) Nuri in RCP8.5 Far Future run, all simulation were from H_DIA runs. Lines denote (red) R17 in control run, (green) R17 in RCP8.5 Far Future run, (purple) RMW in control run, (orange) RMW in RCP8.5 Far Future. Black line denotes the time when the TC enters the SCS. End of the y-axis shows the time of landfall. x-axis shows the distance from the TC center to a radius of 350 km.....	86
Figure 6.5 Hovmöller diagram of filtered 700 mb to 900 mb mean diabatic EPV tendency (unit: PVU h^{-1}) (color) and 700 mb to 850 mb mean EPV (unit: PVU) (contour) for (a) Mary in control run, (b) Mary in RCP8.5 Far Future run, (c) Nuri in control run, (d) Nuri in RCP8.5 Far Future run, all simulation were from H_DIA runs. Lines denote (red) R17 in control run, (green) R17 in RCP8.5 Far Future run, (purple) RMW in control run, (orange) RMW in RCP8.5 Far Future. Black line denotes the time when the TC enters the SCS. End of the y-axis shows the time of landfall. x-axis shows the distance from the TC center to a radius of 250 km.....	88
Figure 6.6 Azimuthally averaged vertical profile of model outputted (color) diabatic PV tendency (PVU hr^{-1}) and (contour) diabatic heating rate (unit: K hr^{-1}) for TC Mary at timestep 1960-06-06-00. (a) shows the control run while (b) shows the RCP8.5 Far Future run. Dotted line means negative diabatic heating rate	89
Figure 6.7 Azimuthally averaged vertical profile of model outputted (color) diabatic PV tendency (PVU hr^{-1}) and (contour) diabatic heating rate (unit: K hr^{-1}) for (a,b) TC Mary at timestep 1960-06-06-00 and (c,d) TC Nuri at 2008-08-21-18. (a,c) shows the control run while (b,d) shows the RCP8.5 Far Future run. Dotted line means negative diabatic heating rate. Black arrows illustrated the absolute vorticity vector	90

Figure 6.8 Composite plots of (a,b) composite reflectivity (dbz), (c,d) 500-700 mb mean EPV (PVU) and (e,f) 875-975 mb mean diabatic EPV tendency of TC Mary at 1960-06-06-00 in (a,c,e) control run and (b,d,f) RCP8.5 Far Future run. Lime or orange circle denoted the R17, black circles denote radius of 50, 100, 150 and 250 km. Thick blue lines in (a,b) showed the vertical cross-section in section 6.5	92
Figure 6.9 Composite plots of (a,b,c,d) composite reflectivity (dbz), (e,f,g,h) 500-700 mb mean EPV (PVU) and (I,j,k,l) 875-975 mb mean diabatic EPV tendency of (a,b,e,f,I,l) TC Mary at 1960-06-07-06 and (c,d,g,h,k,l) TC Nuri at 2008-08-21-18 in (a,e,I,c,g,k) control run and (b,f,j,d,h,l) RCP8.5 Far Future run. Lime or orange circle denoted the R17, black circles denote radius of 50, 100, 150 and 250 km. Thick blue lines in (a,b,c,d) showed the vertical cross-section in section 6.5.....	93
Figure 6.10 Timeseries of Volume averaged EPV budget equation for TC Mary in (a) control run and (b) RCP8.5 Far Future run using a cylindrical volume of radius 150 km, with a lower and upper surface at 1000 hPa and 150 hPa. Lines denote (thin steelblue) 12 hour moving average local EPV tendency, (thin orange) 12 hour moving average diabatic PV tendency, (thin green) 12 hour moving average horizontal EPV convergence, (thin purple) 12 hour moving average vertical EPV convergence, (thick navyblue) 24 hour moving average local EPV tendency, (think red) 24 hour moving average diabatic PV tendency, (thick green) 24 hour moving average horizontal EPV convergence, (thick purple) 24 hour moving average vertical EPV convergence, (thin olive) 24 hour moving average total EPV convergence (horizontal + vertical), (thin blue) 24 hour moving average total EPV convergence and diabatic PV tendency. vertical black line denotes the time of landfall. Data retrieved from H_DIA runs	94
Figure 6.11 Timeseries of Volume averaged (a) EPV (PVU), (b) local EPV tendency (PVU hr ⁻¹), (c) diabatic PV tendency (PVU hr ⁻¹) for TC Mary in a 150 km cylindrical volume from the TC center, bounded by the 1000 hPa and 150 hPa pressure level, lines denotes (steelblue) control run, (orange) RCP8.5 Far Future run, (green) difference between RCP8.5 Far Future and control run, thin and thick line denotes 12 hour and 24 hour moving average respectively. Vertical black line denote the time when the TC landfall at South China. Data retrieved from H_DIA run	95
Figure 6.12 Similar to Figure 6.10, but for TC Nuri within a volume of 450 km radius from the TC center, bounded by the 1000 hPa and 150 hPa pressure level. The 2 vertical black line showed the time when the TC enters the SCS and landfall at the South China coast. Noted that the y-axis for Figure 6.12 is different to Figure 6.10	97
Figure 6.13 Same as Figure 6.11, but for TC Nuri within a volume of 450 km radius from the TC center, bounded by the 1000 hPa and 150 hPa pressure level. The 2 vertical black line showed the time when the TC enters the SCS and landfall at the South China coast. Noted that the y-axis for Figure 6.13 is different to Figure 6.11	98
Figure 6.14 Vertical cross-section for (a,b)TC Mary at 1960-06-06-00 and TC Nuri at 2008-08-21-03 in (a,c) control run and (b,d) RCP8.5 Far Future run. The (color) model output reflectivity (dBz), (contour) model retrieved environmental RH (%), (vector) TC radial and vertical circulation (m s ⁻¹) (vertical motion were exaggerated by 1 order) were shown within (a,b) 350 km radius and (c,d) 500 km radius.....	100
Figure 6.15 Vertical cross-section for (a,b) TC Mary at 1960-06-06-00 and (c,d) TC Nuri at 2008-08-21-03 in (a,c) control run and (b,d) RCP8.5 Far Future run. The (color) microphysics diabatic	

heating rate (K hr^{-1}), (contour) model output reflectivity (dbz), (vector) TC radial and vertical circulation (m s^{-1}) (vertical motion were exaggerated by 1 order) were shown.	101
Figure 6.16 Vertical cross-section for (a,b) TC Mary at 1960-06-06-00 and (c,d) TC Nuri at 2008-08-21-03 in (a,c) control run and (b,d) RCP8.5 Far Future run. The (color) diabatic PV tendency (PVU hr^{-1}), (contour) microphysics diabatic heating rate (K hr^{-1}), (vector) non-advection PV Flux in radial and vertical direction ($\text{K m}^2 \text{kg}^{-1}$) were shown	102
Figure 7.1 Hovmoller diagrams of (color) azimuthally averaged 10 m AAM difference (unit: $10^6 \text{ m}^2 \text{s}^{-1}$) for TCs in (a,b,c,d) RCP8.5 Far Future and (e,f,g,h) RCP4.5 Far Future relative to the control run and (contour) historical outer tangential wind speed (m s^{-1}) for (a,e) TC Gordon, (b,f) TC Hope, (c,g) TC Bess, (d,h) TC Warren. Lines indicate (red) R17 in control run, (green) R17 in warming run, (purple) RMW in control run, (orange) RMW in warming run. Black line indicate the time when the TC enters the SCS.	107
Figure 7.2 Hovmoller diagrams of (color) azimuthally averaged 10m local AAM tendency difference (unit: $\text{m}^2 \text{s}^{-2}$) for TCs in (a,b,c,d) RCP8.5 Far Future and (e,f,g,h) RCP4.5 Far Future relative to the control run and (contour) historical outer tangential wind speed (m s^{-1}) for (a,e) TC Gordon, (b,f) TC Hope, (c,g) TC Bess, (d,h) TC Warren. Lines indicate (red) R17 in control run, (green) R17 in warming run, (purple) RMW in control run, (orange) RMW in warming run. Black line indicate the time when the TC enters the SCS. End of y-axis indicate the time of landfalling.	108
Figure 7.3 Comparison between (color) the (left) azimuthally averaged local AAM tendency (same as Figure 7.2) (unit: $\text{m}^2 \text{s}^{-2}$), and the (right) symmetric radial advection of AAM (unit: $\text{m}^2 \text{s}^{-2}$) in the (a-d) RCP8.5 Far Future run and (e,h) RCP4.5 Far Future relative to the control run for (a,e) Gordon, (b,f) Hope, (c,g) Bess, (d,h) Warren, (right contour) showed the historical outer wind speed (unit m s^{-1}). Lines indicate (red) R17 in control run, (green) R17 in warming run, (purple) RMW in control run, (orange) RMW in warming run. Black line indicate the time when the TC enters the SCS. End of y-axis indicate the time of landfalling.....	110
Figure 7.4 Hovmoller diagrams of (left) $\Delta \log_{10}(-\text{vr} \partial \text{AAM} / \partial r)$, (middle) $\Delta \log_{10}(-\text{vr})$ (positive means inward), (right) $\Delta \log_{10}(\partial \text{AAM} / \partial r)$ for (a) Gordon, (b) Hope, (c) Bess, (d) Warren in the RCP8.5 Far Future run relative to the control run. (contour) showed the historical outer wind speed (unit m s^{-1}). Lines indicate (red) R17 in control run, (green) R17 in RCP8.5 Far Future, (purple) RMW in control run, (orange) RMW in RCP8.5 Far Future, (pink) Vmax in control, (brown) Vmax in RCP8.5 Far Future. Black line indicate the time when the TC enters the SCS. End of y-axis indicate the time of landfalling.	112
Figure 7.5 Hovmoller diagrams of (left) $\Delta \log_{10}(-\text{vr} \partial \text{AAM} / \partial r)$, (middle) $\Delta \log_{10}(-\text{vr})$ (positive means inward), (right) $\Delta \log_{10}(\partial \text{AAM} / \partial r)$ for (a) Gordon, (b) Hope, (c) Bess, (d) Warren in the RCP4.5 Far Future run relative to the control run. (contour) showed the historical outer wind speed (unit m s^{-1}). Lines indicate (red) R17 in control run, (green) R17 in RCP4.5 Far Future, (purple) RMW in control run, (orange) RMW in RCP4.5 Far Future, (pink) Vmax in control, (brown) Vmax in RCP4.5 Far Future. Black line indicate the time when the TC enters the SCS. End of y-axis indicate the time of landfalling.	113
Figure 7.6 Hovmoller diagrams of the (color) difference in SRAMF + SCT in the (a-d) RCP8.5 Far Future and the (e-h) RCP4.5 Far Future period than the control run, positive means inward (unit:	

$10^6 \text{ m}^3 \text{ s}^{-2}$) for (a,e) TC Gordon, (b,f) TC Hope, (c,g) TC Bess, (d,h) TC Warren. (contour) historical outer wind speed (unit: m s^{-1}), intervalled 2 ms^{-2} . Lines indicate (red) R17 in control run, (green) R17 in warming run, (purple) RMW in control run, (orange) RMW in warming run. Black line indicated the time when the TC enters the SCS. End of y-axis showed the time of landfall. 116

Figure 7.7 Hovmoller diagrams of (left) $\Delta \log_{10}(-rvrv\theta)$, (middle) $\Delta \log_{10}(-vr)$ (positive means inward), (right) $\Delta \log_{10}(v\theta)$ for (a) Gordon, (b) Hope, (c) Bess, (d) Warren in the RCP8.5 Far Future run relative to the control run. (contour) showed the historical outer wind speed (unit m s^{-1}). Lines indicate (red) R17 in control run, (green) R17 in RCP8.5 Far Future, (purple) RMW in control run, (orange) RMW in RCP8.5 Far Future. Black line indicated the time when the TC enters the SCS. End of y-axis indicate the time of landfalling. x-axis showed a radius from the TC center to 1250 km radius..... 119

Figure 7.8 Hovmoller diagrams of (left) $\Delta \log_{10}(-rvrv\theta)$, (middle) $\Delta \log_{10}(-vr)$ (positive means inward), (right) $\Delta \log_{10}(v\theta)$ for (a) Gordon, (b) Hope, (c) Bess, (d) Warren in the RCP4.5 Far Future run relative to the control run. (contour) showed the historical outer wind speed (unit m s^{-1}). Lines indicate (red) R17 in control run, (green) R17 in RCP4.5 Far Future, (purple) RMW in control run, (orange) RMW in RCP4.5 Far Future. Black line indicated the time when the TC enters the SCS. End of y-axis indicate the time of landfalling. x-axis showed a radius from the TC center to 1250 km radius..... 121

Figure 7.9 Composite plots of difference in the (color) tangential wind speed (m s^{-1}) and (vector) wind (unit: m s^{-1}) at the lowest model level for (a) R17 increasing TCs and (b) R17 constant TCs averaged in all warming experiments relative to the control run. Dotted showed significantly different tangential wind between R17 increasing TCs and R17 constant TCs in 90% CI 123

Figure 7.10 Composite plots of (color) difference in AAMF ($10^6 \text{ m}^3 \text{ s}^{-2}$) and (vector) wind (unit: m s^{-1}) at the lowest model level for (a) R17 increasing TCs and (b) R17 constant TCs averaged in all warming experiments to control run. Positive AAMF means inward. Dotted represent the AAMF were significantly different bewteen the R17 increasing TCs and the R17 constant TC in 90% CI. 124

Figure 7.11 Composite plots of (color) historical wind speed (unit: m s^{-1}) and (vector) wind (unit: m s^{-1}) for (a) R17 increasing TCs and (b) R17 constant TCs, averaged across all TC selection based on order of R17 increase in all 4 warming experiments. Dotted represent the wind speed were significantly different bewteen the R17 increasing TCs and the R17 constant TC in 90% CI..... 125

Figure 7.12 Time mean of (color) historical outer wind speed beyond R17 (unit: m s^{-1}), (streamplot) historical outer wind (unit: m s^{-1}) and (vector) historical outer wind vector (unit: m s^{-1}) for (a) Mary, (b) Hal, (c) Utor, (d) Gordon, (e) Hagupit selected by the order of the percentage change of R17 in the RCP8.5 Near Future experiment. a-e were ordered in descending order of percentane change in R17 in RCP8.5 Near Future experiment. 126

Figure 7.13 Time mean of (color) historical outer wind speed beyond R17 (unit: m s^{-1}), (streamplot) historical outer wind (unit: m s^{-1}) and (vector) historical outer wind vector (unit: m s^{-1}) for (a) Bess, (b) Nuri, (c) Dujuan, (d) Warren, (e) Hope selected by the order of the percentage change of R17 in the RCP8.5 Near Future experiment. a-e were ordered in ascending order of percentane change in R17 in RCP8.5 Near Future experiment. 128

Figure 7.14 Schematic Diagram of how the historical outer wind speed controlled the variation in the change of TCs' R17 in a warmed climate. (a) showed the TC in the historical run. (b) showed TCs embedded in a historically larger outer wind speed environment. (c) showed TCs embedded in a historically smaller outer wind speed environment.....129

Figure 8.1 Schematic Diagram showing the need in incorporating the spread of the percentage change in Vmax in future climate in the statistical forecast. (a) surface temperature change in different timescale. (b) Change in intensity distribution in future climate, accounting for the increase in intensity, increase in strong TCs frequency but decrease in number of TCs. (c) Change in Vmax distribution for TCs in a warm SCS138

List of Tables

Table 3.1 25 Selected Historical TCs (14TCs selected in the Multiple Linear Regression (MLR) analysis were bolded).....	47
Table 3.2 Summary of Numerical Experiments (bracket shows the number of TC simulations under that experiment). The experiments are: Control, RCP8.5 Far Future, RCP8.5 Near Future, RCP4.5 Far Future, RCP4.5 Near Future. In total there are 125 simulations carried out.	51
Table 3.3 Historical Environmental Variables used as Regressors on Regressing each TC Characteristics	53
Table 3.4 Details of the Multiple Linear Regression Model for all warming experiments and TC characterictics. a, b, c, d, e are the slopes of each normalized regressors. Refered to Table 3.3 for the details of the acronyms.	53
Table 4.1 Mean Statistics in the SCS for the 14 Selected TCs (* and ** shows the difference between the mean of the warming experiment and the control run exceed 90% CI and 95% CI respectively)	59
Table 4.2 Mean, Standard Deviation (STD) and the Coefficient of Variation (CV) of the Mean Statistics Across all 14 TCs in the SCS (*, ** and *** shows the hypothesis that the mean of the warming experiment and the control run were different, with a statistical significance exceed 90% CI, 95% CI and 99% CI respectively) (◊ shows the hypothesis that the mean of the Far Future experiment and the Near Future experiment were different with a statistical significance exceed 95% CI)	61
Table 5.1 Selected 14 TCs according to their Category of Percentage Change in R17 in each Warming Experiments (from Largest to Smallest) (The value of the percentage change is the same as the “+” sign in Figure 4.1)	69

1. Introduction

Tropical Cyclones (TCs) and the associated strong wind, rainfall and storm surge are one of the most devastating hazards to coastal human lives and properties. They are also one of the most severe natural hazards impacting the mega-cities in the Peral River Delta Region. In 2017 and 2018, TC Hato and Mangkhut have caused 129 and 458 injuries in Hong Kong (Choy et.al., 2020). High wind speed due to TCs can destroy loose materials, and the associated flying debris can cause huge damage to buildings (Lee & Wills, 2002). TCs with a stronger intensity and larger size can also lead to higher storm surge at coastal areas (Powell & Reinhold, 2007). Therefore, understanding how TCs' intensity and size will change in an anthropogenic warmed climate in the South China Sea (SCS) are important to help reducing future TCs risks to coastal megacities in the Peral River Delta Region.

TCs are projected to have a change in intensity and size in an anthropogenic warmed climate by various methods utilizing high resolution numerical model simulation, including dynamical downscaling and pseudo-global warming (PGW) experiments (Hill & Lackmann, 2011; Knutson et.al., 2015; Gutmann et.al., 2018). Knutson et.al. (2020) have reviewed and summarized various studies on the influence of global warming to different TC characteristics. They have suggested that to a medium-to-high confidence TC intensity will increase, averaged globally, by 5%, with a range of 1-10%, in a 2°C anthropogenic warmed climate by high resolution model simulations (Knutson et.al., 2020). However, quantitative methods to describe the range of the error for the projected intensity changes have not been proposed before. Several studies have suggested a change in TC sizes in a warmed climate, but, such change is highly variable among each TC, across basins and studies (Knutson et.al., 2015; Gutmann et.al., 2018, Knutson et.al., 2020). Therefore, it is important to understand the possible range of TC intensity and size changes in responding to the same warming signal in the future climate.

The aim of this research is to present a statistical and physical understanding to the variations of the change in TC intensity and size across different TCs to the same warming signal. PGW

experiments were used to study the influence of the warming signal to 25 historical TCs in the SCS by imposing the projected thermodynamical changes in the 2035-2065 and the 2075-2099 period from the CMIP5 RCP8.5 and RCP4.5 emission scenarios. It is hypothesized that the variations of the change in TC intensity and size across different TCs to the same warming signal are related to the historical background environment experienced by a particular TC. Ertel Potential Vorticity (EPV) diagnostics were used to study how the historical environmental relative humidity influenced the changes of TC outer core size of TC Mary (1960) and Nuri (2008) in the RCP8.5 Far Future climate. Moreover, absolute angular momentum (AAM) budget analysis was used to relate the influence of the historical outer wind speed in SCS to the difference in the change of TCs' size. Through the understanding of how the background environment controls the intensity and size changes of the TCs to the warming signal in the PGW experiments, the results provide insights for quantifying the uncertainties in TC intensity and size projection brought by temporal variations of background environment due to various natural climate modes in the SCS. This can help identifying synoptic environments that can potentially lead to significantly enhancement of TC risks in the future.

This project is organized as follows. **Section 2** gave a literature review on the structure and the physics of TCs, climatology of TC characteristics in the present climate, and how the background environment influences TC characteristics. Various parameters describing the intensity and the size of the TCs were presented, and how these parameters will change in future climate were reviewed. **Section 3** described the data and methodology used in this study. **Section 4** presented the results of the PGW experiments. **Section 5** related the variations in changes of TC intensity and size under various warming scenarios to the historical environmental conditions. **Section 6** presented detailed EPV diagnostics applied to TC Mary (1960) and TC Nuri (2008) under RCP8.5 Far Future climate in order to understand the difference in their change of storm size. **Section 7** presented the AAM budget analysis results on the effects of historical outer wind speed in SCS to TC size changes under the same warming forcing. Discussions including limitations of this work are in **Section 8** and conclusions in **Section 9**.

2. Literature Review

2.1 TC structure

2.1.1 Typical Structure of a mature TC

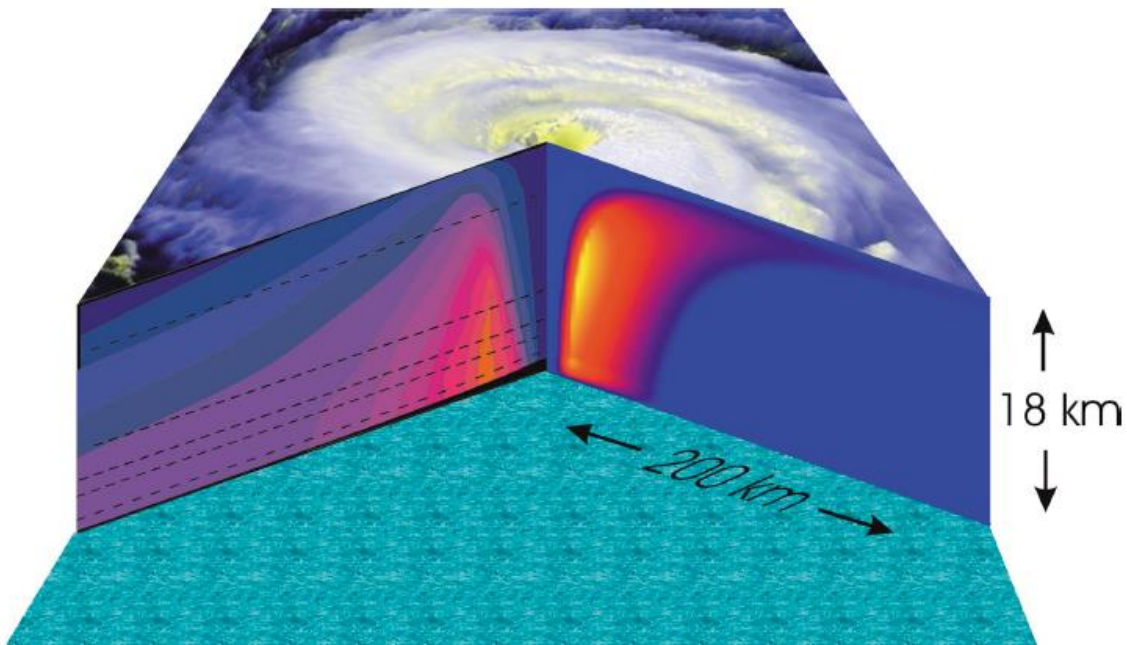


Figure 2.1 Typical Structure of a tropical cyclone. Top photo is based on a satellite photo of the cloud structure of Hurricane Fran in 1996. Right-hand cut shows the vertical velocity from a numerical model and Left-hand cut shows the tangential wind from observation. Figure from Figure 3 of Emanuel, 2003.

Figure 2.1 shows a typical cross-section and satellite photo of a tropical cyclone. At the center of the tropical cyclone there is an eye categorized by downdraft and no convective activities. Therefore, there is no cloud at the eye of a tropical cyclone. Moving slightly radially outward is the eyewall of the tropical cyclone. The eyewall has a typical radius from the TC center of about 20 km – 50 km, and is categorized by the strongest tangential wind speed and the strongest vertical motion, accompanying with strong convective activity and rainfall (Emanuel, 2003; KimBell & Mulekar, 2004). Generally, the magnitude of the tangential wind decreases with increasing radius from the center of the TC. Also, the magnitude of the tangential wind decreases from very near to the surface to the top of the troposphere. From observations, the eyewall tilts radially outward across height (see the maximum value of vertical and tangential motion across different height in the cross-section of the TC in Figure 2.1), which also matches with the fact that the tangential wind speed decrease with

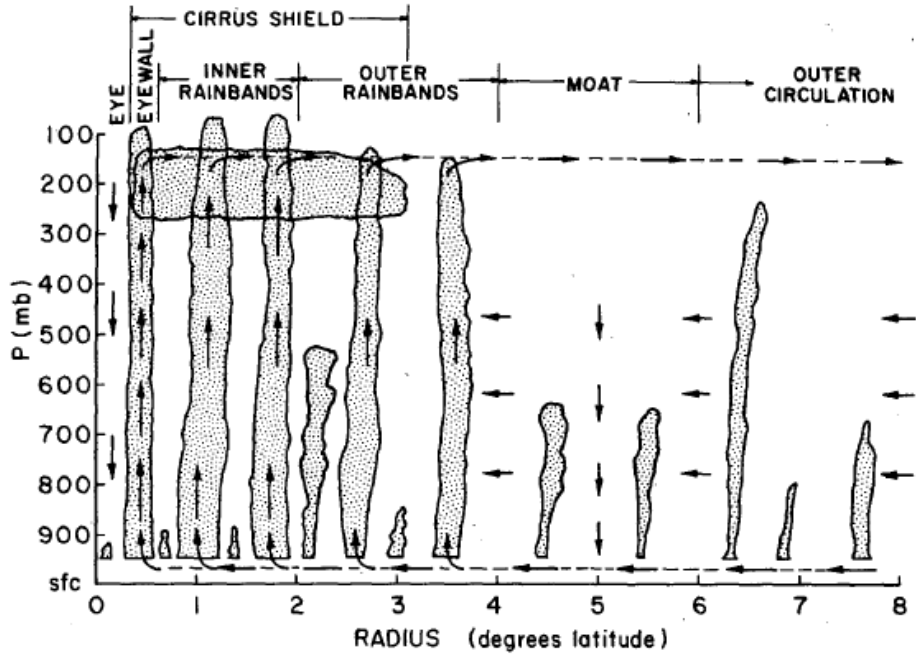


Figure 2.2 Schematic of the secondary circulation of a TC. (Figure from Figure 1 of Frank, 1977)

height in the TC. At the tropopause, the tangential wind spirals out from the center of the tropical cyclone anticyclonically (Emanuel, 2003).

Besides the tangential wind, which shapes the primary circulation of the TCs, the secondary circulation of the TCs moves radially and vertically. Figure 2.2 is a schematic diagram of the TC secondary circulation (see also Figure 2.3b as another example). Wind moves radially inward from outside of the tropical cyclone to the center of the TC except at the top of the troposphere. When the air parcel reaches the eyewall of the tropical cyclone, the air parcel rises and forms the strong vertical motion at the eyewall of the tropical cyclone. At the upper troposphere, the air parcel moves radially outward from the center of the tropical cyclone. Away from the tropical cyclone, the air usually descends back to the lower troposphere, although this descend may interrupt by localized updraft associated with inner and outer spiral rainbands of the TC (Emanuel, 2003).

Spiral rainbands are convective structure spiraled cyclonically inward to the eyewall of a TC. Clouds, precipitation and vertical motions are organized along these spiral rainbands, therefore latent heat is released at these spiral rainbands. Moreover, as these spiral rainbands propagates inward to the center of the TC, spiral rainbands can enhance the intensity of the TC by transporting moisture

and PV to the eyewall, therefore enhancing heating and convection at the eyewall of the TC (Kepert, 2010). Spiral rainbands can also be further classified into inner and outer spiral rainbands. Inner spiral rainbands are elongated and sheared within 2-3 times of the radius of the maximum wind (RMW) of the TC while outer spiral rainbands are loosely organized convective bands that can extend to far away from the center of the TC (Wang, 2008a, 2009). Figure 2.3 shows the model simulated radar reflectivity of a TC (see Wang, 2009 Figure 1 for details). There are several convective maxima denoted by locally higher radar reflectivity at 30 km, 45 km and 60 km from the center of the TC (see bottom panel). These represent the inner spiral rainbands of the TC. Beyond 60 km radius from the center of the TC, there are isolated convective maxima at 90 km and 130 km, which represents the loose outer spiral rainbands as shown in the upper panel of Figure 2.3.

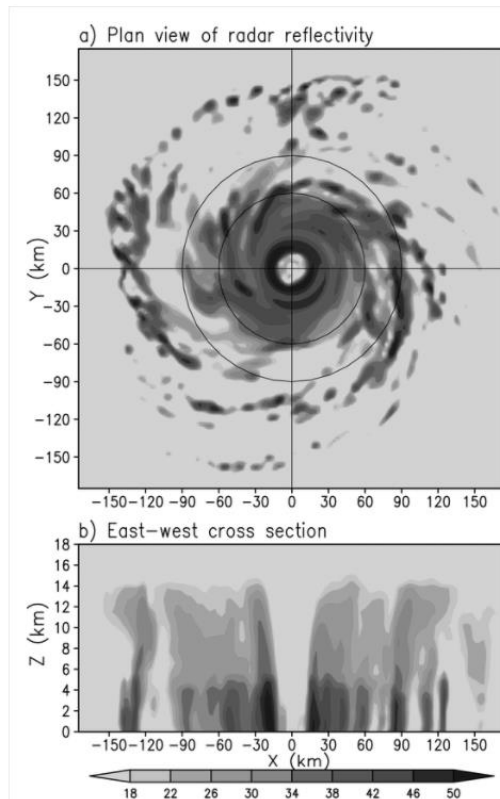


Figure 2.3 Model simulated Radar Reflectivity of top: composite, bottom: radial-vertical cross-section of a TC (Figure from Figure 1 in Wang, 2009)

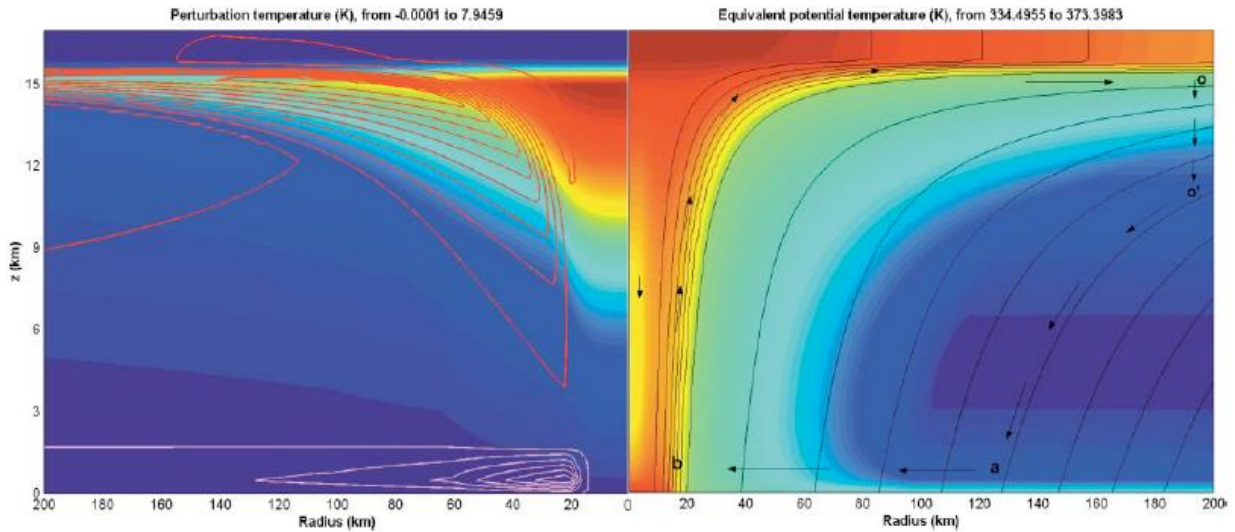


Figure 2.4 Left: Temperature anomaly of a TC (shading), radial motion of the TC (contour). Right: Specific entropy, which can be translated to equivalent potential temperature. Contour: Absolute angular momentum. Vector denotes the secondary circulation (Figure from Figure 4 of Emanuel, 2003)

Thermodynamically, TCs are typical for its “warm core” structure. Figure 2.4 shows a simple numerical model of the thermodynamical aspect of a TC (Emanuel, 2003, see also, Xu & Wang 2010a for another example). From the left panel of Figure 2.4, one can see a high temperature anomaly at the middle to upper troposphere at the center of the TC compared to similar altitude away from the TC. Here, the maximum temperature anomaly is 8 K compared to the typical tropical atmosphere (Emanuel, 2002). Subsidence motion in the eye warms the TC core adiabatically, increases the positive temperature anomaly, and by hydrostatic adjustment lower the surface pressure at the center of the TC (Willoughby, 1998). According to the hypsometric equation, the warm core structure of a TC is associated with a stretched air column, with lower pressure at the surface of the TC and higher pressure at the top of the TC compared to the value away from the TC at the same altitude, creating cyclonic flow at the bottom and anticyclonic flow at the top of a TC.

2.1.2 Physics of the TC circulation

The azimuthally averaged primary circulation of a TC above the frictional boundary layer and below the upper tropospheric outflow layer are approximately in gradient wind balance:

$$-\frac{1}{\rho} \frac{\partial P}{\partial r} + \frac{v_\theta^2}{r} + f v_\theta = 0 \quad (1)$$

where P is the air pressure, ρ is the air density, v_θ is the tangential wind and f is the coriolis parameter at the center of the TC. The first term represents the pressure gradient force along radial direction, the second term is the centrifugal force and the third term is the coriolis force. Therefore, the symmetric component of the primary circulation away from the boundary layer and the top outflow layer is a balance between the pressure gradient force pointing inward from outside of the TC and the sum of the centrifugal force and the coriolis force (Willoughby, 1990). When the pressure at the center of the TC drops, the pressure gradient force increases and the tangential wind strengthens. This wind-pressure-relationship was well documented in both observations, numerical modelling and had been addressed theoretically (Knaff & Zehr, 2007; Knutson et.al., 2015; Chavas et.al., 2017). Nevertheless, at the boundary layer of the TC, as well as the outflow layer at the top, the radial component of wind is large, and the acceleration of the radial wind is comparable to the centripetal acceleration. Therefore, gradient wind approximation breaks down and the full form of the radial momentum equation should be considered (Shapiro & Willoughby, 1982).

The secondary circulation associated with a TC is related to the source of heat and momentum associated with the TC, which can be diagnosed by the Sawyer-Eliassen equation. According to Shapiro and Willoughby (1982), heat source near the RMW induces a pair of counter-rotating gyres outside the RMW in the form of a baroclinic vortex. Air moves inward to the RMW of the TC at the lower troposphere, rises near the RMW and moves outward at the upper troposphere. Moreover, a heating source close to the RMW of the TC creates a compensating subsidence in the eye of the TC, which warms the air by adiabatic compression, forms the eye, and strengthen the primary circulation.

To understand more on the radial motion of air parcels in the TC, inertial stability is introduced. For an asymmetric vortex, the inertial stability is defined as:

$$IS = I^2 = \left(\frac{2v_\theta}{r} + f \right) \left(\frac{1}{r} \frac{\partial(rv_\theta)}{\partial r} - \frac{1}{r} \frac{\partial v_r}{\partial \theta} + f \right) \quad (2)$$

which v_r is the radial velocity, v_θ is the tangential velocity and f is the coriolis parameter. The inertial stability describes the resistance of the system to radial motion (Schubert & Hack, 1982). When the inertial stability is negative, a small radial disturbance grows and the air parcel continues to move radially. When the inertial stability is positive, the system is stable to radial perturbation and the radially perturbed air parcel moves to its original position. Schubert and Hack (1982) has shown that when the TC intensify, the inertial stability increases non-linearly and the secondary circulation is weakened. Therefore, at the lower troposphere away from RMW, as the tangential wind is small, the inertial stability is weak and the secondary circulation moves radially inward following constant isentropic surfaces (Shapiro & Willoughby, 1982). Near RMW, the system is inertially stable. As heating cannot directly change angular momentum, the flow near RMW tend to follow the outward tilted constant angular momentum surfaces as shown by the contour lines in the right figure of Figure 2.4, therefore rising vertically outward (Shapiro & Willoughby, 1982; Kepert, 2010). In the upper troposphere, the tangential wind speed is small, therefore the inertial stability is unstable, causing the wind to move radially away from the TC center.

2.1.3 Physics of the spiral rainbands

Inner spiral rainbands can be related to the vortex Rossby wave activity (Montgomery & Kallenbach, 1997; Chen & Yau, 2000; Corbosiero et.al., 2006). Vortex Rossby wave exists due to the radial vorticity gradient associated within the TC (Montgomery & Kallenbach, 1997). The positive vorticity gradient within the eyewall and negative vorticity gradient outward of the eyewall are observed in both observation and numerical modelling studies (Corbosiero et.al., 2005; Chen & Yau, 2000). Chen and Yau (2001) had found that the vortex Rossby wave are coupled with potential vorticity, water vapor mixing ratio and thus reflectivity. They had also found that bands of potential vorticity maxima are associated with strong vertical motion by frictional interactions near the top of the boundary layer (see also Wang, 2002 for another numerical modelling example). Corbosiero et.al.

(2006) also observed that Fourier transformed wavenumber 2 asymmetry from the radar reflectivity observation of the Hurricane Elena (1985) matches with the local reflectivity maxima and minima along the azimuthal direction.

Montgomery and Kallenbach (1997) had derived the dispersion relation of the vortex Rossby wave in a 2-dimensional barotropic, nondivergent inviscid flow. The dispersion relation in a 3-dimensional barotropic circular vortex in gradient wind balance was derived by Möller and Montgomery (2000). As an illustration of the wave properties, the 2-dimensional dispersion relation of the vortex Rossby wave is introduced here:

$$\omega_{VRW} = n\bar{\Omega}_0 + \frac{n}{r} \frac{\frac{\partial \bar{\zeta}_0}{\partial r}}{k^2 + \frac{n^2}{r^2}} \quad (3)$$

where k and n is the radial and azimuthal wavenumber respectively, r is the radius from center, $\bar{\Omega}_0$ is the mean angular velocity and $\bar{\zeta}_0$ is the mean relative vorticity. The azimuthal phase speed is therefore:

$$c_p^{(\theta)}_{VRW} = \frac{\omega_{VRW}}{n/r} = r\bar{\Omega}_0 + \frac{\frac{\partial \bar{\zeta}_0}{\partial r}}{k^2 + n^2/r^2} \quad (4)$$

Outside the RMW, the relative vorticity decreases with radius. Therefore, the second term in RHS of the azimuthal phase speed is negative, and the phase of the vortex Rossby wave retrogress relative to the mean tangential flow of the TC. Moreover, the radial group velocity of the vortex Rossby wave is:

$$c_g^{(r)}_{VRW} = \frac{\partial \omega_{VRW}}{\partial k} = - \frac{2kn \frac{\partial \bar{\zeta}_0}{\partial r}}{r \left(k^2 + \frac{n^2}{r^2} \right)^2} \quad (5)$$

and the radial wave number is depended on time:

$$k = k_0 - nt \frac{\partial \bar{\Omega}_0}{\partial r} \quad (6)$$

where k_0 is the radial wavenumber at $t = 0$. Outside RMW, the radial derivative of the mean angular velocity is negative, while n is positive. Therefore, the radial wavenumber k increases with time and the radial group velocity decrease with time. From the above analysis, one can observe that there exists a stagnation radius where the wave packet propagation ceases, and the vortex Rossby wave are confined close to the RMW of the TC (Montgomery & Kallenbach, 1997; Chen & Yau, 2000). The stagnation radius confining the radial extent of the inner spiral rainbands are usually 2-3 times of the RMW (Wang, 2008a, 2009). The vortex Rossby wave theory can therefore explain the convectively coupled outward moving, retrogressing inner spiral rainbands within 2-3 times of the radius of the RMW.

Unlike the inner spiral rainbands, there is no commonly accepted theory for the physics of the outer spiral rainbands. Inner spiral rainbands are located within 2-3 times of the radius of the RMW, within the rapid filament zone, while outer spiral rainbands are located outside of the rapid filament zone (Wang, 2008a). Li and Wang (2002) compared the dynamical and the thermodynamical properties of the inner and outer spiral rainbands. While the convective systems of the inner spiral rainband are associated with the convective coupled vortex Rossby wave, isolated cells of convective maxima are found in the outer spiral rainbands (Li & Wang, 2002). Moreover, unlike outward moving inner spiral rainbands, the radial movement of the outer spiral rainbands depends on the circulation of the mesoscale updraft and downdraft associated with the convective cells and the embedded TC circulation. In general, convective cells located far away from the TC center moves radially outward due to the outward gust in the boundary layer initiated by the convective downdraft of the convective cells while convective cells located nearer to the TC center moves inward to the TC inner core, following the inward radial wind of the TC (Li & Wang, 2002). Also, in the azimuthal direction, the outer spiral rainbands are organized along the tangential wind field of the TC.

2.2 Parameters quantifying a TC

Despite similar physics and system of equations that govern the circulation pattern of the TC, TCs can be of very different intensities and sizes. This sub-section introduces various parameters that are used to quantify the intensity and the size of a TC. The climatology, as well as the possible physical meaning behind these parameters were introduced.

2.2.1 Intensity

One of the commonly used parameters to quantify the intensity of the TC is the sustained wind speed at 10 m from the surface. The 10 m 1-minute sustained wind speed is used to categorize the intensity of the TC by the Saffir-Simpson Hurricane Wind Scale (Simpson & Saffir, 1974). TC intensity are categorized from tropical depression, tropical storm (TS), category 1 (C1) and up to category 5 (C5) from smaller than 17 m s^{-1} , 17 m s^{-1} to 33 m s^{-1} , 33 to 42 m s^{-1} and larger than 70 m s^{-1} respectively. Moreover, there is an international best track archive that contains the global 10 m 10-minutes mean sustained wind speed from various data providing agencies (Knapp et.al., 2010). From their report published in 2010, which included the best track data across the globe in all ocean basins from 1848-2007, the ocean basin that the highest mean 10-minutes mean sustained wind speed were found is the Western North Pacific (WNP) basin. However, the basin that had the largest area extent that the mean 10-minutes mean sustained wind speed exceeds 23 m s^{-1} is the North Atlantic basin. TCs reaching C5 are observed in all ocean basins, except the South Atlantic basin, in which only one TC is observed throughout the recorded period (Knapp et.al., 2010). The 10-minutes mean sustained wind speed are also used to compare the 10m maximum wind speed (Vmax) at each observed timestep from reanalysis data (Schenkel & Hart, 2011; Murakami, 2014).

Bister and Emanuel (1998) had derived the potential intensity, which is the theoretical upper bound of the intensity that a TC can reach given the energy generation by surface fluxes from the ocean and the dissipation in the boundary layer. The details and the relationship of the potential intensity to the environment are reviewed in *section 2.3.1*. Using the lifetime maximum potential

intensity to normalize the lifetime maximum intensity in the WNP and the North Atlantic, Emanuel (2000) had found that the cumulative frequency distribution of the lifetime maximum wind speed normalized by the potential intensity attains a linear trend in both ocean basins for TC reaching hurricane force, which mean that all TCs reaching hurricane strength have equal probability to reach an intensity from hurricane force to their potential intensity. Moreover, all TCs reaching the strength of a TS have equal probability to achieve any intensity from TS to hurricane force. Therefore, it shows a close relationship between the maximum sustained wind speed of the TC to the potential intensity of the TC across the WNP and the North Atlantic, which the potential intensity of a TC is related to the sea surface temperature and the temperature profile associate with that TC in that basin, despite detrimental environmental conditions such as high vertical wind shear and TC internal dynamics, as well as the effect of air-ocean coupling that can restrain the intensity of a TC on reaching its potential intensity (Emanuel, 2000; Wang & Wu, 2004).

Apart from the maximum sustained wind speed near the surface, the minimum sea level pressure is also used for representing the intensity of a TC (Weatherford & Gray, 1988a). The non-linear, negative relationship between the Vmax and the minimum sea level pressure are well documented by numerous researchers by aircraft, best-track data and fine resolutions satellite observations (Atkinson & Holiday 1977; Murakami, 2014). This relationship was also used for verification of the numerical model results (Knutson et.al., 2015). However, Chavas et.al. (2015) had derived a relationship between the central pressure deficit with the Vmax and the size of the TC from the gradient wind balance. Their results indicated that TCs with similar Vmax but larger size will have larger central pressure deficit and a lower minimum sea level pressure compared to the environment. Their results showed a better correlation between the predicted TC central pressure deficit and the observed TC central pressure deficit. Therefore, the minimum sea level pressure is not a pure function of Vmax, but a combination of TC intensity and outer size.

2.2.2 *Size*

Quantifying the size of the TC is important because for similar intensity, larger TC brings larger damage to a city. For example, C5 Hurricane Andrew (1992) had brought 40 deaths and \$22 billion insured losses in Miami-Dade County while C3 Hurricane Katrina had brought 1400 deaths and \$42 billion insured losses to Louisiana and Mississippi (Powell & Reinhold, 2007). However, unlike the intensity of the TC, which has a widely accepted parameter across most of the research, there are plenty of parameters used to describe the size of a TC. In general, these parameters can be divided into parameters that describe the size of the inner core and the outer core of the TC.

One of the parameters to quantify the inner core size is the radius of the eye. For stronger TC, the chance of having an eye is larger (Weatherford & Gray, 1988b). The global mean eye radius is 26 km as inferred by satellite images from 1982 to 2015 (Knapp et.al., 2018). Moreover, the mean eye radius varies among basins, with the mean eye radius is 21.7 km and 20 km in the North Atlantic from 1988-2002 best-track data and the WNP from 1980-1982 aircraft data respectively (Weatherford & Gray, 1988b; Kimball & Mulekar, 2004). The distribution of the eye radius is right-skewed in both the North Atlantic and the WNP. Despite the WNP TCs have larger eye, there are more TCs with small eye than the North Atlantic TCs (Kimball & Mulekar, 2004). The range of the distribution is also large, with the 4.6 km minimum eye radius and 50.9 km maximum eye radius in the North Atlantic basin (Kimball & Mulekar, 2004). Moreover, the eye radius is smaller when the TC is in TS strength, or reaches C5 in the Saffir-Simpson Hurricane Wind Scale, while larger in between, in both the North Atlantic and the WNP. TCs also showed a smaller eye size when the TC is intensifying than decaying, which matches with the theory that eyewall contraction occurs when the TC intensifies (Shapiro & Willoughby, 1982; Willoughby, 1990).

Another parameter that describes the size of the inner core of a TC is the 10 m azimuthally averaged radius of maximum wind (RMW). Kimball & Mulekar (2004) had found that the distribution of the RMW in the North Atlantic basin is very right-skewed, with a mean of 64.6 km

and a median of 55.5 km using the best-track data from 1988-2002. Moreover, the stronger the TC, the smaller the RMW of the TC. Their results also match the tropical cyclone theory that when a TC intensifies, the radius of the largest increase in tangential wind speed falls just inside the RMW, which reduces the size of the RMW when the TC intensifies (Willoughby, 1998). Moreover, the stronger the TC, the smaller the spread of the RMW (Kimball & Mulekar, 2004).

Compare to the size of the inner core of the TC, a variety of the radii which the azimuthally averaged wind speed reach a certain wind speed are used to quantify the size of the outer core of the TC, including the radii where the azimuthally averaged wind speed at 10 m reaches 33 m s^{-1} , 17 m s^{-1} , 12 m s^{-1} , and other wind speed are used in a variety of studies among different researchers. Noted that these radii may not necessarily correlate with each other. Merrill (1984) and Chavas and Emanuel (2010) had found that the relationship between the size of the outer core and the intensity in terms of the Vmax of the TC is not large.

Kimball and Mullekar (2004) had found that the distribution of the R17 is right-skewed in the North Atlantic, with more small TCs than large TC. Globally, the median of the R12 is 197 km while the median of the R17 is 191 km (Chavas & Emanuel, 2010; Chan & Chan, 2015). However, the mean outer core sizes are statistically different across different basins. The largest outer core size in terms of the median R17 and R12 are found in the WNP, with a value of 215 km and approximately 250 km as inferred from the QuikSCAT data from 1999-2008 (Figure 1 in Chavas & Emanuel, 2010; Chan & Chan 2015). Meanwhile, the smallest outer core size in terms of the median R17 and R12 are found in the Eastern Atlantic basin, with a value of 114 km and approximately 150 km respectively. The standard deviation of the R17 and R12 is also largest in the WNP and smallest in the Eastern Atlantic (Chavas & Emanuel, 2010; Chan & Chan 2015). Latitudinally, Kimball & Mollekar (2010) and Chavas and Emanuel (2016) had found that the R17 and the R12 of the TC increases with latitude in the North Atlantic while the R17 reaches a peak at $20\text{-}30^\circ\text{N}$ and decreases poleward and equatorward (Chan & Chan, 2012). Seasonally, the R17 of the TC in the WNP peaks in July and

October and that in the North Atlantic peaks in September and November, with smaller confidence interval for November (Kimball & Mollekar, 2010; Chan & Chan, 2012). Therefore, it can be seen that the statistics of the outer core size varies greatly among different basins.

Moreover, there are parameters to quantify the outermost boundary of the TC. One of the examples is the outer radius of the vanishing wind r_0 , which can be estimated by assuming a theoretical model from Emanuel (2004) that the radiative cooling of the outer core of the TC is balanced by the subsidence warming away from the major convective region. Chavas et.al. (2016) had analyzed the statistics for r_0 by assuming some values of the drag coefficient and the subsidence velocity, and found a median of 881 km. Largest and smallest r_0 are also found in the WNP and the Eastern Pacific respectively. The advantage of using the vanishing wind radius to quantify the size of the TC rather than the R12 is it can dampen the dependency of size to latitude (Chavas et.al., 2016).

Another example of the parameter used to quantify the outermost boundary of the TC is the averaged radius of the outer closed isobar (ROCI) (Merrill, 1984). The climatology of the ROCI averaged in the WNP and the North Atlantic is 409 km and 415 km using the data of 1957-1977 for the North Atlantic and 1961-1969 as well as 1999-2009 for the WNP (Merrill, 1984; Chan & Chan, 2012). Chan and Chan (2012) had reported a maximum of ROCI in the North Atlantic in September and November, while Merrill (1984) found that the ROCI in the North Atlantic attending its' maximum in October. This may imply an interdecadal variation for the ROCI in the North Atlantic Basin. Moreover, the ROCI and the R17 are significantly correlated with each other by a correlation coefficient of 0.54 in the WNP and 0.49 in the North Atlantic, implying that there are some relationships between the R17 and the ROCI (Chan & Chan, 2012).

2.3 Factors influencing the structure of a TC

To better predict and explain the changes of the TC in terms of its intensity and size, understanding how the internal processes and the background environmental conditions influence the TC are

important. Therefore, how the TC properties, internal processes and the background environmental conditions can affect the intensity and the size of a TC are reviewed.

2.3.1 Environmental influences on the intensity of a TC

It has long been identified that the primary source of the energy of a TC is the underlying ocean surface. TC cannot be formed at a region with ocean surface temperature smaller than 26°C, where ocean surface having a temperature below this value do not allows conditional instability from the surface to the top of the tropopause (Palmen, 1948). Moreover, Bister and Emanuel (1998) had derived the potential intensity, which is the theoretical Vmax upper bound that a tropical cyclone can achieve, by an analogy of the secondary circulation of a TC to the Carnot cycle. For an air parcel spiral into the center of the TC in the boundary layer, isothermal process occurs, with enthalpy input from the ocean surface. When the air parcel reaches the RMW of the TC, it rises along the constant angular momentum surface, adiabatic expansion occurs. At the bottom of the tropopause, the air parcel moves outward as an isothermal process. Assuming the cycle is closed by the adiabatic compression far away from the center of the TC, the potential intensity of the TC can be estimated by:

$$V_{max}^2 = \frac{C_K}{C_D} \frac{T_s - T_0}{T_0} (K_0^* - K) \quad (7)$$

where C_K and C_D is the transfer coefficient of enthalpy and momentum, T_s is the sea surface temperature, T_0 is the outflow temperature at the angular momentum surface passing through the locus of the maximum wind, at the point where the tangential wind associated with the TC vanishes. K_0^* and K is the saturated enthalpy of the sea surface and the actual enthalpy of the air respectively (Bister & Emanuel, 1998). When the sea surface temperature (SST) is larger, the surface enthalpy flux is larger when the actual enthalpy in the air is kept constant, and the TC intensity is larger, as shown by the last term. Also, the middle term in the RHS act like a thermodynamic efficiency. When the temperature difference between the ocean surface and the temperature at the outflow layer is large,

the TC intensity is large (Emanuel, 2003). Moreover, C_D increases with wind speed at low wind speed and decrease with wind speed at $C_D > 33 \text{ m s}^{-1}$ (Powell et.al., 2003). Given that the actual intensity of the TC has equal probability to reach any portion relative to the potential intensity, the potential intensity, as well as the dependence of the potential intensity to the SST and the atmospheric temperature profile, serves as two of the most important environmental controls of the intensity of a TC (Emanuel, 2000).

Tuleya et.al. (2016) had modelled the sensitivity of TCs intensity to the change in the SST and the atmospheric temperature profile by idealized experiments using the GFDL model, with the inner nest resolution of approximately 6km. By perturbing the SST and the atmospheric temperature profile under a background environment of the North Atlantic basin, while keeping the relative humidity (RH) constant, they had found an increase in TC intensity by increasing the SST while a decreasing TC intensity by increasing the upper tropospheric warming than the surface warming. For example, a 2°C increase in SST and an increase in atmospheric temperature at 300mb relative to 1000mb by 4°C, which translated to an increase in atmospheric stability, will result in a decrease in minimum sea level pressure by 8hPa. Moreover, an increase in SST by 2°C with constant warming for the atmospheric temperature profile results in a 16hPa decrease for the minimum sea level pressure. Therefore, the increase in atmospheric stability dampens the effect of increasing SST to the increase in TC intensity (Tuleya et.al., 2016). Similar results were also obtained by an idealized experiment using an older version of GFDL model (Shen et.al., 2000).

Moreover, Tuleya et.al. (2016) had compared the dependency of TC intensity on the SST and the atmospheric stability to the potential intensity theory and found an underestimation of the TC intensity dependency by the potential intensity theory to the atmospheric stability at high TC intensity region. At higher intensity, the potential intensity becomes mostly a function of SST. They had augured the inaccurate result of the potential intensity in predicting the effect of atmospheric temperature profile stabilization to the intensity of the TC is because of the large sensitivity of

potential intensity to the height of the outflow layer, which may be one of the limitations of the potential intensity theory.

Another environmental conditions that can hinder the development of a TC is strong vertical wind shear. The vertical wind shear is generally defined as the difference in wind speed between the lower troposphere and the upper troposphere, such as the wind speed difference at 800hPa and 200hPa defined in the study of Wong and Chan (2004). Gallina and Velden (2002) had analyzed the wind field of TCs in the reanalysis data from 1996-1998 and found that TC weakens in an environment with large vertical wind shear. TCs in the WNP and the North Atlantic will be weakened when the vertical wind shear is larger than $9\text{-}10 \text{ m s}^{-1}$ and $7\text{-}8 \text{ m s}^{-1}$ respectively (Gallina & Velden, 2002). Moreover, Wong and Chan (2004) had performed idealized, convective permissible, full physics experiment to model the TC intensity difference in different magnitude of easterly vertical wind shear by the mesoscale model (MM5), with the finest resolution of 4 km. They had found that TCs weakens significantly when the easterly wind shear is larger than 8 m s^{-1} . Tuleya et.al. (2016) had further studied the sensitivity of TC intensity to the westerly wind shear, and found similar pattern of decreasing TC intensity at large vertical wind shear magnitude to initially weak TC. Strong TCs were found to be more sustainable to weak vertical shear than weaker TCs while a value of vertical wind shear magnitude larger than $10\text{-}15 \text{ m s}^{-1}$ can cause a rapid decrease in TC intensity (Frank & Ritchie, 2001).

When the vertical wind shear is strong, the upper storm center is displaced away from the lower TC center. Wavenumber 1 asymmetry are developed at the downshear left along the shear direction due to the advection of the upper troposphere potential vorticity from the center of the TC. Then, the high equivalent potential temperature and the potential vorticity were mixed to the surrounding environment rather than to the warm core of the TC, which weaken the warm core structure and raise the surface pressure (Frank & Ritchie, 2001). If the vertical wind shear persists, the vertical tilt of the storm center grows and the TC is then weakened to a weaker steady state (Wong

& Chan, 2004). Moreover, colder environmental air at the upper troposphere will advect into the warm core of the TC by the strong wind shear, therefore weakening the TC structure (Wong & Chan, 2004). However, diabatic heating due to the vertical motion at the down-tile side of the TC reduces the cold anomaly at the down-tile side of the TC formed by the vertical wind shear. For an intense TC, the inertial stability is stronger and the vertical penetration depth of the secondary circulation is larger, which even stronger vertical wind shear is needed to tilt the vertical axis of the storm center, therefore stronger TC resists more to the vertical wind shear (Tuleya, et.al., 2016).

When the SST warming is included, TCs intensity increase can be mostly determined by the increase in SST for stronger TC even in an environment with large vertical wind shear (Tuleya, et.al., 2016). TCs intensity increase more in an environment with SST warming and easterly vertical wind shear than in westerly wind shear when the effects of ocean coupling are also included. In an environmental with easterly wind shear, a TC moves faster and the ocean coupling effect is weaker, which reduces the decrease in TC intensity due to air-sea interaction (Tuleya, et.al., 2016).

The effects of air-ocean coupling are important to the intensity of the TC. When the intensity of the TC increases, strong turbulent mixing induced by the increased wind stress exerted to the ocean surface cause the upwelling of cooler ocean water from the thermocline, thus lowering the SST and reduce the intensity of the TC (Bender & Ginis, 2000). This negative feedback mechanism is sometime called “cold-wake”. The decrease in SST due to air-ocean coupling reduces the evaporation and the convergence of high equivalent potential temperature air into the center of the TC, therefore reducing the moist static energy and the intensity of the TC (Bender & Ginis, 2000). Bender and Ginis (2000) had compared the modelled TC intensities with and without the coupling to the ocean, and found a significant improvement in simulating the TCs’ intensity, by a full physics simulation using GFDL model coupled with the 3-dimension, primitive equation Princeton Ocean Model, despite a course horizontal resolution of about 18.5 km, which cannot resolve the inner structure of the TC. For example, the modelled intensity changes of Hurricane Gilbert (1988) with and without ocean

coupling was 10 hPa and 25 hPa deepening within 48h of integration respectively. The ocean-coupling included model result was closer to the observation of 4 hPa deepening (Bender & Ginis, 2000). Moreover, their simulations of ocean-coupling reassembled the larger cold-wake for TCs with lower translation speed, which was observed by float measurements and analyzed by Fu et.al. (2014).

The depth of the 26 °C isotherm also influences the ability of reducing TC intensity due to ocean cold wake. Lin et.al (2013) had studied the change in the intensity of 3 TCs, namely Megi, Fanapi and Malakas in 2010 in the WNP basin. The 26 °C isotherm for these 3 TCs were located at a depth of 110 m, 70 m and 45 m. During the passage of Megi, the air-sea temperature and humidity remains nearly constant, and the enthalpy fluxes increased with increasing wind speed. Therefore, the intensity of TC Megi reached C5. Compared to Megi, Fanapi and Malakas were located at a region where the 26 °C isotherm are much closer to the sea surface. Therefore, SST cooled due to cold wake, reducing the enthalpy fluxes from the ocean to the atmosphere, and limit the intensities of Fanapi and Malakas (Lin et.al., 2013). To sum up, slower translating TCs with a shallower 26°C isotherm limits the intensity of the TCs.

2.3.2 Environmental influences on the outer core size of a TC

Perhaps the most obvious dependency of the TC size to the environment is the dependence to the Coriolis parameter, as observed by the increasing R12 of the TC with latitude in the North Atlantic basin (Chavas et.al., 2016). However, observational analysis shows that TCs are the largest at a latitude of 20°N – 30°N in the WNP basin (Chan & Chan, 2012). The dependency of TC size to the latitude may varies, and not increasing monotonically among all basins. Chan and Chan (2014) had analyzed the change of TC size under different latitude by idealized experiments on synthetic vortexes using the Weather Research and Forecasting model (WRF) version 3.3.1 with a 9 km horizontal resolution. The concept of the azimuthally averaged absolute angular momentum flux (AAMF), was used to diagnose the effect of the latitude to the outer core size of the TC, which the AAMF is defined as:

$$\overline{AAMF} = r\bar{v}_r\bar{v}_\theta + r\bar{v}'_r\bar{v}'_\theta + \frac{f_0 r^2 \bar{v}_r}{2} + \frac{r^2 \bar{f} v'_r}{2} \quad (8)$$

where v_r is the radial wind, v_θ is the tangential wind, f_0 is the planetary vorticity at the TC center, the overbar denotes azimuthally average, and the prime denotes the asymmetry (eddy) from the azimuthally averaging. The first term and the second term indicate the symmetric relative angular momentum flux (SRAMF) and the asymmetric (eddy) relative angular momentum flux (ARAMF) respectively while the third term and the fourth term are the symmetric Coriolis torque (SCT) and the asymmetric (eddy) Coriolis torque (ACT) respectively. Moreover, the inertial stability (equation 2 in this study, assuming azimuthal symmetry, equation 6 in Chan and Chan 2014) increases with increasing planetary vorticity. TCs at a higher latitude have larger azimuthally averaged AAMF due to the increase of the SCT, albert a larger inertial stability and a smaller SRAMF. As the TC size growth increases when the AAMF increases, the compensating effect of increasing SCT but decreasing SRAMF results in an optimum latitude for largest TC size at 25°N (Chan & Chan, 2012, 2014). However, Chan and Chan also argued a difference of optimum latitude for maximum size growth of different TC. This, together with the difference in the synoptic environment that can change the AAMF, may be able to explain the difference in the pattern observed in the WNP and the North Atlantic basin, but the details should be further investigated in the future. Moreover, one should be noted that a theoretical upper bound of the potential intensity divided by the Coriolis parameter to the r_0 may exists, despite most of the TCs have a size below this theoretical upper bound (Chavas et.al., 2016).

Apart from the latitude, another important environmental condition that can influence in TC size is the boundary layer AAMF (Merrill, 1984; Chan & Chan 2013, 2015). From the statistical analysis of the scatterometer wind field data in the WNP from 1999-2009, Chan and Chan had divided the TCs wind field into groups of increasing or decreasing size or intensity, and found that size increasing TCs are associated with an increase in boundary layer AAM import within 24 hours during the TCs' lifetime (Chan & Chan, 2013). Most of the lower tropospheric AAMF into the TC circulation

are distributed in the outer core due to the high inertial stability of the inner core, which hinder radial movement of air parcel to import AAM (Holland & Merrill, 1984). Moreover, Chan and Chan (2015) had studied the effects of enhanced initial outer tangential wind speed at the outer core of the TC using the WRF version 3.3.1 idealized experiments, with a horizontal resolution of 9 km. They had found that an enhancement in initial outer tangential wind beyond R17, R9 and R5 increases the SRAMF and SCT between the 200-400 km radius, which then increases the AAM import tendency between the 200-400 km radius, and the size of the TC in terms of R17 increases rapidly when compared to the control run (Chan and Chan, 2015). If the initially enhanced outer tangential wind speed is closer to the R17, the R17 of the TC increases earlier during the model simulation hours (Chan & Chan, 2015). The enhancement of the initial outer tangential wind also induces subsequence enlargement of the TC wind field, which indicates that the onset of larger outer tangential wind speed can subsequently increase the TC size in the idealized experiment (Chan and Chan, 2015).

As the boundary layer AAMF is important to TC size changes, various researchers had analyzed the synoptic environment associated with TCs that had a large increase in their size during their lifetime. Liu and Chan (2002) had found that large TCs in the WNP are associated with a strong southwesterly flow at the south of the TC, which most of them were recurving to higher latitude (Liu & Chan, 2002). Similar monsoonal westerlies originated equatorially were also observed to be associated with larger TCs in the southern hemisphere (Holland & Merrill, 1984). Moreover, large TCs can be embedded westward of the subtropical ridge throughout the TC season, and eastward of the northern winter monsoon in the late season when the TCs are recurving (Liu & Chan, 2002). The enhanced outer tangential wind speed due to the subtropical ridge and the anticyclone to the west of the TC can increase the AAMF into the TC, which expand the TC wind field (Chan & Chan, 2012). On the other hand, small TCs are usually located south of the subtropical ridge (Chan & Chan, 2012).

Despite the importance of the dynamical influence of the environmental wind field to the size of the TC, the thermodynamical influences of the environmental relative humidity (RH) are also

important to control the TC size. Hill and Lackmann (2009) had analyzed the difference in TC size under different RH environment using idealized experiments by WRF version 2.2, with an inner most horizontal resolution of 2 km (Hill & Lackmann, 2009). By altering the outward decaying profile of the environmental RH between 100-150 km from the TC center initially, they had found an increase in TC size in terms of R33 (Figure 4 in Hill and Lackmann 2009) and the outer core size (Figure 5 in Hill and Lackmann 2009) for increasing environmental RH. When the environmental RH is larger, spiral rainband activities are stronger and the spiral rainbands spread to a larger horizontal extend, which produces more EPV by an enhancement of the diabatic PV production. Therefore, more EPV are transported to the inner core of the TC and expand the TC size (Hill & Lackmann, 2009). Moreover, the broadening of the central EPV tower due to an increase in radial influx of EPV further enhanced and expanded the inner spiral rainbands, which then enhance the inner spiral rainband activities, causing a positive feedback. The increase in outer spiral rainband activities can also increase the local EPV produced by diabatic PV tendency, and lower the sea surface pressure by hydrostatic adjustment from diabatic heating of the air column, which both of them can increase the TC size (Wang, 2008).

Ma et.al. had carried out idealized experiments using the background dynamical and thermodynamical state of the WNP and the North Atlantic, which the WNP environment is moister and the atmosphere is more unstable compared to the North Atlantic (Ma et.al., 2019). Idealized experiments result from the WRF version 3.3, with the inner most horizontal resolution of 3 km, revealed a decrease in TC size difference between the TCs in the WNP and the North Atlantic environmental condition, but with an averaged environmental moisture content (Ma et.al., 2019). Therefore, the environmental moisture content, which can be translated to the RH by the Clausius-Clapeyron equation, is an important factor in controlling the TC size. Higher atmospheric moisture content in the WNP than the North Atlantic basin caused the TCs in the WNP to be larger compared to that in the North Atlantic basin.

Relative SST, which is defined as the difference between the local SST and the averaged tropical mean SST, is another environmental condition that can control the TC size. Chavas et.al. (2016) had found a positive statistical relationship between the R12 and the r_0 to the relative SST, which is invariant to the intensity category of the TCs. Moreover, Ma et.al. had found that the SST and atmospheric temperature profile difference between the WNP and the North Atlantic basin contribute a time more to the size difference of the TC between the two basins as compared to the difference in the specific humidity (Ma, et.al., 2019). As the relative SST are found to be highly correlated to the local mid-tropospheric RH, the thermodynamical effects of the relative SST and the atmospheric temperature profile can then be translated into the effect of RH to the TC size by the Clausius-Clapeyron equation (Stephens, 1990).

2.3.3 Environmental influences on the inner core size of a TC

By far there was little research on how the synoptic environment affects the RMW of the TC. Most of the studies relate the change of the inner core size to the spiral rainband activities. Wang (2009) had performed idealized experiments on the effect of modifying the diabatic heating associated with the outer spiral rainband activities to the RMW of the TCs using a nonhydrostatic, convective resolving, primitive equation model TCM4 with an inner most horizontal resolution of 2.5 km. He had found that when the diabatic heating is enhanced, or the diabatic cooling is reduced at the outer core, the outer spiral rainband activities become stronger, which warm the air column and reduced the surface pressure by hydrostatic adjustment. The reduction of radial pressure gradient enlarges the RMW of the TC. Opposite mechanism occurs when the diabatic cooling is enhanced or the diabatic heating is reduced at the outer core, which reduce the RMW of the TC (Wang, 2009). He had also proposed the high sensitivity of outer spiral rainband activities to the environmental RH, which was confirmed later by Hill and Lackmann (2009) and Xu and Wang (2010b) that larger RH environment will promote the spiral rainband activities and enlarge the RMW by eyewall replacement when the outer spiral rainbands move into the inner core to form concentric eyewall (Wang, 2009; Hill & Lackmann, 2009, Xu & Wang, 2010b).

Apart from the environmental RH, surface entropy flux can also affect the inner core size of a TC. By removing the surface entropy flux from the ocean at a radius away from the TC center, idealized experiments were performed by Xu and Wang (2010a) on studying the consequences to the inner core size using TCM4, with an inner most horizontal resolution of 2.5 km (Xu & Wang, 2010a). For a reduction of surface entropy flux within the eye of the TC, the RMW increases due to the reduction of equivalent potential temperature within the eye and thus weakening of the circulation and causing eyewall expansion (Xu & Wang, 2010a). Moreover, reducing the surface entropy flux outside the RMW of the TC reduces the convective active potential energy (CAPE), which suppress the rainband activities and causes eyewall contraction. Moreover, outer spiral rainbands are usually assumed to be blocking the boundary layer inflow by the convective updraft at the outer core (Wang, 2008). However, Xu and Wang (2010a) had found a decrease in boundary layer inward radial wind for weaker outer spiral rainband activities (Figure 14 in Xu & Wang, 2010a). The decrease in inward radial wind limits the radial influx of vertical absolute vorticity in the tangential momentum equation, then reduced the tangential acceleration outside the RMW, therefore reduce the RMW (Xu & Wang, 2010a). To sum up, the increase in outer spiral rainband activities reduces the radial pressure gradient near the RMW by hydrostatic adjustment and increase the tangential acceleration outside the RMW by increasing radial inflow in the boundary layer, therefore increase the RMW of the TC. Yet, the role of the spiral rainbands to the radial flow of the TC in the boundary layer was still remained unsolved (Kepert, 2009).

2.3.4 Internal properties and processes influence on the intensity of a TC

Asymmetries near to the RMW of the TC can reduce the intensity of a TC. One of the most important asymmetries that reduces the intensity of a TC is the formation of concentric eyewall and the secondary eyewall formation (Camp & Montgomery, 2000). Willoughby and Shoreibah (1982) had analyzed aircraft data of TC wind field measurements, and found a formation of concentric eyewall outside of the primary eyewall together with the dissipation of the innermost primary eyewall before the weakening of the TC intensity (Willoughby & Shoreibah, 1982). Moreover, the convective

downdraft associated with the secondary wind maxima creates surface divergence and outflow, which slowly erase away the primary eyewall (Kepert, 2009). Hawkins and Helveston (2004) had found that about 80% and 40% of the TC in the WNP and the North Atlantic experienced secondary eyewall formation and eyewall replacement in their lifetime by analyzing microwave satellite imagery from 1993-2003 (Hawkins & Helveston, 2004). The secondary eyewall is originated from the inward propagating inner spiral rainbands in the rapid filamentation zone (Wang, 2008; Hill & Lackmann, 2009).

2.3.5 Internal properties and processes influence on the outer core size of a TC

Chan and Chan (2012) had analyzed the monthly mean TC size in the WNP, and found that months with largest mean TC size matches well with the monthly mean TC lifetime. They have proposed that TCs with longer lifetime have more time to expand the wind field in a favorable environment by angular momentum transport and moisture convergences (Chan & Chan, 2012). This argument was later proved by idealized experiments of Chan and Chan (2014), that despite initially larger TCs grow faster to a larger size, initially smaller TCs can still grow to a large TC given long enough lifetime by increasing local AAMF (Chan & Chan, 2014).

Another property associated with the TC that can influence the size difference among each TC is the initial size of the vortex when the TCs are formed. Lee et.al. (2010) had found that most of the small TCs remain small and large TCs remain large in the WNP by observational data from 2000-2005 (Lee et.al., 2010). In particular, 67%, 50% and 72% of small, medium and large TCs remains in the same size category throughout their lifetime. Chan and Chan (2014) had studied the physical mechanisms behind the constant size evolution of the TC by idealized experiments using WRF version 3.3.1, with the horizontal resolution of 9 km. they had found that larger vortex is associated with larger AAM transport into the vortex compared to the smaller vortex. Despite the larger frictional dissipation associated with the large vortex, the larger radial advection of AAM compensate the dissipation effect, causing larger TC remains large throughout their lifetime.

2.3.6 Internal properties and processes influence on the inner core size of a TC

Very few studies stressed on the influences of the TC properties that can affects the inner core size of a TC. One of the most important properties that controls the inner core size of a TC is the initial size of the vortex (Xu and Wang, 2010b). They had performed idealized experiments on how the initial size of the TC caused differences in the RMW using the TCM4, with an inner most horizontal resolution of 2.5 km. Larger initial vortex have a wider wind field, which enhance the surface entropy flux and favors outer spiral rainbands activities. Reduction of pressure gradient near the RMW was then occurred due to the hydrostatic adjustment at the outer core. Then, inward radial wind near the RMW of the TC expands to a larger radial extend, which increase the local AAM tendency and expand the RMW (Xu & Wang, 2010b). Moreover, the expansion of RMW indicates an expansion of absolute vorticity near the core of the TC, which further enlarge the RMW by radial advection of AAM as seen in the symmetric radial advection of AAM in the AAM budget equation. Therefore, the initial vortex size plays an important role in determining the outer spiral rainband activities, thus the RMW size.

2.4 Impact of global warming to the characteristics of TCs

As TCs can bring huge destruction to human life, properties and impact to coastal environment, it is necessary to review the effects of global warming to the intensity and the size of the TCs due to the modification of the synoptic background environment. However, it should be reminded that caution is needed when reviewing the results from numerical models with different model resolution. It was shown that TC intensity distributions were better simulated using high-resolution numerical models (Wehner, et.al., 2015; Walsh, et.al., 2016, Knutson, et.al., 2019). Moreover, a horizontal resolution of 4 km or below can produce reasonable intensity and track compared to the observation while a horizontal resolution of 2 km or below is needed to resolve the structure and evolution of the eye (Gentry & Lackmann, 2010). Therefore, the influences of global warming to the TC intensity and size are reviewed in this section with the results from high-resolution numerical models.

2.4.1 Intensity changes

Various high-resolution numerical modelling studies predicted an increase in global mean Vmax for a 2 °C warming by a mean of 5%, with a range of 1% to 10% globally (Knutson et.al., 2020). For example, Knutson et.al (2015) had used the method of dynamical downscaling to model the TC changes by GFDL with a horizontal resolution of 6 km with ocean coupling, which the GFDL High Resolution Atmospheric Model of 50 km resolution were used to generate the initial TCs and the boundary conditions of a projected climate in 2081-2100 under the RCP4.5 scenario relative to the present-day climate. They had found an increase in global Vmax of all hurricanes by 3.6% (Knutson et.al., 2015). Moreover, the change in the intensity of the TC varies across each ocean basin, which more pronounced increase in intensity can be found in the Northeast Pacific and the WNP, with an increase of 8% and 7% for TS respectively. They had predicted a decrease in TS intensity in the Southwest Pacific for 5.6% (Knutson et.al., 2015). Also, Hill and Lackmann (2011) had carried out a large ensemble of 2 km idealized simulations of typical North Atlantic TC in 2090-99 climate under the CMIP3 B1, A1B and A2 emission scenario, and found an increase in global TCs central pressure deficit of 11%, 12% and 19% respectively (Hill & Lackmann, 2011).

The increase in TC intensity scales to the increase in the SST in the future climate projected by different emission scenario. They had also observed the dampening of increasing TC intensity of about 50% by an increase in atmospheric stability, which is generally projected in the future climate by GCMs despite large variance at the upper troposphere, compared to an increase in SST only (Hill & Lackmann, 2011). This matches the results of the idealized experiments from Tuleya et.al. (2016), which an increase in the SST by 2°C together with upper atmosphere warming of 4°C damped the increase in TC intensity by 50% compared to pure surface warming (Tuleya et.al., 2016). Moreover, the increase in moisture in the troposphere enhance the diabatic PV production associated with the deep convection near the eyewall, which increases the intensity of the TC (Hill & Lackmann, 2011). To sum up, the increase in SST and moisture in the troposphere enhance the TC intensity in a warmed climate, while the stabilization of the troposphere damped the effect.

2.4.2 Size changes

Compared to the more robust result of increasing TC intensity in an anthropogenic warmed climate in the future, the prediction of size changes in a warmer future climate have lower confidence because they are more diverse among different studies (Knutson et.al., 2020). Knutson et.al. (2015) had predicted no significant change in global mean TC size in terms of R12, with a mean increase of 1% globally in their dynamical framework (Knutson et.al., 2015). However, there were large variations across different basins. TC size decrease in the WNP by 8% but increase by 7% to 15% in other basins except in the North Indian basin, which the TC size remain nearly constant. Yamada et.al. (2017) had predicted a statistically significant increase of global TC size in terms of R12 by about 10% when the TCs attain their maximum intensity, using a nonhydrostatic global atmospheric model of a horizontal resolution of 14 km with no cumulus parametrization in the 2075-2099 climate forced by the CMIP3 A1B emission scenario (Yamada, et.al., 2017). However, their results should be viewed in caution as numerical models with coarser resolution tend to simulate a larger TC (see Figure 1 in McDonald et.al., 2005). This should be possible because the size of the TC can be determined by the radial distribution of pressure gradient, which can be sensitive to the finer scale convective activities at the spiral rainbands and the eyewall (Wang, 2009, Xu & Wang, 2010b). Convective unresolvable horizontal resolution will therefore introduce uncertainties in the prediction of future TC size changes.

Moreover, Gutmann et.al. (2018) had used another approach, namely the pseudo-global warming method (PGW), to access the changes in TC size in terms of R33 in the projected 2075-2099 climate under the CMIP5 RCP8.5 emission scenario in the North Atlantic basin by WRF version 3.4.1 with a horizontal resolution of 4 km, which is convectively resolvable (Gutmann et.al., 2018). They had found no significant changes for R33 in the future climate, despite large variations among different TCs. In 22 simulated TCs, 4 of them had a significant increase in R33 while 2 of them had a decrease in R33 significantly. They had also pointed out a possible relationship between the location of the storm and the changes in TC size, yet their data was not sufficient to test their hypothesis

(Gutmann et.al., 2018). This serves as one of the literature supports for the hypothesis of this research that TC intensity and size variations across different TCs in the same future climate projection are related to the historical environment associated with that TC.

Very few studies had discussed the changes in inner core size due to global warming. Careful research from the author of this research had found only one paper addressing the changes of inner core size from Kanada et.al. (2013). They had used a convective permitting, nonhydrostatic model with a horizontal resolution of 2 km to study the changes of inner core structure of 6 extremely intense TCs near Japan in 2075-2099 climate under the CMIP3 A1B emission scenario. A significantly decrease of mean RMW across the 6 TCs by 30%, from 54 km to 38 km and 56 km to 39 km with 2 different planetary boundary layer parametrization schemes in future climate (Kanada et.al., 2013). Moreover, the boundary layer inflow intrude more inward and overshoot into the eye of these extremely intense TCs, despite similar magnitude of radial inflow in the future climate compared to the present day climate. However, the horizontal resolution adopted in their numerical model (2 km) was not enough to fully simulated the structure of the RMW, as well as some finer-scaled physical mechanisms that could alter the size of the RMW (Gentry & Lackmann, 2010). A recent paper from Ren et.al. (2022) showed the simulated RMW of a TC converges when the model horizontal resolution was between 500 m to 200 m. Therefore, more researches with finer horizontal resolution adopted are needed to understand the robustness of RMW contraction due to global warming for TCs with different intensities.

3. Data and Methodology

As seen in the literature review, the background environment plays a strong role in determining the climatology of the TC intensity and size. Moreover, the change in background environment, such as the change in SST, atmospheric stability, RH and the background synoptic wind field due to anthropogenic warming may increase the intensity and size of the TC in the future. Yet, reviews on the literatures revealed that there are uncertainties on how the changes in the future atmosphere and ocean due to global warming can influences the TC characteristics. Moreover, large uncertainties arise in predicting the changes in TC outer core size in the future climate among different TCs, as seen in Gutmann et.al. (2018). Therefore, the aim of this research is to understand why there are large differences in the changes of TC intensity and size among each TC, given that a uniform warming forcing is imposed to the historical environment. Our hypothesis is that *the historical atmospheric and oceanic conditions that the TC was embedded in controlled the future changes of TC intensity and size among each TC to the same warming signal, thus result in large variations in TC intensity and size prediction among each TC used in an anthropogenically warmed future climate.* This section

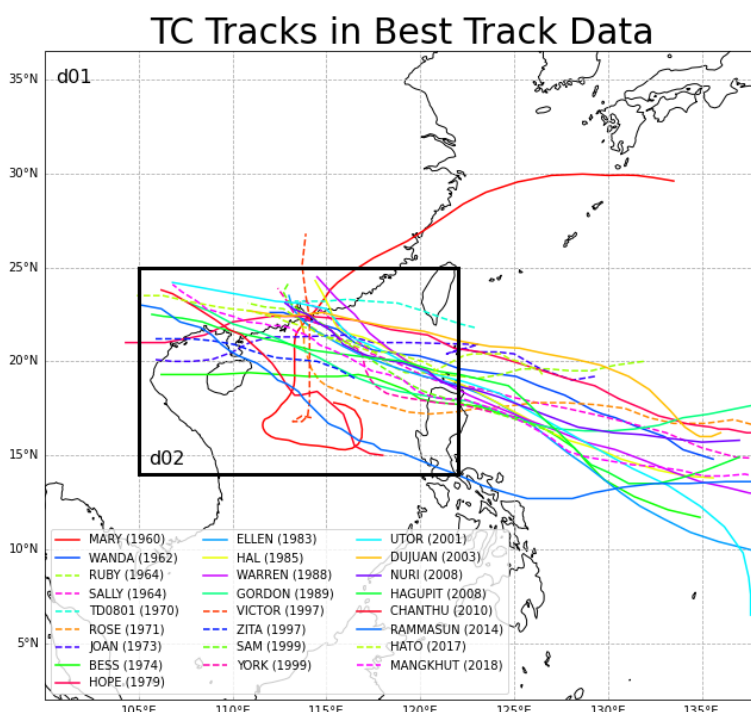


Figure 3.1 Historical Tracks of the TC selected from the Best Track data. Solid line showed the 14TC studied in the Multiple Linear Regression (MLR) analysis. Figure boundary (labeled as d01) showed the outer domain and black rectangle (labeled as d02) showed the inner domain of the WRF model..

introduces the data and methodology used to analyze the differences in the percentage change of TC intensity and size in the warming climate among each TCs, as well as establishes statistical relations to the historical environmental conditions and diagnoses the physics behind the differences in TC intensity and size changes in the future climate in the SCS Region.

3.1 Model configuration

3.1.1 TC selected

A total of 25 TCs were selected to examine the changes of their intensity and size in the future climate under different predicted emission scenarios. The name and the year of occurrence of the TCs are listed in Table 3.1. Best-track data from the Hong Kong Observatory were used to locate the historical tracks except for Mary (1960) because the Hong Kong Observatory data started in 1961. For Mary, best-track data from the China Meteorological Administration (CMA) were obtained from the International Best Track Archive for Climate Stewardship program (IBTrACS) (Knapp et.al., 2010). The tracks of the TCs are shown in Figure 3.1. These selected TCs had entered the SCS and made their landfall at the Southern China. Moreover, the selection of these 25 TCs covered a wide range of genesis location. For example, Mary (1960) was born in the SCS, while Ellen (1983) was born near the dateline. Also, the selected TCs have spanned across 58 years, and from June to October. This selection was therefore believed to represent possible interdecadal, interannual and monthly variations of TC characteristics.

Table 3.1 25 Selected Historical TCs (14TCs selected in the Multiple Linear Regression (MLR) analysis were bolded)

Year	1960	1962	1964	1964	1970	1971	1973	1974	1979
Name	Mary	Wanda	Ruby	Sally	TD0801	Rose	Joan	Bess	Hope
Year	1983	1985	1988	1989	1997	1997	1999	1999	2001
Name	Ellen	Hal	Warren	Gordon	Victor	Zita	Sam	York	Utor
Year	2003	2008	2008	2010	2014	2017	2018		
Name	Dujuan	Nuri	Hagupit	Chanthu	Rammasun	Hato	Mangkhut		

3.1.2 WRF Model

The Advanced Research Weather Research and Forecast Model (WRF-ARW) version 3.7 was used to simulate the selected 25 TCs, which were embedded in their associated historical background environment, as the control run (Skamarock et.al., 2008). Historical atmospheric, ocean and surface properties for the TC cases before 1979 were obtained from the ECMWF twentieth century reanalysis hourly data (ERA-20C) 6 hourly while the fifth generation ECMWF reanalysis hourly data (ERA5) for each 6 hours were used for the TC cases since 1979 as the initial and boundary conditions of the control run (Poli. P. et.al., 2016; Hersbach, H. et.al., 2018).

2 nested domains were set up with one-way nesting, with a horizontal resolution of 15 km and 3 km for the outer and inner domain respectively (the domain size is 339×249 and 400×580 grid points respectively). Reason for choosing 3 km as the inner domain horizontal resolution but not finer scale was a balance between limited computer resources and the ability to resolve convection and therefore a better representation of TC intensity (Gentry & Lackmann, 2010). Noted that a horizontal resolution of 3 km is not enough to resolve the finer-scaled structures in the eyewall (Gentry & Lackmann, 2010). There were 45 eta levels across the vertical direction. The outer and inner domain set up was displayed in Figure 3.1 by the figure outer boundary and the black rectangle inside respectively. It can be seen that the finer resolution domain covers the whole northern SCS region, which enable the analysis of some finer scaled structures of the TCs within the SCS. Eta (Ferrier) Scheme (Rogers, E. et.al. (2001) was used to model the microphysics while Yonsei University (YSU) Scheme (Hong et.al., 2006) was applied to model the planetary boundary layer physics. The shortwave and longwave radiation were modelled by the Dudhia Shortwave Scheme (Dudhia, 1989) and the RRTM Longwave Scheme (Mlawer, E. J. et.al., 1997). The Unified Noah Land Surface model (Mukul Tewari et.al., 2004) was used to model the land surface while the Revised MM5 Scheme (Jiménez, P. A. et.al., 2012) was used to model the surface layer physics. Moreover, the Kain-Fritsch Scheme (Kain et.al., 2004) was used to parametrize the convection in the outer domain while in the inner domain, cumulus parametrization was turned off. It was suggested by Gentry and Lackmann

(2010) that the localized updraft cores within the eyewall could be resolved with a horizontal resolution of below 4 km (Gentry & Lackmann, 2010). Therefore, convection was resolved in the inner domain of the setup in this study. Also, model zonal and meridional velocity above 500 hPa with wavelength of about 1600 km were spectrally nudged towards their reanalysis values. Moreover, a Rankine vortex was used to replace the initial TC circulation from the reanalysis by directly applying the WRF bogus scheme, so as to improve the simulated TCs intensity and track performance when comparing to the best track data (Srinivas & Rao, 2014). Each TC case was integrated for at least 96 hours, with model output stored for each 3 hours and 1 hour for the outer and inner domain respectively. The results of these 25 TC cases associated with their background environment condition were used as the reference of the intensity and the size historically as the control set up.

3.1.3 Pseudo global warming method (PGW)

In order to investigate how the projected thermodynamical changes in the warmed climate influence the TC intensity and sizes, pseudo global warming method was used to superimpose the warming forcing to the historical environment associated with the selected 25 TC cases. Projected atmospheric and surface conditions in the future were obtained from the fifth phase of the Coupled Model Intercomparison Project (CMIP5), following the Representative Concentration Pathways 4.5 and 8.5 (RCP4.5 and RCP8.5) (Taylor et.al., 2012). A total of 31 and 5 models from the CMIP5 were selected to obtain the projected future changes following the RCP8.5 and RCP4.5 emission scenario respectively. The name of the CMIP5 models chosen were listed in APPENDIX I. The climate conditions in the 1975 – 1999 were selected as the reference of the historical climate while the climate conditions in the 2036 – 2065 and 2075 – 2099 were selected as the near future and the far future climate respectively. The SST, land surface temperature, atmospheric temperature and the specific humidity profiles in the historical climate, as well as in the projected near future and the far future climate were averaged across that period for each month separately to obtain the mean monthly climatic condition in the historical, near future and far future period. After that, the SST, land surface temperature, atmospheric temperature and specific humidity in the near future and the far future were

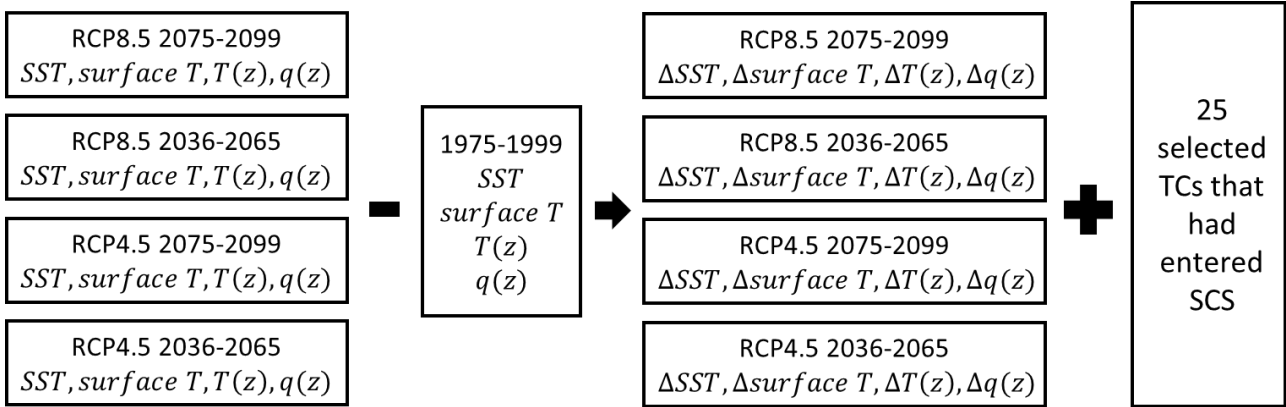


Figure 3.2 Procedures of the PGW Experiments. Changes in monthly mean SST, land surface temperature (surface T), atmospheric temperature profile ($T(z)$) and the specific humidity profile ($q(z)$) in the near future and the far future in the RCP8.5 and RCP4.5 emission scenarios were subtracted by the values in the historical climate, and then imposed to each of the selected TCs according to their month of occurrence.

subtracted by the historical climate conditions, obtaining the change of surface temperature, atmospheric temperature and the specific humidity profile in the near and the far future relative to the historical period. An example of the PGW signal computed were shown in APPENDIX II.

Then, the change in the monthly mean SST, land surface temperature, atmospheric temperature profile and the specific humidity profile in the near future and the far future relative to the historical climate were superimposed on the historical environment of the 25 selected TCs according to the month of occurrence in the past for each TC to create a total of 4 warming experiments, each contain 25 TC cases. Therefore, there are 1 control simulation and 4 warming experiments for each of the 25 TC cases, and a total of 125 simulations. The procedures of the PGW method were summarized in Figure 3.2 while the combination of experiments is shown in Table 3.2. Moreover, the reason for not imposing the projected change in wind field in the future climate to the TCs were to examine the change in thermodynamical environment due to global warming to the intensity and the size of the TCs, while not changing the track of the TC. The author aimed to reduce the complexity brought by the possible changes of the TC track in the future environment due to a change of steering wind, which then allowed a comparison between the response of different TCs in a warmed climate by attributing the different in the percentage change of TC intensity and size to the difference in the historical environment and the imposed warming signal. Therefore, the following results of the projected TC intensity and size in the warming future climate could be interpreted as

Table 3.2 Summary of Numerical Experiments (bracket shows the number of TC simulations under that experiment). The experiments are: Control, RCP8.5 Far Future, RCP8.5 Near Future, RCP4.5 Far Future, RCP4.5 Near Future. In total there are 125 simulations carried out.

Scenario	Experiments	
Control run	Time period of occurrence in the past (25 TCs)	
RCP8.5	Far Future (2075-2099) Climate (25 TCs)	Near Future (2036-2065) Climate (25 TCs)
RCP4.5	Far Future (2075-2099) Climate (25 TCs)	Near Future (2036-2065) Climate (25 TCs)

the intensity and size of that TC with the same track compared to the past, but in a thermodynamically much warmer climate. Moreover, difference definition of the historical period and the far future period (namely 1960-1989 and 2081-2109 respectively) was tested for the sensitivity of the TC simulation results to the definition of the historical climate and future climate period, and found that the results were not sensitive to the period chosen to define the historical climate and the far future climate.

3.2 Regression Analysis

3.2.1 Multiple Linear Regression (MLR) analysis

In order to test the hypothesis by finding out the possible historical environmental conditions that determine the variations between the difference in the percentage change of TC intensity and size among each TC in the SCS when imposing the same PGW forcing, the percentage change of Vmax, RMW and R17 of the TCs in warming runs relative to the control run in the SCS were obtained in each warming experiment, and were used to regress to the historical environmental conditions associated with these TCs. Specifically, 14 TCs were further chosen based on the results of the simulated track compared to the best-tracked data. The detail comparison between the simulated track, intensity, RMW and R17 of the 25 TCs and that from the best-tracked data, as well as the TC selection criteria, were presented in APPENDIX V. After the model verification, the percentage changes of Vmax, RMW and R17 of these 14 TCs in the SCS in the same warming experiment relative to the control run were regressed to the variables that can represent the historical environmental conditions associated with each of the TCs. It was defined that the TC enters the SCS when the center of the TC

was located at a longitude westward of 119.4°E. Moreover, only the time when the TC had a strength exceeding TS category ($V_{max} > 17\text{ms}^{-1}$) was considered.

The effects of the historical detrended SST, atmospheric instability in terms of the difference between the environmental 1000 mb and the 500 mb to 700 mb mean moist static energy, 600 mb relative humidity and the 850 mb minus 200 mb vertical wind shear in the SCS were selected to be regressed to the difference in the percentage change of V_{max} and RMW in each warming experiment among the 14 selected TCs. As the SST had shown a significant increasing trend in 99% confidence interval across our selected TCs that span across 58 years in the past, the historical SST associated with each of the TCs were detrended from the linear regression slope of the historical SST with time.

The moist static energy (MSE) is defined as:

$$MSE = c_p T + \Phi + L_v q \quad (9)$$

which c_p is the specific heat at constant pressure, T is the temperature, Φ is the geopotential, L_v is the latent heat of vaporization and q is the specific humidity. When the air rises adiabatically, the enthalpy (first term) decreases while the potential energy increases. Moreover, in saturated adiabatic ascent, the enthalpy and the latent heat content (third term) decrease with the increase in potential energy. However, the total moist static energy of the air parcel remains constant for adiabatic and saturated adiabatic motion (Wallace, J. M. & Hobbs, P. V., 2006). Therefore, if the 1000 mb MSE is larger than the 500 mb to 700 mb mean MSE, the atmosphere is unstable. The vertical wind shear was calculated by the subtraction of the mean wind within 500 km radius from the TC center at each timestep when the TC had entered the SCS, at a level of 850 mb and 200 mb, which was then interpolated to each $1^\circ \times 1^\circ$ grid in the SCS.

Historical environmental variables were obtained from the control run of each of the 14 TCs 6 hourly. Then, the values were interpolated to $1^\circ \times 1^\circ$ resolution in order to eliminate the finer scaled circulation associated with the TC itself. After that, the values were averaged across time dimension

of each TCs to obtain the mean environmental conditions in the SCS when the TC had entered the SCS in the past, creating maps of mean environmental variables with $1^\circ \times 1^\circ$ resolution in the SCS. Specifically, the SCS region was defined to be bounded from 105°E to 119.5°E and 15°N to 25°N . Then, the mean historical environmental conditions in the SCS across the 14 TCs were normalized across the selected 14 TCs. The percentage changes of Vmax and RMW in each warming experiment relative to the control run across the 14 TCs were then regressed on these normalized mean historical environmental conditions. Apart from these 4 environmental variables, the historical outer wind speed (OWS), which was defined as the mean 10 m wind speed outside the R17 of the TC at each timestep in the SCS, was also used as one of the historical environmental variables to be regressed by the

Table 3.3 Historical Environmental Variables used as Regressors on Regressing each TC Characteristics

Normalized Historical Environmental conditions	Vmax	RMW	R17
SST		Detrended SST	
Atmospheric instability ($MSE_{1000-500700mean}$)		1000mb – 500mb to 700mb mean MSE	
Relative Humidity (RH_{600})		600mb RH	
Vertical wind shear (VWS)		850mb – 200mb wind shear magnitude within 500km radius from the TC center	
Outer wind speed (OWS)			10m wind speed beyond r17

Table 3.4 Details of the Multiple Linear Regression Model for all warming experiments and TC characteristics. a, b, c, d, e are the slopes of each normalized regressors. Refered to Table 3.3 for the details of the acronyms.

Warming Experiments	Difference across each TC for percentage change of:	Historical Environmental Conditions
RCP8.5 Far Future	$Vmax =$	$aSST + bMSE_{1000-500700mean} + cRH_{600} + dVWS$
	$RMW =$	$aSST + bMSE_{1000-500700mean} + cRH_{600} + dVWS$
	$R17 =$	$aSST + bMSE_{1000-500700mean} + cRH_{600} + dVWS + eOWS$
RCP8.5 Near Future	$Vmax =$	$aSST + bMSE_{1000-500700mean} + cRH_{600} + dVWS$
	$RMW =$	$aSST + bMSE_{1000-500700mean} + cRH_{600} + dVWS$
	$R17 =$	$aSST + bMSE_{1000-500700mean} + cRH_{600} + dVWS + eOWS$
RCP4.5 Far Future	$Vmax =$	$aSST + bMSE_{1000-500700mean} + cRH_{600} + dVWS$
	$RMW =$	$aSST + bMSE_{1000-500700mean} + cRH_{600} + dVWS$
	$R17 =$	$aSST + bMSE_{1000-500700mean} + cRH_{600} + dVWS + eOWS$
RCP4.5 Near Future	$Vmax =$	$aSST + bMSE_{1000-500700mean} + cRH_{600} + dVWS$
	$RMW =$	$aSST + bMSE_{1000-500700mean} + cRH_{600} + dVWS$
	$R17 =$	$aSST + bMSE_{1000-500700mean} + cRH_{600} + dVWS + eOWS$

difference in the percentage change of R17 in each warming experiment among 14 selected TCs. A summary of environmental variables used in the MLR model was shown in Table 3.3. Moreover, the multiple linear regression equations for each warming experiments and for each TC characteristics were illustrated in Table 3.4. Moreover, filter from Kurihara et.al. (1993) were also used to try to remove the TC associated atmospheric instability and RH field within a radius of 500 km from the TC center by a cylindrical filter (Kurihara et.al., 1993). Similar MLR results were obtained from using the filtered atmospheric instability and RH and without cylindrical filtering. Therefore, results of MLR by unfiltered historical environmental variables were shown throughout the whole project. Apart from the model outputted historical environmental conditions, variables were also obtained from the ERA5 and ERA-20C reanalysis dataset and regressed to the difference in the percentage change of Vmax, RMW and R17 in across the selected 14 TCs. Qualitatively similar relationships were obtained compared to the historical environment variables extracted from the model. More or less TCs were also tested to be included in the MLR model, and the results showed the MLR regression slope were not sensitive to the choice of TCs.

3.2.2 Stepwise Regression Analysis

To find out which historical atmospheric and oceanic variables are important in explaining the variations in the percentage change of TC intensity and size to the same PGW forcing, stepwise

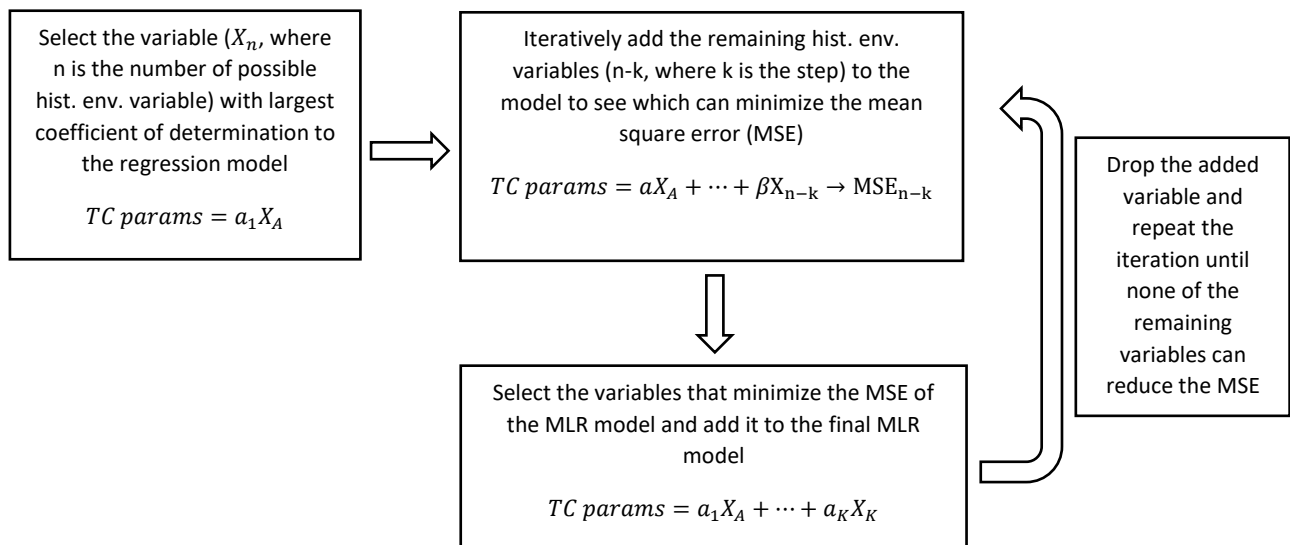


Figure 3.3 Illustration of the process of stepwise regression

regression analysis was performed to the regression models listed in Table 3.4. First, the variable with largest coefficient of determination was selected to be included in the MLR regression model for each warming experiment and each TC characteristics, and each $1^{\circ} \times 1^{\circ}$ grid in the SCS separately. At the next step, each of the remaining environmental variables were tried to add to the regression model, and the one which could minimize the mean square error of the MLR model was chosen to be added to the final regression model. After that, this process was repeated iteratively until none of the newly added variables could reduce the mean square error of the final MLR model. Finally, the rank of environmental conditions that could explain the variations of percentage changes of TC characteristics to the same PGW forcing were obtained according to the steps that the variables were added to the MLR model. Figure 3.3 illustrates the procedures of the stepwise regression.

4. TC Mean Intensity and Size Changes in the SCS in PGW Experiments

Before accessing the influence of the historical environment in the SCS to the different percentage change of TC intensity and size to the same PGF forcing, the capability of the WRF model in reproducing the track, intensity and the inner core size of the TC in the control run shall be examined first. Based on the simulated tracks and the intensities, TCs that were poorly simulated were discarded. After that, the mean changes of the TC intensity and size in the SCS in 4 different future climate periods and emission scenarios relative to the control simulation were shown.

4.1 TC Selection based on the Comparison to the Best Track Data

To select the TC samples used in the following analysis on the mean change of the TCs' intensity and size, as well as their variations in the same warming experiments, the following criteria were considered:

- 1) The simulated TC track in the historical run and all warming experiments compared to the best track data
- 2) Number of timesteps in the SCS when the TC were located over ocean and exceeded TS intensity
- 3) Uncommon features were not observed throughout the lifetime of the TCs

The first criteria were applied in order not to introduce larger degree of freedom due to a difference in TC tracks in the control run and the warming experiments compared to the best track data when considering the background environment that the TCs had travelled in the past and the future climate. For the second criteria, as this project focused on the change in the TC characteristics in the SCS, small number of timesteps recorded in the SCS would make a time average too sensitive to the bias at that few timesteps. For the third criteria, some very uncommon features like rapid intensification and anonymously large RMW were discarded as the physics behind these features were less known by past literature, therefore creating larger uncertainties when one tried to explain the possible changes for these TCs in the future climate.

Figure 4.1 showed the simulated TC tracks in the control run and 4 warming runs compared to the best-tracked data. From the Figure, TC Ruby (1964), TC Joan (1973) and TC York (1999) did not make their landfall in either one of the simulations at the South China coast. Moreover, the track of TC Sally (1964), TC TD0801 (1970), TC Rose (1971), TC Victor (1997) and TC Sam (1999) were largely deviated from the best-tracked data. Therefore, to reduce the complexity brought by the deviation of the simulated tracks compared to the best tracked data, these 8 TCs were then discarded in subsequent sections based on criteria 1.

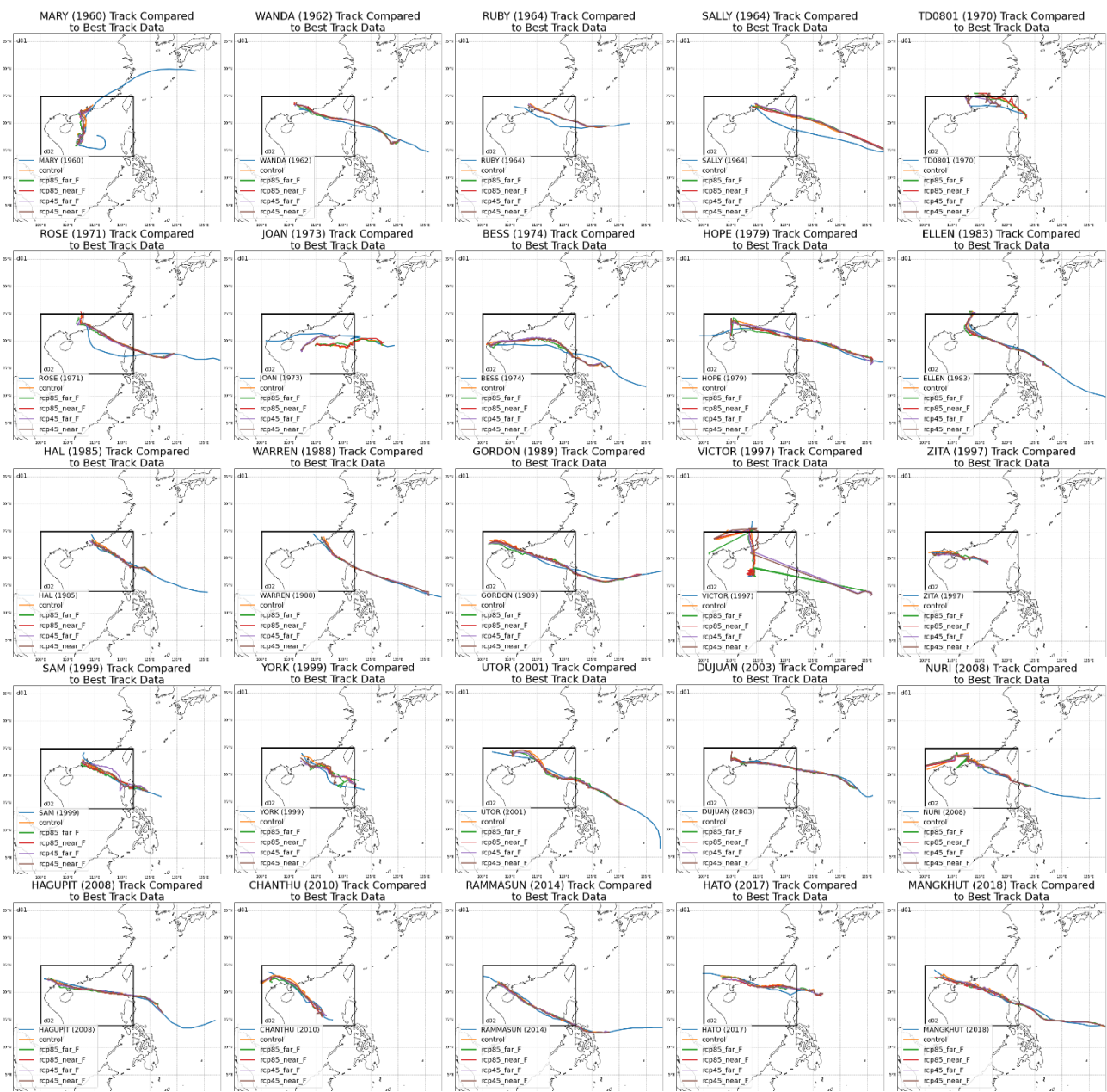


Figure 4.1 Simulated TC tracks in (orange) control run, (green) RCP8.5 Far Future, (red) RCP8.5 Near Future, (purple) RCP4.5 Far Future, (brown) RCP4.5 Near Future compared to the (blue) best-tracked data. TCs were ordered in chronological order from top-left to lower-right.

Secondly, TC Zita (1997) was found to have only one timestep that was in the SCS and exceed TS intensity (APPENDIX Figure 5). Therefore, TC Zita (1997) were also not considered in the later part based on criteria 2. Moreover, Choy et.al. (2020a, 2020b) had reported that TC Hato (2017) and TC Mangkhut (2018) had undergone unusual development processes in their lifetime, and had developed structures that were not typical. Therefore, these 2 TCs were also dropped in the following discussion based on criteria 3, and the effects of global warming to these special cases were left for future studies. A total of 14 TCs in the control run and the 4 warming experiments were then remained, which were listed in Table 3.1 by bolded text. Details of the TCs' track, intensity, RMW and R17

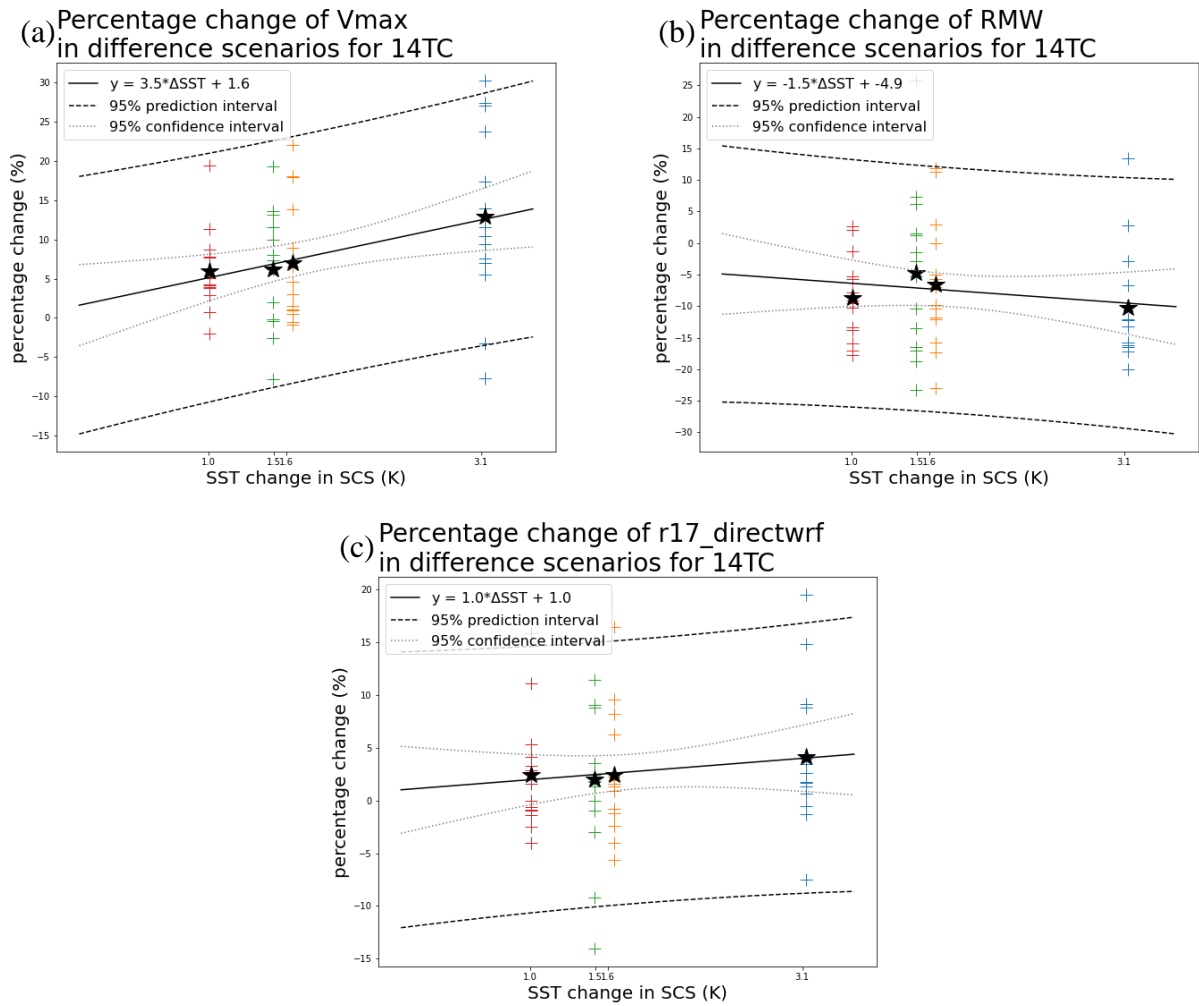


Figure 4.2 Percentage changes of mean (a) Vmax, (b) RMW, (c) R17 in the SCS for 14 selected TC in 4 warming experiments, scaled to the change of mean SST in the SCS in (blue) RCP8.5 Far Future, (yellow) RCP8.5 Near Future, (green) RCP4.5 Far Future, (red) RCP4.5 Near Future. The percentage changes for each individual TC relative to the control were indicated by + symbol. * indicate the mean percentage change across all 14 TCs in that warming experiment. Black line indicates the linear regression of mean SST changes in the SCS to the mean percentage change across 14 TCs, which the slope for percentage change of mean Vmax and the mean R17 in the SCS is significantly different to 0 in 95% CI. Black dashed line showed the 95% prediction interval of the sample while grey dotted line showed the 95% confidence interval of the regression function. Details of the prediction interval and the confidence interval of the regression model were discussed in section 8.1

compared to the best-tracked data were listed in APPENDIX V. The detailed criteria applied to select the 14 TCs were also presented in the last paragraph of APPENDIX V.

4.2 Mean changes in the SCS

As this study focused on the projected TC intensity and size changes in the SCS region, the mean intensity and sizes for these 14 TCs in the SCS from 6 hourly moving averaged model output before landfalling at the South China coast were computed. 10 m azimuthally averaged Vmax were used to define the TC intensity while the corresponding radius were defined as the RMW. The outermost radius away from the RMW that reached 17 m s^{-1} at 10 m height were defined as the R17, which represented the outer core size of the TC.

Figure 4.2 showed the simulated percentage changes of mean Vmax, RMW and R17 in the SCS for 14 TCs in each warming experiment, which the future climate periods and emission scenarios were indicated by the mean change of SST in the SCS region. SCS SST were projected to be increased by 3.1°C , 1.6°C , 1.5°C and 1.0°C in the projected RCP8.5 Far Future, RCP8.5 Near Future, RCP4.5 Far Future and RCP4.5 Near Future climate respectively. Moreover, the percentage changes of mean Vmax, RMW and R17 for each TC in each warming experiment, as well as the mean statistics at each scenario were summarized in Table 4.1 and Table 4.2 respectively. From Figure 4.2a, it can be seen that there was an increase in projected mean Vmax in the SCS for all future climate periods and emission scenarios for the mean of these 14 TCs (stars in Figure 4.2). In all warming experiments,

Table 4.1 Mean Statistics in the SCS for the 14 Selected TCs (* and ** shows the difference between the mean of the warming experiment and the control run exceed 90% CI and 95% CI respectively)

Name	Period	Vmax (ms^{-1})	RMW (km)	R17 (km)	% change of Vmax	% change of RMW	% change of R17
Mary (1960)	Current	26.43	56.67	168.33			
	RCP8.5 Far Future	33.58*	46.94	201.11*	27.04*	-17.16	19.47*
	RCP8.5 Near Future	32.28*	46.88	195.94*	22.11*	-17.28	16.4*
	RCP4.5 Far Future	29.08	57.50	193.61	10.03	1.47	15.02
	RCP4.5 Near Future	31.58*	47.67	195.00	19.47*	-15.88	15.84
Wanda (1962)	Current	42.81	35.00	154.00			
	RCP8.5 Far Future	45.20	34.00	158.00	5.56	-2.86	2.6
	RCP8.5 Near Future	44.77	33.00	157.00	4.56	-5.71	1.95
	RCP4.5 Far Future	43.65	34.00	156.00	1.95	-2.86	1.3
	RCP4.5 Near Future	44.98	33.00	159.00	5.06	-5.71	3.25

Bess (1974)	Current	29.43	50.00	196.11		
	RCP8.5 Far Future	32.50*	46.67	203.89	10.43*	-6.67
	RCP8.5 Near Future	29.59	46.50	185.00	0.54	-7
	RCP4.5 Far Future	31.58	41.50	178.00	7.32	-17
	RCP4.5 Near Future	32.77	41.11	201.67	11.38	-17.78
Hope (1979)	Current	40.58	50.00	201.67		
	RCP8.5 Far Future	51.73	40.00**	220.00	27.47	-20**
	RCP8.5 Near Future	40.24	50.00	200.00	-0.85	0
	RCP4.5 Far Future	40.49	38.33**	173.33	-0.22	-23.33**
	RCP4.5 Near Future	42.12	43.33*	196.67	3.78	-13.33*
Ellen (1983)	Current	34.71	48.75	154.38		
	RCP8.5 Far Future	38.72	40.71**	153.57	11.55	-16.48**
	RCP8.5 Near Future	37.79	42.86**	156.43	8.89	-12.09**
	RCP4.5 Far Future	39.28*	40.71**	157.14	13.19*	-16.48**
	RCP4.5 Near Future	36.60	44.29*	160.71	5.45	-9.16*
Hal (1985)	Current	32.35	73.00	235.00		
	RCP8.5 Far Future	34.61	63.33**	239.17	6.96	-13.24**
	RCP8.5 Near Future	34.48	81.25*	257.50	6.56	11.3*
	RCP4.5 Far Future	32.24	77.50*	239.17	-0.35	6.16*
	RCP4.5 Near Future	33.73	69.17*	231.67	4.24	-5.25*
Warren (1988)	Current	40.48	51.25	205.00		
	RCP8.5 Far Future	43.55	45.00*	206.25	7.6	-12.2*
	RCP8.5 Near Future	40.92	46.25	202.50	1.09	-9.76
	RCP4.5 Far Future	42.99	41.67**	205.00	6.21	-18.7**
	RCP4.5 Near Future	43.64	42.50**	203.75	7.8	-17.07**
Gordon (1989)	Current	35.59	61.67	225.83		
	RCP8.5 Far Future	41.77**	54.17**	259.17**	17.36**	14.76**
	RCP8.5 Near Future	42.04**	47.50**	240.00	18.12**	-22.97**
	RCP4.5 Far Future	42.45**	53.33**	251.67*	19.28**	-13.51**
	RCP4.5 Near Future	37.09	63.33	250.83*	4.21	2.7
Utor (2001)	Current	38.83	56.67	265.83		
	RCP8.5 Far Future	44.23*	47.50**	289.17	13.92*	-16.18**
	RCP8.5 Near Future	39.19	58.33	287.50	0.93	2.94
	RCP4.5 Far Future	41.94	55.83	289.17	8.01	-1.47
	RCP4.5 Near Future	40.37	50.83**	280.00	3.97	-10.29**
Dujuan (2003)	Current	45.15	48.33	206.67		
	RCP8.5 Far Future	41.66	42.50	191.25	-7.72	-12.07
	RCP8.5 Near Future	44.92	43.33	201.67	-0.51	-10.34
	RCP4.5 Far Future	48.01	43.33	211.67	6.33	-10.34
	RCP4.5 Near Future	45.50	41.67	210.00	0.78	-13.79
Nuri (2008)	Current	30.95	50.00	187.50		
	RCP8.5 Far Future	29.95	51.43	185.00	-3.24	2.86
	RCP8.5 Near Future	31.43	47.50	180.00	1.55	-5
	RCP4.5 Far Future	30.16	50.63	185.63	-2.56	1.25
	RCP4.5 Near Future	31.83	49.38	187.50	2.85	-1.25
Hagupit (2008)	Current	39.06	47.50	221.88		
	RCP8.5 Far Future	50.89**	40.00**	225.63	30.29**	-15.79**
	RCP8.5 Near Future	44.46*	41.88*	226.88	13.82*	-11.84*
	RCP4.5 Far Future	44.40	51.00	242.00	13.66	7.37
	RCP4.5 Near Future	42.48	43.75	220.00	8.76	-7.89
Chanthu (2010)	Current	31.88	34.29	132.14		
	RCP8.5 Far Future	34.88	38.89	136.67	9.43	13.43
	RCP8.5 Near Future	32.84	38.33	133.33	3.03	11.81
	RCP4.5 Far Future	29.37	43.13*	128.13	-7.88	25.78*
	RCP4.5 Near Future	31.25	35.00	126.88	-1.95	2.08
Rammasun (2014)	Current	40.70	47.50	256.00		
	RCP8.5 Far Future	50.35**	40.00**	259.29	23.72**	-15.79**
	RCP8.5 Near Future	47.99**	40.00**	260.00	17.93**	-15.79**
	RCP4.5 Far Future	45.41	45.00	265.00	11.58	-5.26
	RCP4.5 Near Future	43.85	43.00**	253.50	7.74	-9.47**

Table 4.2 Mean, Standard Deviation (STD) and the Coefficient of Variation (CV) of the Mean Statistics Across all 14 TCs in the SCS (*, ** and *** shows the hypothesis that the mean of the warming experiment and the control run were different, with a statistical significance exceed 90% CI, 95% CI and 99% CI respectively) (◊ shows the hypothesis that the mean of the Far Future experiment and the Near Future experiment were different with a statistical significance exceed 95% CI)

Period	Mean % change of Vmax	Mean % change of RMW	Mean % change of R17	STD of % change of Vmax	STD of % change of RMW	STD of % change of R17
RCP8.5 Far Future	12.88***◊	-10.3***	4.15**	11.35	9.19	6.88
RCP8.5 Near Future	6.98***◊	-6.55**	2.45	7.87	10.17	5.90
RCP4.5 Far Future	6.18***	-4.78	1.98	7.34	13.08	7.74
RCP4.5 Near Future	5.97***	-8.72***	2.41	5.12	6.67	5.44
Period	CV of Vmax	CV of RMW	CV of R17			
RCP8.5 Far Future	0.88	0.89	1.66			
RCP8.5 Near Future	1.13	1.55	2.41			
RCP4.5 Far Future	1.19	2.74	3.90			
RCP4.5 Near Future	0.86	0.76	2.26			

the mean of the Vmax across all TCs were significantly different to that in the control run in 99% confidence interval (Table 4.2), indicated that the increase in Vmax was significant in future climate. Moreover, linear regression showed that the increase in mean Vmax in the SCS were scaled to the increase in the SST in the SCS. From the regression model, an increase in SST in the SCS by 2 °C, together with the modification of atmospheric temperature profile and humidity profile, resulted in an increase in mean Vmax in the SCS by 8.6%. This result matches with the review of high-resolution numerical modelling studies from Knutson et.al. (2020) that the projected increase in global Vmax for a 2 °C increase in surface temperature is 5% (range is 1% - 10%). Moreover, this result was statistically significant in 95% confidence interval (p-value 0.01), which matches the previous literatures that the projected change in SST scaled to the change in TC intensity in the future (Tuleya et.al., 2016).

Figure 4.2b shows the percentage change of mean RMW in the SCS in all warming experiments. From the figure, all warming scenarios predicted a mean decrease in mean RMW for the TCs in the SCS. Statistical testing showed the mean of RMW in the SCS in the RCP8.5 Far Future and RCP4.5 Near Future runs were significantly different to that in the control run by 99% CI while that in the RCP8.5 Near Future were significantly different to that in the control run, exceeding 95% CI (Table

4.2). Moreover, linear regression model showed a decreasing trend with increasing SST warming, yet the slope was not significantly different to 0 in 95% CI. The connection of the mean RMW decrease in the SCS to the change in mean SCS SST may resulted from the relationship between the increasing Vmax and the contracting RMW. Regression model of the percentage change of mean Vmax to the mean RMW showed a -0.51 correlation coefficient between the two (not shown), which was significantly different to no correlation in 99% CI. Therefore, theories linking the Vmax and RMW should be reviewed on whether there exist a $\frac{1}{2}$ relationship between Vmax and RMW, as well as their projected percentage change in the future climate in later studies. Possible reasons that could account for the projected decrease in the mean RMW in the SCS were discussed in section 8.2.

However, questions arise on whether the horizontal resolution of the inner domain were fine enough to resolve the possible RMW changes in the future climate. As the mean decrease in RMW in the SCS were only 6%, which were approximately 4 km, whether the change in RMW could be resolved by a 3 km inner domain resolution was highly questionable. Future research with finer resolution are needed to confirm the change in RMW in the future climate, and the results related to the change in RMW in this study should be treated with caution. Details of the limitations caused by the horizontal resolution of the inner domain in resolving the RMW changes in a warmed climate were discussed in section 8.5.2. It should also be noticed that the change in RMW outside the SCS could not be resolved using a 15 km horizontal resolution outer domain, which introduced errors during the early development stage of the TC, when the RMW contracted rapidly.

The percentage change of mean R17 in the SCS in all future climate periods and emission scenarios were shown in Figure 4.2c. It can be seen that there was a slight predicted increase in the mean R17 in the SCS for the mean of 14 TCs in all warming experiments. For example, the mean increase in mean R17 in the SCS in RCP4.5 Far Future was 1.98% compared to the control run, which could be compared to the 1% increase in global R12 in the projected late-twenty-first-century climate in RCP4.5 emission scenario from the dynamical downscaling experiments from Knutson et.al.

(2015). Statistical tests showed only the mean R17 in the SCS in RCP8.5 Far Future warming experiment were significantly different to that in the control run in 95% CI. This might show that future changes in the thermodynamical environment due to global warming, including the increase in SST, stabler atmosphere and an increase in the atmospheric moisture content may not be important in causing a change in future TC size in terms of R17. Moreover, the results here matched with that in Knutson et.al. (2020) that there was no general consensus on a significant change in TC size in the future climate among different research. Therefore, more TCs should be considered in the future in order to enhance the statistical significance in projecting future TC R17 changes, except for RCP8.5 Far Future run which the stronger warming signal may be large enough to induce a significant change.

Despite a smaller confidence in projecting the mean statistics of the R17 in the future climate compared to the control run, linear regression shows a slightly positive and statistically significant relationship (p-value 0.04) between the change in mean SST in the SCS to the percentage change in mean R17 in the SCS. For a 2 °C surface warming, the R17 of the TCs were projected to have an increase by 3%, which was small compared to the increase in the Vmax. Therefore, it can be seen that larger increase in SST in the future climate period and emission scenarios slightly increased the mean R17 of the TCs in the SCS. Yet, the projected change in R17 in the future climate were not scaled to the increase in the SST as it could only explained a small part of R17 change in the future climate.

Interest may arise on whether the changes in TC intensity and size in the SCS were significantly different in the near future and the far future era. Statistical significance tests showed only the percentage change in Vmax in the SCS were significantly different with each other in the near future and far future era under RCP8.5 emission scenario in 95% CI (p-value 0.04) (Table 4.2). This may because of the strong scaling of Vmax changes to the increase in SST (Tuleya, et.al., 2015). As the increase in SST in the SCS in the RCP8.5 Far Future experiment were one time (1.5 °C) of that in the Near Future experiment, the imposed SST changes were large enough to cause a significant increase

in TCs' Vmax in the far future era compared to that in the near future era under RCP8.5 emission scenario. However, there was only 50% increase (0.5°C) in SST in the SCS in RCP4.5 Far Future period compared to the Near Future period. This SST change may not be enough to cause a significant difference in Vmax in the near future and far future under a RCP4.5 emission scenario. Moreover, as the change in RMW and the R17 were not strongly scaled to the SST, there were no large difference in TC sizes between different future climate periods.

Nevertheless, if one looked at the spread between the percentage change of the R17 for each TCs in each warming experiment, which can be inferred from the distance of each + sign to the star in each scenario in Figure 4.1c, there was a large difference of the percentage change of mean R17 for different TCs in the same warming experiment. For example, Table 4.1 showed a percentage increase of R17 for TC Mary (1960) by 19.47% in the RCP8.5 Far Future experiment while a percentage decrease in 7.46% for TC Dujuan (2001) in the same warming experiment. These variations between the responses of different TCs' Vmax, RMW and the R17 to the same PGW forcing were examined in the next section.

5. Statistical Relationships between Differences in TC Intensity and Sizes Changes to the Historical Environment

Despite the small mean percentage change of average R17 in the SCS in projected future climate, the percentage change of mean R17 in the SCS had large variations across individual TCs in the same future period and emission scenario. Large variations were also observed for the percentage change of Vmax and RMW among different TCs to the same forcing. The variations of the projected percentage change of TC intensity and size to the same forcing had created large uncertainties in predicting future behaviors of individual TCs, and thus creating large possible risks brought by the extreme change of TC intensity and size. Therefore, factors controlling the differences in the projected percentage change of TC intensity and size in the SCS in future climate shall be examined, so as to better describe the variances of the change in TC characteristics in the future by PGW experiments.

Each of the PGW experiment in the same future period and emission scenario consist of the changes in thermodynamical quantities like the SST, atmospheric temperature and the water vapor content in the atmosphere in the future climate following particular emission scenarios compared to the historical climate, as well as the past background environment associated with each of the TC. If there were large variations in the change of TC intensity and size of each TCs, regardless the same warming signal added, the variations should arise from the past environment associated with the selected TC. Therefore, this main hypothesis of the research was examined in this section by MLR analysis and stepwise regression analysis. First, the statistics of variations for TC intensity and size changes in the SCS were displayed by the box and whisker diagram and quantified by the coefficient of variation. Then, the MLR map and stepwise regression map between the historical environmental conditions and the variations of TC intensity and size changes in the SCS were presented.

5.1 Variations of TC intensity and size changes in each warming experiments

Figure 5.1 shows the box and whisker diagram for percentage changes in the mean (a) Vmax, (b) RMW, (c) R17 in the SCS in future climate experiments relative to the control simulations for the selected 14 TCs. The mean percentage change in each warming experiment was denoted by the orange line, which was the same as the stars in Figure 4.2. The upper and the lower boundary of the box shows the 25th and the 75th quantiles respectively, which represent the middle 50% of the data. The range between the box is called the inter-quartile range (IQR), which describe the spread of the TC intensity and size percentage change for different TCs in the same warming experiment. Outside the box there is a bounded line, which is called whisker. The whisker bound the values of the 25th quantile minus 1.5 times of the IQR and the 75th quantile plus 1.5 times of the IQR. Data outside the whisker were defined as the outliers and were denoted by circles.

The increasing, slightly decreasing and slightly increasing trend of percentage change of Vmax, RMW and R17 with the increasing PGW forcing in terms of mean SST change in the SCS were again indicated by the orange line. For Vmax, the whisker increased for increasing PGW forcing. In RCP8.5 Far Future experiment, the whisker span across a difference of 37% while in RCP4.5 Near Future experiment, the whisker extended for 13%. Moreover, the spread of the percentage change in RMW in the SCS increased with decreasing PGW forcing, except in the RCP4.5 Near Future experiment. The whisker for the percentage change in RMW in the RCP8.5 Far Future experiment was 23% while that in RCP4.5 Far Future experiment was approximately 50%. For the percentage change of mean

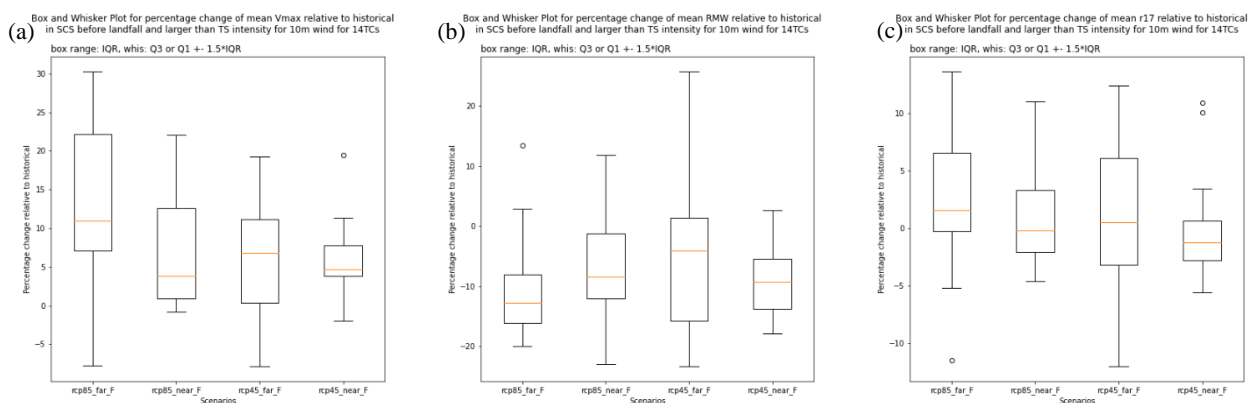


Figure 5.1 Box and whisker diagram of mean percentage change in (a) Vmax, (b) RMW, (c) R17 in each warming experiment relative to the control run for 14 TCs. See text for explanation for box and whisker diagram

R17 in the SCS, there was no clear trend across different warming experiment. The range of the whisker was also large, with a value of 24% in RCP4.5 Far Future and 9% in RCP4.5 Near Future. Results from the box and whisker diagram shows large variations between the projected percentage change of Vmax, RMW and R17 in the SCS across different TCs in all warming experiments. Despite the fact that the possible trend of the spread across different warming experiments was interesting, it was not the main focus of this study, and were left for future research.

The coefficient of variation (CV) was used to better quantify the spread of the percentage change of TCs' Vmax, RMW and R17 for different TCs in the same warming experiments. The coefficient of variation is defined as:

$$CV = \frac{\sigma}{\mu} \quad (10)$$

which σ indicates the standard deviation while μ indicates the mean of the sample distribution. Throughout the search by the author, there were no statistical test in testing the significance of the spread. However, the coefficient of variation could be analogized to the signal-to-noise ratio, which is the reciprocal of the CV. A CV of one means that the amplitude of the noise is the same as that of the signal. Therefore, a CV of larger than one is reasonable to define as a large spread compared to the mean. Table 4.2 listed out the CV of the percentage change in Vmax, RMW and R17 for each

(a) Mean 10m azimuthally averaged wind field of TC GORDON in the SCS (b) Mean 10m azimuthally averaged wind field of TC WARREN in the SCS

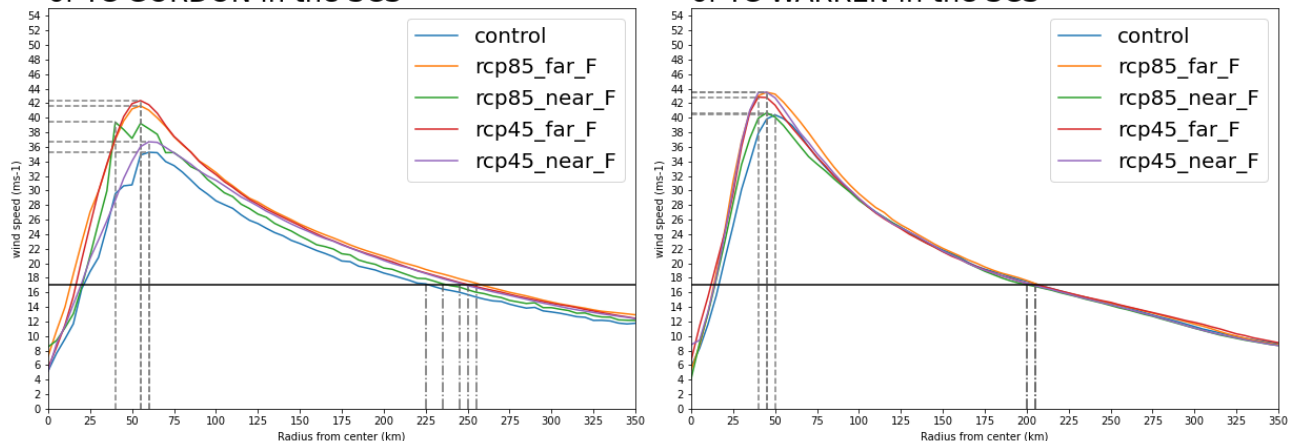


Figure 5.2 10 m azimuthally averaged wind field in control and warming experiment for (a) TC Gordon (1989) and (b) TC Warren (1988) averaged across time in the SCS region. Black line denotes the 17 m s^{-1} , dashed line denotes the Vmax and the RMW while dash-dot line denotes the R17

warming experiment. Results showed that nearly all CV for the percentage change of intensity and size in all warming experiments were larger than 1, except for that of the Vmax and the RMW in RCP8.5 Far Future and RCP4.5 Near Future experiment. This meant that the spread were significant compared to the mean change in intensity and size. For example, the mean CV of the percentage change of R17 in the SCS was 2.1 across all warming experiments, which means that the standard deviation was 2 times of the mean increase in R17. If the sample distribution of the percentage change of R17 in the SCS could be assumed as following the normal distribution, only 68% of the TCs had a percentage change of R17 that lies within the range of -3.3% to 9.3%. The risks brought by other TCs lied outside this range could therefore be greatly underestimated in a warmed climate, bringing huge potential risk to coastal area. The large CV showed that the spread of the Vmax, RMW and R17 percentage change in the SCS in each warmed climate period and emission scenario were large, and therefore the spread was an important statistic that worth high attention.

To visualize the variations of the percentage changes of Vmax, RMW and the R17 across different TCs in every warming experiment relative to the control run, the mean azimuthally averaged 10 m wind field of TC Gordon (1989) and TC Warren (1988) were shown in Figure 5.2. From Figure 5.2a and b, it can be seen that both TC Gordon and TC Warren had an increase in Vmax and a decrease in RMW in nearly all warming experiments. Noted that the percentage differences of the Vmax and the RMW between the warming runs and the control run showed here represent 2 “+” symbols in Figure 4.2a and 4.2b for each warming experiment. Despite an increase in Vmax, the R17 did not necessarily increase for these 2 TCs, even responding to the same warming forcing. From Figure 5.2a, it can be seen that the R17 of TC Gordon increased in all warming experiments relative to the control run. However, the R17 of TC Warren were nearly the same in all warming experiments and the control run. Therefore, this demonstrated that the percentage change of R17 in the warmed climate were not necessarily related to the increase in Vmax. Moreover, variations of R17 percentage change between different TCs were large, even in the same warming experiment. Similar difference in the responses of the percentage change in Vmax and RMW were also observed across different TCs in the same

Table 5.1 Selected 14 TCs according to their Category of Percentage Change in R17 in each Warming Experiments (from Largest to Smallest) (The value of the percentage change is the same as the “+” sign in Figure 4.1)

	RCP8.5 Far Future		RCP8.5 Near Future		RCP4.5 Far Future		RCP4.5 Near Future	
Category	Name	R17 change (%)	Name	R17 change (%)	Name	R17 change (%)	Name	R17 change (%)
R17 increasing TCs	Mary (1960)	19.47	Mary (1960)	16.4	Mary (1960)	15.02	Mary (1960)	15.84
	Gordon (1989)	14.76	Hal (1985)	9.57	Gordon (1989)	11.44	Gordon (1989)	11.07
	Hope (1979)	9.09	Utor (2001)	8.15	Hagupit (2008)	9.07	Utor (2001)	5.33
	Utor (2001)	8.78	Gordon (1989)	6.27	Utor (2001)	8.78	Ellen (1983)	4.11
Other TCs	Bess (1974)	3.97	Hagupit (2008)	2.25	Ramasun	3.52	Wanda (1962)	3.25
	Chanthu (2010)	3.42	Wanda (1962)	1.95	Dujuan (2003)	2.42	Bess (1974)	2.83
	Wanda (1962)	2.6	Ramasun	1.56	Ellen (1983)	1.79	Dujuan (2003)	1.61
	Hal (1985)	1.77	Ellen (1983)	1.33	Hal (1985)	1.77	Nuri (2008)	0
	Hagupit (2008)	1.69	Chanthu (2010)	0.9	Wanda (1962)	1.3	Warren (1988)	-0.61
	Ramasun (2014)	1.28	Hope (1979)	-0.83	Warren (1988)	0	Hagupit (2008)	-0.85
	Warren (1988)	0.61	Warren (1988)	-1.22	Nuri (2008)	-1	Ramasun (2014)	-0.98
	Ellen (1983)	-0.52	Dujuan (2003)	-2.42	Chanthu (2010)	-3.04	Hal (1985)	-1.42
R17 constant TCs	Nuri (2008)	-1.33	Nuri (2008)	-4	Bess (1974)	-9.24	Hope (1979)	-2.48
	Dujuan (2003)	-7.46	Bess (1974)	-5.67	Hope (1979)	-14.05	Chanthu (2010)	-3.99

warming experiment. The order of the percentage change of R17 in each warming experiments were shown in Table 5.1. Therefore, the relationship between the historical background environment and the variations of the percentage change of Vmax, RMW and the R17 should be studied, and were established by the results of the MLR analysis in the next sub-section.

5.2 Relationship between historical environment to the variations of TC intensity and size changes in PGW experiments

Various environmental variables were selected to represent the historical environment associated with the TCs. It had been found that SST, vertical wind shear and the atmospheric stability were possible contributors to the variations of TC intensity in present climate and influences the change in TC intensity in future climate projections. Moreover, some studies had pointed out the possible

influence of environmental RH to the TC intensity (Wu et.al., 2012). Therefore, the mid-tropospheric RH were also selected to represent the environmental moisture content. Moreover, as Chan and Chan (2015) had analyzed the effect of outer tangential wind speed to the TC size, the outer wind speed, defined as the wind speed beyond the R17 of the TC in the SCS, was also being chosen as one of the environmental conditions for R17 in this study (Chan & Chan, 2015). A summary of the method to calculate the historical environmental SST, atmospheric instability, mid-tropospheric RH, the vertical wind shear and the outer wind speed can be found in section 3.2.1. Moreover, as the historical SST showed a long-term increasing trend over 99% confidence interval in the SCS, this long-term increasing background SST was detrended and the detrended SST, but not the SST, were used as one of the environmental parameters in the MLR analysis.

Results of the MLR slope for different environmental parameters extracted from the ERA-20C for TCs before 1979 and ERA5 reanalysis data for TCs after 1979 were averaged across the 4 warming experiments to show the most robust relationship between the historical environmental

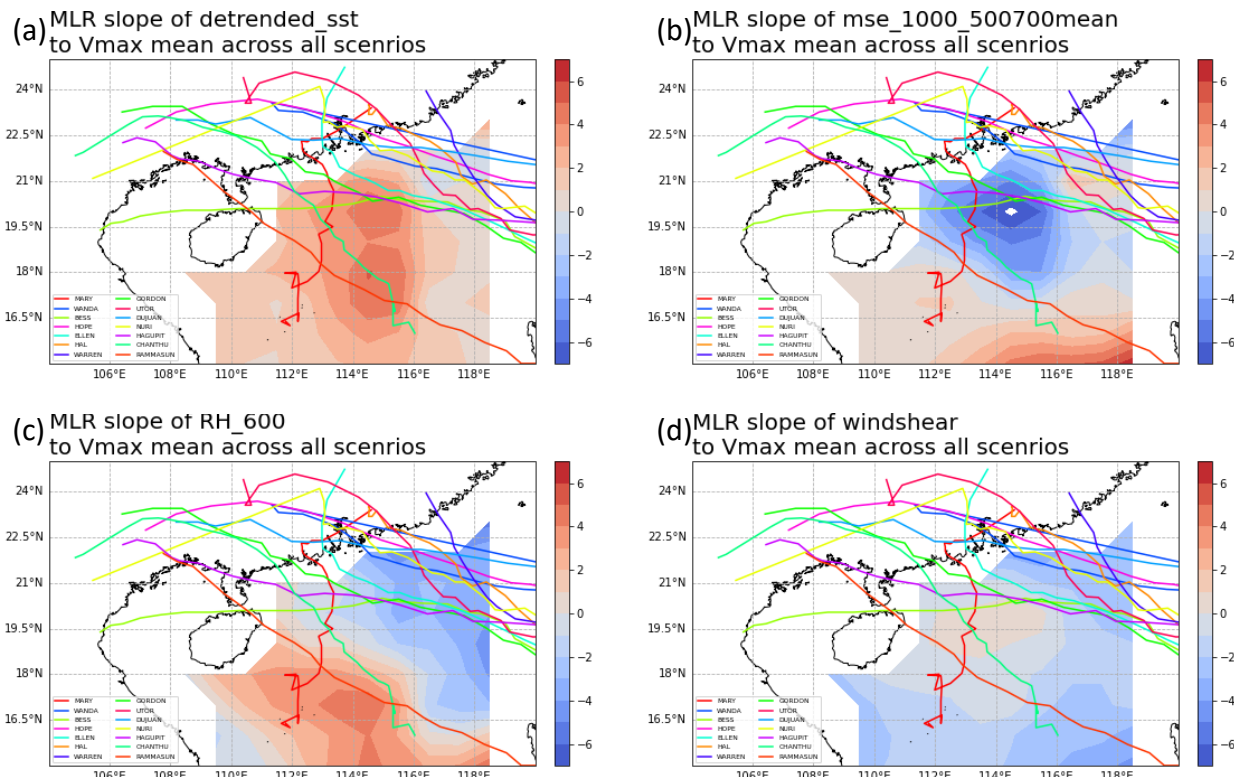


Figure 5.3 MLR slope of normalized (a) detrended SST, (b) Atmospheric instability, (c) mid-tropospheric RH, (d) Vertical wind shear regressed to the percentage change of Vmax in each scenario and averaged across all warming experiments. Units of the colorbar were % of Vmax change per 1 unit of standardized environmental parameters. Overlayed were the TC tracks in the control run

parameters and the variations of the percentage change of TC characteristics, regardless of the PGW signal imposed. Apart from the 14 TCs selected, TC Hato and TC Mangkhut were also tried to be included in the sample pool, and were test in the MLR analysis, which also showed similar relationship between the historical environment to the variations of percentage changes of TC intensity and size in future climate. This implied that the relationship established by MLR analysis here were not sensitive to the case selected and the particular warming period as well as the emission scenario. Statistical significance tests on whether the MLR slope obtained from the analysis were significantly different from 0 were also carried out, which the assumptions, details and the results were presented in APPENDIX VI. Readers were asked to be addressed to APPENDIX VI if they were questioning on the sample size of the MLR analysis.

5.2.1 Relationship Between Historical Environment to the Variations of Vmax Changes in PGW Experiments

Results for the historical environmental parameters regressing to the variation of Vmax percentage changes for different TCs were shown in Figure 5.3. From the MLR slope map, the strongest relationship between the historical environment which could possibly control the variations of the Vmax percentage changes in future climate among different TCs was the historical detrended SST (Figure 5.3a). For TC with larger historical detrended SST, the Vmax increased more in the future climate compared to other TCs. Moreover, Figure 5.3d showed a negative relationship between the historical vertical wind shear to the variations of Vmax percentage changes among each TC. For larger historical vertical wind shear environment, the TC intensity increased less in the projected future climate compared to other TCs. The results matched the findings from Tuleya et.al. (2016) that vertical wind shear tends to limit the development of a weak TC.

The regression relationship between the atmospheric instability and the mid-tropospheric RH to the variations of the percentage increase of Vmax for different TCs were less robust across all warming experiments as shown in Figure 5.3b and 5.3c. One may question whether this was due to the coarse horizontal resolution of 0.1° of the ERA5 reanalysis data, which could not resolve the

convective structures at the eyewall and the spiral rainbands of the TC (Gentry & Lackmann, 2010).

However, the MLR using the historical environmental variables extracted from the control simulation

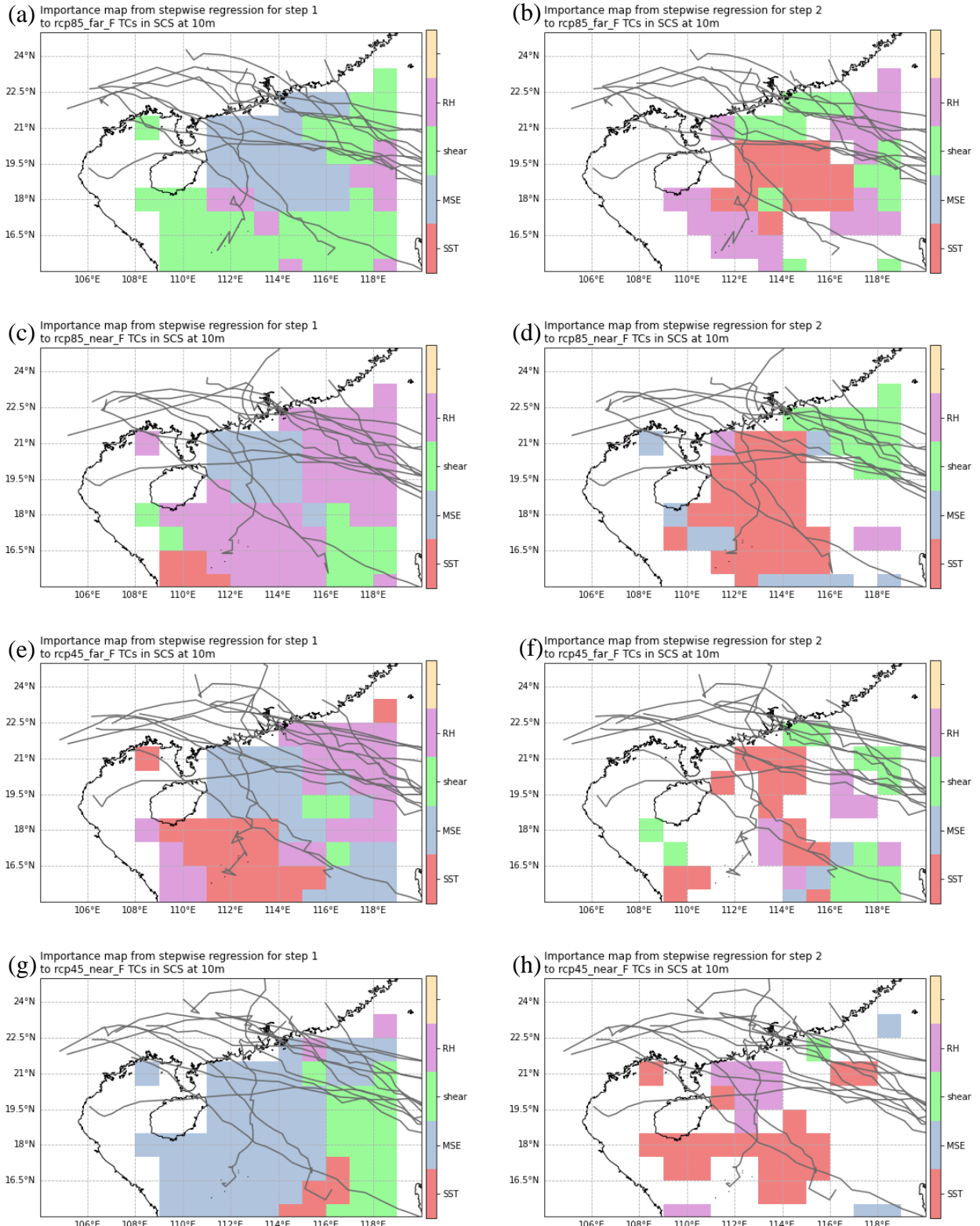


Figure 5.4 Left column: (a,c,e,g) Step 1 and Right column: (b,d,f,h) step 2 of the stepwise regression map between the historical environmental variables of the 14 TCs to the variations of the Vmax percentage change of 14 TCs in (a,b) RCP8.5 Far Future, (c,d) RCP8.5 Near Future, (e,f) RCP4.5 Far Future and (g,h) RCP4.5 Near Future. color denotes (red) detrended SST, (blue) 1000 mb – 500 mb to 700 mb mean MSE, (green) vertical wind shear within 500 km from the TC center, (purple) 600 mb RH. Grey lines are the tracks of the 14TCs in control experiment.

also did not show a robust relationship between the atmospheric instability and the mid-tropospheric RH to the Vmax variations across all future climate periods and emission scenarios (not shown). As Tuleta et.al. (2016) had reported a 0.5 times importance of the atmospheric stability to the SST in contributing to the TC intensity changes, the atmospheric instability should have less importance compared to the detrended SST in explaining the variations of Vmax percentage change in warming experiments for different TCs, and thus the signal of the atmospheric instability was less robust in this study. Nevertheless, the relationship between the mid-tropospheric RH to the variations of Vmax percentage change for different TCs were not clear. As Wu et.al. (2012) had found that how the environmental RH controlled the Vmax of different TCs was not linear and less significant statistically, their results matched with this study that the mid-tropospheric RH was less robust and important in controlling the variations in TCs Vmax in future climate compared to the mean.

Stepwise regression was used to quantify the relative importance of each historical environmental conditions in explaining the variations of Vmax percentage changes in the future climate among different TCs by providing the rank in reducing the mean squared error of the MLR model. Details of how the stepwise regression were performed were explained in section 3.2.2. Figure 5.4 presented the step 1 and step 2 of the stepwise regression map for historical environment associated with the selected 14 TCs regressing to the variations of Vmax percentage changes in the warming experiments. Despite the apparently more important atmospheric instability and mid-tropospheric RH in explaining the variations of the percentage increase of Vmax for different TCs in a warmed climate in step 1, the results were less robust across 4 warming experiments. However, step 2 of the stepwise regression showed that the detrended SST were the most important and robust environmental conditions that controlled the variations of Vmax increase for different TCs. Moreover, the historical vertical wind shear magnitude were found to be less important in limiting the Vmax increase for different TCs compared to the detrended SST, as indicated by fewer green grids in both step 1 and step 2 of the stepwise regression map compared to the red grids. Results also matched previous literature from Tuleya et.al. (2016) that stronger TCs were more resist to the vertical wind

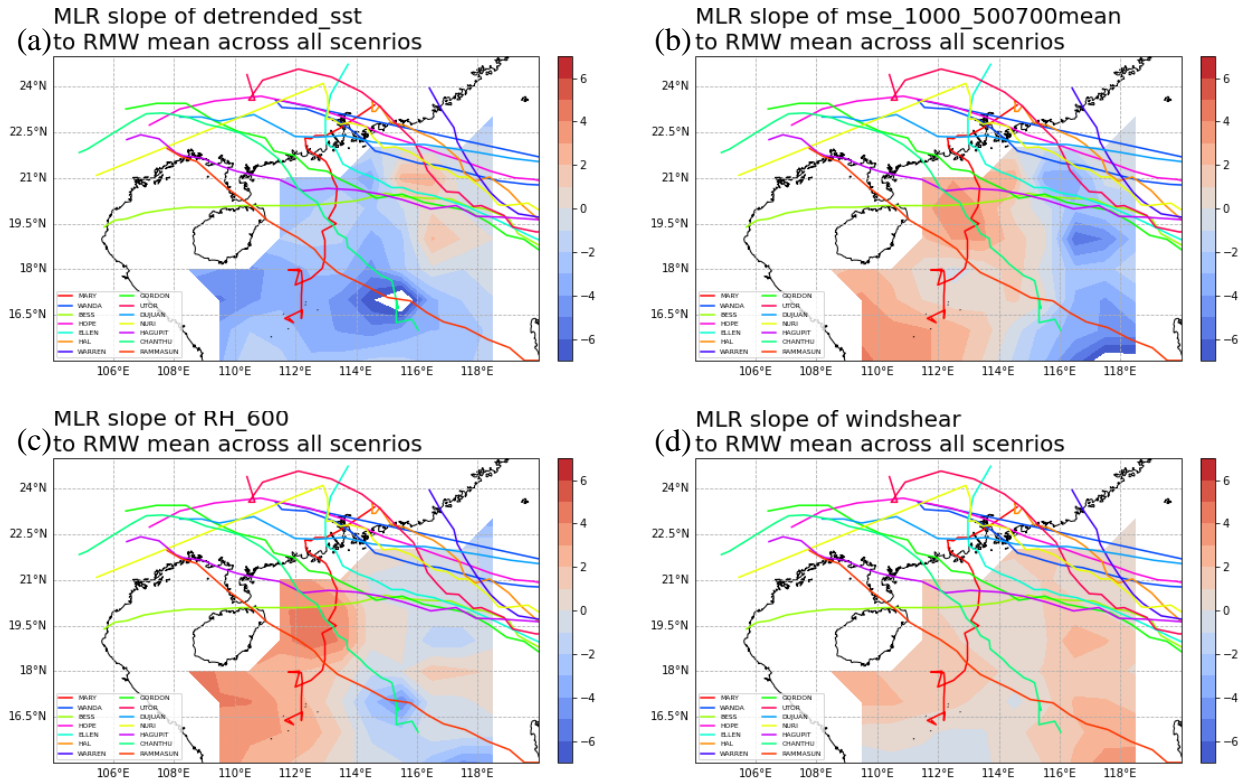


Figure 5.5 MLR slope of normalized (a) detrended SST, (b) Atmospheric instability, (c) mid-tropospheric RH, (d) Vertical wind shear regressed to the percentage change of RMW in each scenario, and averaged across all warming experiments. Units of the colorbar were % of RMW change per 1 unit of standardized environmental parameters. Overlayed were the TC tracks in the control run

shear, which possibly restrained the effect of the vertical wind shear to TC Vmax variations for strong TCs, therefore resulted in smaller variation explained by the vertical wind shear here.

5.2.2 Relationship Between Historical Environment to the Variations of RMW Changes in PGW Experiments

Figure 5.5 shows the MLR slope map between the historical environmental variables to the variations of RMW percentage change in each future climate period among different TCs, and averaged across all warming experiments. Figure 5.5a and 5.5d showed a negative relationship between the historical detrended SST and a positive relationship between the historical vertical wind shear to the variations of the RMW decrease of different TCs in the warming experiments respectively. Larger historical detrended SST environment, or smaller historical vertical wind shear environment were related to a larger decrease in RMW in a warmed climate relative to other TCs. The opposite relationship of the historical detrended SST and the vertical wind shear regression slope between the percentage change of Vmax and RMW should be resulted from the negative correlation between the

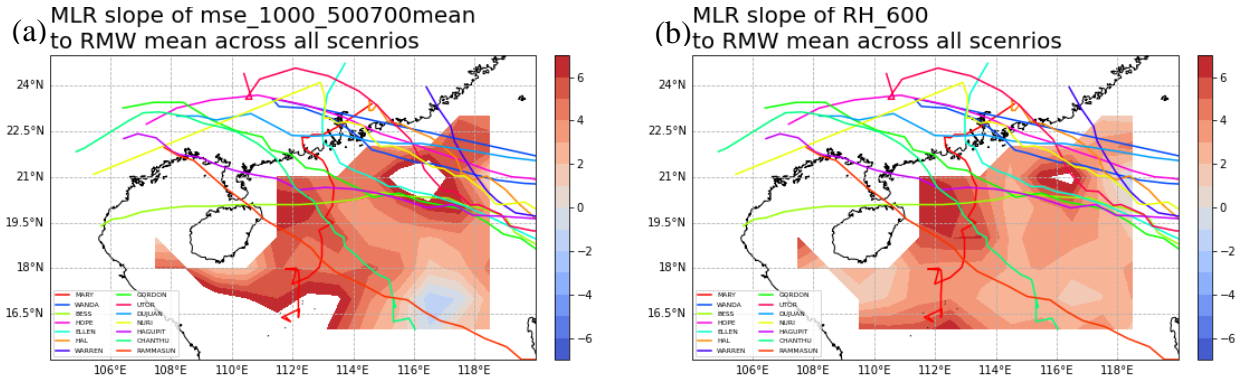


Figure 5.6 Same as Figure 5.5b and 5.5c respectively, but for environmental variables extracted from the control run

percentage change of Vmax and RMW. Relationship of Vmax and RMW changes will be discussed in section 8.2.

Despite the less robust relationship between the atmospheric instability and the mid-tropospheric RH extracted from the ERA5 data to the variations of the percentage change of RMW, the relationships were far stronger and more robust when the data from the control run were used as the regressors. Figure 5.6 showed positive relationships between the historical atmospheric instability and the mid-tropospheric RH to the variations of the decreasing RMW. If the historical environment in the SCS were stabler or wetter, the percentage decrease of RMW in the warming experiments were smaller compared to other TCs. The magnitude of the regression slope were also stronger compared to the detrended SST or the vertical wind shear, which showed the mid-tropospheric RH and the stability of the atmosphere should be the more important environmental conditions in controlling the RMW percentage decrease for different TCs, given a fine enough model resolution. Possible physics behind the relationships were discussed later in section 8.3.

To confirm the relative importance in explaining the variations of the percentage change of RMW, Figure 5.7 showed the step 1 and step 2 of the stepwise regression results of the historical environmental variables extracted from the control simulation regressing to the variation of the RMW percentage change in the warming experiments. From the Figure 5.7a, c, e, g, which showed the most important parameters in explaining the variations of the RMW percentage decrease among different TCs, both the mid-tropospheric RH and the detrended SST were the most important. How might the

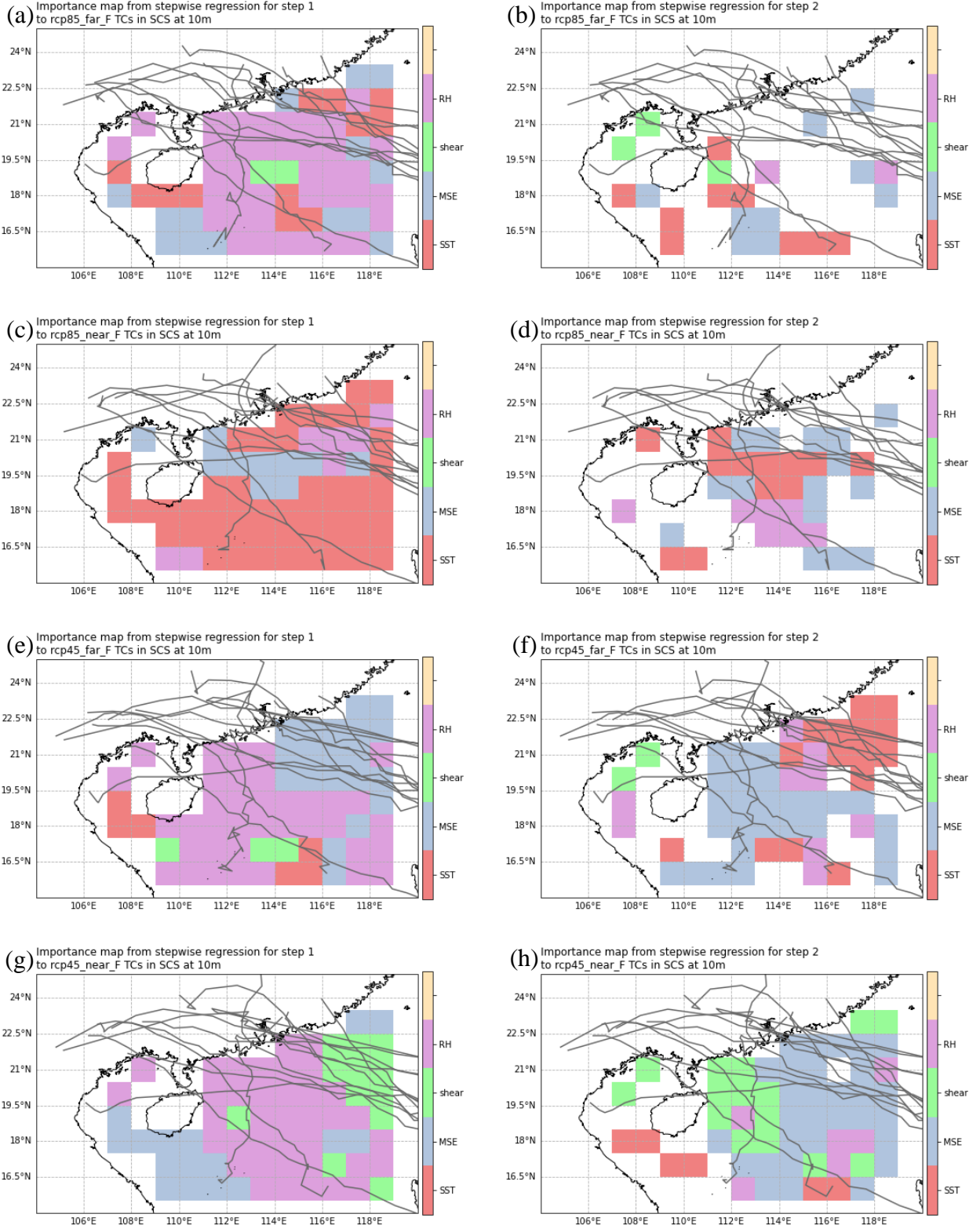


Figure 5.7 Left column: (a,c,e,g) Step 1 and Right column: (b,d,f,h) step 2 of the stepwise regression map between the historical environmental variables extracted from the control run of the 14 TCs to the variations of the RMW percentage change of 14 TCs in (a,b) RCP8.5 Far Future, (c,d) RCP8.5 Near Future, (e,f) RCP4.5 Far Future and (g,h) RCP4.5 Near Future. color denotes (red) detrended SST, (blue) 1000 mb – 500 mb mean MSE, (green) vertical wind shear within 500 km from the TC center, (purple) 600 mb RH. Grey lines are the tracks of the 14TCs in control experiment.

mid-tropospheric RH control the variations of the RMW percentage changes among different TCs

were discussed in section 8.3. Relationship of the detrended SST to the percentage change of RMW

in warming experiments should be related to the negative correlation between the percentage change of Vmax and RMW in the warmed climate. Moreover, step 2 of the stepwise regression showed that the historical atmospheric instability might have some role in influencing the variations of the RMW percentage changes in the future climate. The possible relationships between the historical atmospheric instability to the RMW variations in the future climate were discussed in section 8.3.

5.2.3 Relationship Between Historical Environment to the Variations of R17 Changes in PGW Experiments

Figure 5.8 shows the MLR slopes of historical environmental variables to the difference in the percentage change of R17 among each TC in the warming experiments. From Figure 5.8e, a TC embedded in a historically windier SCS would have a larger percentage increase in R17 in a warmed climate compared to other TCs. Moreover, regression to the environmental variables obtained from the control run showed a strong positive relation between the variations of the R17 percentage change for different TCs in each warming experiment and the mid-tropospheric RH (not shown). This represented a historically moister environment were associated with a larger percentage increase of R17 in a warmed climate compared to other TCs in the same warming experiment.

Figure 5.9 showed the stepwise regression results for the historical environmental variables for each TCs to the difference in the percentage change of R17 in different future climate and different emission scenarios. From Figure 5.9a, c, e, g, one can be seen that both the mid-tropospheric RH and the outer wind speed were important contributors to the variations of percentage changes of R17 among different TCs in all 4 warming experiments, as indicated by the large area covered by the purple grids and wheat-coloured grids respectively. The results were robust across all future climate periods and emission scenarios. Step 2 of the stepwise regression (Figure 5.9b, d, f, h) also showed that the mid-tropospheric RH and the outer wind speed were important contributors to the variations of R17 changes for different TCs. Other historical environmental variables were not important in

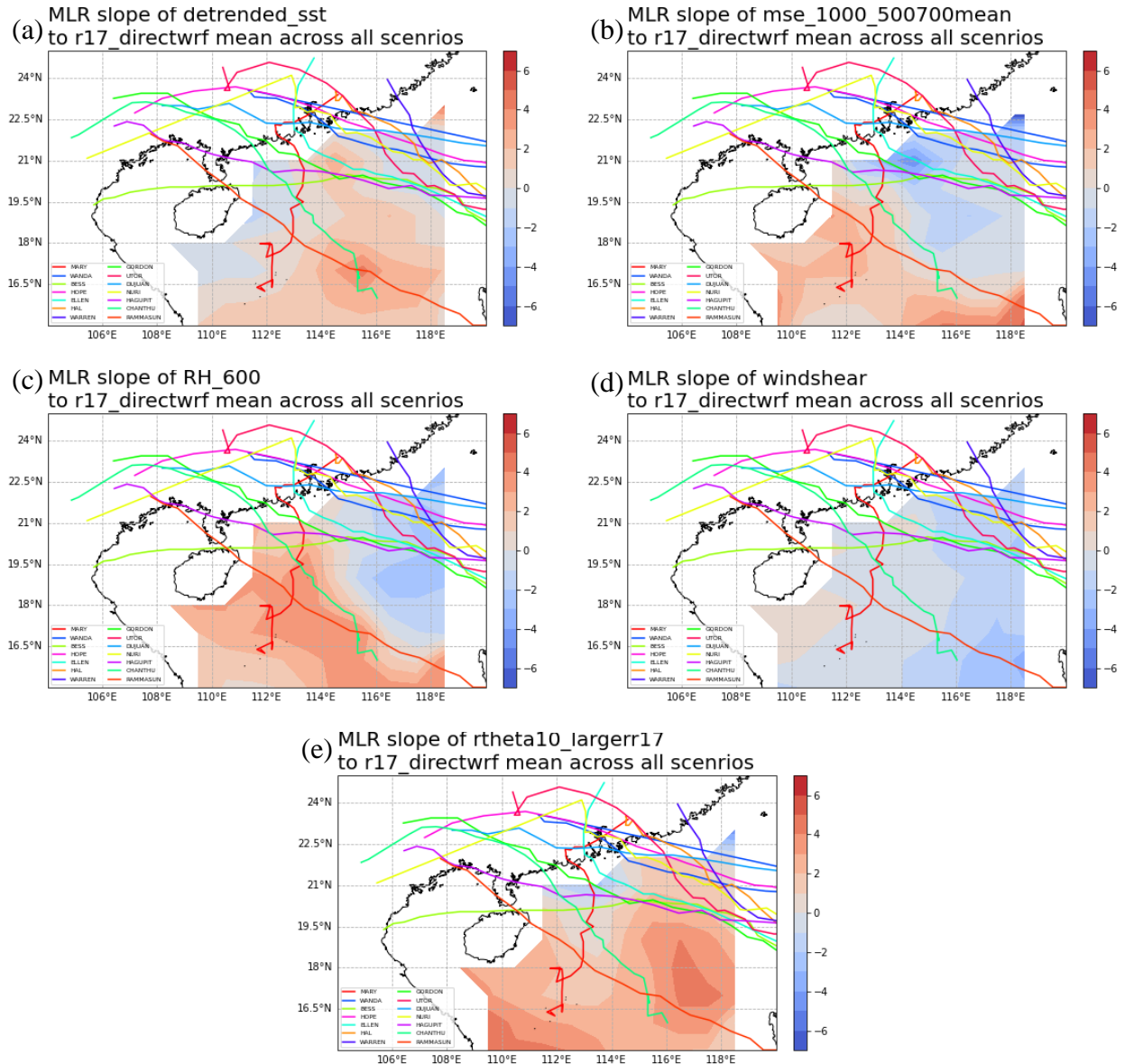


Figure 5.8 MLR slope of normalized (a) detrended SST, (b) Atmospheric instability, (c) mid-tropospheric RH, (d) Vertical wind shear , (e) 10m outer wind speed regressed to the percentage change of R17 in each scenario, and averaged across all warming experiments. Units of the colorbar were % of R17 change per 1 unit of standardized environmental parameters. Overlayed were the TC tracks in the control run

influencing this variation. Therefore, for TCs located in a historically moister or windier environment in the SCS, the R17 will increase more in future climate projections.

Moreover, nearly all step 1 of the stepwise regression map to the R17 showed a pattern of higher importance of mid-tropospheric RH at the south of the northern SCS domain. The TC tracks were mostly concentrated at the north of this RH importance band. Wu et.al. (2012) had found that rear quadrant of a TC tends to have larger RH, while Lonfat et.al. (2004) had found that rainfall of a TC tends to be concentrated at the front left quadrant of a TC to the front right quadrant of a TC, depending on its intensity (Lonfat et.al., 2004; Wu et.al., 2012). The direction of the vertical wind

shear may also contribute to the asymmetry of the convective activities associated with the TC, thus RH distribution of a TC (Frank & Ritchie, 2001). All these literatures suggested that RH could be

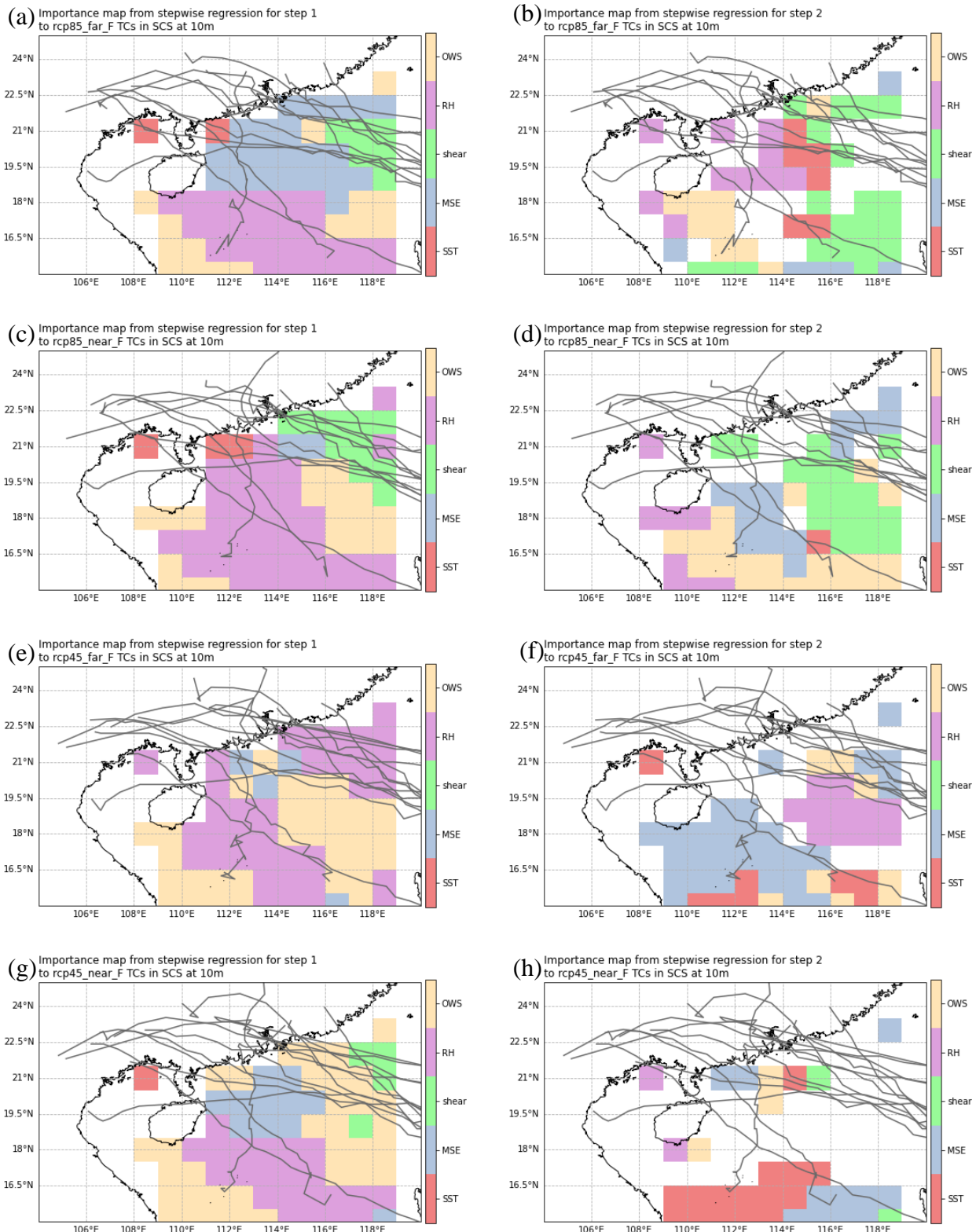


Figure 5.9 Left column: (a,c,e,g) Step 1 and Right column: (b,d,f,h) step 2 of the stepwise regression map between the historical environmental variables of the 14 TCs to the variations of the R17 percentage change of 14 TCs in (a,b) RCP8.5 Far Future, (c,d) RCP8.5 Near Future, (e,f) RCP4.5 Far Future and (g,h) RCP4.5 Near Future. color denotes (red) detrended SST, (blue) 1000 mb to 500 mb to 700 mb mean MSE, (green) vertical wind shear within 500 km from the TC center, (purple) 600 mb RH, (wheat) 10 m outer wind speed ($m s^{-1}$). Grey lines are the tracks of the 14TCs in control experiment.

asymmetric associated with TCs. Moreover, later figures in Section 7.5 showed that most of the moisture source were from the southwesterlies at the southern quadrant of the TC in the SCS. Yet, more literature should be reviewed on the asymmetry of RH distribution associated with a TC. Despite a less certainty, large asymmetry of the RH distribution due to the possible environmental influence, as well as the asymmetrical moisture source in the SCS might be the explanation the observed pattern here.

6. EPV Diagnostics of Relationship between Historical Environmental RH to R17 Change Variations in Future Climate for selected TCs

MLR analysis and stepwise regression showed that the variations of TC Vmax changes in future climate projections among each TCs were influenced by the historical detrended SST and the vertical wind shear. Moreover, the historical environmental RH controlled the variations of TC RMW changes in the future climate for different TCs. Historical environmental RH and the 10 m outer wind speed also showed important roles in controlling the future changes of R17 for different TCs to the same warming forcing. As the changes in Vmax in future climate projection were comparatively better established (e.g. Knutson et.al., 2015; Knutson et.al., 2020), while the variations of the percentage change of R17 were less emphasized in past literatures (see Gutmann et.al., 2018 for the only example). The following 2 sections provided a more physical and dynamical explanations on how historical environment with different RH and outer wind speed could cause large differences in R17 changes for different TCs in the same future climate condition.

EPV diagnostics were used to diagnose the effect of historical environmental RH in controlling the future R17 changes among each TCs to the same warming forcing as it had been found that diabatic heating associated with the spiral rainbands played a great role in determining the size of different TCs (Hill & Lackmann, 2009). Hill and Lackmann (2009) had found that the size of the TC wind field was related to the environmental RH, which the precipitation associated with the spiral rainband is sensitive to. Moister environment enables more precipitation, diabatic heating and diabatic EPV production associate with the spiral rainbands, thus forming stronger and more wide-spread EPV tower and enlarged the size of a TC (Hill & Lackmann, 2009). Therefore, the effect of historical RH to the variations of R17 changes in future climate were diagnosed by the EPV budget equation, which details of the equation were presented in the APPENDIX III.

2 TCs, namely TC Mary (1960) and TC Nuri (2008) were further selected, re-simulated under the Far Future climate period following RCP8.5 emission scenarios in order to archive the model

microphysics scheme outputted diabatic heating rate. Reasons for choosing these 2 TCs were: 1. The percentage change of R17 for TC Mary (1960) and TC Nuri (2008) were the most robust across all warming experiments. TC Mary were the TC having largest percentage change of R17 in all warming experiments while TC Nuri were in the category of R17 constant TCs in 3 out of 4 warming experiments (Table 5.1). 2. TC Mary and TC Nuri had similar outer core size in the past (Table 4.1), which could reduce possible influence of the size of the TC in the historical climate to the difference in the percentage change of TC size among the two TCs in a warmer climate. To better distinguish the re-simulated TC Mary and TC Nuri with the previous simulation, the newly simulated TCs were named as H_DIA. For consistency, all the data and graphs presented in this section were extracted from the H_DIA runs.

6.1 Model Verification and TC Mean Wind Field

Results of the simulated TC tracks of TC Mary (1960) and TC Nuri (2008) in both the control run and the RCP8.5 Far Future run were similar to the previous simulations (Figure 4.1). Figure 6.1 showed the azimuthally averaged 10m wind field for TC Mary and TC Nuri in the control run and the RCP8.5 Far Future run averaged in the SCS. From the Figure, it can be seen that the R17 of TC Mary had increased by approximately 25% in the SCS while the R17 of TC Nuri had a slight increase only in the RCP8.5 Far Future climate period. Moreover, the projected 10 m Vmax for TC Mary also

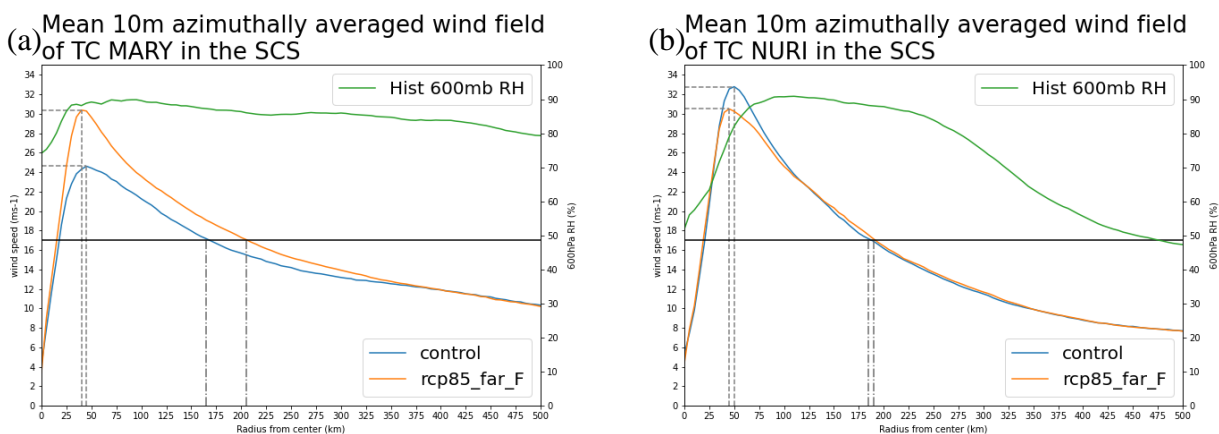


Figure 6.1 Azimuthally averaged 10 m wind field of TC Mary (1960) and TC Nuri (2008) in the control run and the RCP8.5 Far Future run from H_DIA simulations. Black line denotes the 17 m s^{-1} wind speed, grey dashed line represented the Vmax and RMW while dash-dotted line showed the R17 of the TC. Also showed the Historical 600 mb RH for TC Mary and TC Nuri from the model output (green, right y-axis)

increased in the RCP8.5 Far Future run while that for TC Nuri had a slight decrease in the SCS. This demonstrated the variations of TC R17 and Vmax percentage changes among different TCs in the future climate period and emission scenarios. Therefore, this section was trying to provide a physical explanation on why some TCs like TC Mary were projected to have a large increase in R17 in the future climate while some TCs like TC Nuri were projected to have a nearly constant R17 in a warmed climate. Despite only 2 TCs were chosen to be diagnosed by EPV budget, similar argument could also be extended to all R17 increasing TCs and R17 constant TCs.

6.2 Azimuthally Averaged EPV Diagnostics

As the mid-tropospheric RH were found to be an important environmental parameter in controlling the variations of R17 percentage change in a warmed climate between different TCs by MLR analysis, the azimuthally averaged historical mid-tropospheric RH profile in the SCS were plotted for TC Mary and TC Nuri in Figure 6.1. From the Figure, it can be seen that the historical mid-tropospheric RH for TC Mary excess 80% even at a radius of 500 km from the TC center.

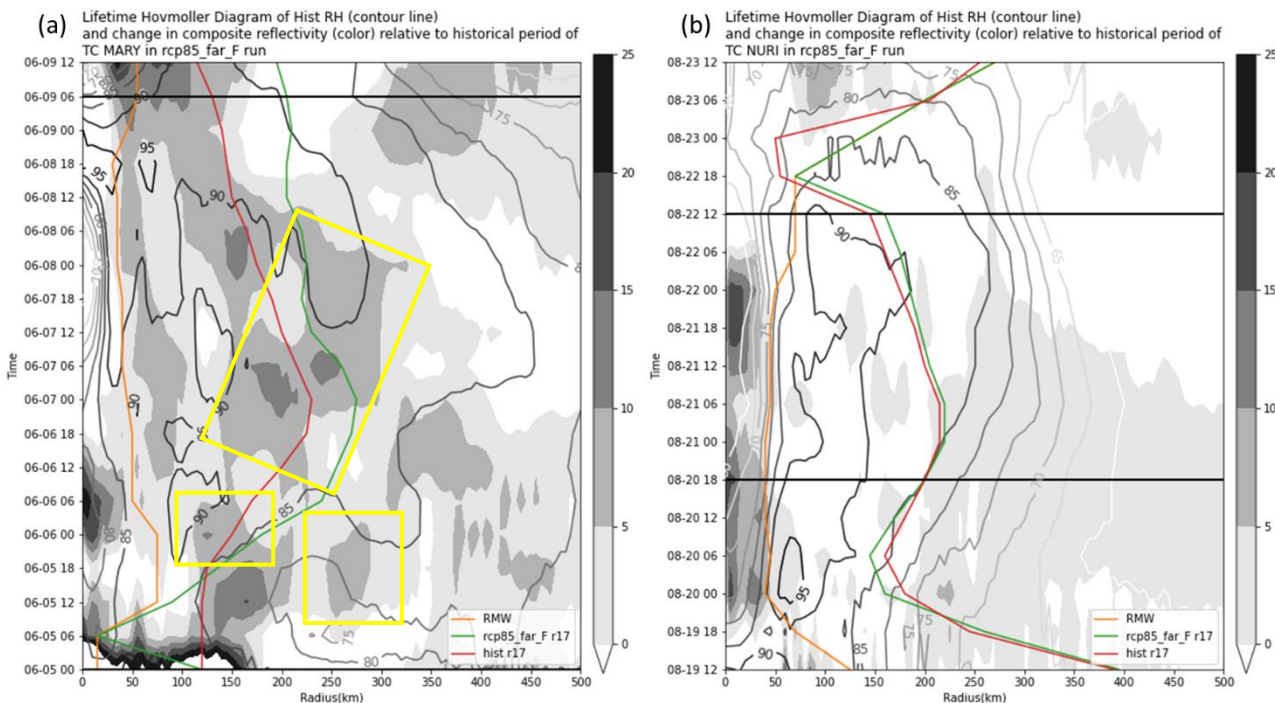


Figure 6.2 Hovmöller diagrams of azimuthally averaged model outputted composite reflectivity difference between RCP8.5 Far Future run and control run (unit: dbz) (color), and historical environmental 600 mb RH (unit: %) (contour), each contour indicate 5% RH, for (a) TC Mary, (b) TC Nuri. lines denote (red) R17 in control run, (green) R17 in RCP8.5 Far Future run, (orange) RMW in RCP8.5 Far Future run. 2 black line indicate the time when the TC enters the SCS and landfall at the South China coast

However, compared to TC Mary, the historical environment for TC Nuri were drier, with only 50% RH at 500 km radius from the TC center. Because Hill and Lackmann (2009) had found that the TCs' spiral rainband activities, which produced diabatic EPV, were sensitive to the environmental RH, the hovmöller diagrams of the composite reflectivity, EPV, diabatic heating and the diabatic EPV tendency for TC Mary and TC Nuri were studied and contrasted in this section.

Figure 6.2 showed the azimuthally averaged model outputted composite reflectivity difference of TC Mary (1960) and TC Nuri (2008) in control run and RCP8.5 Far Future climate together with the historical environmental RH retrieved from the model. Note that the translation speed for TC Mary (1960) was slower in the RCP8.5 Far Future climate compared to the control run. From Figure 6.2a, it can be seen that the composite reflectivity for TC Mary were stronger at time 1960-06-06-00 at a radius of 275 km from the TC center and between 100-150 km radius (2 yellow rectangles at the bottom of Figure 6.2a). Moreover, stronger convective activities signal in the warming run were found

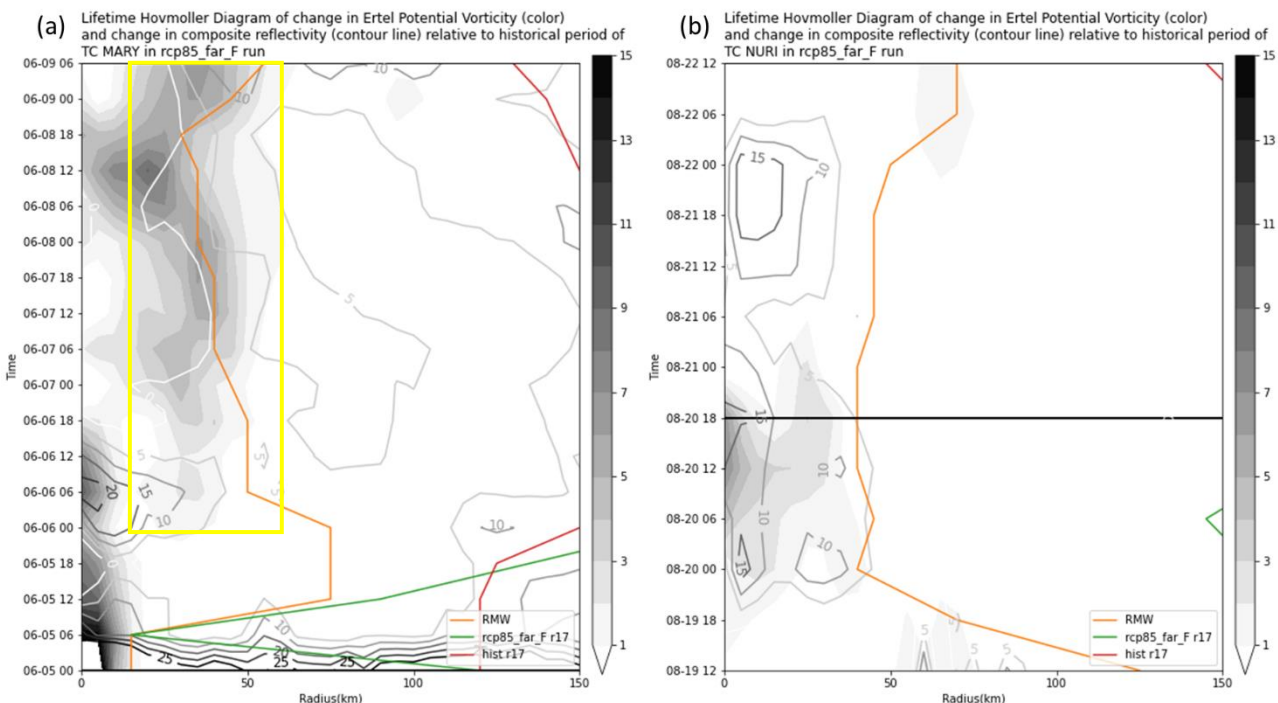


Figure 6.3 Hovmöller diagrams of azimuthally averaged 700 mb to 850 mb mean EPV between RCP8.5 Far Future run and control run (unit: PVU) (color), and difference in model outputted composite reflectivity in RCP8.5 Far Future relative to the control run (unit: dBz) (contour), each contour indicate 5 dBz, for (a) TC Mary, (b) TC Nuri. lines denote (red) R17 in control run, (green) R17 in RCP8.5 Far Future run, (orange) RMW in RCP8.5 Far Future run. The black line denotes the time when the TC enters the SCS. End of y-axis is the time of landfalling at the South China coast. x-axis is from the TC center to 150 km radius

for TC Mary after 1960-06-06-18 at a radius of 150 km to 250 km (largest yellow rectangle). However, the composite reflectivity for TC Nuri in control run and in RCP8.5 Far Future experiment were similar both in the magnitude and the radial structure (Figure 6.2b), which the difference in the composite reflectivity were close the 0 dBz. It showed that the symmetrical part of the inner and outer core convective structure were similar for TC Nuri in control run and in far future climate period.

Moreover, TC Mary were located in a historically moister SCS, while TC Nuri were located in a historically drier environment. This could be seen from Figure 6.1 (green line), as well as the contour lines in Figure 6.2a and 6.2b. From Figure 6.2a, the historical environmental mid-tropospheric RH were larger than 80% within 500 km from the TC center. However, the environmental RH of TC Nuri quickly decayed to smaller than 65% at 350 km radius in the SCS. These results indicated that TCs in a historically moister SCS could develop stronger convective activities in a warmed future climate compared to TCs located in a historically drier environment, which the convective activities were nearly the same. Reasons for the relation between the historical environmental RH to the convective activities in the warmed climate were discussed in the last 2 paragraphs in section 6.5.

Figure 6.3 showed the hovmöller diagram of azimuthally averaged lower tropospheric EPV difference in the control run and the RCP8.5 Far Future simulation from H_DIA runs for TC Mary and TC Nuri. From Figure 6.3a, it can be seen that the strength of the central EPV tower for TC Mary was larger in the RCP8.5 Far Future runs compared to the control run starting from 1960-06-06-00 (yellow rectangle in Figure 6.3a). Moreover, the region exceeding 1 PVU extended wider since 1960-06-06-06, from 110 km in the control run to 160 km in the RCP8.5 Far Future run (not shown). However, the strength of the central EPV tower associated with TC Nuri were similar in the control run and the RCP8.5 Far Future run. But the RCP8.5 Far Future run for TC Nuri also showed a slightly wider distribution of location which the EPV exceed 1 PVU (not shown). This should reflect the slight increase in R17 for TC Nuri in the RCP8.5 Far Future simulation compared to the control run (as indicated in Figure 6.1b). Yet, both the change in the strength of the central EPV tower and the

radial distribution of EPV for TC Mary were much more obvious compared to TC Nuri. The EPV of the TC can be used to recover the wind field of the TC by PV inversion (Wang & Zhang 2003).

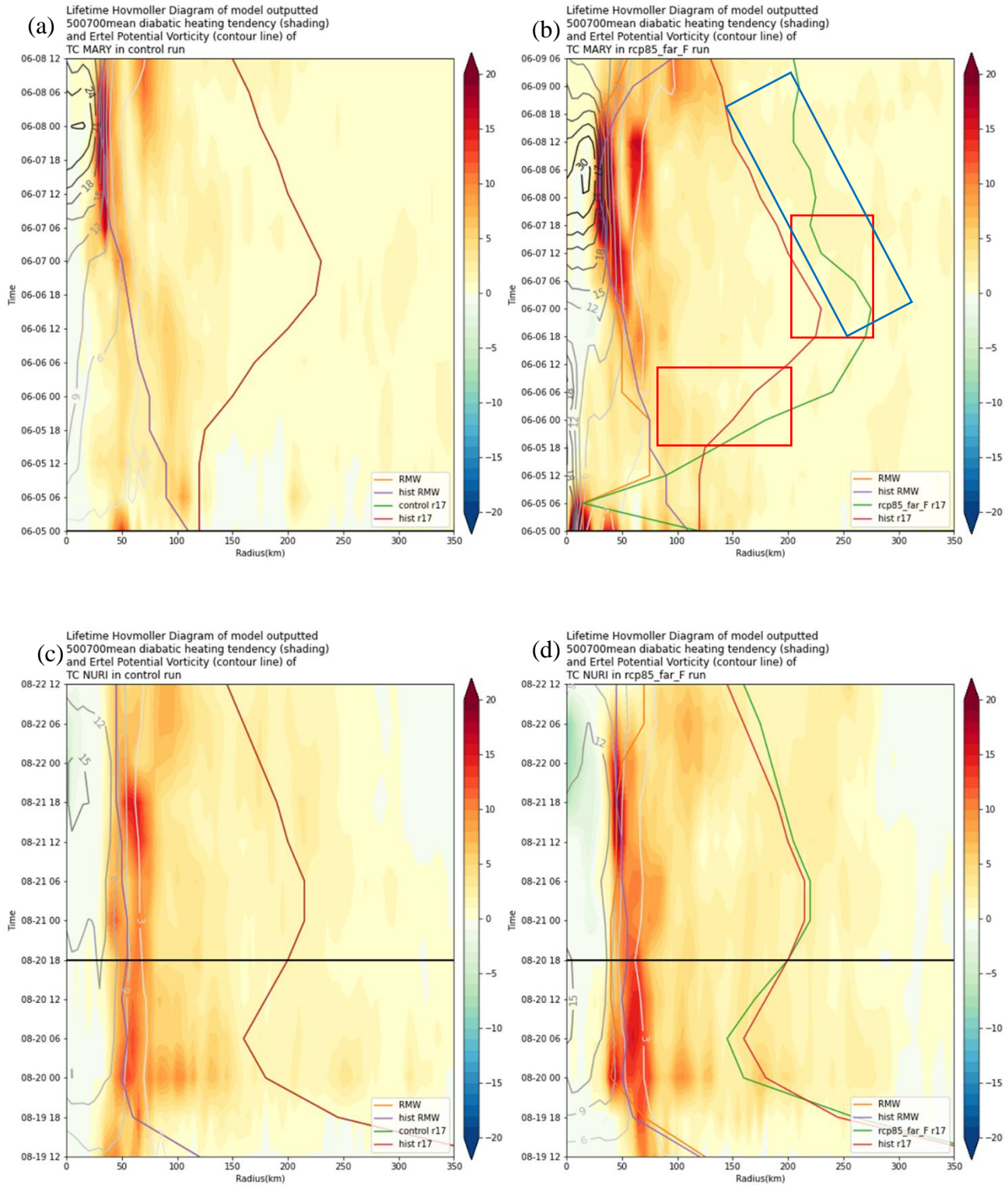


Figure 6.4 Hovmöller diagram of 500 mb to 700 mb mean model outputted diabatic heating rate (unit: $K h^{-1}$) (color) and 700 mb to 850 mb mean EPV (unit: PVU) (contour line) for (a) Mary in control run, (b) Mary in RCP8.5 Far Future run, (c) Nuri in control run, (d) Nuri in RCP8.5 Far Future run, all simulation were from H_DIA runs. Lines denote (red) RI7 in control run, (green) RI7 in RCP8.5 Far Future run, (purple) RMW in control run, (orange) RMW in RCP8.5 Far Future. Black line denotes the time when the TC enters the SCS. End of the y-axis shows the time of landfall. x-axis shows the distance from the TC center to a radius of 350 km

Stronger and more wide-spread central EPV tower for TC Mary in the RCP8.5 Far Future run should be associated with stronger and larger wind field, while TC Nuri had a similar wind field and Vmax in the control and warming simulations. Because the stronger EPV in RCP8.5 Far Future for TC Mary were resulted from a stronger local EPV tendency for TC Mary in the warming experiment, therefore, the source term in the EPV budget equation was investigated next.

From the EPV budget equation ([1] in APPENDIX III), the local EPV tendency is related to the gradient of the diabatic heating rate projecting onto the absolute vorticity vector. Therefore, the model outputted diabatic heating tendency were first studied. Figure 6.4 showed the azimuthally averaged 500 mb to 700 mb mean model outputted diabatic heating rate (K h^{-1}) of TC Mary and TC Nuri in control run and RCP8.5 Far Future run. From Figure 6.4a and b, the diabatic heating rate were stronger for TC Mary in RCP8.5 Far Future experiment compared to the control run at the outer core. For example, the diabatic heating tendency were stronger at 200-250 km at 1960-06-07-00 and between 100-150 km at model time 1960-06-06-00 (red rectangles in Figure 6.4b). Moreover, the stronger diabatic heating tendency at 250 km from the TC center at model time 1960-06-07-00 propagates inward to 150 km at 1960-06-08-18 (blue rectangle in Figure 6.4b). The inward propagation of diabatic heating tendency matched with the inward propagation of the inner portion of the outer spiral rainbands. Moreover, the diabatic heating tendency within 150 km of the radius, which is approximately 3 times of the RMW, for TC Mary in RCP8.5 Far Future was stronger and filamented (lowest red rectangle for example), thus a larger area was associated with stronger diabatic heating tendency in the warming run. However, the change in the magnitude of the diabatic heating tendency for TC Nuri was not obvious, despite a small increase in diabatic heating rate near to the R17 of TC Nuri in the SCS.

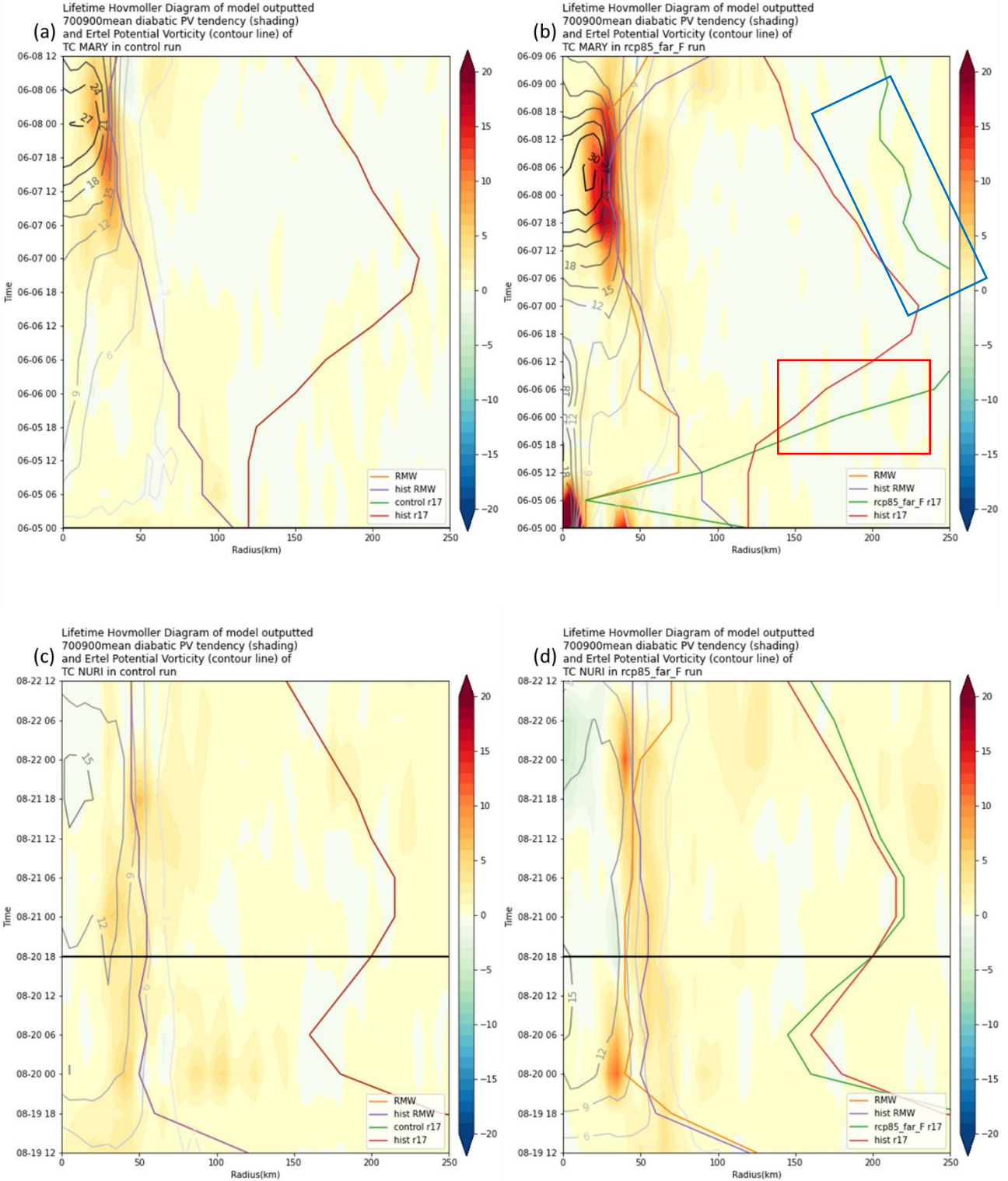


Figure 6.5 Hovmöller diagram of filtered 700 mb to 900 mb mean diabatic EPV tendency (unit: PVU h^{-1}) (color) and 700 mb to 850 mb mean EPV (unit: PVU) (contour) for (a) Mary in control run, (b) Mary in RCP8.5 Far Future run, (c) Nuri in control run, (d) Nuri in RCP8.5 Far Future run, all simulation were from H_DIA runs. Lines denote (red) R17 in control run, (green) R17 in RCP8.5 Far Future run, (purple) RMW in control run, (orange) RMW in RCP8.5 Far Future. Black line denotes the time when the TC enters the SCS. End of the y-axis shows the time of landfall. x-axis shows the distance from the TC center to a radius of 250 km.

Assuming the frictional contribution to the local EPV tendency is small, Figure 6.5 showed the azimuthally averaged 700 mb to 900 mb diabatic EPV tendency computed from the last term of

Equation [1] in APPENDIX III. From Figure 6.5b, isolated bands of diabatic EPV tendency were observed at model time 1960-06-06-00 at 160 km, 220 km from the TC center (red rectangle in Figure 6.5b), yet the difference in strength for these bands in RCP8.5 Far Future run to control run were not obvious. The inward propagating band of diabatic #PV production from model time 1960-06-07-00 to 1960-06-08-18 were also observed in the diabatic #PV tendency hovmöller diagram (blue rectangle in Figure 6.5b). Also, the diabatic EPV tendency at the eyewall were stronger in the RCP8.5 Far Future run since model time 1960-06-06-00 compared to the control run. However, for TC Nuri, the diabatic EPV tendency were only slightly stronger at 240 km from the TC center 2008-08-21-18 in RCP8.5 Far Future run compared to the control run. which could be attributed to the stronger composite reflectivity and diabatic heating tendency at the SCS for TC Nuri.

Vertical profiles of the azimuthally averaged diabatic heating rate and the diabatic EPV tendency for TC Mary at model time 1960-06-06-00 were plotted in Figure 6.6. Compare Figure 6.6a and 6.6b, regions with positive diabatic heating had spread to a larger area from the TC center in the warmed climate. For example, regions having a diabatic heating rate of larger than 2 K hr^{-1} were spread to a larger distance from the TC center, at a radius of 125 km in control run to over 150 km in the RCP8.5 Far Future run in the mid-troposphere. Moreover, stronger and more wide-spread diabatic EPV tendency at a pressure level of 950 hPa in the warmed climate were observed compared to the control run (red rectangles in Figure 6.6a and b) due to a more wide-spread diabatic heating. At the

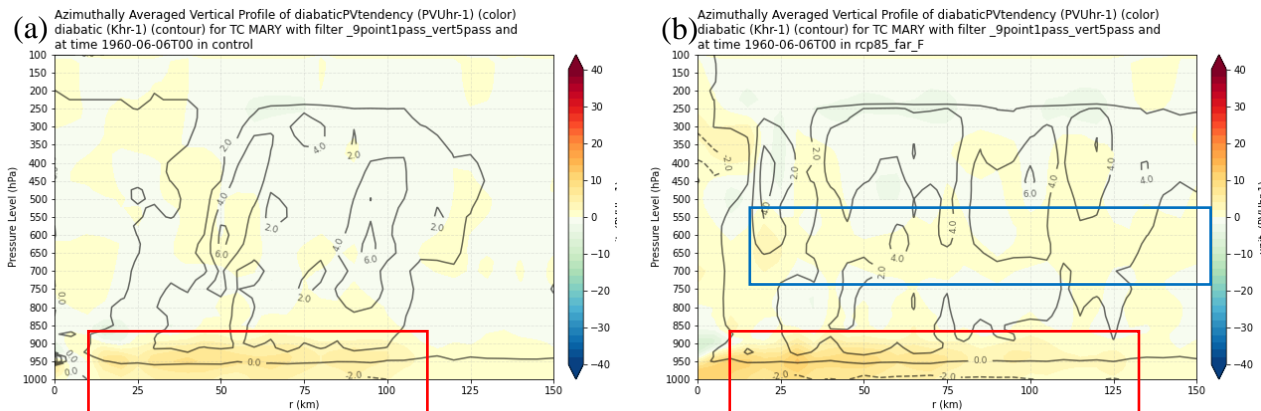


Figure 6.6 Azimuthally averaged vertical profile of model outputted (color) diabatic PV tendency (PVU hr^{-1}) and (contour) diabatic heating rate (unit: K hr^{-1}) for TC Mary at timestep 1960-06-06-00. (a) shows the control run while (b) shows the RCP8.5 Far Future run. Dotted line means negative diabatic heating rate

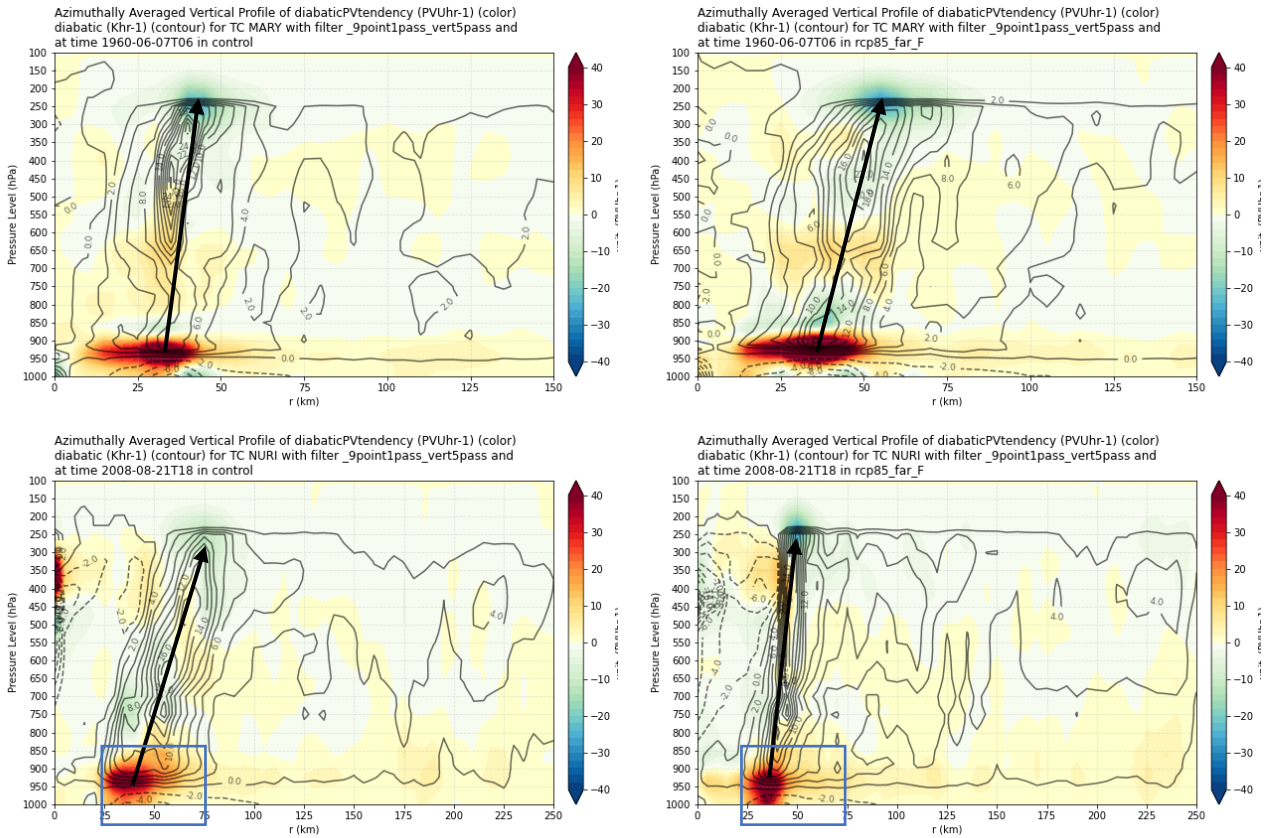


Figure 6.7 Azimuthally averaged vertical profile of model outputted (color) diabatic PV tendency (PVUhr^{-1}) and (contour) diabatic heating rate (unit: Khr^{-1}) for (a,b) TC Mary at timestep 1960-06-06-00 and (c,d) TC Nuri at 2008-08-21-18. (a,c) shows the control run while (b,d) shows the RCP8.5 Far Future run. Dotted line means negative diabatic heating rate. Black arrows illustrated the absolute vorticity vector

650 hPa pressure level, the diabatic EPV tendency were also stronger in the warming run compared to the control run (blue rectangle in Figure 6.6b) due to the more wide-spread mid-tropospheric heating. All of these signals indicated stronger diabatic EPV production were observed at 1960-06-06-00 for TC Mary in the warming experiment than the control run, which leaded to a larger local EPV tendency and expanded the R17 of TC Mary in a warmed climate.

Figure 6.7 contrasted the model outputted diabatic heating rate and the diabatic EPV tendency for TC Mary at 1960-06-07-06 and TC Nuri at 2008-08-21-18 in the RCP8.5 Far Future experiment and the control run. Despite a relatively stronger diabatic heating tendency at the eyewall of TC Mary in the control run, region with large diabatic heating rate were spread to a larger radial distance in the RCP8.5 Far Future experiment. Moreover, the diabatic EPV production near 950 hPa and 650 hPa were stronger and more widespread in the RCP8.5 Far Future compared to that in the control run (red rectangles in Figure 6.7a, b). However, despite the stronger diabatic heating and diabatic EPV

tendency for TC Nuri in the warming run due to a more compacted eyewall structure, the diabatic EPV tendency was more widespread in the control run for TC Nuri (blue rectangles in Figure 6.7c, d). Therefore, the total diabatic EPV tendency for TC Nuri were similar in both the control run and in the RCP8.5 Far Future climate.

The vertical profile of the diabatic heating and the diabatic EPV tendency matched quite well to the EPV budget theory. Positive diabatic EPV tendency were found at the location with positive diabatic heating gradient (eg: red rectangles in Figure 6.7a, b) while negative diabatic EPV tendency were found at location with decreasing diabatic heating. Moreover, the black arrows, which illustrated the absolute vorticity vector and approximate the location of the eyewall indicated that the diabatic EPV tendency was the gradient of diabatic heating projected to the absolute vorticity vector. Therefore, the results recovered the theory of diabatic EPV production term illustrated in APPENDIX Figure 3.

6.3 Horizontal Structures

As the inner spiral rainbands and the outer spiral rainbands are highly asymmetric, the horizontal structure of the composite reflectivity, EPV, diabatic heating and the diabatic EPV tendency were presented in this section in order to better understand the asymmetric contribution of diabatic EPV production to the total EPV from the inner and the outer spiral rainbands in warming experiments than the control run.

Figure 6.8 showed the horizontal composite reflectivity, EPV and the diabatic EPV tendency for TC Mary at model time 1960-06-06-00 in the control run and the RCP8.5 Far Future experiment. It was the timestep when the R17 of TC Mary increased faster in the warmed climate than the control run. Figure 6.8c to f showed that the EPV and the diabatic EPV tendency were closely related to the convective activity indicated by the composite reflectivity in Figure 6.8a and b. Moreover, by comparing the features indicated by the red and blue rectangles in Figure 6.8a and b, the convective activities of TC Mary at the inner and outer spiral rainbands were stronger in the warming run at the

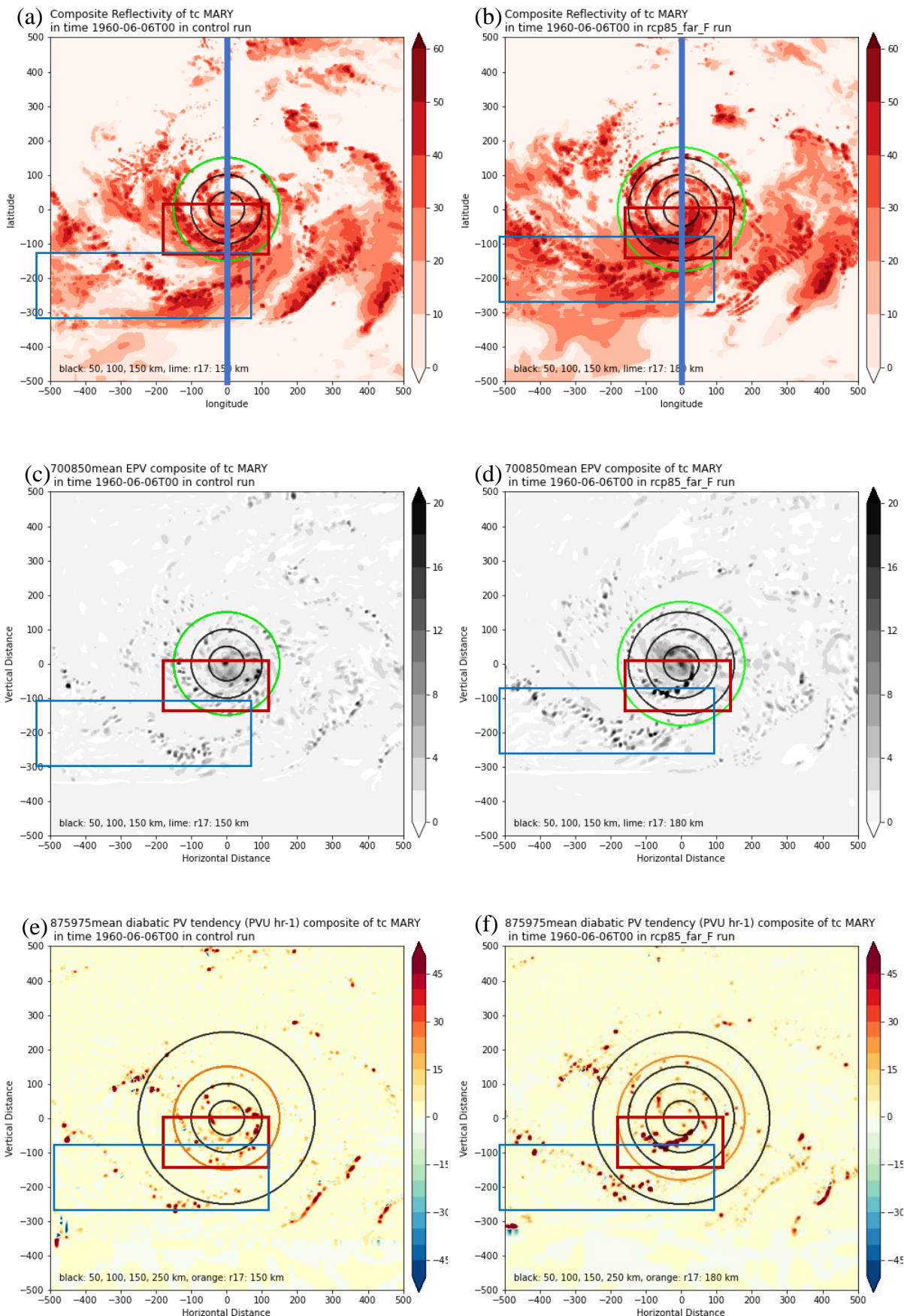


Figure 6.8 Composite plots of (a,b) composite reflectivity (dbz), (c,d) 500-700 mb mean EPV (PVU) and (e,f) 875-975 mb mean diabatic EPV tendency (PVU hr⁻¹) composite of TC Mary at 1960-06-06-00 in (a,c,e) control run and (b,d,f) RCP8.5 Far Future run. Lime or orange circle denoted the R17, black circles denote radius of 50, 100, 150 and 250 km. Thick blue lines in (a,b) showed the vertical cross-section in section 6.5

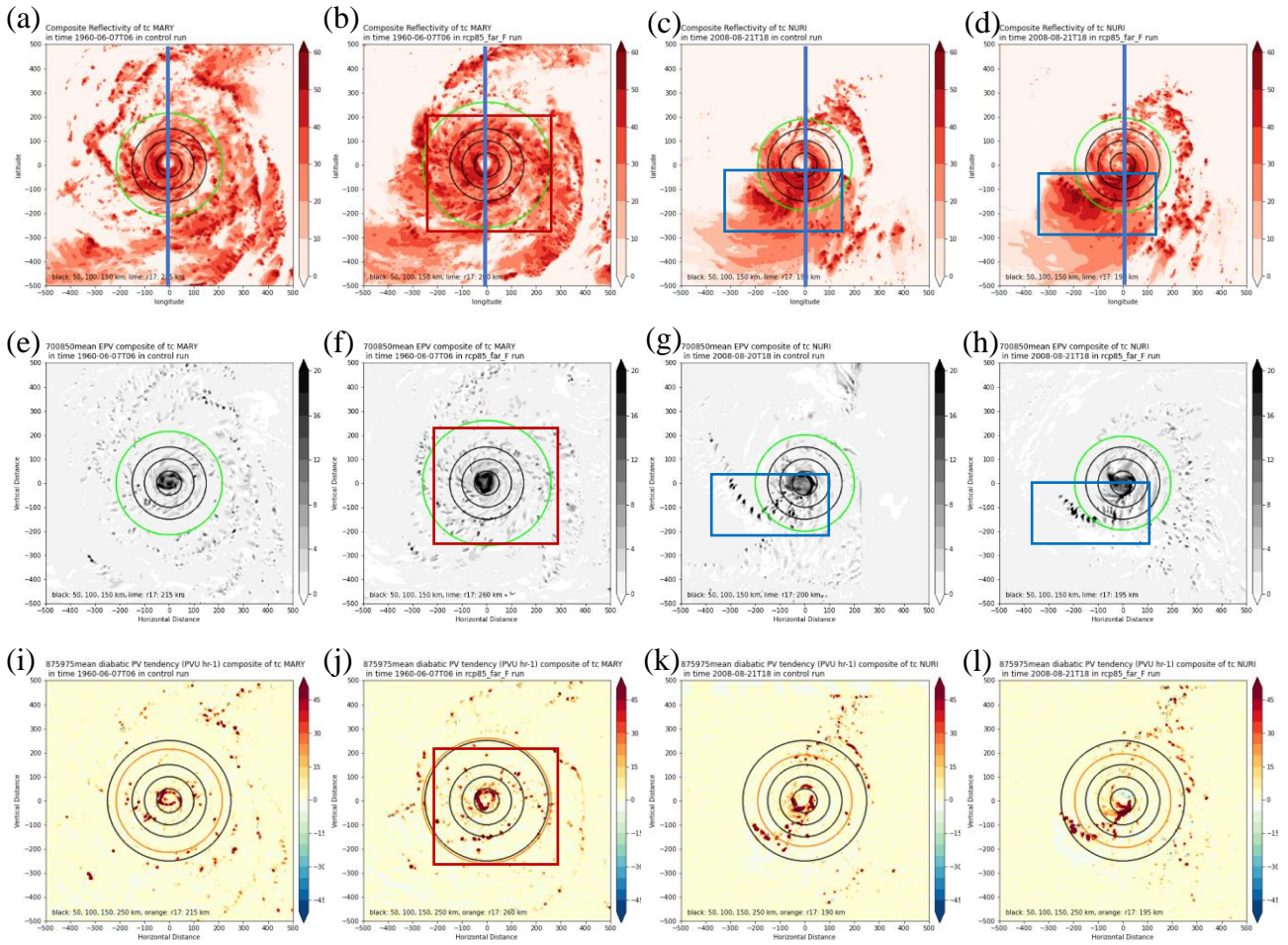


Figure 6.9 Composite plots of (a,b,c,d) composite reflectivity (dbz), (e,f,g,h) 500-700 mb mean EPV (PVU) and (i,j,k,l) 875-975 mb mean diabatic EPV tendency of (a,b,e,f,I,l) TC Mary at 1960-06-07T06 and (c,d,g,h,k,l) TC Nuri at 2008-08-21T18 in (a,e,I,c,g,k) control run and (b,f,j,d,h,l) RCP8.5 Far Future run. Lime or orange circle denoted the R17, black circles denote radius of 50, 100, 150 and 250 km. Thick blue lines in (a,b,c,d) showed the vertical cross-section in section 6.5

southern quadrant. It was accompanied by a stronger EPV and diabatic EPV tendency, as shown by the red and blue rectangles in Figure 6.8d, f.

Differences between the R17 increased TCs and R17 constant TCs were shown in Figure 6.9 by contrasting the composite reflectivity, EPV and diabatic EPV tendency in the warming run and the control run. From Figure 6.9 b, f, j, the convective activity, EPV and the diabatic EPV tendency within 250 km radius of TC Mary in the warming experiment (red rectangles in Figure 6.9 b, f, j) were much stronger and more widely spread compared to the control run. A more widespread rapid filamentation zone could be observed for TC Mary in the warming run than the control run, which implied that the inner spiral rainband activities were stronger and spread to a larger area in the warming experiment. The associated diabatic EPV production were also stronger at the lower

troposphere for TC Mary in the control run. Larger diabatic EPV production produced more EPV, thus enlarging the R17 of TC Mary in a warmed climate. Moreover, the TC structure of Mary were more organised in the warming run, which details were discussed in APPENDIX VII.

However, the convective activity indicated by the composite reflectivity of TC Nuri at model time 2008-08-21-18 were similar in both the control run and the warming run, as indicated by the blue rectangles in Figure 6.9c and d. Associated with the convective bands were similar EPV structure, and similar magnitude of diabatic EPV production within 250 km radius for TC Nuri. Therefore, the R17 for TC Nuri were similar in both the control run and a warmed climate. The results demonstrated that stronger and more widespread convective activities in a warmed climate, which could be developed due to a historically wetter environment, could produce more EPV diabatically at the inner and outer spiral rainbands, thus producing stronger and more widespread EPV structure and enlarged the R17 of the TC in the warmed climate.

6.4 Volume Averaged EPV Diagnostics

In order to present a more quantitative framework for the contribution of diabatic EPV production to the strength of the EPV associated with TC Mary and TC Nuri in control run and in the

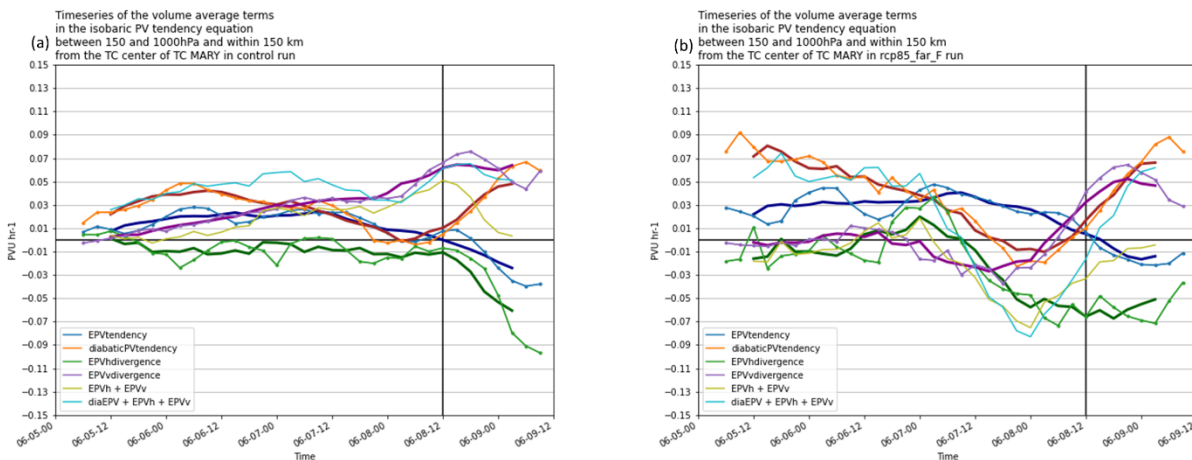


Figure 6.10 Timeseries of Volume averaged EPV budget equation for TC Mary in (a) control run and (b) RCP8.5 Far Future run using a cylindrical volume of radius 150 km, with a lower and upper surface at 1000 hPa and 150 hPa. Lines denote (thin steelblue) 12 hour moving average local EPV tendency, (thin orange) 12 hour moving average diabatic PV tendency, (thin green) 12 hour moving average horizontal EPV convergence, (thin purple) 12 hour moving average vertical EPV convergence, (thick navyblue) 24 hour moving average local EPV tendency, (think red) 24 hour moving average diabatic PV tendency, (thick green) 24 hour moving average horizontal EPV convergence, (thick purple) 24 hour moving average vertical EPV convergence, (thin olive) 24 hour moving average total EPV convergence (horizontal + vertical), (thin blue) 24 hour moving average total EPV convergence and diabatic PV tendency. vertical black line denotes the time of landfall. Data retrieved from H_DIA runs

far future climate period following the RCP8.5 emission scenario, volume averaged EPV diagnostics were performed in this section. The EPV budget equation were integrated from the surface to the 150 hPa pressure level within certain radius from the TC center, and the diabatic EPV tendency term of TC Mary and TC Nuri were compared against each other. The frictional dissipation term was treated as residual throughout this study.

Figure 6.10a and b showed the results of the volume averaged EPV budget equation for TC Mary in the control run and the RCP8.5 Far Future experiment using a volume with radius of 150 km from the TC center respectively. Details for the representation of each line were listed in the caption of Figure 6.10. From the Figure 6.10, it can be seen that at the developing stage (1960-06-06-00 to

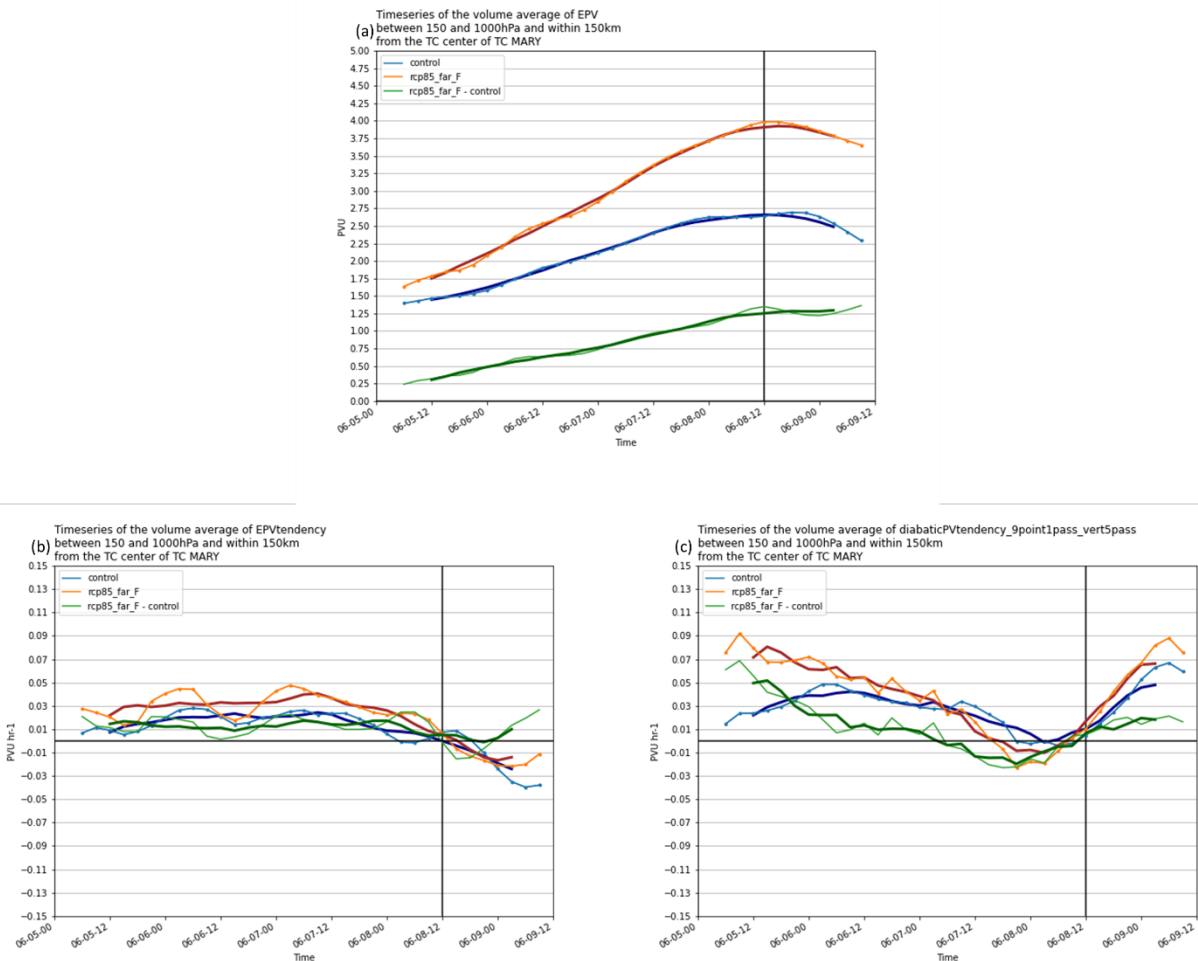


Figure 6.11 Timeseries of Volume averaged (a) EPV (PVU), (b) local EPV tendency (PVU hr⁻¹), (c) diabatic PV tendency (PVU hr⁻¹) for TC Mary in a 150 km cylindrical volume from the TC center, bounded by the 1000 hPa and 150 hPa pressure level, lines denotes (steelblue) control run, (orange) RCP8.5 Far Future run, (green) difference between RCP8.5 Far Future and control run, thin and thick line denotes 12 hour and 24 hour moving average respectively. Vertical black line denote the time when the TC landfall at South China. Data retrieved from H_DIA run

1960-06-07-12) of the TC Mary in the control run and the RCP8.5 Far Future experiments, the total contributions at the RHS of the EPV budget equation tend to overestimate the local EPV tendency due to a larger diabatic EPV production or a neglection of frictional dissipation. Yet, the total EPV convergence were close to 0 before model time 1960-06-07-06, which correspond well to the volume integral of the divergence of advective EPV flux. At the later time, the total contribution from the RHS of the EPV budget equation tend to overestimate the local EPV tendency in the control run. The overestimation may arise from the neglection of frictional dissipation at the boundary layer or because of the error accumulation problem due to the large cancellation between the adiabatic vertical motion and the diabatic heating (Tori et.al., 2012). In the RCP8.5 Far Future experiment before landfall, the total contribution of the RHS terms in the EPV budget equation tend to underestimate the local EPV tendency. This may be resulted by the neglection of residual or the accumulation of error. yet, at the volume averaging at the development stage, which was before 1960-06-07-12, it was still able to contrast the difference in the diabatic EPV tendency to the local EPV tendency of the TC Mary in the control run and the RCP8.5 Far Future experiment.

Figure 6.11 showed the difference in the timeseries of volume averaged EPV, local EPV tendency and the diabatic EPV tendency within 150 km radius for TC Mary in the control run and the RCP8.5 Far Future experiment. From Figure 6.11a, it can be seen that the total EPV within 150 km radius of TC Mary was larger in the RCP8.5 Far Future run than the control run, and the difference increased with time. At the time of landfalling, the EPV of TC Mary was 1 PVU larger in the RCP8.5 Far Future experiment than the control simulation. This larger EPV within 150 km reflected the larger R17 in the warming run than the control run.

Figure 6.11b showed the difference in local EPV tendency for TC Mary between the RCP8.5 Far Future and the control run was approximately 0.01 PVU per hour throughout the whole simulation (green line in Figure 6.11b). As TC Mary landfallled at the South China after 84 hours from genesis, the local EPV difference (0.84PVU) could approximately explained the 1 PVU larger EPV within

150 km radius cylindrical volume in the warming run. Figure 6.11c showed the difference in the diabatic EPV tendency for TC Mary in RCP8.5 Far Future experiment and the control run. If the first 24 hour of the simulation time was considered as the spin-up period, while the TC become mature after 1960-06-07-12, the difference in volume averaged diabatic EPV tendency in remaining intensification stage for warming run to the control run was approximately 0.01 PVU per hour. This larger diabatic EPV tendency within 3 times of the RMW in the RCP8.5 Far Future climate contributed to the larger local EPV tendency, and thus the larger EPV and R17 for TC Mary in the warming run than the control run. Moreover, other radius were tried to performed the volume averaging (not shown), and the use of 150 km as the radius of the cylindrical volume gave the best explanation to the local EPV tendency. Therefore, it could be concluded that the stronger inner spiral rainband activities in the warming run for TC Mary produce more EPV diabatically and expanded the R17 of the TC in the far future climate following RCP8.5 emission scenario, but the contribution from the outer spiral rainbands were small. However, future studies should be carried out to study the effect of frictional dissipation to the EPV of the TC when the TC moved closer to the coastal landmass.

Figure 6.12a and b showed the timeseries of the volume averaged EPV budget equation for TC Nuri with a 450 km radius in the control run and the RCP8.5 Far Future climate respectively. From the Figure, it can be seen that the computed total budget from the RHS of the EPV budget

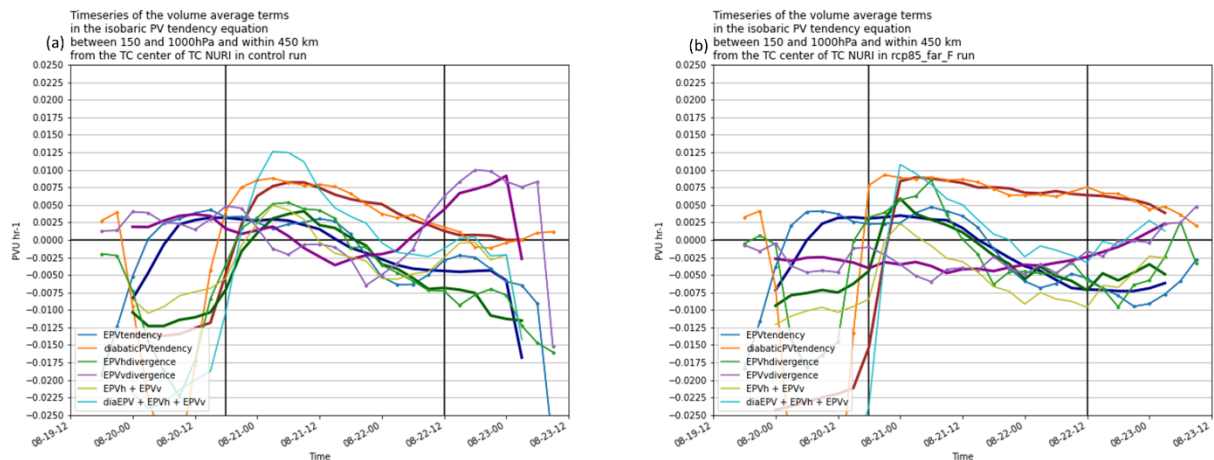


Figure 6.12 Similar to Figure 6.10, but for TC Nuri within a volume of 450 km radius from the TC center, bounded by the 1000 hPa and 150 hPa pressure level. The 2 vertical black line showed the time when the TC enters the SCS and landfall at the South China coast. Noted that the y-axis for Figure 6.12 is different to Figure 6.10

equation tend to overestimate the local EPV tendency in the SCS. This might be a consequence of treating the frictional dissipation as the residual. Yet, the total contribution of the EPV convergence and the diabatic EPV production captured the shape of the local EPV tendency development across time well. The advective EPV flux convergence term was close to 0, which reflected the theory of a volume integral of the divergence of the advection term tends to 0 given a large enough volume. Using a volume with 450 km radius were also the best among other radius for TC Nuri in terms of recovering the local EPV tendency compared to 150 km radius using for volume averaging of TC Mary. Reasons for this structural difference was discussed in APPENDIX VII for TC Mary and TC Nuri.

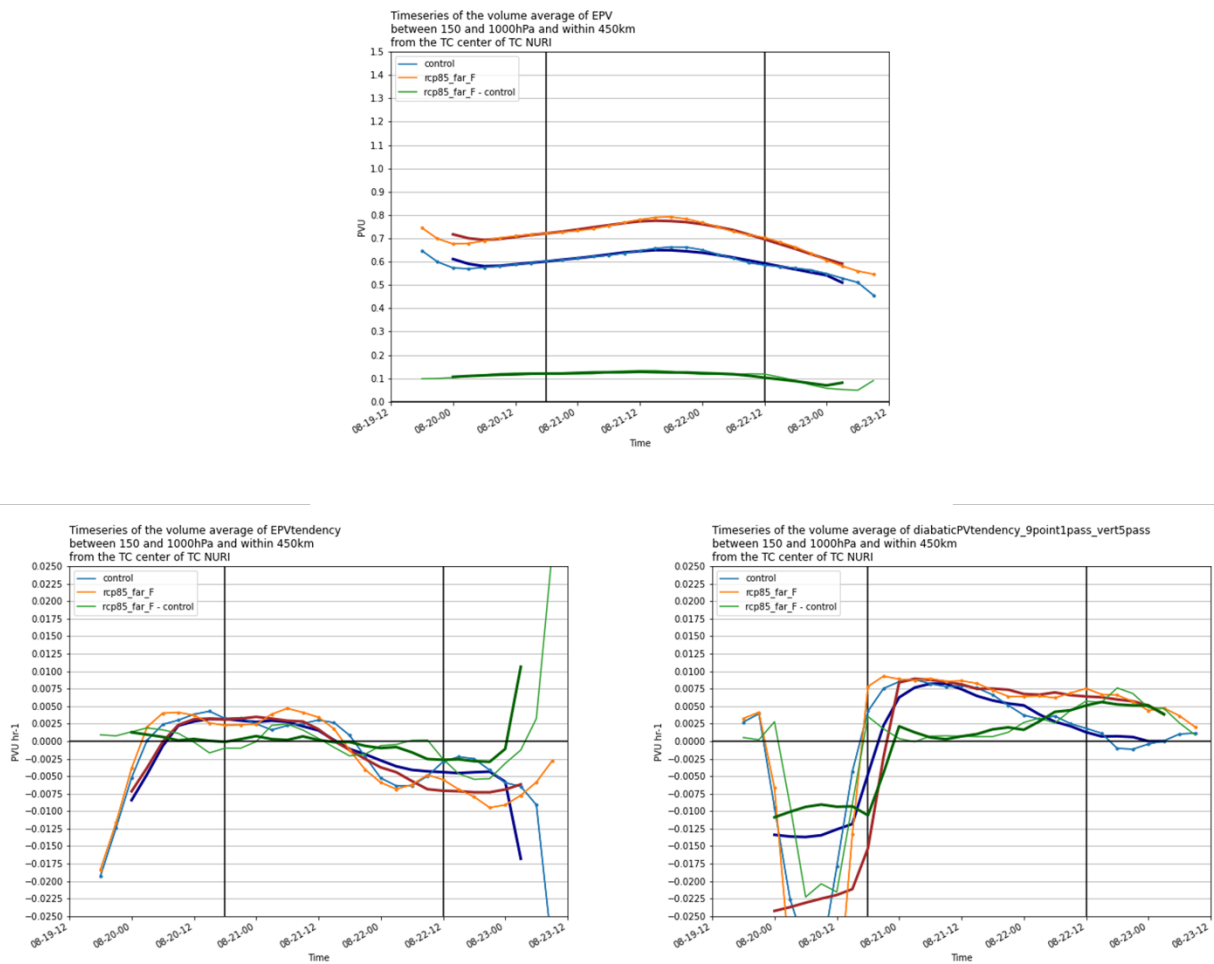


Figure 6.13 Same as Figure 6.11, but for TC Nuri within a volume of 450 km radius from the TC center, bounded by the 1000 hPa and 150 hPa pressure level. The 2 vertical black line showed the time when the TC enters the SCS and landfall at the South China coast. Noted that the y-axis for Figure 6.13 is different to Figure 6.11

Figure 6.13 compared the difference in volume averaged EPV, local EPV tendency and the diabatic EPV tendency for TC Nuri in the RCP8.5 Far Future experiment and the control run within 450 km radius from the TC center. From Figure 6.13a, the EPV difference between the warming run and the control run was 0.1 PVU throughout the whole simulation period. The development of EPV were similar for TC Nuri in both the warming run and the control run, and the R17 were therefore similar in the present climate and the future climate.

Figure 6.13b showed a close to 0 local EPV tendency difference between the control run and the warming in the SCS. The nearly 0 difference of EPV tendency in the warming run to the control run was also a reason for the nearly constant R17 for TC Nuri in the control run and the warming run. Moreover, the difference in the diabatic EPV production for TC Nuri in the warming run and the control run was found to be close to 0 when TC Nuri just entered the SCS, yet, the difference started to increase to a positive value near the landfall. Despite the fact that the diabatic EPV tendency started to increase before landfall, the diabatic EPV production associated to the eyewall and the spiral rainbands for TC Nuri were similar in both the control run and the warming run when the TC was on the sea, which produced similar amount of EPV and resulted in similar R17 for TC Nuri.

In conclusion, it was important to have a historically moister environment for a TC to have an increase in R17 in the future climate because historically moister environment enabled an even more favourable environment to convective activities and precipitation associated with the inner spiral rainbands. Stronger and more wide-spread inner spiral rainband activities were associated with stronger diabatic heating rate, producing more diabatic EPV, which then increasing the local EPV tendency and the EPV of the vortex, therefore enlarging the R17 of the TC when these EPV were produced locally near the R17 of the TC, or were spiralled into the R17 of the TC. Positive feedback process might also play a role in the expansion of R17. When there were stronger inner spiral rainband activities, more EPV were produced by diabatic EPV generation and the radial EPV gradient increased. Then, larger area would become favourable for inner spiral rainband activities, which

caused a radially outward expansion of inner spiral rainband and produced more EPV by diabatic EPV generation.

6.5 Vertical cross-sections for TC Mary and TC Nuri at Selected Timesteps

To conclude how the TC located in a historically moister environment can cause a larger increase in TC size in future climate projection compared to TC located in a drier historical environment, some vertical cross-sections were presented to contrast the historical environment, and the influences on the structure of TC Mary and TC Nuri in a warmed climate.

Figure 6.14 showed the vertical cross-section of the model output reflectivity, historical environmental RH and the secondary circulation for TC Mary at the development stage and TC Nuri in the control run and the RCP8.5 Far Future experiment. From the Figure, it can be seen that the environment associated with TC Mary in the past had a large RH, with higher than 80% RH within 350 km of TC Mary. Moreover, the RH were higher at the southern quadrant of TC Mary, which

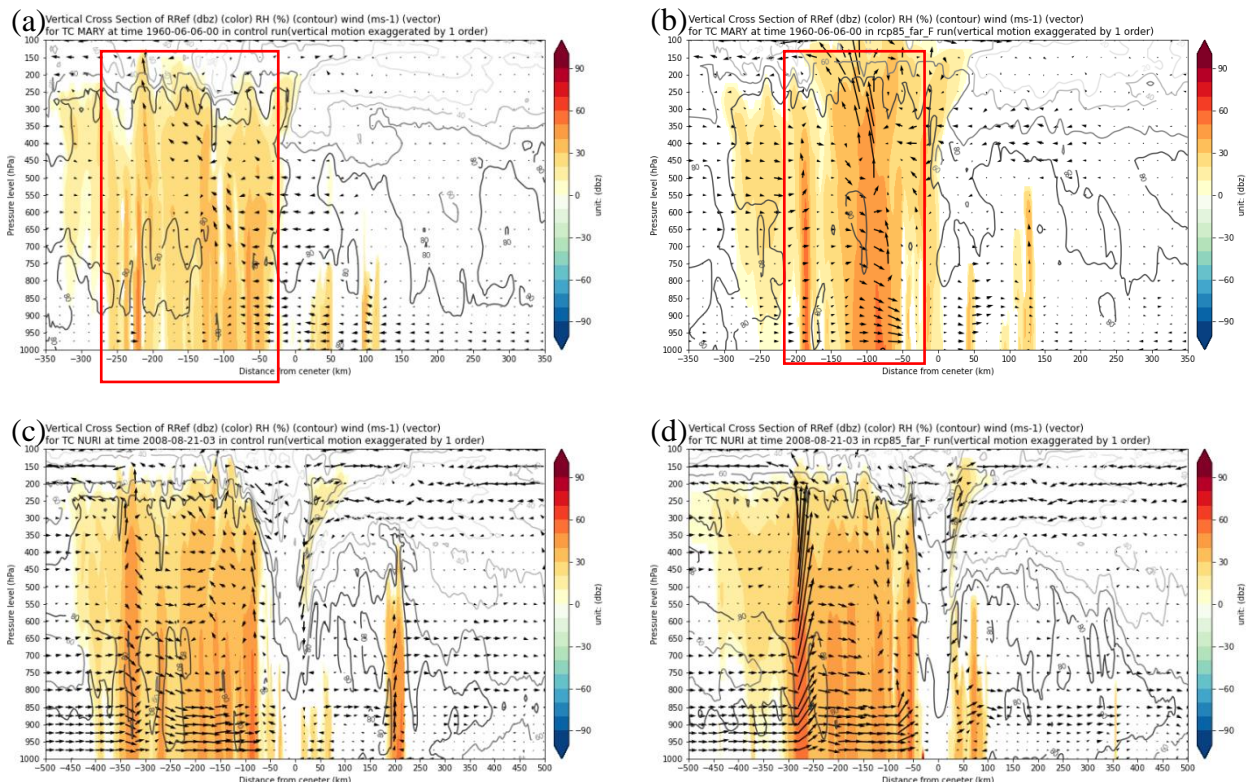


Figure 6.14 Vertical cross-section for (a,b)TC Mary at 1960-06-06-00 and TC Nuri at 2008-08-21-03 in (a,c) control run and (b,d) RCP8.5 Far Future run. The (color) model output reflectivity (dBz), (contour) model retrieved environmental RH (%), (vector) TC radial and vertical circulation ($m s^{-1}$) (vertical motion were exaggerated by 1 order) were shown within (a,b) 350 km radius and (c,d) 500 km radius

echoed the band pattern of larger RH importance at the south of the TC tracks found in the stepwise regression (Figure 5.9). At these regions with high historical RH, convective activities were more developed as represented by the positive signal of model output reflectivity in Figure 6.14a and b. Moreover, it can be seen that the convective activities in the warming run (Figure 6.14b) were stronger than the control run for TC Mary, as revealed by the stronger and larger coverage of reflectivity of ~ 30 dBz and larger vertical motion associated with the inner spiral rainband at -100 km radius from the TC center (red rectangle in Figure 6.14a and b), correspond well to the location of larger composite reflectivity in Figure 6.8b. However, by comparing Figure 6.14a, b with 6.14c, d, the historical environment for TC Nuri was less wet. Nevertheless, the strength and the area coverage of convective activities for TC Nuri were similar in both the control run and the RCP8.5 Far Future experiment. Therefore, a historically moister SCS were more favourable to stronger convective activities development in a warmed climate.

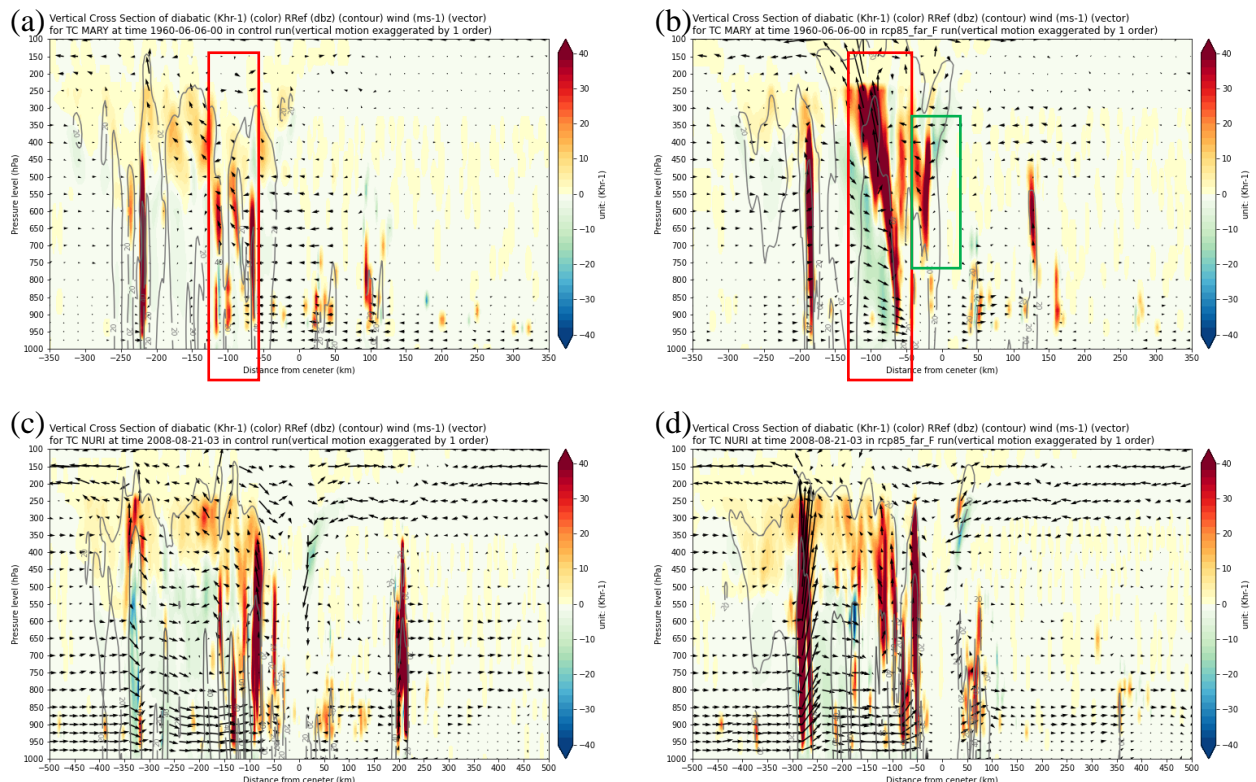


Figure 6.15 Vertical cross-section for (a,b) TC Mary at 1960-06-06-00 and (c,d) TC Nuri at 2008-08-21-03 in (a,c) control run and (b,d) RCP8.5 Far Future run. The (color) microphysics diabatic heating rate ($K\text{hr}^{-1}$), (contour) model output reflectivity (dbz), (vector) TC radial and vertical circulation ($m\text{s}^{-1}$) (vertical motion were exaggerated by 1 order) were shown.

Figure 6.15 showed the vertical cross-section of the model outputted microphysics scheme diabatic heating rate for TC Mary at the development stage and TC Nuri in the control run and the Far Future run. Stronger diabatic heating rate were found in the warming run for TC Mary, at the ~-75 km radius due to the stronger vertical motion and stronger inner spiral rainband activities (red rectangle in Figure 6.15a and b). Stronger diabatic heating rate were also found at the eyewall, at a radius of -25 km from the TC center (green rectangle in Figure 6.15b). However, compared to the stronger diabatic heating rate found in the warming run for TC Mary, the diabatic heating rate were similar for TC Nuri in the warming run and the control run. The apparently smaller diabatic heating at the southern quadrant of TC Nuri in the control run (Figure 6.15c) were compensated by the band of strong diabatic heating at 200 km radius north of the TC center. Therefore, diabatic heating rate for TC Nuri were similar in the control run and in the future climate, while the diabatic heating rate was stronger in the warming run for TC Mary.

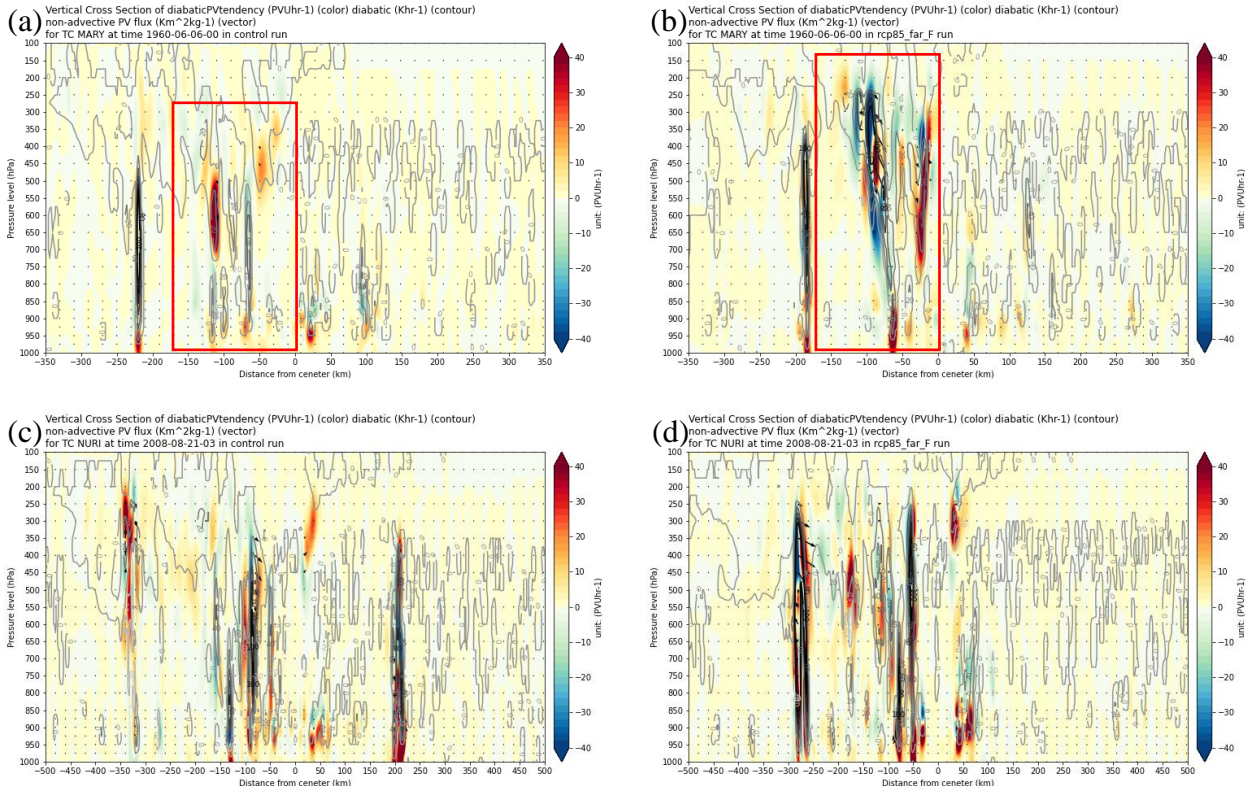


Figure 6.16 Vertical cross-section for (a,b) TC Mary at 1960-06-06-00 and (c,d) TC Nuri at 2008-08-21-03 in (a,c) control run and (b,d) RCP8.5 Far Future run. The (color) diabatic PV tendency (PVU hr⁻¹), (contour) microphysics diabatic heating rate (K hr⁻¹), (vector) non-advective PV Flux in radial and vertical direction (K m² kg⁻¹) were shown

Stronger diabatic heating gradient for TC Mary at the inner spiral rainbands produced more EPV diabatically in the warming run. Figure 6.16 contrasted the diabatic EPV tendency and the non-advection EPV flux of TC Mary and TC Nuri in the warming run and the control run. From Figure 6.16, one general characteristics of the diabatic EPV tendency and the non-advection PV flux was the region with negative diabatic EPV tendency were associated with the divergence of non-advection EPV flux while positive diabatic EPV tendency were associated with the convergence of non-advection EPV flux. In this sense, the non-advection PV flux act like transporting the diabatic EPV from the upper troposphere to the lower troposphere, following the tilted eyewall and the convective spiral rainbands. The diabatic EPV tendency for TC Mary in the warming run associated with the inner spiral rainband at the southern quadrant were stronger than that in the control run (red rectangle in Figure 6.16a,b). Nevertheless, the diabatic EPV production for TC Nuri were similar in both the warming run and the control run. Therefore, vertical cross-sections confirmed that the inner spiral rainbands were stronger in a historically moister environment for TC Mary in the warming run than the control run. Stronger inner spiral rainbands produced more EPV diabatically and expanded the R17 of the TC. However, the spiral rainbands activities of TC Nuri were similar in both the control and the warmed climate in the SCS, thus the R17 of TC Nuri were similar in the control run and the warming run.

Questions may arise on why a historically moister environment caused a stronger convective activity in a warmed climate compared to a historically drier environment. This should be related to the increase in the entrainment of moist air in a warmed climate. Sanderson et.al. (2010) had found that the depth of the convection depends on how humid the surrounding environment is, which controlled the humidity of the entrained air into convective systems. Here, as the radial inflow increased due to a stronger heating at the eyewall, more air converged into the TC in a warmed climate. If the historical environment were wetter, more moist air would be entrained to feed the spiral rainbands, which then enhanced the convection and the diabatic heating. However, a historically drier environment, like that for TC Nuri, caused more dry air entrained into the spiral rainbands in a warmer

climate. Therefore, the convection activities were killed at the rainbands for TC Nuri in a warmer climate, despite the fact that there might be stronger convection at the center of the TC. Wang et.al. (2014) had modelled an increase in TC rainfall in the current climate relative to the 1950-1969 climate background for 2 TC cases. They had found that most of the increase in precipitation in a warmer climate could be attributed to the increase in the convergence of vapor flux relative to the local evaporation. Therefore, the increase in the entrainment of moist air in a historically moister SCS in a warmed climate should be the reason for the enhancement of convection in a historically wetter SCS.

However, it should be noted that despite the importance of the historical RH in determining the difference in the percentage change in size for TC Mary and TC Nuri in responding the same warming signal, other factors, including the length of the lifetime of the TC in the SCS, and the outer tangential wind speed, might contribute to the difference in the percentage increase of R17 in the warmed climate for different TCs. In the next section, the effects of outer wind speed in influencing the change of R17 for different TC to the same warming signal were analysed.

7. AAM Diagnostics of Relationship between Historical Outer Wind Speed to R17 Change Variations in Future Climate

Apart from the historical environmental RH, the outer wind speed in the SCS was another important environmental condition in influencing the variations in the percentage change of TC R17 in each future climate period and emission scenario. MLR analysis revealed a similar importance of historical outer wind speed in the SCS compared to the historical environmental mid-tropospheric RH. TCs in a historically windier environment tended to have larger percentage increase of R17 in a warmed climate compared to other TCs, and the results were robust across all scenarios, despite a smaller but substantial importance in the RCP8.5 Far Future (not shown). The outer wind speed was defined as the 10 m wind speed outside the R17 of a TC. It was believed that by filter away the circulation within the R17 of the TC, the typical circulation pattern associated with each TC itself was substantially removed, and the difference between the outer wind speed for each TC were due to the difference in the environmental background wind speed at 10 m from the surface if one treated the outer wind speed as the superposition of the TC circulation beyond the R17 and the environmental wind structure.

Chan and Chan (2015) had found a positive relationship between the initial outer tangential wind and the size of a TC in terms of R17 by idealized simulations. By modifying the initial symmetric component of the tangential wind speed, they had found TCs with initially larger outer tangential wind speed could grow to larger size compared to TCs with smaller outer tangential wind speed. Moreover, the growth could sustain for a long time after the onset of larger outer tangential wind speed at the beginning of the simulation. By AAMF analysis, they had found that larger initial tangential wind speed environment increased the symmetric AAMF near the R17 of the TC, which then increased the local AAM tendency and expanded the wind field. Moreover, Chan and Chan (2012) found that size increasing TCs were associated with an increase in AAMF in the boundary layer by analysing the observational data of TCs in the WNP basin.

Due to the close linkage of AAMF and TC size, AAM budget analysis were carried out in this section to diagnose the effects of historical outer wind speed in influencing the variations of percentage change of R17 in future climate projections among each TC. Moreover, we had extended the linkage between the TC size and the outer tangential wind speed to the outer wind speed as both the MLR of using the outer tangential wind speed and the outer wind speed yield similar results on the relationship and the importance in controlling the variations of percentage change of TC R17 in each warming experiment. On the sake of clarity, only 4 TCs, namely TC Gordon (1989), TC Warren (1988), TC Bess (1974) and TC Hope (1979) in RCP8.5 Far Future run and RCP4.5 Far Future run relative to the control run were shown by figures in this section, but the results were robust across all 14 TCs. TC Gordon and TC Warren were identified as a robust choice of R17 increasing TCs and R17 constant TCs across all warming experiments (Table 5.1). Their mean azimuthally averaged 10 m wind field in the SCS were shown in Figure 5.2. Moreover, TC Hope and TC Bess were 2 TCs having largest R17 increase in RCP8.5 Far Future experiment, and smallest R17 increase in RCP4.5 Far Future experiment. The completely different behaviour in the 2 warming experiments were therefore worth analysing.

This section was organised as follows. First, the local AAM and local AAM tendency were contrasted between the 4 TCs. Then, azimuthally averaged AAM budget analysis was preformed to link the local AAM tendency to the budget terms. Relative contribution between the change in radial wind and the change in AAM radial gradient to the local AAM tendency were discussed. Then, AAMF analysis were carried out, following the method of Chan and Chan (2015). Details of the AAM budget and the AAMF analysis were presented in APPENDIX IV. Relative contribution of the change in radial wind and tangential wind to the AAMF were also discussed. The change in AAMF were linked to the difference in historical outer wind speed by carrying out statistical analyses on wind composites. The related historical synoptic wind environment to R17 increasing TCs and R17 constant TCs were presented at last. However, it should be reminded that the projected changes in wind field in the future climate were not superimposed by the PGW signal, and the difference in the

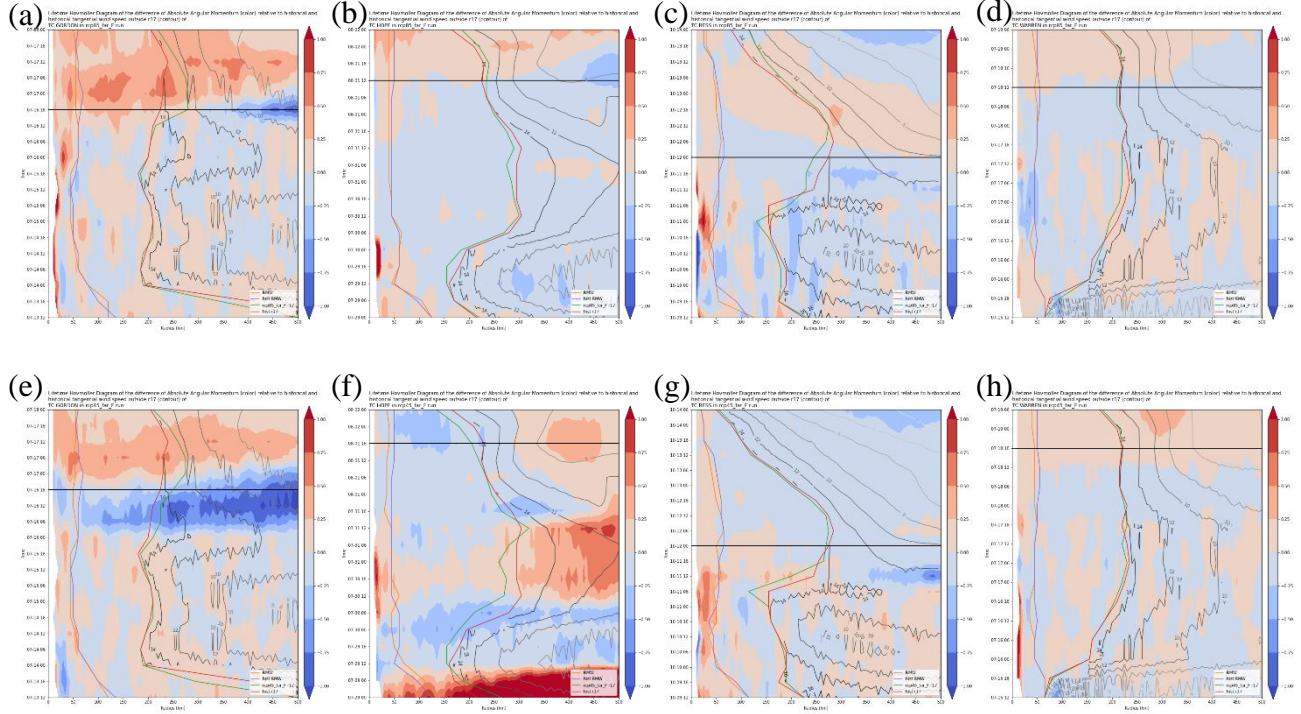


Figure 7.1 Hovmöller diagrams of (color) azimuthally averaged 10 m AAM difference (unit: $10^6 \text{ m}^2 \text{ s}^{-1}$) for TCs in (a,b,c,d) RCP8.5 Far Future and (e,f,g,h) RCP4.5 Far Future relative to the control run and (contour) historical outer tangential wind speed (m s^{-1}) for (a,e) TC Gordon, (b,f) TC Hope, (c,g) TC Bess, (d,h) TC Warren. Lines indicate (red) R17 in control run, (green) R17 in warming run, (purple) RMW in control run, (orange) RMW in warming run. Black line indicate the time when the TC enters the SCS.

circulation pattern far away from the TC were the consequences of superimposed thermodynamical changes in the future climate period following the RCP8.5 or RCP4.5 emission scenarios, as well as from the non-linear nature of the atmospheric and oceanic system itself.

7.1 Difference in Percentage Change of R17 in terms of AAM and Local AAM tendency

The azimuthally averaged 10 m AAM hovmöller diagram for the selected TCs in RCP8.5 Far Future and RCP4.5 Far Future relative to the control run were shown in Figure 7.1, together with their associated historical outer tangential wind speed. Compare Figure 7.1a and 7.1e with 7.1d and 7.1h, TC Gordon had a positive AAM difference in the SCS, as indicated by deeper red colour, compared to TC Warren, which the AAM were similar in both the warming run and the control run. Moreover, in RCP8.5 Far Future experiment, TC Hope and TC Bess had a larger 10 m AAM in the SCS in the warming experiment than the control run, while that were smaller in the RCP4.5 Far Future to the control run. Therefore, it made sense that TCs with larger R17 in the warming experiment had larger 10 m AAM. TCs with similar R17 in the warming experiment and the control run were

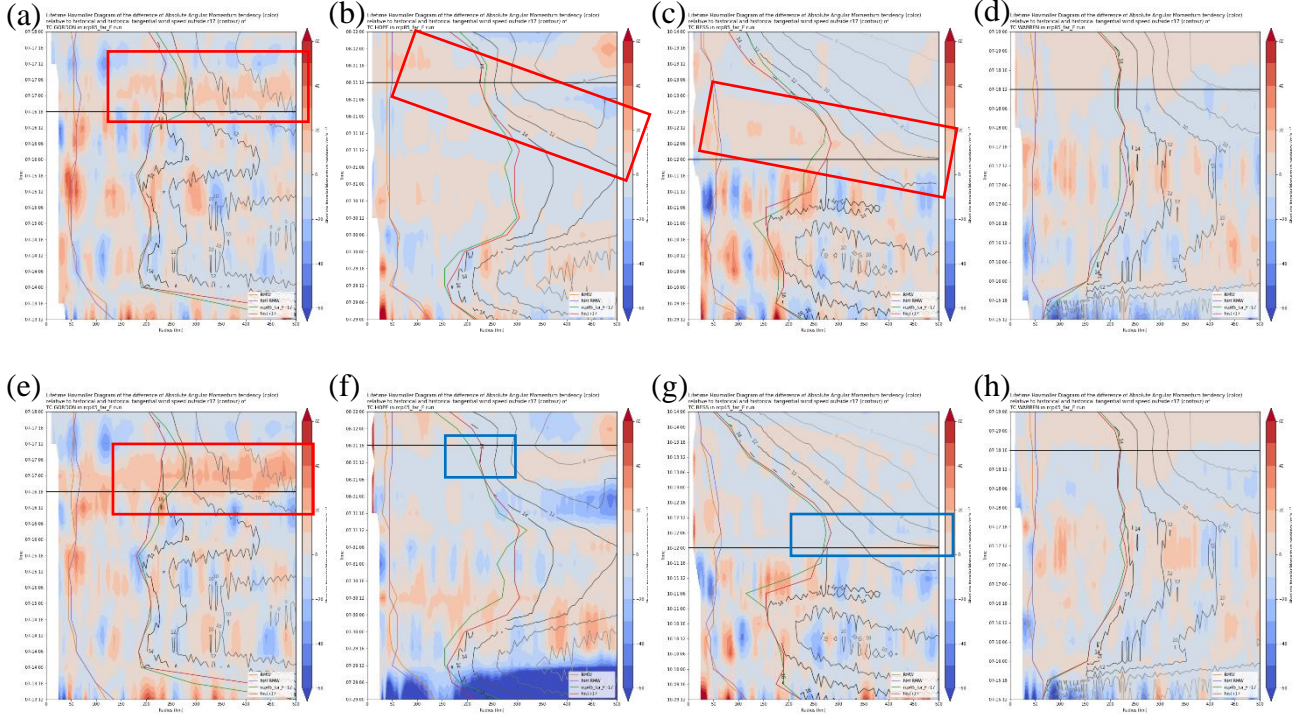


Figure 7.2 Hovmöller diagrams of (color) azimuthally averaged 10m local AAM tendency difference (unit: $m^2 s^{-2}$) for TCs in (a,b,c,d) RCP8.5 Far Future and (e,f,g,h) RCP4.5 Far Future relative to the control run and (contour) historical outer tangential wind speed ($m s^{-1}$) for (a,e) TC Gordon, (b,f) TC Hope, (c,g) TC Bess, (d,h) TC Warren. Lines indicate (red) R17 in control run, (green) R17 in warming run, (purple) RMW in control run, (orange) RMW in warming run. Black line indicate the time when the TC enters the SCS. End of y-axis indicate the time of landfalling.

associated with similar 10 m AAM in the SCS. Moreover, compare the gradient of the contour for TC Gordon (Figure 7.1a) and TC Warren (Figure 7.1d) in the SCS, the outer tangential wind speed of TC Gordon was larger in the SCS than TC Warren. It also showed that larger R17 increasing TCs were associated with historically windier SCS.

Local AAM tendency of selected TCs in RCP8.5 and RCP4.5 Far Future experiments relative to the control run were shown in Figure 7.2a-d and 7.2e-h respectively. Noted that the lineation noise along time for TCs before entering the SCS were caused by the coarse resolution of output from the outer domain, and the interpolation to cylindrical coordinate, which then caused the mismatch of the radial location of TC outer spiral circulation feature between the warming experiments and the control run. From Figure 7.2a, b, c and e, which showed TCs with an increase in R17 in the warming run, the time when the rate of change of R17 in the warming run was larger than the control run were captured by an increase in local AAM tendency near the R17 (red rectangles). For example, TC Gordon (1989) had a much larger R17 in the SCS in model time 1989-07-17-06, which was accompanied with a

larger local AAM tendency by $15 \text{ m}^2 \text{ s}^{-2}$ in the RCP8.5 Far Future experiment than the control simulation. Compared to the R17 increasing TCs, TCs with similar R17 in the warming run and the control run, like TC Warren, had a similar rate of change in AAM. Nevertheless, the smaller or nearly constant R17 for TC Hope and TC Bess in the RCP4.5 Far Future experiment were captured by a decrease in local AAM tendency near the R17 (blue rectangles in Figure 7.2f, g). As the azimuthally averaged local AAM tendency well captured the difference in the rate of change of R17 in warming run and the control run, terms that influence the azimuthally averaged local AAM tendency were analysed in the next section.

7.2 AAM Budget Analysis

7.2.1 Azimuthally Averaged AAM Budget Equation

As the difference in the rate of change of TCs' R17 in the warming experiment to the control run were well captured by the difference in the surface azimuthally averaged local AAM tendency between the warming runs and the control run, terms that contributed to the local AAM tendency were analysed. Here, the azimuthally averaged AAM budget equation (equation [6] in APPENDIX IV) was used in relating the azimuthally averaged local AAM tendency to potential contributors. The lowest model level ($\eta = 0.9965$) value for the budget terms and the local AAM tendency were analysed because of several reasons. First, the lowest model level was close to the surface, which the values could be approximated as the surface value. Second, using the directly output values can reduce the error in estimating the 10 m values from the model. Third, the use of lowest model level and the second lowest model level in calculating the vertical derivative can reduce error arise from interpolating values to 20 m altitude.

Chan and Chan (2014, 2015) had shown that the main contributors to the azimuthally averaged local AAM tendency were the symmetric radial advection of AAM and the symmetric frictional dissipation/diffusion term (Chan & Chan 2014, 2015). The frictional dissipation/diffusion term was calculated by residual method in this study as the frictional dissipation term from the planetary

boundary layer scheme were not archived due to limitations in computer resources. It had been found that the difference in the radial advection of AAM and the frictional dissipation term in the warming run to the control run were larger than other terms by 1 order in contributing to the local AAM

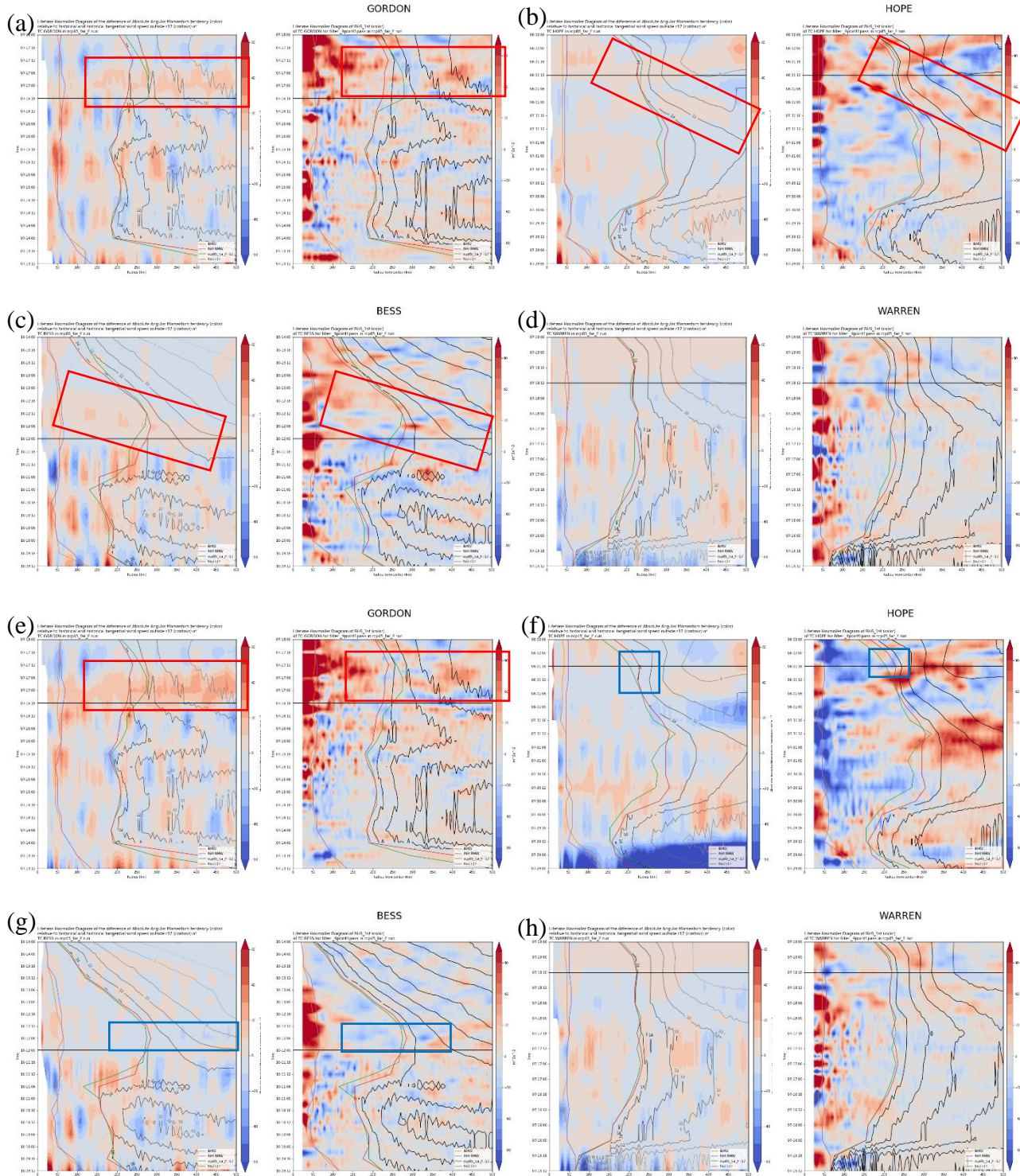


Figure 7.3 Comparison between (color) the (left) azimuthally averaged local AAM tendency (same as Figure 7.2) (unit: $m^2 s^{-2}$), and the (right) symmetric radial advection of AAM (unit: $m^2 s^{-2}$) in the (a-d) RCP8.5 Far Future run and (e-h) RCP4.5 Far Future relative to the control run for (a,e) Gordon, (b,f) Hope, (c,g) Bess, (d,h) Warren, (right contour) showed the historical outer wind speed (unit $m s^{-1}$). Lines indicate (red) R17 in control run, (green) R17 in warming run, (purple) RMW in control run, (orange) RMW in warming run. Black line indicate the time when the TC enters the SCS. End of y-axis indicate the time of landfalling.

tendency at the lowest model level. Therefore, the asymmetric radial flux of vertical absolute vorticity, symmetric vertical advection of AAM, asymmetric vertical advection of AAM and the eddy pressure gradient term were treated as residual in this study, which were also similar to previous studies of Chan and Chan (2014, 2015). Moreover, as the symmetric radial advection of AAM increases AAM, the difference in the symmetrical radial advection of AAM in the control run and the warming run were plotted.

Results were shown in Figure 7.3. The difference in azimuthally averaged local AAM tendency in the warming experiments to the control run were, to a first approximation, captured by the difference in the symmetric radial advection of AAM in the warming runs and the control run. For example, the larger local AAM tendency when TC Gordon, TC Hope and TC Bess entered the SCS in the RCP8.5 Far Future were captured by an increase in the radial advection of AAM near the R17 (red rectangles). Moreover, the negative local AAM tendency of TC Hope and TC Bess were captured by a decrease in radial advection of AAM near the R17 (blue rectangles in Figure 7.3f and 7.3g). Therefore, to a first approximation larger local AAM tendency associated with the R17 increasing TCs were due to an increase in radial advection of AAM at the lowest model level.

7.2.2 *Relative contribution of the change in radial wind and the radial gradient of AAM in the symmetric radial advection of AAM*

From the previous sub-section, it was shown that the difference in the local AAM tendency, which could be used to represent the rate of change of R17, in the warming runs than the control run, could be approximated by the difference in the symmetric radial advection of AAM in the warming runs than the control run. As the symmetric radial advection of AAM is defined as $-\bar{v}_r \frac{\partial \overline{AAM}}{\partial r} = -r\bar{v}_r \bar{\zeta}_a$, where $\bar{\zeta}_a = \bar{f} + \frac{1}{r} \frac{\partial(r\bar{v}_\theta)}{\partial r}$, taking the common logarithm to the radial advection of AAM, and computing the difference in the warming run with the control run yield:

$$\Delta \log_{10} \left(-\bar{v}_r \frac{\partial \overline{AAM}}{\partial r} \right) = \Delta \log_{10} (-\bar{v}_r) + \Delta \log_{10} \left(\frac{\partial \overline{AAM}}{\partial r} \right) \quad (11)$$

where Δ indicates the difference between the warming experiment and the control run. Thus, the

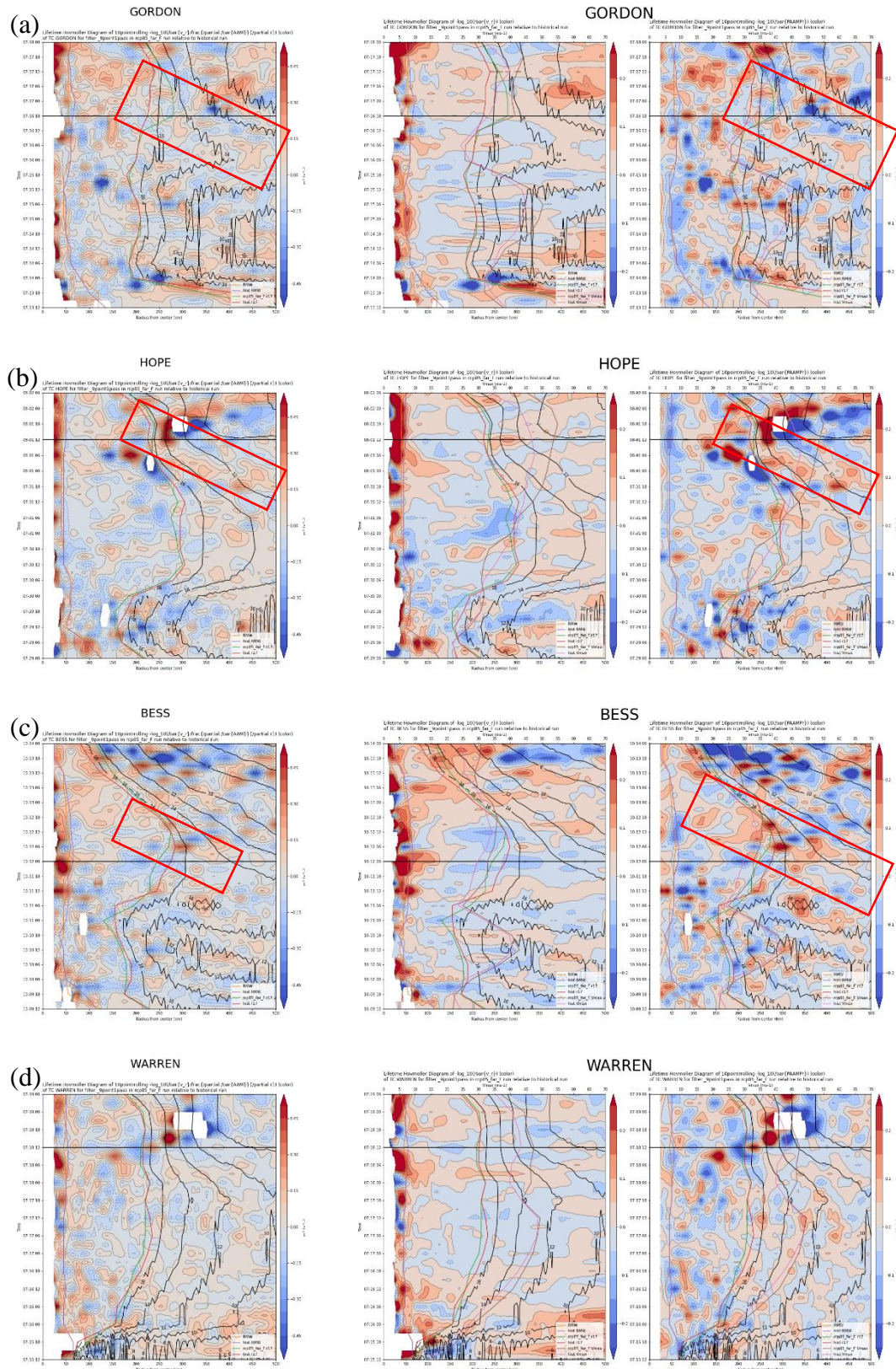


Figure 7.4 Hovmoller diagrams of (left) $\Delta \log_{10}(-\bar{v}_r \frac{\partial AAM}{\partial r})$, (middle) $\Delta \log_{10}(-\bar{v}_r)$ (positive means inward), (right) $\Delta \log_{10}(\frac{\partial AAM}{\partial r})$ for (a) Gordon, (b) Hope, (c) Bess, (d) Warren in the RCP8.5 Far Future run relative to the control run. (contour) showed the historical outer wind speed (unit m s⁻¹). Lines indicate (red) R17 in control run, (green) R17 in RCP8.5 Far Future, (purple) RMW in control run, (orange) RMW in RCP8.5 Far Future, (pink) Vmax in control, (brown) Vmax in RCP8.5 Far Future. Black line indicate the time when the TC enters the SCS. End of y-axis indicate the time of landfalling.

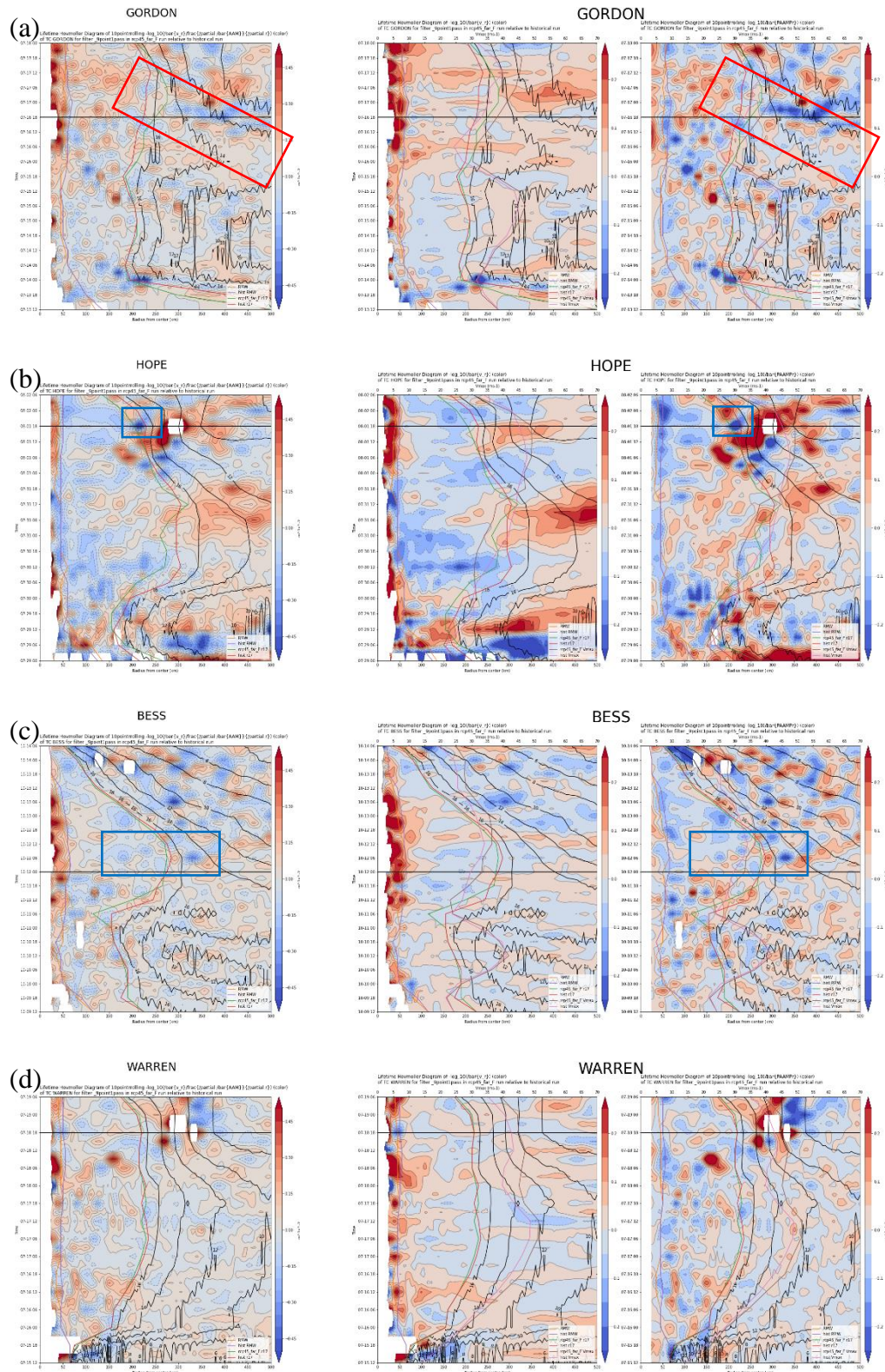


Figure 7.5 Hovmöller diagrams of (left) $\Delta \log_{10}(-\bar{v}_r \frac{\partial \overline{AAM}}{\partial r})$, (middle) $\Delta \log_{10}(-\bar{v}_r)$ (positive means inward), (right) $\Delta \log_{10}(\frac{\partial \overline{AAM}}{\partial r})$ for (a) Gordon, (b) Hope, (c) Bess, (d) Warren in the RCP4.5 Far Future run relative to the control run. (contour) showed the historical outer wind speed (unit $m s^{-1}$). Lines indicate (red) R17 in control run, (green) R17 in RCP4.5 Far Future, (purple) RMW in control run, (orange) RMW in RCP4.5 Far Future, (pink) Vmax in control, (brown) Vmax in RC48.5 Far Future. Black line indicate the time when the TC enters the SCS. End of y-axis indicate the time of landfalling.

contribution of the change in radial wind and the change in radial AAM gradient could be separated.

Moreover, the change in the radial wind of the TC can be treated as the change in the internal

responses of the TC in a warmer climate, while the change in the radial AAM gradient can be treated as the change in the synoptic environment.

Figure 7.4 and 7.5 showed the relative contribution of the difference in the logarithm of the radial wind and the radial AAM gradient compared to the total difference of symmetric radial AAM advection in the RCP8.5 Far Future and the RCP4.5 Far Future experiment relative to the control run respectively. From the Figure, one can see that at the R17 or outside the R17 of a TC, the radial AAM gradient were more important in contributing to the symmetric radial advection of AAM. For example, the positive radial advection of AAM difference of TC Gordon, TC Hope and TC Bess in the RCP8.5 Far Future experiment were associated with an increase in the radial advection of AAM in the warming experiment (red rectangles in Figure 7.4a, b, c). Moreover, the radial AAM gradient plots showed some of the TCs were associated with a band of larger radial AAM gradient in the warming run, which propagated from outside of the TC into the R17 of the TC when the TC entered the SCS. It turns out that this signal was important in increasing the R17 of the TC in the warming experiment, and would be discussed in section 7.3.2.

Similarly, the negative difference in the symmetric radial advection of AAM for TC Bess and TC Hope in the RCP4.5 Far Future experiment relative to the control run were also a result from the smaller radial AAM gradient near to the R17 in the RCP4.5 Far Future run than the control run (blue rectangles in Figure 7.5b, c). Therefore, the relative importance plots showed that the change in the synoptic environment were more important in increasing the symmetric radial advection of AAM compared to the change in the internal responses of the TC, thus the azimuthally averaged local AAM tendency and the R17 of the TC in the projected future climate.

7.3 AAMF Analysis

As the difference in the local AAM tendency in the warming experiments and the control run could be qualitatively explained by the difference in the radial advection of AAM in the warming experiments and the control run, the results motivated the study of the difference in the AAMF in the

warming experiments and the control run. Chan and Chan (2014, 2015) had used a simplified framework of AAMF to approximate the radial advection of AAM (Chan & Chan, 2014, 2015). Moreover, various researchers had found a relationship between the AAMF in the boundary layer and the expansion of the TC size (Merrill, 1984; Chan & Chan, 2012). Therefore, following the method of Chan and Chan (2014, 2015), AAMF analysis were also carried out to approximate the radial advection of AAM in the AAM budget equation.

A simplified study of AAMF difference in the warming runs and the control run were carried out to investigate the difference in AAMF in contributing to the difference in the azimuthally averaged local AAM tendency, which was then related to the difference in TCs' R17 in a warmed climate. Across a circle with radius r from the TC center at the lowest model level, the AAMF were calculated by equation 8 in section 2.3.2. It was found that the difference in the ARAMF and the ACT terms in the warming runs and the control run were relatively small compared to the symmetric terms in contributing to the total AAMF difference of the TCs. Therefore, the asymmetric AAMF were neglected. Details of the AAMF analysis were presented in APPENDIX IV.

7.3.1 Difference in AAMF in warming runs and the control run

Figure 7.6 displayed the difference in the sum of SRAMF and SCT for TCs in the RCP8.5 Far Future, and RCP4.5 Far Future relative to the control simulation respectively. From Figure 7.6a, b, c and e, it can be seen that when there was a positive rate of change of symmetric AAMF (SF) difference between the warming experiment and the control simulation near the R17 with time (along y-axis), the size of the TC was expending faster or contracting slower in the future climate experiments compared to the control simulation. For example, TC Gordon showed a positive tendency for the difference in SF in the RCP8.5 Far Future run than the control run when it entered the SCS (red rectangle in Figure 7.6a). It was accompanied by an increase in R17 in the RCP8.5 Far Future compared to the control run. Positive tendency of the difference in the SF were also found for TC Bess and TC Hope when they entered the SCS in the RCP8.5 Far Future (red rectangle in Figure 7.6b

and c). All of these larger SF tendency near the R17 in the warming run than the control were found after the onset of the larger outer wind speed, as shown by the ridge structure of the contour.

For R17 constant TCs such as TC Hope in the RCP4.5 Far Future experiment, the smaller R17 in the SCS in the warming experiment were captured by a decrease in SF tendency when TC Hope entered the SCS (green rectangle in Figure 7.6f). Moreover, R17 constant TCs were associated with a decrease in SF in the warming experiments. Therefore, it could be concluded that for R17 increasing TCs, there were more SF influx into the R17 of the TC in the future climate period relative to the control simulation. Larger SF influx near the R17 of the TC in the warming experiments enhanced the symmetric radial advection of AAM, and thus the local AAM tendency, then increased the AAM of the TC near the R17 and finally expanded the wind field. However, for R17 constant TCs (green and blue rectangles in Figure 7.6d, f, g and h), the SF were similar in both the warmed future climate for difference warming scenarios and the control simulation. As the SF were similar, the symmetric radial AAM advection were similar, hence the local AAM tendency near the R17 were

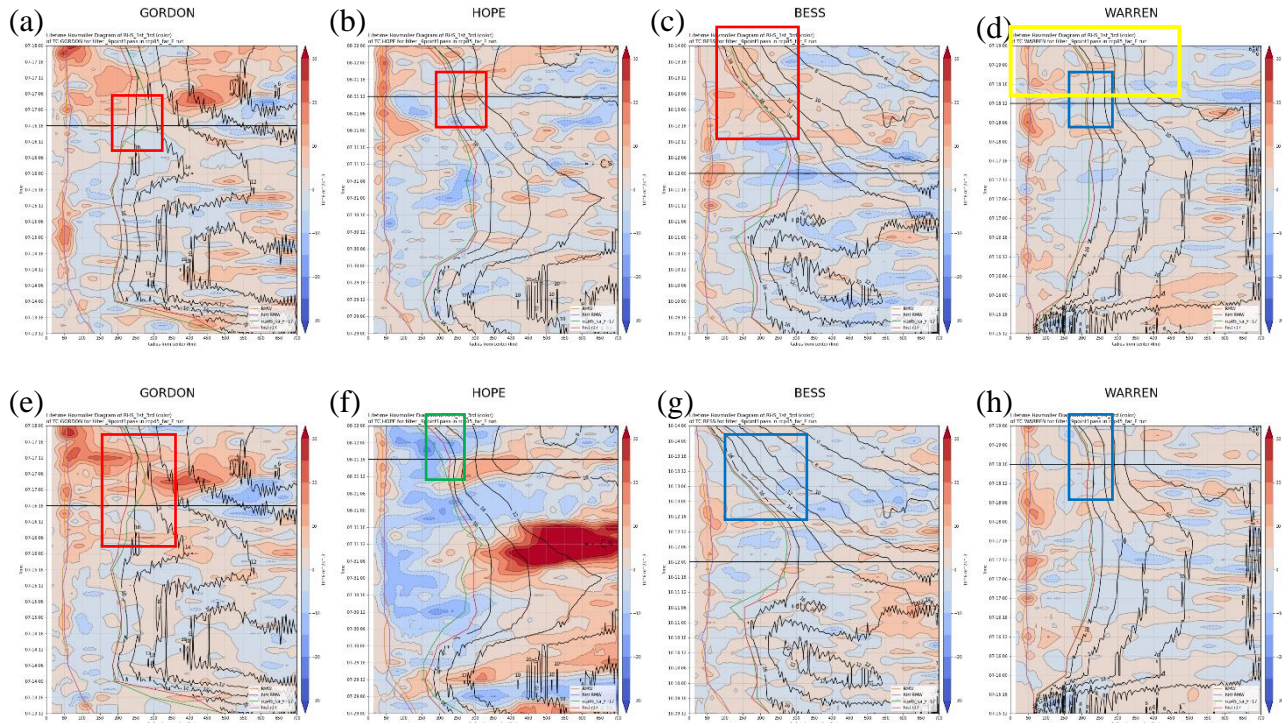


Figure 7.6 Hovmöller diagrams of the (color) difference in SRAMF + SCT in the (a-d) RCP8.5 Far Future and the (e-h) RCP4.5 Far Future period than the control run, positive means inward (unit: $10^6 \text{ m}^3 \text{ s}^{-2}$) for (a,e) TC Gordon, (b,f) TC Hope, (c,g) TC Bess, (d,h) TC Warren. (contour) historical outer wind speed (unit: m s^{-1}), intervalled 2 ms^{-2} . Lines indicate (red) R17 in control run, (green) R17 in warming run, (purple) RMW in control run, (orange) RMW in warming run. Black line indicated the time when the TC enters the SCS. End of y-axis showed the time of landfall.

similar, and therefore these TCs were found to have a similar R17 in the warmed climate compared to the present climate.

7.3.2 *Relative contribution between the change in radial wind and the tangential wind to the SF in a warmed climate*

As the SF depends on the radial wind and the AAM, questions arise on whether it was the increase in radial wind, or the increase in AAM, or both, that contributed to the increase in the SF in a warmed climate. Moreover, questions still remained on why TC Bess (1974) and TC Hope (1979) had an increase in R17 in the RCP8.5 Far Future climate period but a similar R17 in other climate periods and emission scenarios. Also, the linkage between the historical outer wind speed to the increase in SF in the warmed climate was yet to be developed. These questions were tackled in this section.

To separate the contribution between the change in the radial wind and the background AAM to the change in the SF in the warmed climate than the control run, common logarithm was taken to the AAMF equation, and then the common logarithm of AAMF in the warming run were subtracted by that in the control run to yield the difference:

$$\Delta \log_{10}(AAMF) = \Delta \log_{10}(r\bar{v}_r\bar{v}_\theta) + \Delta \log_{10}(r\bar{v}'_r\bar{v}'_\theta) + \Delta \log_{10}\left(\frac{f_0 r^2 \bar{v}_r}{2}\right) + \Delta \log_{10}\left(\frac{r^2 \bar{f} v'_r}{2}\right) \quad (12)$$

where Δ denote the difference between the warming run and the control run. As in previous section, the contribution of the asymmetric term to the AAMF were found to be very small, thus the ARAMF and the ACT term were neglected. Also, as the tracks for the TCs in the warming run and the control run were nearly the same (section 4.1 Figure 4.1), which means that the difference between the SCT term in the warmed climate and the control run were largely from the difference in the radial wind. Therefore, in this section, only the SRAMF term were investigated. By expanding the SRAMF term, the contribution to the logarithm of the AAMF can be expressed by:

$$\Delta \log_{10}(AAMF) \approx \Delta \log_{10}(r\bar{v}_r\bar{v}_\theta) = \Delta \log_{10}(\bar{v}_r) + \Delta \log_{10}(\bar{v}_\theta) \quad (13)$$

which the first term can be treated as the difference in the internal responses and the TC properties in a warmed climate and the second term is the change in the synoptic environment if it is far enough from the TC center. Each of the terms in equation 13 were computed for the 14 selected TCs, and the results for the 4 selected TCs were plotted to illustrate the relative contribution between the change in the internal responses of the TC and the change in the synoptic environment to the SF.

Figure 7.7 and 7.8 showed the total change in SRAMF (left) compared to the change in radial wind (middle) and the tangential wind (right) in the RCP8.5 Far Future and the RCP4.5 Far Future experiment respectively. By comparing the total SRAMF changes to the change in radial wind, it seems contradictory to the previous results that the change in the radial wind were more important in contributing to the SRAMF changes. However, as the change in the background AAM gradient is composed by the radial gradient of the radius multiplied to the tangential wind, a small increase in the tangential wind could cause a large increase in the background AAM gradient, therefore causing large increase in local radial advection of AAM. For example, an increase in the tangential wind by 1 m s^{-1} at 200 km radius increases the background AAM by $200000 \text{ m}^2 \text{ s}^{-1}$. Therefore, the change in the tangential wind prior to the increase in R17 was more important in leading to an increase in local symmetric radial advection of AAM.

If one observed carefully to the difference in the tangential wind in the warming experiment than the control run for R17 increasing TCs, a band of larger tangential wind after the onset of the historically larger outer wind speed propagated from outside the TC circulation into the R17 of the TC (red rectangles in Figure 7.7a, b, c and 7.8a). In the observer perspective away from the TC, the propagation of larger tangential wind from outside of the TC to the R17 of the TC could also be viewed as the TC moving closer and closer to the region with larger tangential wind in the warmed climate. For example, this band of positive propagating tangential wind could be observed at 1250 km from the TC center of TC Gordon at 1989-07-15-06, just after the onset of larger outer wind speed,

propagating to a radius of 200 km at 1989-07-16-18, then the R17 increased in the RCP8.5 Far Future

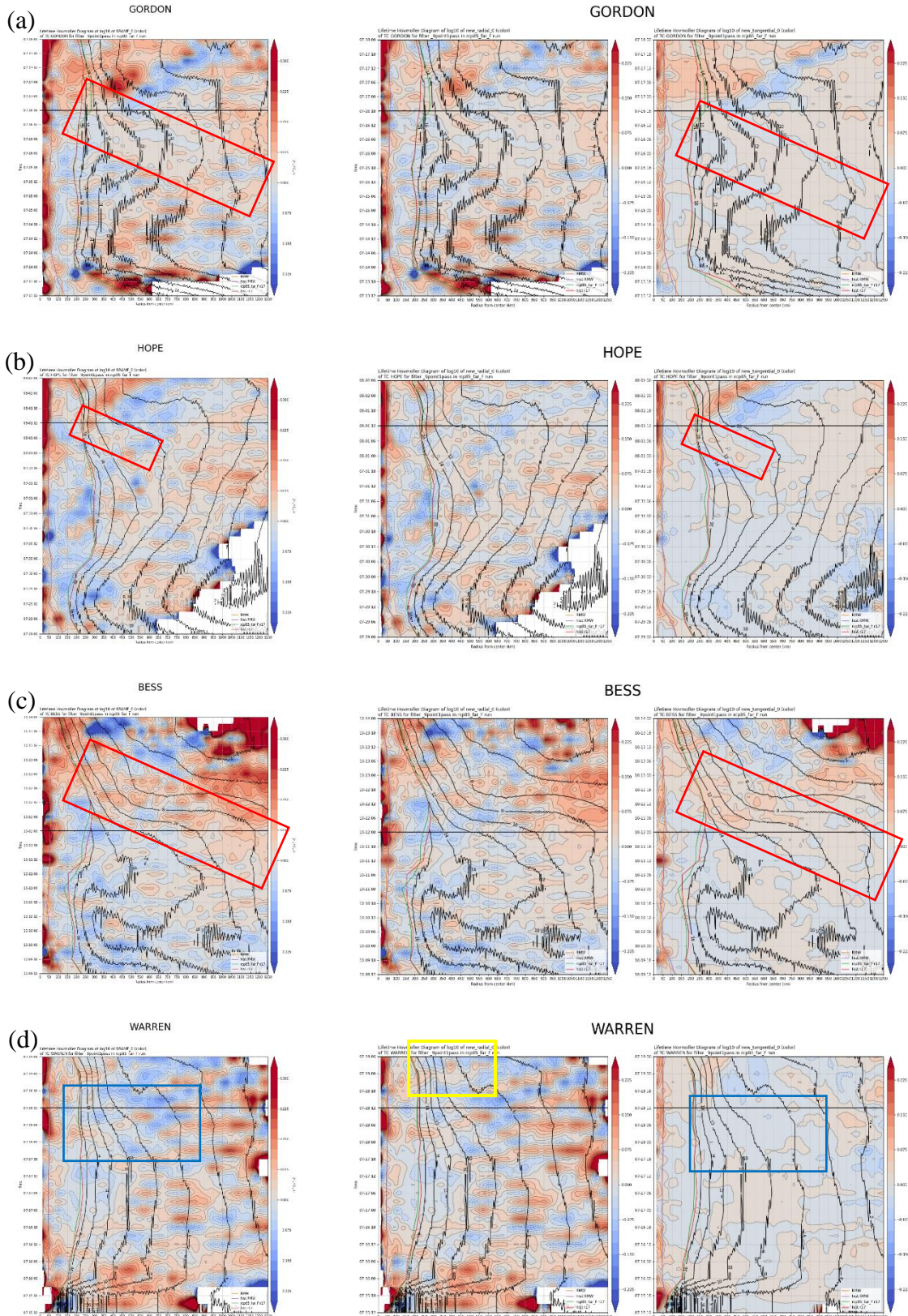


Figure 7.7 Hovmöller diagrams of (left) $\Delta \log_{10}(-r\bar{v}_r\bar{v}_\theta)$, (middle) $\Delta \log_{10}(-\bar{v}_r)$ (positive means inward), (right) $\Delta \log_{10}(\bar{v}_\theta)$ for (a) Gordon, (b) Hope, (c) Bess, (d) Warren in the RCP8.5 Far Future run relative to the control run. (contour showed the historical outer wind speed (unit $m s^{-1}$). Lines indicate (red) R17 in control run, (green) R17 in RCP8.5 Far Future, (purple) RMW in control run, (orange) RMW in RCP8.5 Far Future. Black line indicated the time when the TC enters the SCS. End of y-axis indicate the time of landfalling. x-axis showed a radius from the TC center to 1250 km radius

experiment (red rectangle in Figure 7.7a). This band of larger tangential wind in the warming run, propagating into the R17 of the TC from a location very far away were also observed for TC Gordon in all scenarios (such as in RCP4.5 Far Future in Figure 7.8a). Meanwhile, there were no inward propagating of larger tangential wind band in the warming run than the control run for R17 constant TCs, such as TC Warren. Despite an increase in radial wind in the warmed climate for TC Warren (1988) at model timestep 1988-07-19-00 from the TC center to a location near the R17 (yellow rectangles in Figure 7.6 and 7.7), no increase in the R17 were observed. Therefore, the band of larger tangential wind propagated from outside of the TC to a location near to the R17 of the TC in the warming run seems to be an important reason for the TC to expand its R17 in the warmed climate.

This observation was further confirmed by the behaviour of TC Bess (1974) and TC Hope (1979) in the RCP8.5 Far Future period compared to the RCP4.5 Far Future experiment. In the RCP8.5 Far Future, TC Hope and TC Bess were TCs having a larger increase in R17. Moreover, from Figure 7.7b and c, it can be seen that there was a positive difference of tangential wind for TC Hope (1979) in the RCP8.5 Far Future period at 500 km at model time 1979-08-01-06 (red rectangle in Figure 7.7b). This positive tangential wind signal propagated into the R17 of TC Hope at 250 km in model time 1979-08-01-18, at the time when TC Hope entered the SCS, which then caused an increase in R17 in the SCS region. Also, from Figure 7.7c, a positive signal of larger tangential wind in the RCP8.5 Far Future experiment were observed for TC Bess at model time 1974-10-11-12 at 1250 km from the TC center. This band also propagated inward, and reached the R17 of TC Bess at 250 km radius at 1974-10-12-12, which then caused the increase in R17 of TC Bess in RCP8.5 Far Future experiment (red rectangle in Figure 7.7c). However, this increased band of tangential wind were not observed in other warming experiment for TC Bess. Despite there was an increase in the radial wind for TC Bess in the RCP4.5 Far Future experiment at 1974-10-12-15, the R17 for TC Bess in the RCP4.5 Far Future experiment remained similar to the control run (blue rectangle in Figure 7.8c).

This showed the importance of increasing outer tangential wind in the warming experiments to expand the TC wind field. Moreover, there were an increase in tangential wind speed for TC Hope in

the RCP4.5 Far Future experiment at 1250 km at model time 1979-07-31-06 to 400 km at 1979-08-06

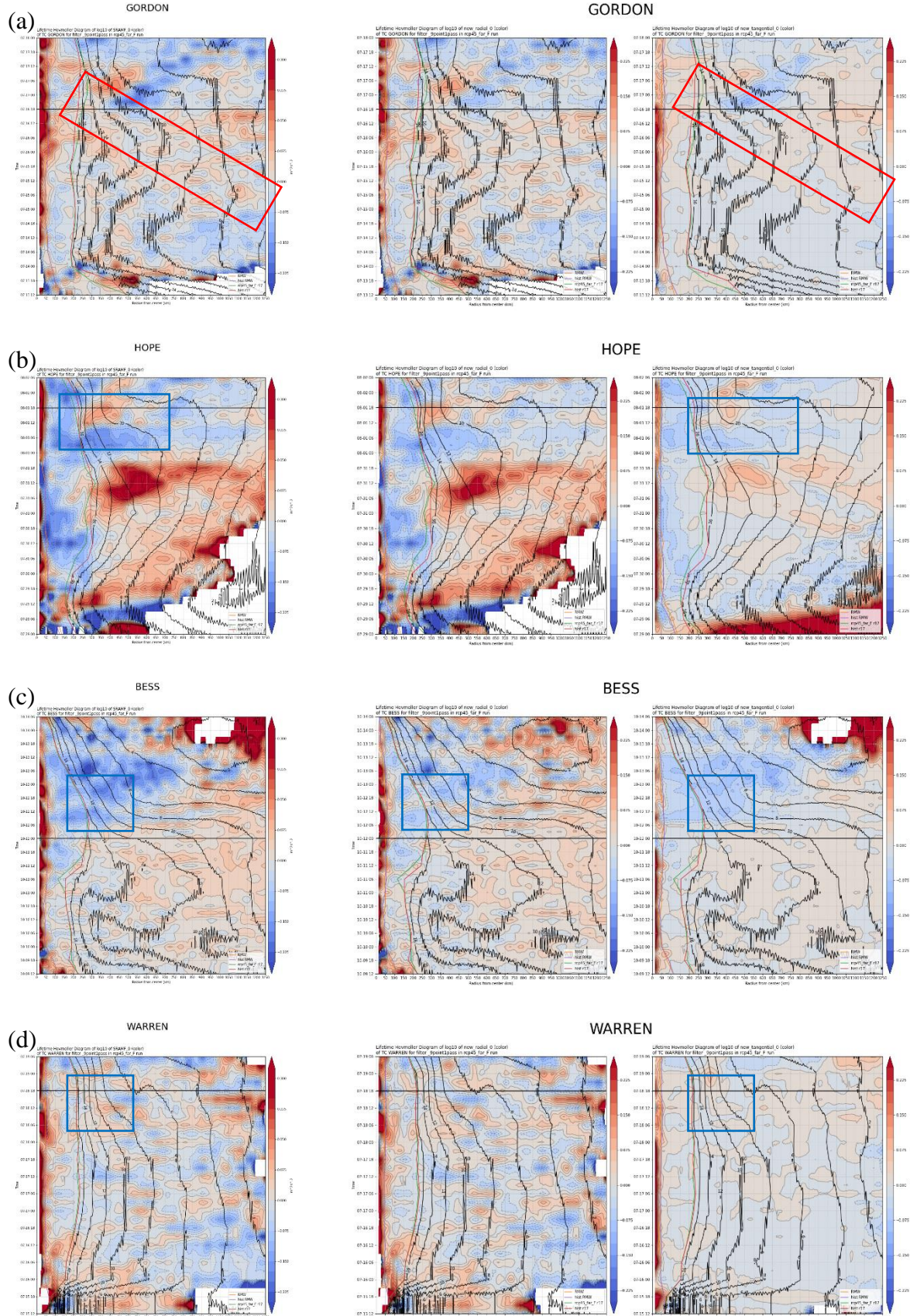


Figure 7.8 Hovmoller diagrams of (left) $\Delta \log_{10}(-r\bar{v}_r \sqrt{\bar{v}_\theta})$, (middle) $\Delta \log_{10}(-\bar{v}_r)$ (positive means inward), (right) $\Delta \log_{10}(\bar{v}_\theta)$ for (a) Gordon, (b) Hope, (c) Bess, (d) Warren in the RCP4.5 Far Future run relative to the control run. (contour) showed the historical outer wind speed (unit $m s^{-1}$). Lines indicate (red) R17 in control run, (green) R17 in RCP4.5 Far Future, (purple) RMW in control run, (orange) RMW in RCP4.5 Far Future. Black line indicated the time when the TC enters the SCS. End of y-axis indicate the time of landfalling. x-axis showed a radius from the TC center to 1250 km radius

01-18. However, the increasing tangential wind could not reach the R17 of TC Hope in the RCP4.5 Far Future experiment (blue rectangle in Figure 7.8b), which also did not lead to an increase in R17 for TC Hope in the RCP4.5 Far Future experiment. Therefore, an increase in tangential wind from outside the TCs, which then propagated into the R17 of the TCs, were one of the important reasons causing an increase in TCs' R17.

Relationship between the larger historical outer wind speed and the larger tangential can be demonstrated by TC Gordon (1989) and TC Warren (1988). Compared to TC Warren (1988), TC Gordon (1989) had a larger historical outer wind speed in the SCS and the WNP as shown by the smaller radial gradient of the contour lines in Figure 7.7a and d. Moreover, the positive signal of tangential wind for TC Gordon, which propagated from outside of the TC into the R17 of TC Gordon, were found after the onset of historically larger outer wind speed, and also followed the pattern of historically larger outer wind speed. As the radial wind of TC Gordon increased in the warming experiment, more AAM were transported from outside of the TC into the R17 of the TC, therefore causing larger AAMF and an increase in background AAM gradient. However, TC Warren were located at a historically less windy WNP and SCS region. There was no larger tangential wind signal in the warming run compared to the control run as shown by Figure 7.7d. Although the radial wind associated with TC Warren increased in a warmer climate, weak historical outer wind speed act as a limiting factor to limit the increase in AAMF. Therefore, the results showed that a historically windier environment promoted an even larger outer tangential wind in the warming runs as more AAM were influx into the TC before dissipated by friction, thus enlarged the TC R17 if the signal propagated into the R17 of the TC.

To conclude, in a historically windier SCS, more AAM can be transported into the TCs' R17 by an increase in radial wind in a warmer climate. Then, the AAMF at the R17 of the TC in a warmer climate increase. The azimuthally averaged local AAM tendency increased, which then increased the AAM of the TC and expanded the R17 of the TC in the warming run. However, in a historically less

windy SCS, the outer tangential wind away from the TC were similar in the warming experiment and the control run, despite an increase in radial wind. Lack of strong AAM outside the TC in the SCS environment act as a limiting factor in restraining the increase in the inward transport of AAM. The AAMF, radial advection of AAM and the local AAM tendency were similar in both the warmed climate and the control run, which also caused a similar R17 for these TCs in the warmed climate and the present climate.

7.4 Composites of R17 increasing TCs and R17 constant TCs

To test the statistical significance of increasing AAMF and outer tangential wind speed in contributing to the expansion of R17 for R17 increasing TCs compared to the R17 constant TCs, as well as the importance of historical outer wind speed in controlling the increase in outer tangential wind speed in the warming experiments, several sets of composite analyses were carried out in this sub-section. For each warming experiments, 5 TCs with largest R17 percentage change and 5 TCs with smallest R17 percentage were selected to represent the R17 increasing TCs and R17 constants TCs. Table 5.1 showed the order of the percentage changes of R17 for each TCs in each warming experiment. Then, 6 hourly wind vectors, AAMF, tangential wind speed and historical wind speed in the SCS were averaged separately for each TC to obtain composite maps for each TC. These

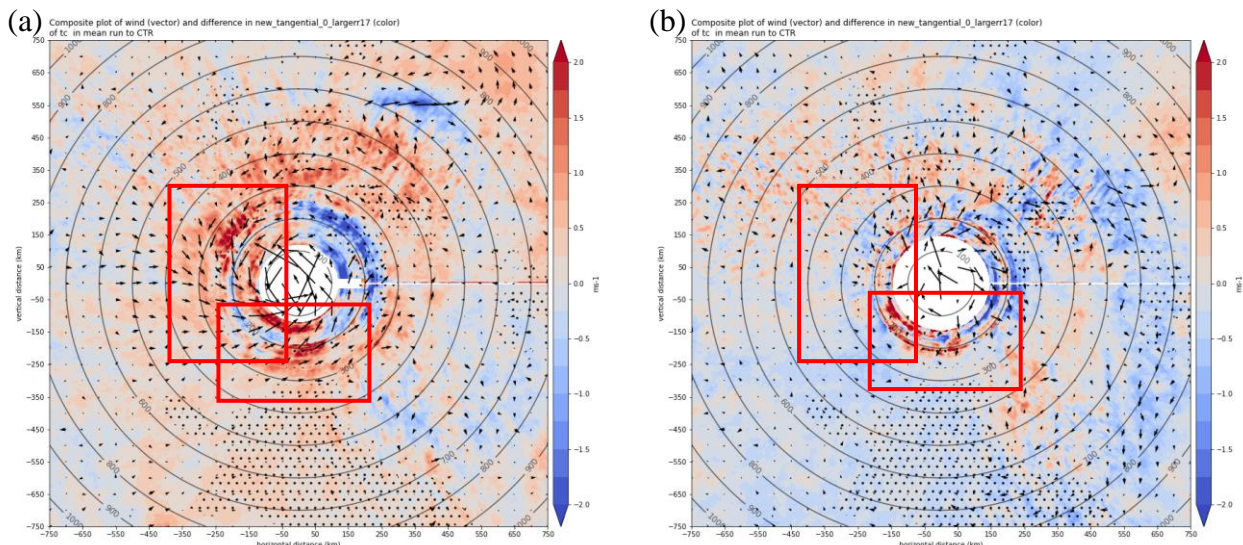


Figure 7.9 Composite plots of difference in the (color) tangential wind speed ($m s^{-1}$) and (vector) wind (unit: $m s^{-1}$) at the lowest model level for (a) R17 increasing TCs and (b) R17 constant TCs averaged in all warming experiments relative to the control run. Dotted showed significantly different tangential wind between R17 increasing TCs and R17 constant TCs in 90% CI

composite maps were further averaged across the R17 increasing TCs and R17 constant TCs to obtain composite maps that can represent the R17 increasing TCs and R17 constant TCs. Statistical test on the whether the composites of the R17 increasing TCs and R17 constant TCs were different from each other were tested in 90% CI. Results of the 4 warming experiments were averaged to show the most robust difference among all warming experiments. The aim for this part was to study the difference in tangential wind field, and establish a statistically significant difference between AAMF and the historical outer wind speed for R17 increasing TCs and R17 constant TCs. Moreover, 4 TCs and 6 TCs for R17 increasing TCs and R17 constant TCs were tried and had yield similar results. Therefore, the statistical relationships established here were not sensitive to the number of choices of TC.

First, regions with larger tangential wind speed in the warming experiments than the control run were identified by plotting the composites of the difference in the tangential wind speed. Results were shown in Figure 7.9a and b. Larger difference between the R17 increasing TCs and the R17 constant TCs were found in the southern and western quadrant of the TC (red rectangles in Figure 7.9). From Figure 7.9a, there was an increase in the outer tangential wind speed in the warming run than the control run for R17 increasing TCs compared to the R17 constant TCs. Results from the composite

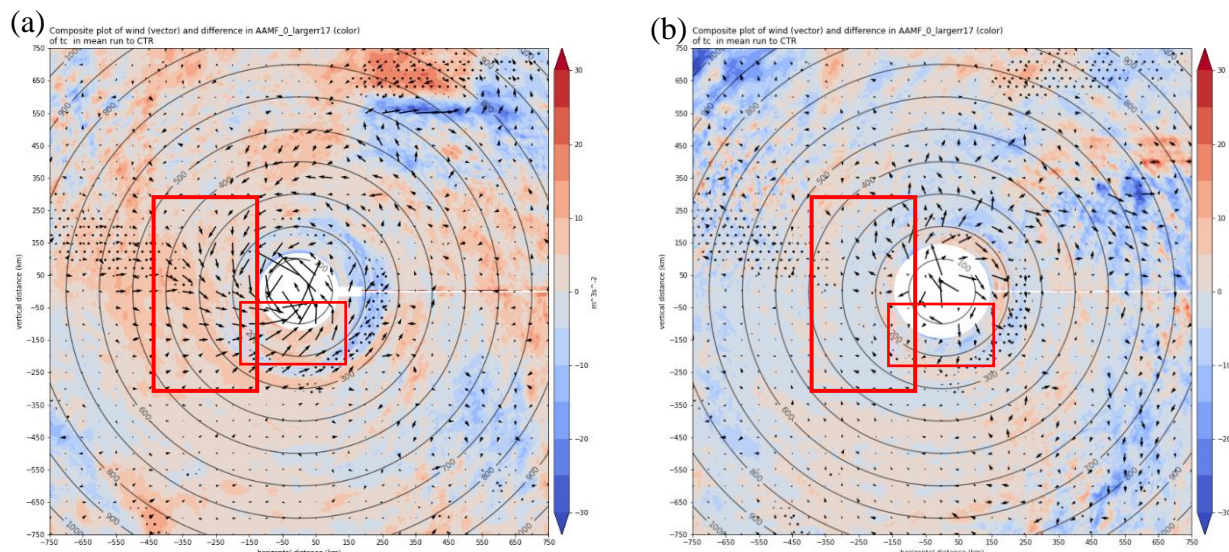


Figure 7.10 Composite plots of (color) difference in AAMF ($10^6 \text{ m}^3 \text{ s}^{-2}$) and (vector) wind (unit: m s^{-1}) at the lowest model level for (a) R17 increasing TCs and (b) R17 constant TCs averaged in all warming experiments to control run. Positive AAMF means inward. Dotted represent the AAMF were significantly different bewteen the R17 increasing TCs and the R17 constant TC in 90% CI.

map matches with the results of the hovmöller diagram that TCs with an increase in R17 in a warmer climate were associated with an increase in tangential wind near and outside of the R17. Moreover, the increase in outer tangential wind in a warmer environment for R17 increasing TCs in the southern quadrant were significantly different to that for R17 constant TCs in the southern quadrant in 90% CI (indicated by black dots). This showed that most of the increase in background AAM were found at the southern quadrant of the TCs in a warmer climate in the SCS.

Second, the difference between the AAMF in the warming runs to the control run for R17 increasing TCs and R17 constant TCs were tested. Results for the difference in AAMF and wind vector composites in warming runs to the control run were shown in Figure 7.10a and b. Compared Figure 7.10a and 7.10b, R17 increasing TCs were associated with a larger AAMF at the southern and western quadrant of the TC compared to the R17 constant TCs (red rectangles) across all 4 warming experiments. The difference in AAMF at the western quadrant of R17 increasing TCs and R17 constant TCs were significant in 90% CI. Moreover, by comparing the snapshots of the AAMF difference for TC Bess (1974), TC Hope (1979) and TC Gordon (1989) in RCP8.5 Far Future than RCP4.5 Far Future runs, the inward propagating bands of larger tangential wind shown in Figure 7.7 and 7.8 were associated with an increase in tangential wind and AAMF at the western quadrant of the

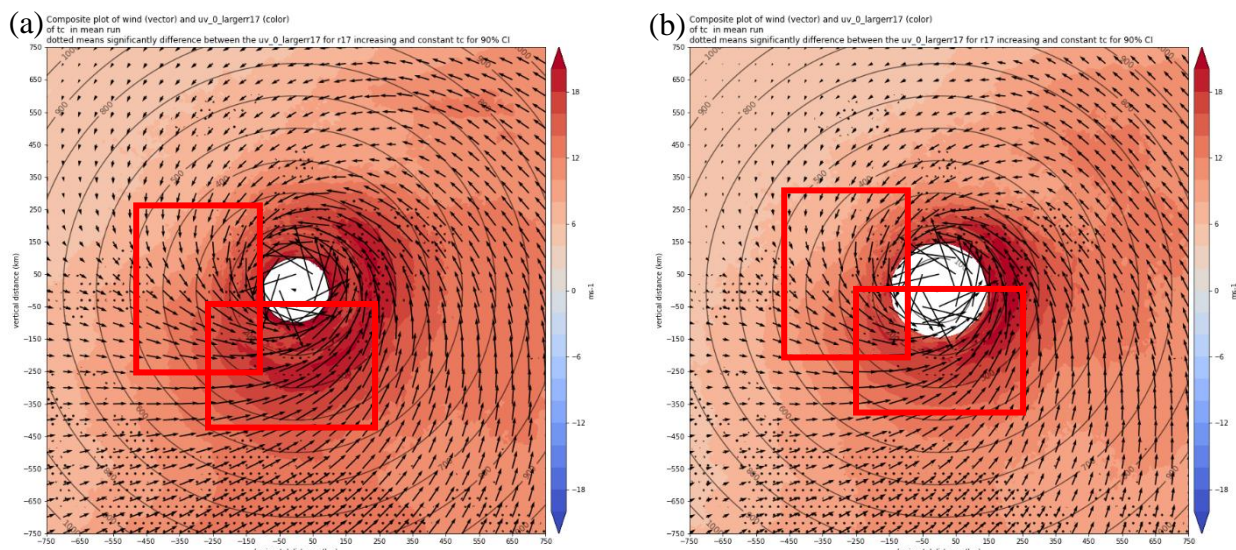


Figure 7.11 Composite plots of (color) historical wind speed (unit: $m s^{-1}$) and (vector) wind (unit: $m s^{-1}$) for (a) R17 increasing TCs and (b) R17 constant TCs, averaged across all TC selection based on order of R17 increase in all 4 warming experiments. Dotted represent the wind speed were significantly different bewteen the R17 increasing TCs and the R17 constant TC in 90% CI.

TCs. Yet, increased AAMF at the western quadrant and southern quadrant were both important in causing a larger increase in R17 for R17 increasing TCs, as indicated by Figure 7.10 (red rectangles). Therefore, historical northwesterlies and southwesterlies wind in the SCS could be attributed to cause the larger expansion of R17 for some of the TCs.

The historical outer wind speed for R17 increasing TCs and R17 constant TCs were compared in Figure 7.11a and b respectively. The historical wind speed in the southern quadrant of the R17 increasing TCs were much stronger compared to that of the R17 constant TCs. Moreover, the historical wind speed at the western quadrant of the R17 increasing TCs were slightly stronger than the R17 constant TCs. Reasons for the stronger historical northwesterlies associated with R17 increasing TCs than R17 constant TC being not that obvious compared to that for the historical southwesterlies were because strong historical northwesterlies were only associated to TC Bess and TC Hope, which these 2 TCs were only identified to be R17 increasing TCs in RCP8.5 Far Future experiment, therefore the signal was smoothed out during averaging the composites across all

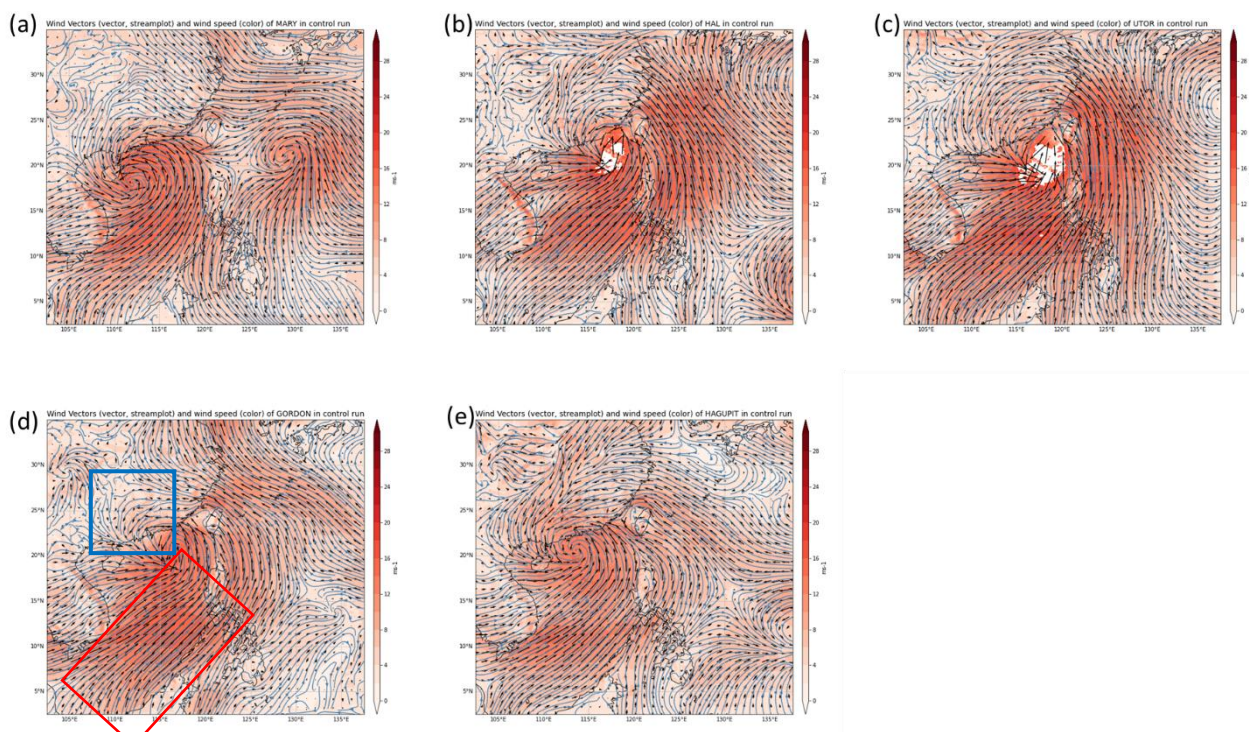


Figure 7.12 Time mean of (color) historical outer wind speed beyond R17 (unit: $m s^{-1}$), (streamplot) historical outer wind (unit: $m s^{-1}$) and (vector) historical outer wind vector (unit: $m s^{-1}$) for (a) Mary, (b) Hal, (c) Utor, (d) Gordon, (e) Hagupit selected by the order of the percentage change of R17 in the RCP8.5 Near Future experiment. a-e were ordered in descending order of percentane change in R17 in RCP8.5 Near Future experiment.

experiments. Moreover, TC Utor (2001), TC Hal (1985) and TC Hagupit (2008) were all embedded in a strong southwesterlies SCS environment. To sum up, it could be concluded that TCs located in a historically windier SCS, with strong northwesterlies and southwesterlies being the source of AAM transported into the R17 of the TCs, would have a higher chance of expanding more of their R17 in a warmer climate. Yet the non-linear relation of the frictional dissipation to the wind speed, as well as the surrounding topography may hinder the expansion of R17 for these TCs. The change in the frictional dissipation term in a warmer climate should be investigated in future research.

7.5 Synoptic Environment Associated with R17 Increasing TCs

In the last part of the AAM analysis, the synoptic wind pattern in the past associated with the R17 increasing TCs and the R17 constant TCs were analysed. It had been found that TCs located in a historically stronger southwesterlies and northwesterlies SCS environment could be more favourable in expanding its R17 in the warming run. Therefore, the synoptic wind pattern associated with these stronger wind speed environments were analysed.

Illustrated by the R17 increasing TCs and the R17 constant TCs in the RCP8.5 Near Future period, Figure 7.12 and 7.13 showed the mean outer wind speed beyond the R17 and streamline plot averaged timely when each TC was in the SCS for R17 increasing TCs and R17 constant TCs respectively. Compare Figure 7.12 with 7.13, the R17 increasing TCs were associated with strong southwesterlies surges from the equator (see an example of TC Gordon and TC Warren (red rectangle in Figure 7.12d and 7.13d). Large area at the southern SCS region of the R17 increasing TCs were covered by a wind speed of larger than 14 m s^{-1} . These southwesterlies wind were originated near to the equator, which may be originated from the cross-equatorial flow between 105°E and 110°E .

However, compared to the R17 increasing TCs, the R17 constant TCs were associated with a much weaker southwesterlies wind at the southern SCS region. For TC Nuri (2008) and TC Warren (1988), there were only a small region at the southern SCS that was covered by a wind speed exceeding 10 m s^{-1} . Moreover, for TC Bess (1974), TC Hope (1979) and TC Dujuan (2003), the

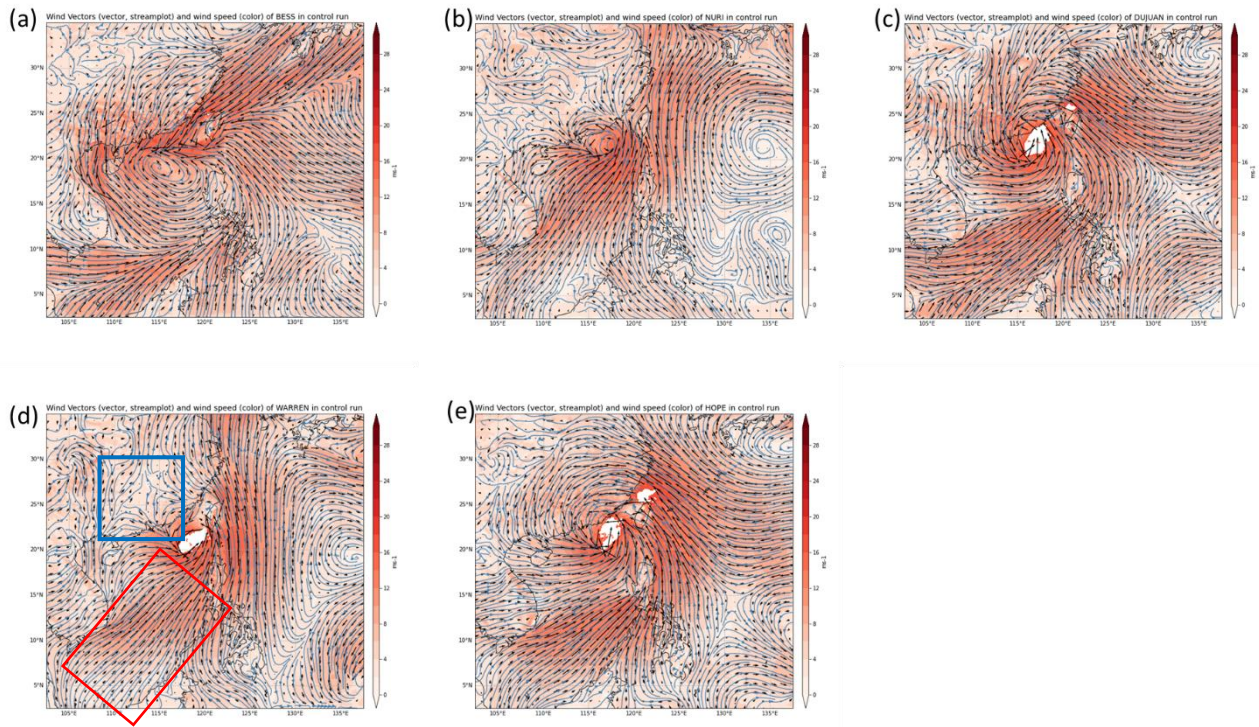


Figure 7.13 Time mean of (color) historical outer wind speed beyond R17 (unit: $m\ s^{-1}$), (streamplot) historical outer wind (unit: $m\ s^{-1}$) and (vector) historical outer wind vector (unit: $m\ s^{-1}$) for (a) Bess, (b) Nuri, (c) Dujuan, (d) Warren, (e) Hope selected by the order of the percentage change of R17 in the RCP8.5 Near Future experiment. a-e were ordered in ascending order of percentane change in R17 in RCP8.5 Near Future experiment.

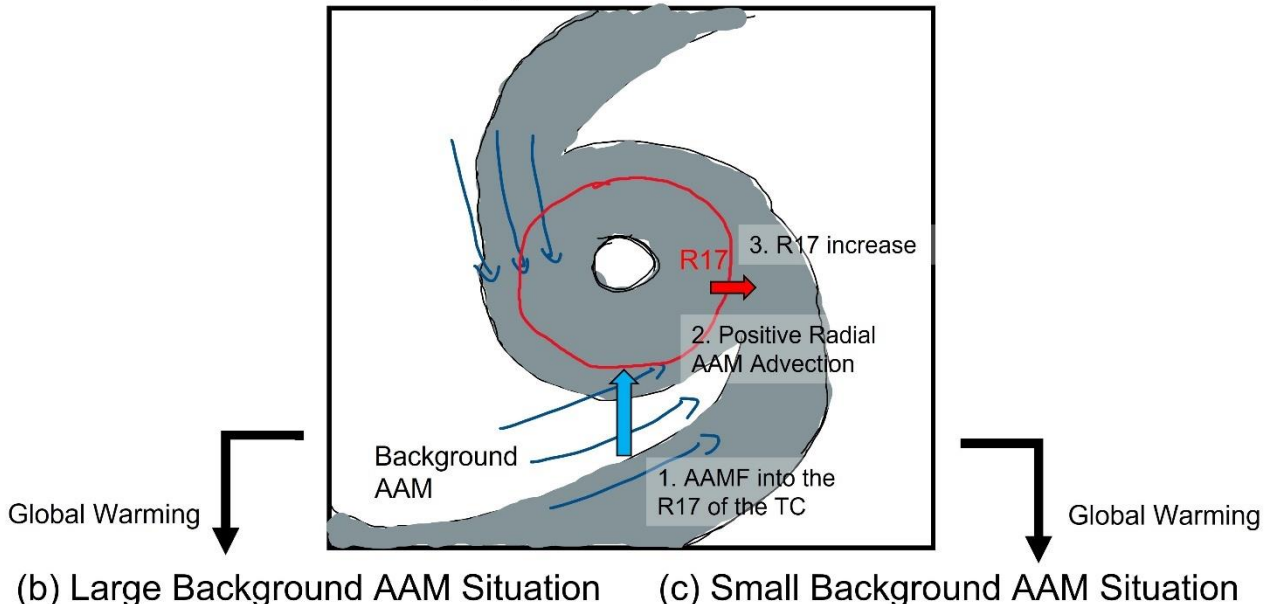
southwesterlies wind from the southern SCS region could not reach the southern quadrant of the TC.

Instead, the wind at the southern quadrant of these TCs were originated from the Indochina Peninsula and the Bay of Bengal. The westerlies from the Peninsula blocked the southwesterlies originated from the southern SCS, which resulted in weaker wind speed in the past due to larger frictional drag of the land. Moreover, some TCs (for example TC Gordon compared to TC Warren) were embedded in an environment with stronger northwesterlies (blue rectangles in Figure 7.12 and 7.13). TCs located in the SCS with strong northwesterlies could also cause a larger increase in R17 in a warmer climate.

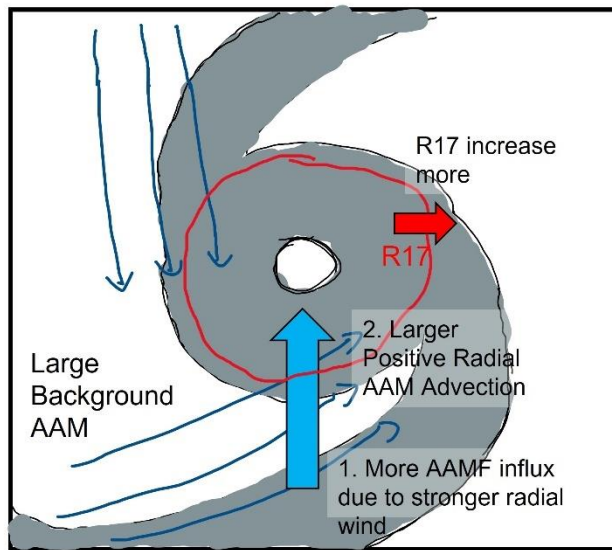
7.6 Summary for AAM Budget Analysis

Figure 7.14 summarized how the historical outer wind speed in the SCS controlled the variations of TCs R17 changes in a warmer climate compared to the mean change. Figure 7.14a showed how AAMF relates to the increase in R17. When there were an increasing AAM transported into the R17 of the TC with time, the radial advection of AAM will be larger than the friction dissipation, which caused an increase in the local AAM tendency near the R17 and the expansion of the R17. Moreover,

(a) Historical Run



(b) Large Background AAM Situation



(c) Small Background AAM Situation

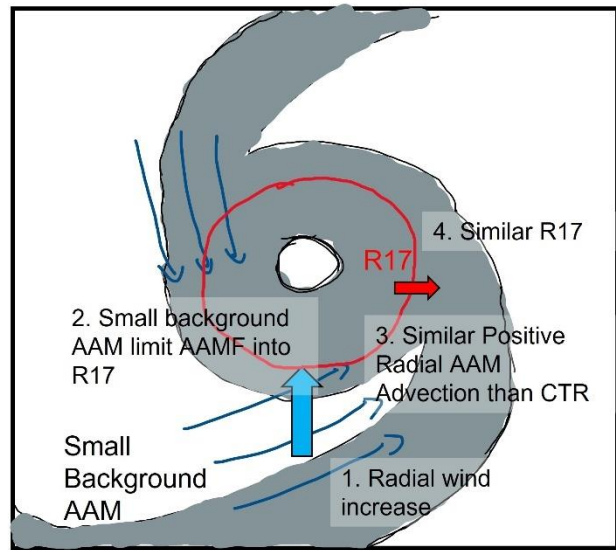


Figure 7.14 Schematic Diagram of how the historical outer wind speed controlled the variation in the change of TCs' R17 in a warmed climate. (a) showed the TC in the historical run. (b) showed TCs embedded in a historically larger outer wind speed environment. (c) showed TCs embedded in a historically smaller outer wind speed environment

in a warmer climate (Figure 7.14b and c), radial wind associated with the TC increased. If the background AAM was large enough, more AAMF would be transported into the R17 of the TC (Figure 7.14b step 1). Then, the radial advection of AAM increased, which increased the local AAM tendency and further increase the R17 (Figure 7.14b). However, in a historically weaker outer wind speed environment (Figure 7.14c), although the radial wind associated with the TC could increase, small background AAM act as the limiting factor of the AAMF (Figure 7.14c step 2). AAMF that could influx into the R17 of the TC remain similar to the historical period. Therefore, the radial

advection of AAM, local AAM tendency and the R17 of these TCs remained similar as the historical run. Results showed that TCs located in a historically stronger outer wind speed SCS expands their R17 more in a warmed climate compared to TCs embedded in a historically less windy SCS.

8. Discussion and Limitations

8.1 Implications to future TC intensity and size projection

8.1.1 Variations and error estimation for mean TC intensity and size changes

Perhaps the most important applications of studying the variations of the percentage change in the intensity and size of different TCs in different future climate periods and emission scenarios were to establish an error bar to the projected mean change of TC intensity and size, which described the uncertainties in mean intensity and size prediction under natural variability of different climate modes in the SCS in this study. Knutson et.al. (2020) had summarized a number of high-resolution numerical model predictions on the projection of the TC intensity changes in future climate periods under different emission scenarios, and found a global increase in TC mean intensity in terms of Vmax of 5% for a 2 °C increase in surface temperatures. They also found that the range spread across 1% to 10% for the changes in TC Vmax across multiple researches.

Despite multiple researches, including high-resolution idealized experiments, PGW experiments by regional climate model and GCM global experiments were used to reach a range of 1% to 10% changes in the mean TC intensity in a 2 °C warmer climate, results were inevitably subjected to uncertainties in these researches. One of the uncertainties can be the sampling bias from TC selection in PGW experiments, which may not adequately cover a long enough period to represent the interdecadal variation of tropical synoptic environment that can influence the intensity or the size of the TCs (Liu & Chan, 2008). Moreover, the ability of the GCM to revolve the intraseasonal, interannual and interdecadal climate variability in the current climate could be another source of uncertainties in producing accurate TCs intensity and size distributions embedded in reasonable background synoptic environment in the current climate (Feng, et.al., 2014; Guilyardi, et.al., 2020). Apart from that, the limited ability of the GCMs to simulate climate modes of different timescales in the WNP in the future climate can create uncertainties in predicting future TC mean intensity and size changes (Knutson, et.al., 2020). Subjected to these uncertainties, together with the uncertainties

brought by limited model resolution, choice of model physics schemes, various literatures had reached different projected future TCs' intensity and size mean change. The previous approach to provide a range of uncertainties in intensity prediction was to summarize the results from multiple high-resolution numerical modelling experiments, and then reach a range for TC intensity projection (Knutson, et.al., 2020). However, questions remained on whether the range for future TCs' intensity prediction obtained from literature review could have adequate theoretical support.

This study, however, had presented another approach in estimating the mean change and the uncertainties of TCs' intensity and size in the future climate statistically. In each warming experiment, the sample distribution of the percentage change in the TCs' intensity and size were found to be related to the embedded historical synoptic environment by MLR analysis. If one can neglect the change in the amplitude and phase of different climate modes in the future climate, the synoptic environment associated with the TCs in a warmed climate can be attributed to similar climate modes in the historical period. Therefore, by carefully selecting historical TC cases, which could represent the temporal variations of the important synoptic environment controlling TCs intensity and size changes, the sample distribution projected for TCs' intensity and size change can adequately represent the seasonal, interannual and interdecadal variations of TCs' intensity and size in a warmed climate, assuming there is no change of climate modes in the future. Linear regression model established for the mean intensity and size changes for these TCs can therefore reduce the uncertainties brought by natural variability in intraseasonal, interannual and interdecadal variations. Moreover, the confidence interval of the linear regression model can serve as the error bar (see Fig. 7 in Nicholas (2014) for an example of error bar, and the grey dotted line in Figure 4.2) of the projected mean change in TCs' intensity and size under natural variability brought by temporal variations of different climate modes. In this case, an "educated guess" could be provided for the TCs intensity and size changes in the future climate, which could raise the confidence in projecting future TCs' intensity and size.

Figure 4.2 showed an example of the 95% confidence interval of the projected TCs' mean intensity and size changes in future climate, as indicated by the grey dotted lines. The 95% confidence interval of the regression model were computed by:

$$\hat{y} \pm 1.96 s_{\bar{y}|x_0}, \text{ where } s_{\bar{y}|x_0}^2 = s_e^2 \left[\frac{1}{n} + \frac{(x_0 - \bar{x})^2}{\sum_{i=1}^n (x_i - \bar{x})^2} \right] \quad (14)$$

where \hat{y} is the regressed dependent variable, $s_{\bar{y}|x_0}^2$ was the confidence variance, s_e^2 was the mean squared error (MSE) and n is the number of samples. The 95% confidence interval of the regression model means that 95% of the regression line predicted by similar number of TC samples will be bound by this interval, therefore providing the range of the mean change in TC intensity and size. As indicated by equation 14, the range of the predicted mean change in TCs' intensity and size depends on the MSE, uncertainties for estimating the true mean from the sample mean, and the uncertainties in estimating the slope of the model (Wilks 2011). Moreover, the uncertainties brought by the MSE of the samples were due to the variations of historical background synoptic environment, which were related to different climate modes. Therefore, the MSE emphasized the importance of selecting the TCs that span across a wide yet representative historical environmental conditions that are important in controlling the spread, in order to reduce the TCs sampling bias due to insufficient temporal coverage of different climate modes in future studies.

Using the percentage change of TCs' intensity in a warmed climate in the SCS as an example (Figure 4.2a), the TC mean intensity changes in the SCS for a 2 °C warming was 8.6% (range 7% to 11%). This range of the error in estimated the mean change of TCs' intensity in the SCS in a warmed climate were due to the variations in the percentage change of TCs' intensity, which ultimately were related to different historical SST and vertical wind shear magnitude. Moreover, the variations of historical SST and vertical wind shear magnitude in the SCS in the past were related to different climate modes like the El-Niño Southern Oscillation (ENSO), the Pacific Decadal Oscillation (PDO) or the Madden-Julian Oscillation (MJO) (Wang, et.al., 2006; Zhao & Wang, 2019; Zheng et.al., 2020). Therefore, the 95% CI of the mean intensity percentage changes in a warmed climate in the SCS as

shown in Figure 4.2a provides an estimation of error due to the natural variability of these climate modes for the sample used in this project in a warmed climate. Similarly, the uncertainties brought by the temporal variations of the mid-tropospheric RH and wind speed in the SCS could also be shown for TCs future outer core size projection (Figure 4.2c).

Despite the samples selected in this project did not necessarily be able to represent a full range of related historical environmental conditions, the results served as to provide a method to estimate the error bar of the predicted TCs' intensity and size changes in the future climate. Yet, uncertainties due to the inaccurate simulation of the change in the phase, amplitude and spatial coverage of different climate modes, like the change in the strength of ENSO, in a warmed climate were not addressed (Christensen et.al., 2013). Moreover, the uncertainties due to the choice of the numerical model, physical schemes and the model resolution were not accounted. Despite other uncertainties remains, the method presented here can reduce uncertainties brought by natural variability of climate modes in different temporal timescale. The regression model and error bar established also served as an educated guess of the percentage change of mean TCs' intensity and size in the SCS in future climate, which raise the confidence in future TCs' intensity and size projection.

8.1.2 Risk Assessment for Individual TC

Government and insurance industry utilized the projection in TCs' intensity in the future climate to estimate TCs risks, as well as providing mitigation plans and planning certain policies (Peduzzi et.al., 2012). Peduzzi et.al. (2012) had predicted an increase in population exposure to TC hazard, despite a projected decrease in TCs frequency but increase in TCs mean intensity in the near future era (Peduzzi et.al., 2012). However, results in this project showed that the percentage change in TCs' intensity and size for different TCs were very difference compared to the mean change. Instead, the spread of the percentage change in TCs intensity and size was also an important statistic apart from the mean change. For example, Figure 4.2c showed that the mean R17 of the TCs in the SCS were predicted to have a slight increase of 4.39% in the far future era under RCP8.5 emission

scenario. However, the range of the change in R17 in the RCP8.5 Far Future experiment for the sample chosen spread across +19.5% to -7.46%. In fact, single intense storm in a quiet TC season can bring catastrophic damage to coastal cities (Klotzbach et.al., 2018). Moreover, stronger TCs imposed larger population exposure in mortality risk, thus heavier loss in human life and properties (Peduzzi et.al., 2012). Therefore, policy makers and insurance companies should take into account of the large spread in projected TCs' intensity and size changes relative to the mean in future climate, so as not to underestimate the huge TCs' risks increase relative to the mean change in certain TC-favourable environment.

This project had provided a method, which is the 95% prediction interval, to incorporate the spread of the change in TCs' intensity and size aside of the mean change to future risk assessment. Using the percentage change of R17 as an example, from the samples and the regression model, the 95% prediction interval of the percentage change in R17 in the future climate was established, and was indicated by the black dashed lines in Figure 4.2c. The predication interval is computed by

$$\hat{y} \pm 1.96s_{\hat{y}}, \text{ where } s_{\hat{y}}^2 = s_e^2 \left[1 + \frac{1}{n} + \frac{(x_0 - \bar{x})^2}{\sum_{i=1}^n (x_i - \bar{x})^2} \right] \quad (15)$$

which all variables were having the same meaning as that in the equation 14, and $s_{\hat{y}}^2$ represent the prediction variance (Wilks 2011). The 95% prediction interval of the R17 percentage change means the probability for drawing a random sample other than the sample used in this study, given the same population distribution, will have 95% chance being bounded within the 95% prediction interval. In this case, the 95% prediction interval act as the upper and lower bound of the projected change in TCs' intensity and size for individual TC in the future climate. As the MLR results showed that larger percentage increase in TCs' R17 in the SCS were related to a historically moister and windier SCS, random TC sample in the future climate embedded in these environments will have a larger percentage increase in R17 relative to the mean change brought by global warming. In this case, the prediction interval can act as an additional information on the spread of the percentage change in R17

in the future climate for relevant stakeholders in hazard assessment, aside of the mean change, in the future climate.

However, the TC samples being selected here did not necessarily cover all possible synoptic environmental conditions that had happened in the SCS in the past. Extremely warm SST or humid mid-troposphere can alter the distribution of the percentage changes for TCs' intensity and size found in this research. Therefore, future researches should be carried out by a thorough TCs sample selection regarding the possible range of the environment in the SCS, so as to generate a better distribution of percentage change in the intensity and size in a warmed climate in the SCS.

8.1.3 Extreme Value Statistics

The 95% prediction interval computed in Figure 4.2 means that 95% of the future TCs intensity and size changes in the SCS would be bound by the prediction interval. Moreover, TCs outside the 95%, or 99% prediction interval can be treated as the TCs having an extreme change in TCs' intensity and size in the future. These extreme changes in TCs' intensity and size in the future climate should be studied carefully as unexpectedly larger risk can be possessed to the coastal cities.

Knutson et.al. (2020) had found an increase in global increase in C4-5 TC frequency in future climate projection by a median of 13% due to a decrease in global TC frequency with an increase in TC intensity (Knutson et.al., 2020). Whether their results can be linked to the TCs having a larger increase in TCs' Vmax in historically warmer SST and weaker vertical wind shear environment can be a future research direction. However, similar analysis should be carried out on predicting the extreme aspect of the TC size as large TC can bring huge damage to the coastal cities (Powell & Reinhold, 2007). As we have found that historically wetter and windier SCS promotes a large increase in TCs' R17, future research should be carried out on whether the increase in size for these TCs in a favourable environment but a warmer climate background increases the number of very large TC in the SCS, therefore imposing huge risks to coastal cities by storm surge (Needham & Kalm, 2014).

8.1.4 Statistical Forecast of Individual TC in the Future Climate

Another implication of the spread of the percentage change in TCs intensity and size was drawn to the statistical forecast. Currently, statistical, dynamical, or hybrid-statistical-dynamical methods were used for different meteorological agencies and research institutes to forecast seasonal TC activities in the WNP basin (Zhan et.al., 2012). Statistical forecast utilized observations of important atmospheric and oceanic predictors such as the ENSO index and tropical SST preceding the TC season to predict the TC activities and intensity at that year. Moreover, hybrid-statistical-dynamical forecasts retrieved these important predictors from numerical simulations, and matches the values to the past records to forecast the TC activity. Apart from that, operational forecast on TCs' intensity and R17 relied on past observational record on the TCs intensity and outer core size, as well as the corresponding synoptic environment to forecast the intensity and size for up to 7 days (Tsai & Elsberry, 2014; Sampson & Knaff, 2015; Knaff, et.al., 2017; Leroux et.al., 2018). All of these forecast methods that utilized past observation on synoptic environmental variables to form the regression model were subjected to limitation that the record did not capture long-term climate variabilities and shift, therefore showing deficiency in forecasting effects on global warming to the temporal variations of TC activities (Zhan et.al., 2012).

One may ask whether the change in TCs' intensity and size due to anthropogenic warming in the future climate could be directly incorporated into the regression model in the statistical forecast. Despite the advancement in predicting the mean change in TCs intensity and size in the future warmed climate, there were few predictions on whether there will be a change in TCs intensity and size distribution in an interannual, or even seasonal timescale in the future climate. For example, Knutson et.al. (2015) had removed the interannual “noise” by averaging the present day and late-21st century SST and external forcing within 20 years period. Their idea of simulating the TCs characteristics changes can be illustrated by Figure 8.1a. In their paper, they had averaged the recorded SST and other external forcing between the current climate (bounded by 2 vertical dotted line, labelled as

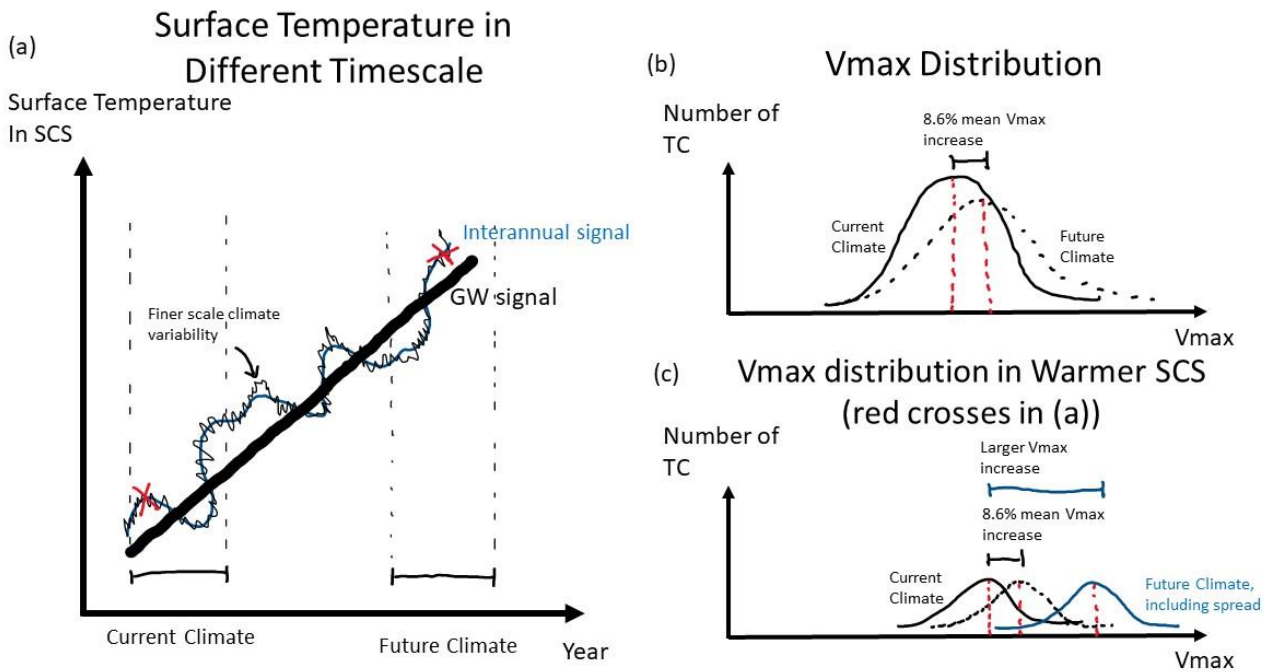


Figure 8.1 Schematic Diagram showing the need in incorporating the spread of the percentage change in Vmax in future climate in the statistical forecast. (a) surface temperature change in different timescale. (b) Change in intensity distribution in future climate, accounting for the increase in intensity, increase in strong TCs frequency but decrease in number of TCs. (c) Change in Vmax distribution for TCs in a warm SCS

current climate in Figure 8.1a), and 20 years of future climate variables changes (future climate period minus current climate period in Figure 8.1a) to obtain the effect of long-term global warming signal to the TC statistics. Despite the significance in studying the future TC activities in a warmer background climate, TC activities in each year, as well as individual TC change in a warmed climate background (red crosses in Figure 8.1a, which are embedded in various timescale climate modes) are also important as ultimately it is each individual TC that brings risks to coastal regions. As slight increase in TCs mean size could be contributed by a cancellation between the decrease or increase in TCs size in some specific background environment when the spread is large, the TC mean statistics should be treated with caution in terms of future TCs' intensity and size forecast.

The importance in incorporating at least the natural variability of different climate modes, which can alter the synoptic environment in different TC basins and ultimately affect the percentage change of intensity and size of individual TC, could be illustrated by comparing Figure 8.1b and 8.1c. Knutson et.al. (2015) had found an increase in global mean TC intensity and a decrease in TCs number in the future climate (Figure 6 in Knutson et.al., 2015). Moreover, in this research, the

increase in mean TCs' Vmax in the SCS were found to be 8.6% for a 2 °C warming, as illustrated in Figure 8.2b. However, if we just compare the TCs located in a historically warmer SCS, where the interannually warmer SST in the SCS were found to be associated after the onset of El-Niño, the historical distribution of TCs Vmax can be illustrated by the solid black line in Figure 8.1c (Wang, et.al., 2006). As TCs in a historically warmer SST environment increases their intensity more in a warmed climate, the intensity for these TCs in the future climate background will be underestimated if one just considers the mean increase (compared the blue solid line and the black dotted line). Therefore, it is important to consider the variations of the background environment when one tries to predict future TCs changes in interannual, interdecadal or even seasonal timescale.

To generalize the argument to different TC statistics like the TC size, Figure 4.2 was referred. If one could neglect the change in the phase, intensity and the spatial coverage of different climate mode, every synoptic environment can at least be partly related to different timescale climate modes. For example, warmer SST environment in the SCS could be related to the year following the onset of El-Niño (Wang, et.al., 2006). Therefore, by just considering the natural variability of the ENSO, TCs in El-Niño year were projected to have larger increase in SST in the SCS relative to the mean. Similarly, different climate modes can be attributed to the historical environment which controls the background synoptic environment in the SCS. In this case, one could find out the climate modes that could lead to larger increase in TCs' intensity and size, benefiting future TCs' intensity and size forecast in seasonal, interannual and interdecadal timescale.

As the percentage change in TCs' intensity and size were different in different phase of climate modes, one cannot just impost the mean change to the statistical forecast model in future climate. Moreover, modification of the regression coefficient in the statistical forecast regression model should be carried out in order to update the change in the long-term climate background. Caution should also be taken during the comparison between the TC being forecast and the past TC during historical analogy when forecasting the TCs' intensity and size (Knaff et.al., 2016; Leroux, et.al.,

2018). Moreover, we have not studied the changes in the climate modes in future climate, which the confidence in projecting the future variability in climate modes like the ENSO remains low (Christensen et.al., 2013). This was left for future study.

8.2 Projected RMW decrease in future climate

In section 4.2, a decrease in mean RMW were found by PGW experiments in the future climate, despite the fact that the change might not be resolved by the 3 km horizontal resolution inner domain. The limitation raised by the model horizontal resolution were discussed in section 8.5.2. Yet, we hope to investigate whether there will be a proposed change in the RMW in the future climate according to the past literatures. However, there were no past studies that systematically discuss the behaviours of the RMW in the future climate, except a decrease of RMW found from a case study of Hurricane Catarina in a warmed ocean and a stabilized atmosphere using 3 km horizontal resolution numerical experiment (Radu et.al., 2014). Therefore, physical mechanisms of explaining the contraction of RMW in the warmed climate should be established in the future by high resolution idealized experiments and regional climate modelling.

Moreover, by utilizing diagnostic tools developed from TC theory in the past, the behaviour of RMW in the future climate could be inferred. Willoughby (1990) had found a contraction of RMW concurrent with the strengthening of the TC (Willoughby, 1990). Also, Shapiro and Willoughby (1982) had linked the secondary circulation of a TC to the heating and the momentum source (Shapiro & Willoughby, 1982). Their diagnostic model for baroclinic vortex explained that a heating source induces inward radial wind, which overshoots the eyewall and caused the largest increase in tangential wind located just inside the RMW of a TC, therefore resulting in a contraction of RMW when the TC is intensifying. Moreover, they had argued that the continued contraction of the RMW depends on whether the heating near to the RMW can sustain. Xu and Wang (2010a, b) had analysed the RMW contraction by the azimuthally averaged radial and tangential momentum equation. As the local rate of change of tangential wind depends on the vertical absolute vorticity and the radial wind, an

overshoot of radial wind into the RMW of a TC caused the contraction of RMW as the radius of maximum increase in tangential wind speed is location just inside of the RMW, if the vertical absolute vorticity maxima were also located inside the RMW (Xu & Wang, 2010a, 2010b).

CMIP5 models projected an increase in SST and an increase in atmospheric stability in terms of larger upper tropospheric warming than the increase in temperature in the lower troposphere. Moreover, from the result of a projected increase in mean Vmax and a decrease in minimum sea level pressure in the SCS, an increase in warm core temperature anomaly should also occurred as a consequence of the hydrostatic adjustment. Therefore, a drop of central pressure causes larger radial pressure gradient across the RMW by the radial momentum equation, and the RMW contracts more in the warmed climate. Moreover, a correlation coefficient of -0.51 were found between the percentage change of Vmax and the percentage change of RMW for TC samples in the SCS. This large correlation may serve as a prove that part of the contraction of RMW was a response to an increase in the Vmax in the future climate. From Ren et.al. (2022), TCs located in a warmer SST environment contracted faster, therefore the RMW were smaller for the TCs in a warmer oceanic environment before the RMW eventually converges in day 5 of the integration time (Ren, et.al., 2022). A smaller RMW in the future climate was also predicted by a case study of Hurricane Catarina in the South Atlantic Basin by imposing an increase in SST but decrease in atmospheric instability in a 3 km resolution modelling study (Radu et.al., 2014). All of these past literature and relationship supported the reduction of TCs' mean RMW in the future climate was at least partly scaled with the increase in SST, despite the model resolution applied in this study was not able to fully resolve the RMW.

8.3 Relationship between variations of RMW percentage change in the future climate to the historical environment conditions

Perhaps the most important historical environment that directly influence the variations of the percentage change in RMW for different TCs in the future climate period was the historical environmental RH. It was found that, by MLR analysis in section 5.2, larger environmental RH

associated with the selected TCs in the past was found to be associated to a smaller RMW decrease in the future climate period. Xu and Wang (2010b) had discussed the effect of environmental RH to the RMW size by idealized experiments. They had found that a moister environment favours more active outer spiral rainband activities, which increased the diabatic heating at the TC outer core. By hydrostatic adjustment, the radial pressure gradient reduced and caused a reduction of radial influx of vertical absolute vorticity near the RMW and an increase in RMW (Xu & Wang, 2010b). Moreover, in this study, it was found that a historically moister SCS favoured inner and outer spiral rainband activities, which generated larger diabatic heating at the outer core. A larger heating away from the center of the TC caused a drop of pressure away from the TC center by hydrostatic adjustment, reduced the radial pressure gradient and the radial wind, thus caused a smaller contraction of RMW for these TCs in a warmed climate. This argument also matches the discussion from Wang (2009) that an increase in diabatic heating at the outer core of a TC increases the RMW (Wang, 2009).

The relationship between the historical atmospheric instability and the difference in the percentage change of RMW for different TCs to the same warming signal should be separated to the historical atmospheric instability near to the center of the TC and at the TC outer core. For historically more unstable atmosphere near to the center of the TC, the unstable atmosphere was more favourable to convection, which should be associated with large heating near the center of the TC and a drop of central pressure. Stronger heating at the eyewall caused an increase in radial advection of AAM across the RMW, therefore contracting the eyewall (Ren, et.al., 2022). However, for historically more unstable atmosphere at the outer core of the TC, stronger convective activities could be found at the outer rainbands due to an increase in the entrainment of moist air from the environment, which caused a drop of surface pressure away from the TC center. The first cases will cause a larger RMW decrease while the second cause will cause a smaller decrease in RMW in the future climate compared to other TCs.

However, as the model resolution of the inner domain chosen in this study could not fully resolve the RMW, one should be reminded that the percentage change in the RMW may not be adequately resolved. Moreover, the model horizontal resolution limited the simulation of the smaller scaled deep convective activities associated with the eyewall and the spiral rainbands. The choice of microphysics schemes also imposed error by underestimating the diabatic heating compared to the WRF double moment 6-class scheme (Chan & Chan 2016). Therefore, future research with finer resolution and better microphysics scheme used should be carried out to confirm the historical environment in controlling the RMW percentage change variations in the future climate.

8.4 Relationship between variations of Vmax percentage change in the future climate to the historical environment conditions

Stepwise regression analysis showed that the historical detrended SST in the SCS was the most important environmental variables in controlling the variations of the percentage change of Vmax for different in the warming experiments. The relationship between the SST and the intensity of a TC was long documented, and the relationship between global warming and the TC intensity were also studied as early as Emanuel (1987). By idealizing a mature TC into a Carnot engine, the potential intensity of a TC was found (equation 7 in section 2.3.1) (Emanuel, 1987). As a TC acquires its energy from the underlying ocean by surface enthalpy flux, higher historical SST environment caused a larger enthalpy flux, which then by non-linear processes related to the potential intensity like the non-linear dependence of drag coefficient of wind speed and surface enthalpy flux, results in an even larger increase in the potential intensity of a TC. This result of larger increase in potential intensity for a warmer SST was also documented in past research (Figure 4 of Camp & Montgomery 2001). As a TC had equal probability in reaching any proportion of its potential intensity, an increase in potential intensity also indicates an increase in the intensity of a TC (Emanuel, 2000). Therefore, historically warmer SST in the SCS region caused an even larger increase in Vmax for these TCs compared to other TCs in the same warming experiment.

Tuleya et.al. (2016) had found that a strong vertical wind shear magnitude can limit the intensification of the TC. By imposing a 10 m s^{-1} vertical wind shear an initially weak TC vortex with 1000 hPa minimum sea level pressure, vortex in a strong vertical wind shear environment cannot intensify to form a TC. They had found that by imposing a vertical wind shear to an initially weak vortex, the warm core at the upper troposphere was displayed from the TC center at the surface, and the TC were then weakened. Therefore, large environmental wind shear inhibits the intensification of a TC. Historically larger vertical wind shear environment can also inhibit the further intensification of the TC at the early stage of development in the warming experiment. Therefore, TCs located in a historically stronger vertical wind shear environment cannot intensity as much as other TCs, resulting in a smaller increase in Vmax for these TCs to the same warming signal compared to other TCs located in a historically weaker vertical wind shear environment, which could intensity more.

Questions arise on whether the larger increase in TCs' intensity found in historically warmer SCS with weaker vertical wind shear magnitude could be related to the increase in the proportion of C4-C5 TCs. Knutson et.al. (2013) had attributed the increase in the frequency of C4-C5 TCs in the North Atlantic Basin to be related with the increase in the SST and the potential intensity in the North Atlantic Basin in future climate. As we have found that TCs in a warmer SST environment had a larger increase in the intensity in the future climate, the frequency of TCs reaching C4-C5 should be larger. However, whether the difference in the responses for different TCs in a warmed climate could be simulated by the previous dynamical downscaling model were not examined before. Therefore, future study can try to link the increase in C4-C5 TCs to the associated historical environment, thus confirming the discussion here.

8.5 Limitations

8.5.1 Experimental Design

Reasons for adopting the regional model experimental design presented in section 3.1, as well as the limitations of this experimental design compared to other methods were discussed in this

section. First, the setup of a regional domain for WRF simulations on 25 historical TCs, and their changes in a thermodynamically warmed climate allowed one to directly compare the intensity and size of real TC cases to their intensity and size in the past. By direct comparison, the risk of TCs brought due to a change in intensity and size in the future climate were better illustrated to the public. Moreover, the importance in studying the variations of TCs' intensity and size among each TC in the future climate could be emphasized because a particular TC could have a change in intensity and size that could deviate significantly from the mean, creating much larger threat to the Peral River Delta Region compared to the threat brought by the mean change in intensity and size. Using real TC cases could provide a more concrete picture on the importance in studying the spread of the TCs' intensity and size changes in terms of hazard mitigation and risk management.

Another advantage on using regional model to study the spread of the TCs' intensity and size changes was it allowed a more comprehensive identification on the possible historical environment that could influence the spread of the TCs' intensity and size changes in the future climate. Careful research on past literatures reveals that this should be the first project to study the spread of the percentage change in TCs' intensity and size in future climate relative to the mean change. By the time of the start of this study, there were no information about which environmental variables could influence the spread of the TC intensity and size changes in the future climate. Therefore, simulating real TC cases in a regional climate model allowed a higher degree of freedom in selecting the historical environmental variables to be used in the MLR analysis. Different environmental variables could be freely chosen and tested to check the relative importance in controlling the spread of TCs' intensity and size changes, therefore helped identifying which environmental conditions were or were not important to control the spread of TC intensity and size changes in future climate. Compared to the use of idealized experiment, which perturb one background environmental condition each time only, using real TCs allowed a more comprehensive test on a variety of background environmental variables.

However, there were some limitations for this experimental design. First, compared to the use of a set of idealized experiments, this model setup introduced more complexity to the variations in TC intensity and size changes. The asymmetry in moisture distribution, background synoptic flow pattern, surrounding topography, as well as case dependent factors could contribute to the variations in TCs intensity and size changes in the future climate, thus introduce more uncertainties in explaining the contribution of each environmental variables quantitatively (Ying & Zhang, 2012). Using idealized experiments, however, enabled a direct perturbation of one historical background environment at a time in the SCS for each idealized vortex, therefore generating less uncertainties and enable quantitative description on how the perturbed historical environmental controlled the TCs' intensity and size changes in the future. Moreover, the choice of using 25 real TCs in this research was inevitably subjected to some natural randomness of the occurrence behind these TCs in the past. Therefore, the uncertainties in projecting the spread of the TCs intensity and size using real TCs were larger than that of using idealized experiments. However, for carrying out idealized experiments, it was difficult to decide which environmental variable to be perturbed, especially when there were no past literatures focusing on this problem. Despite the fact that there were some studies on the environmental control of TC intensity and size climatologically, one could not assume that these environmental conditions directly caused the spread of the change in TCs' intensity and size in a long-term warming background in the future. Therefore, idealized experiments were not chosen as the model design adopted in this study.

Nevertheless, several idealized experiments could be carried out in the future by perturbing the background environment, like the background RH and outer wind speed before superimposing PGW signals onto some idealized vortices. This should be done in future studies to confirm the results in this study, as well as to better quantify how the historical environment controls the spread of TCs' intensity and size change in the future climate. Moreover, another method to confirm the statistical relationship established here could be performing global dynamical downscaling experiments. By comparing TCs in similar background environment in the simulated present and future climate with

a detrended background, statistical relationship between the percentage change of TCs' intensity and size under different background environment can then be confirmed by using larger dataset.

Another limitation brought by the experimental design was the choice of the 25 TCs. Questions arise on whether all TCs recorded that had entered the SCS in the past could be included in the study to increase the robustness of the statistical relationship established by the MLR analysis. However, due to the limitation brought by the computational resources, only 25 TCs were chosen to be simulated in their historical environment and 4 warming experiments. Future studies can consider including more TCs in the SCS to enhance the statistical robustness of the slope between the historical environment and the variations in the TCs' intensity and size changes compared to the mean in the future climate. Moreover, including more TCs associated with different phase of the natural climate modes can reduce possible sampling bias by including a more comprehensive representation of different source of background environmental variabilities associated with variating phase and magnitude of different timescale climate modes. Despite only 14 TCs were adopted in the MLR analysis in this study, the results had passed the statistically significant test that the slopes were significantly different to 0 in 90% CI for some important environmental conditions, assuming all the warming experiments were independent to each other, as presented in APPENDIX VI. Therefore, as a start on studying the relationship between the historical environment and the spread of the change in TCs intensity and size, the statistical relationship established should be robust enough.

8.5.2 Model Horizontal Resolution in Simulating the Responses of RMW

A 3 km horizontal resolution inner domain was setup to cover the whole northern part of the SCS. The rationale behind the use of 3 km as the horizontal resolution of the inner domain was to balance the ability to simulate the intensity of the TCs compared to the best track data and the limitation of the computational resources. Despite the fact that the simulated Vmax of the TCs in the control run can be compared to the best track data for some of the TCs (APPENDIX V for details), the inner structure of the TCs were not well resolved. Walters (2000) had proposed that the minimum

wavelength of a wave that could be fully resolved in terms of the phase and the spatial derivatives were $10\Delta x$, where Δx is the horizontal resolution of the numerical model. Therefore, in the configuration of this project, only structures that were larger than 30 km were fully resolved. As the modelled decrease in RMW in the future climate were only approximately 3-6 km, which was only 1-2 grids, the change in RMW were not resolved. Therefore, the model outputted percentage changes of RMW in future climate in this study should be limited by the coarse resolution of the inner domain.

Moreover, Gentry and Lackmann (2010) had tested the sensitivity of simulated size of RMW to the horizontal resolution of the model, and found that the simulated RMW did not converge even using a horizontal resolution as fine as 1 km. This was because the physical processes that could influences the size of the RMW were not resolved. For example, in 1 km resolution, only the largest realistic updraft and downdraft in the eyewall were resolved, which then caused an error in the prediction of diabatic heating along the convective bands and thus the contraction of RMW (Shapiro & Willoughby, 1982; Gentry & Lackmann, 2010). Moreover, as the size of the RMW were found to be positively correlated to the angle of the vertical eyewall tilting, the relatively coarse resolution in the inner domain may not be able to resolve the change in the eyewall tilt, therefore causing uncertainties in predicting the change in RMW in the future climate (Stern & Nolan, 2009). Ren et.al., (2022) had performed idealized simulations of prescribed vortex in different environmental SST background, with a horizontal resolution as fine as 60 m. They had found that the RMW converged in a model horizontal resolution smaller than 500 m for different background SST, despite the fact that the model integration for finer domain were not start at the beginning of the simulation. Moreover, they had not investigated the ability of resolving the physical processes that could affect the size of the RMW in fine resolution domain. Therefore, future studies of horizontal resolution finer than 500 m should be used to investigate whether it can fully resolve the possible changes in RMW in the future climate, and to confirm the results here.

8.5.3 Sensitivity of the results to the choice of numerical model and the physics scheme

By far, all the PGW experiments were carried out by the WRF-ARW version 3.7, despite using 2 different set of computer hardware for the initial 125 PGW experiments and the H_DIA experiments. The sensitivity of the results to the numerical model chosen, as well as the physics scheme were not yet tested. Tuleya et.al. (2016) had compared the relationship between the TC intensity with the atmospheric temperature profile, surface temperature and the vertical wind shear by a numerical simulation using the GFDL 2014 version to the previous study, which had used the GFDL 2000 version of a different physics schemes and horizontal resolution (Shen et.al., 2000; Tuleya et.al., 2016). They had found a similar relationship between the TC intensity with the SST and the vertical wind shear between the 2 versions of GFDL model. Hill and Lackmann (2009) had also found that a different choice of planetary boundary layer scheme in the WRF model results in different surface heat flux magnitude and spatial distribution, thus a difference in predicted maximum intensity of a TC by 10 m s^{-1} (Hill & Lackmann, 2009). Moreover, Chan and Chan (2016) had found a sensitivity of simulated TC intensity and size to the choice of microphysics scheme (Chan & Chan, 2016). Therefore, multiple experiments should be performed by other numerical model, such as the GFDL model or the mesoscale model (MM5) to check the sensitivity between the MLR results to the choice of model. Moreover, sensitivity test should be carried out to test the sensitivity of MLR results to the physics schemes chosen, such as the planetary boundary layer scheme and the cloud microphysics schemes to yield a more robust results across different models and physics schemes.

9. Conclusion

Tropical cyclones were one of the most devastating nature hazards that can harm human live and properties (Emanuel, 1987). Moreover, accurate projection on the changes in the TC intensity and size distribution in a warmed future climate enables a better hazard mitigation in coastal regions like the Peral Rivel Delta in the South China in the future. In this project, 25 TCs which had entered the SCS in the past were modelled by the WRF-ARW version 3.7, with an inner most horizontal resolution of 3 km. Changes of these TCs in the climate period of 2075-2099 and 2036-2065 relative to the historical climate following the RCP8.5 and RCP4.5 emission scenarios from the CMIP5 project were investigated by PGW experiments.

The aim of this project is to investigate the mean change and variations in TC intensity and size in the SCS in a total of 4 different future climate periods and emission scenarios. Across the better simulated 14 TCs and a total of 70 simulations, it had been found that TC mean intensity in terms of Vmax in the SCS were projected to have an increase of 8.6% by a 2 °C increase in surface temperature. Moreover, results showed a decrease in mean RMW by 7.9% and a slightly increase in mean R17 by 3% of the TCs in the SCS for a 2 °C increase in surface temperature. PGW results also showed large variations of the projected percentage change of Vmax, RMW and R17 in the SCS among each TC in each warmed climate period.

The hypothesis that the variations in the projected percentage changes in Vmax, RMW and R17 in a warmed climate relative to the control for different TCs to the same PGW signal are related to the historical environment associated with the selected TCs were tested by the MLR and stepwise regression analysis. Results showed the variations of the percentage changes in Vmax in a warmed climate in SCS for different TCs were related positively to the historical detrended SST and negatively to the vertical wind shear magnitude. Moreover, the variations of the percentage change in the RMW for different TCs in future climate in the SCS in each warming scenario were found to be correlated to the historical environmental RH positively. Also, the variation of the change in R17

in the SCS in a warmed climate for each TC were related to the historical environmental RH and the historical outer wind speed variations among these TCs in the SCS. Historically wetter and windier SCS caused a larger increase in R17 for these TCs in the warmed climate.

EPV analysis were performed to diagnose the effects of different historical environmental mid-tropospheric RH to the difference in the percentage change of R17 for TC Mary (1960) and TC Nuri (2008) in the far future era under RCP8.5 emission scenario. It was found that a historically moister SCS were more favourable for deep convective activities associated with a TC in a warmed climate than a TC located in a historically drier SCS. Stronger and more wide-spread deep convective activities were developed associated with the TCs' inner spiral rainbands for TC Mary (1960), which was located in a historically moister SCS. Associated with these enhanced convective activities were an enhancement of diabatic heating rate, which produced more diabatic EPV at the inner spiral rainbands. The locally produced EPV at the inner spiral rainbands, as well as the EPV swirl into the central EPV tower of TC Mary (1960) strengthened and expanded the TC EPV tower, therefore expanding its R17 in a warmed climate. Opposite results were found for TC Nuri (2008), which was located in a historically drier SCS. Drier SCS caused similar convective activities for TC Nuri (2008) in the warming run and the control run, which produced similar amount of diabatic EPV by similar strength of diabatic heating, resulting in similar distribution of EPV and a nearly constant R17 in the warming experiment and the control run.

AAM budget analysis were carried out to diagnose the influence of outer wind speed to the difference in the percentage change of R17 for different TCs to the same warming signal. It had been found that a larger historical outer wind speed, in particular stronger southwesterlies and northwesterlies in the SCS, contributed to a larger increase in radial influx of AAM. As more AAM could be transported into the R17 of these TCs in a warmed climate, the radial advection of AAM near the R17 increased in the warming runs. Then, the local AAM tendency was enhanced, which expanded the R17 of these TCs in the warmed climate. However, despite an increase in the radial

wind for some TCs like TC Warren (1988) in the warmed climate experiment, there were no increase in radial advection of AAM in the warmed climate. This was because these TCs were embedded in a historically weaker background AAM environment. Weaker outer wind speed environment limited the transport of AAM despite an increase in inward radial circulation. There were no more AAM that could be transported into the R17 of these TCs compared to the TCs embedded in a historically stronger background AAM environment. Therefore, the local AAM tendency for these TCs remained the same in the warmed climate and the control run, and the R17 were similar in the present and the future climate. The background AAM act as a limiting factor in controlling the radial AAM influx in a warmed climate.

Results from this study had confirmed that historical environmental conditions can lead to a variation of TC Vmax, RMW and R17 changes to a similar PGW signal. Therefore, even though the anthropogenically induced changes in different climate modes like the ENSO or the PDO were not considered in the PGW experiment, the natural climate variability of different timescales can also cause variations in the response of TCs projected change in intensity and size in future climate among each TC. As the relationship between different environmental condition to the variations in the percentage change in TCs intensity and size were established, it is proposed that, by carefully selecting TCs that can represent a wide range of realistic environmental conditions in the present-day climate, the distribution of the percentage change of Vmax, RMW and R17 in the future climate under different climate modes can be better represented. After that, confidence interval of the regression model relating the surface warming to the percentage change in TC intensity and size could be established with physical background. The confidence interval of the regression model can be served as an educated guess of TCs' mean intensity and size changes in the future climate, which represented the uncertainties in TC intensity and size prediction due to natural variability of different climate modes. Moreover, prediction intervals could be established in order to predict future TCs' intensity and size under different naturally variating climate modes. Therefore, uncertainties in predicting future TCs' intensity and size changes under a warming background and different natural climate

modes could be better understood, therefore benefitting individual TC risk assessment and hazard prediction in a warmed climate.

Despite insight were drawn to the uncertainties in TCs' intensity and size prediction under naturally variated climate modes in different timescale, future researches should also be carried out to raise the confidence of the established statistical relationship between TCs intensity and size percentage change and the related natural climate variability that controls the background environment by a different experimental design such as by performing idealized experiments. Moreover, the robustness of the percentage change in the RMW of different TCs in a warmed climate should be confirmed by finer resolution numerical modelling experiments. The hypothesis of relating the contraction of RMW to the radial wind and the vertical absolute vorticity gradient, as well as the heating rate at the eyewall in a warmed climate were left to be studied in the future. The relationship between the historical RH and the variations of the percentage change of RMW in future climate to the same warming signal should also be analysed. Despite the limitations in this research, it is hoped that this project provides insight in reducing TCs' intensity and size projection uncertainties in a warmed climate due to natural variating climate modes, like the interannual and interdecadal variations, therefore contributing to future TC risk assessment and hazard mitigation policy making for coastal regions.

10. Reference

- Atkinson, G. D., & Holliday, C. R. (1977). Tropical cyclone minimum sea level pressure/maximum sustained wind relationship for the western North Pacific. *Monthly Weather Review*, 105(4), 421-427.
- Bender, M. A., & Ginis, I. (2000). Real-case simulations of hurricane–ocean interaction using a high-resolution coupled model: Effects on hurricane intensity. *Monthly Weather Review*, 128(4), 917-946.
- Camp, J. P., & Montgomery, M. T. (2001). Hurricane maximum intensity: Past and present. *Monthly Weather Review*, 129(7), 1704-1717.
- Chan, K. T., & Chan, J. C. (2012). Size and strength of tropical cyclones as inferred from QuikSCAT data. *Monthly weather review*, 140(3), 811-824.
- Chan, K. T., & Chan, J. C. (2014). Impacts of initial vortex size and planetary vorticity on tropical cyclone size. *Quarterly Journal of the Royal Meteorological Society*, 140(684), 2235-2248.
- Chan, K. T., & Chan, J. C. (2015). Global climatology of tropical cyclone size as inferred from QuikSCAT data. *International Journal of Climatology*, 35(15), 4843-4848.
- Chan, K. T., & Chan, J. C. (2015). Impacts of vortex intensity and outer winds on tropical cyclone size. *Quarterly Journal of the Royal Meteorological Society*, 141(687), 525-537.
- Chan, K. T., & Chan, J. C. (2016). Sensitivity of the simulation of tropical cyclone size to microphysics schemes. *Advances in Atmospheric Sciences*, 33(9), 1024-1035.
- Chavas, D. R., & Emanuel, K. A. (2010). A QuikSCAT climatology of tropical cyclone size. *Geophysical Research Letters*, 37(18).
- Chavas, D. R., Lin, N., Dong, W., & Lin, Y. (2016). Observed tropical cyclone size revisited. *Journal of Climate*, 29(8), 2923-2939.

Chavas, D. R., Reed, K. A., & Knaff, J. A. (2017). Physical understanding of the tropical cyclone wind-pressure relationship. *Nature communications*, 8(1), 1-11.

Chen, Y., & Yau, M. K. (2001). Spiral bands in a simulated hurricane. Part I: Vortex Rossby wave verification. *Journal of the Atmospheric sciences*, 58(15), 2128-2145.

Choy, C. W., Lau, D. S., & He, Y. (2020a). Super typhoons Hato (1713) and Mangkhut (1822), part I: analysis of maximum intensity and wind structure. *Weather*.

Choy, C. W., Lau, D. S., & He, Y. (2020b). Super typhoons Hato (1713) and Mangkhut (1822), part II: challenges in forecasting and early warnings. *Weather*.

Christensen, J. H., Kanikicharla, K. K., Aldrian, E., An, S. I., Cavalcanti, I. F. A., de Castro, M., ... & Zou, L. (2013). Climate phenomena and their relevance for future regional climate change. In Climate change 2013 the physical science basis: Working group I contribution to the fifth assessment report of the intergovernmental panel on climate change (pp. 1217-1308). Cambridge University Press.

Corbosiero, K. L., Molinari, J., & Black, M. L. (2005). The structure and evolution of Hurricane Elena (1985). Part I: Symmetric intensification. *Monthly weather review*, 133(10), 2905-2921.

Corbosiero, K. L., Molinari, J., Aiyyer, A. R., & Black, M. L. (2006). The structure and evolution of Hurricane Elena (1985). Part II: Convective asymmetries and evidence for vortex Rossby waves. *Monthly weather review*, 134(11), 3073-3091.

Dudhia, J. (1989). Numerical study of convection observed during the winter monsoon experiment using a mesoscale two-dimensional model. *Journal of Atmospheric Sciences*, 46(20), 3077-3107.

Emanuel, K. (2000). A statistical analysis of tropical cyclone intensity. *Monthly weather review*, 128(4), 1139-1152.

Emanuel, K. (2003). Tropical cyclones. *Annual review of earth and planetary sciences*, 31(1), 75-104.

Emanuel, K. A. (1987). The dependence of hurricane intensity on climate. *Nature*, 326(6112), 483-485.

Feng, J., Wei, T., Dong, W., Wu, Q., & Wang, Y. (2014). CMIP5/AMIP GCM simulations of East Asian summer monsoon. *Advances in Atmospheric Sciences*, 31(4), 836-850.

Frank, W. M. (1977). The structure and energetics of the tropical cyclone I. Storm structure. *Mon. Wea. Rev*, 105(1), 1.

Frank, W. M., & Ritchie, E. A. (2001). Effects of vertical wind shear on the intensity and structure of numerically simulated hurricanes. *Monthly weather review*, 129(9), 2249-2269.

Fu, H., Wang, X., Chu, P. C., Zhang, X., Han, G., & Li, W. (2014). Tropical cyclone footprint in the ocean mixed layer observed by Argo in the Northwest Pacific. *Journal of Geophysical Research: Oceans*, 119(11), 8078-8092.

Gallina, G. M., & Velden, C. S. (2002). 3C. 5 Environmental vertical wind shear and tropical cyclone intensity change utilizing enhanced satellite derived wind information. *Atlantic*, 58, 12.

Gentry, M. S., & Lackmann, G. M. (2010). Sensitivity of simulated tropical cyclone structure and intensity to horizontal resolution. *Monthly Weather Review*, 138(3), 688-704.

Guilyardi, E., Capotondi, A., Lengaigne, M., Thual, S., & Wittenberg, A. T. (2020). ENSO modeling: History, progress, and challenges. *El Niño Southern Oscillation in a changing climate*, 199-226.

Gutmann, E. D., Rasmussen, R. M., Liu, C., Ikeda, K., Bruyere, C. L., Done, J. M., ... & Veldore, V. (2018). Changes in hurricanes from a 13-yr convection-permitting pseudo-global warming simulation. *Journal of Climate*, 31(9), 3643-3657.

Hawkins, J. D., & Helveston, M. (2004, May). Tropical cyclone multiple eyewall characteristics. In *Preprints, 26th Conf. on Hurricanes and Tropical Meteorology, Miami, FL, Amer. Meteor. Soc. P* (Vol. 1).

Held, I. M., & Soden, B. J. (2006). Robust responses of the hydrological cycle to global warming. *Journal of climate*, 19(21), 5686-5699.

Hersbach, H., Bell, B., Berrisford, P., Biavati, G., Horányi, A., Muñoz Sabater, J., Nicolas, J., Peubey, C., Radu, R., Rozum, I., Schepers, D., Simmons, A., Soci, C., Dee, D., Thépaut, J-N. (2018): ERA5 hourly data on single levels from 1979 to present. Copernicus Climate Change Service (C3S) Climate Data Store (CDS). (Accessed on < 29-08-2020 >), 10.24381/cds.adbb2d47

Hill, K. A., & Lackmann, G. M. (2009). Influence of environmental humidity on tropical cyclone size. *Monthly Weather Review*, 137(10), 3294-3315.

Hill, K. A., & Lackmann, G. M. (2011). The impact of future climate change on TC intensity and structure: A downscaling approach. *Journal of Climate*, 24(17), 4644-4661.

Holland, G. J., & Merrill, R. T. (1984). On the dynamics of tropical cyclone structural changes. *Quarterly Journal of the Royal Meteorological Society*, 110(465), 723-745.

Hong, S. Y., Noh, Y., & Dudhia, J. (2006). A new vertical diffusion package with an explicit treatment of entrainment processes. *Monthly weather review*, 134(9), 2318-2341.

Irish, J. L., Resio, D. T., & Ratcliff, J. J. (2008). The influence of storm size on hurricane surge. *Journal of Physical Oceanography*, 38(9), 2003-2013.

Jiménez, P. A., Dudhia, J., González-Rouco, J. F., Navarro, J., Montávez, J. P., & García-Bustamante, E. (2012). A revised scheme for the WRF surface layer formulation. *Monthly weather review*, 140(3), 898-918.

Kanada, S., Wada, A., & Sugi, M. (2013). Future changes in structures of extremely intense tropical cyclones using a 2-km mesh nonhydrostatic model. *Journal of climate*, 26(24), 9986-10005.

Kepert, J. D. (2010). Tropical cyclone structure and dynamics. *Global perspectives on Tropical cyclones: from science to mitigation*, 3-53.

Kimball, S. K., & Mulekar, M. S. (2004). A 15-year climatology of North Atlantic tropical cyclones. Part I: Size parameters. *Journal of Climate*, 17(18), 3555-3575.

Klotzbach, P. J., Bowen, S. G., Pielke, R., & Bell, M. (2018). Continental US hurricane landfall frequency and associated damage: Observations and future risks. *Bulletin of the American Meteorological Society*, 99(7), 1359-1376.

Knaff, J. A., & Zehr, R. M. (2007). Reexamination of tropical cyclone wind-pressure relationships. *Weather and Forecasting*, 22(1), 71-88.

Knaff, J. A., Sampson, C. R., & Chirokova, G. (2017). A global statistical-dynamical tropical cyclone wind radii forecast scheme. *Weather and Forecasting*, 32(2), 629-644.

Knapp, K. R., Kruk, M. C., Levinson, D. H., Diamond, H. J., & Neumann, C. J. (2010). The international best track archive for climate stewardship (IBTrACS) unifying tropical cyclone data. *Bulletin of the American Meteorological Society*, 91(3), 363-376..

Knapp, K. R., Velden, C. S., & Wimmers, A. J. (2018). A global climatology of tropical cyclone eyes. *Monthly Weather Review*, 146(7), 2089-2101.

Knutson, T. R., Sirutis, J. J., Vecchi, G. A., Garner, S., Zhao, M., Kim, H. S., ... & Villarini, G. (2013). Dynamical downscaling projections of twenty-first-century Atlantic hurricane activity: CMIP3 and CMIP5 model-based scenarios. *Journal of Climate*, 26(17), 6591-6617.

Knutson, T. R., Sirutis, J. J., Zhao, M., Tuleya, R. E., Bender, M., Vecchi, G. A., ... & Chavas, D. (2015). Global projections of intense tropical cyclone activity for the late twenty-first century

from dynamical downscaling of CMIP5/RCP4.5 scenarios. *Journal of Climate*, 28(18), 7203-7224.

Knutson, T., Camargo, S. J., Chan, J. C., Emanuel, K., Ho, C. H., Kossin, J., ... & Wu, L. (2020).

Tropical cyclones and climate change assessment: Part II: Projected response to anthropogenic warming. *Bulletin of the American Meteorological Society*, 101(3), E303-E322.

Knutti, R., & Sedláček, J. (2013). Robustness and uncertainties in the new CMIP5 climate model projections. *Nature climate change*, 3(4), 369-373.

Kurihara, Y., Bender, M. A., & Ross, R. J. (1993). An initialization scheme of hurricane models by vortex specification. *Monthly weather review*, 121(7), 2030-2045.

Lackmann, G. M. (2002). Cold-frontal potential vorticity maxima, the low-level jet, and moisture transport in extratropical cyclones. *Monthly Weather Review*, 130(1), 59-74.

Lee, B. E., & Wills, J. (2002). Vulnerability of fully glazed high-rise buildings in tropical cyclones. *Journal of architectural engineering*, 8(2), 42-48.

Leroux, M. D., Wood, K., Elsberry, R. L., Cayanan, E. O., Hendricks, E., Kucas, M., ... & Yu, Z. (2018). Recent advances in research and forecasting of tropical cyclone track, intensity, and structure at landfall. *Tropical Cyclone Research and Review*, 7(2), 85-105.

Lin, I. I., Black, P., Price, J. F., Yang, C. Y., Chen, S. S., Lien, C. C., ... & D'Asaro, E. A. (2013). An ocean coupling potential intensity index for tropical cyclones. *Geophysical Research Letters*, 40(9), 1878-1882.

Lin, Y., Zhao, M., & Zhang, M. (2015). Tropical cyclone rainfall area controlled by relative sea surface temperature. *Nature Communications*, 6(1), 1-7.

- Ling, Z., Wang, Y., Wang, G., & He, H. (2020). Impact of intraseasonal oscillations on the activity of tropical cyclones in summer over the South China Sea: Nonlocal tropical cyclones. *Frontiers in Earth Science*, 8, 622.
- Liu, K. S., & Chan, J. C. (2008). Interdecadal variability of western North Pacific tropical cyclone tracks. *Journal of Climate*, 21(17), 4464-4476.
- Lonfat, M., Marks Jr, F. D., & Chen, S. S. (2004). Precipitation distribution in tropical cyclones using the Tropical Rainfall Measuring Mission (TRMM) Microwave Imager: A global perspective. *Monthly Weather Review*, 132(7), 1645-1660.
- Ma, C., Peng, M., Li, T., Sun, Y., Liu, J., & Bi, M. (2019). Effects of background state on tropical cyclone size over the Western North Pacific and Northern Atlantic. *Climate Dynamics*, 52(7), 4143-4156.
- McDonald, R. E., Bleaken, D. G., Cresswell, D. R., Pope, V. D., & Senior, C. A. (2005). Tropical storms: representation and diagnosis in climate models and the impacts of climate change. *Climate Dynamics*, 25(1), 19-36.
- Mlawer, E. J., Taubman, S. J., Brown, P. D., Iacono, M. J., & Clough, S. A. (1997). Radiative transfer for inhomogeneous atmospheres: RRTM, a validated correlated-k model for the longwave. *Journal of Geophysical Research: Atmospheres*, 102(D14), 16663-16682.
- Montgomery, M. T., & Kallenbach, R. J. (1997). A theory for vortex Rossby-waves and its application to spiral bands and intensity changes in hurricanes. *Quarterly Journal of the Royal Meteorological Society*, 123(538), 435-465.
- Mukul Tewari, N. C. A. R., Tewari, M., Chen, F., Wang, W., Dudhia, J., LeMone, M., ... & Cuenca, R. H. (2004, January). Implementation and verification of the unified NOAH land surface model in the WRF model (Formerly Paper Number 17.5). In *Proceedings of the 20th*

Conference on Weather Analysis and Forecasting/16th Conference on Numerical Weather Prediction, Seattle, WA, USA (Vol. 14).

Murakami, H. (2014). Tropical cyclones in reanalysis data sets. *Geophysical Research Letters*, 41(6), 2133-2141.

Needham, H. F., & Keim, B. D. (2014). An empirical analysis on the relationship between tropical cyclone size and storm surge heights along the US Gulf Coast. *Earth Interactions*, 18(8), 1-15.

Nicholls, A. (2014). Confidence limits, error bars and method comparison in molecular modeling. Part 1: the calculation of confidence intervals. *Journal of computer-aided molecular design*, 28(9), 887-918.

N-Krishnamurti, T., Stefanova, L., & Misra, V. (2013). *Tropical Meteorology: An Introduction*. Springer.

Palmen, E. (1948). On the formation and structure of tropical hurricanes. *Geophysica*, 3(1), 26-38.

Peduzzi, P., Chatenoux, B., Dao, H., De Bono, A., Herold, C., Kossin, J., ... & Nordbeck, O. (2012). Global trends in tropical cyclone risk. *Nature climate change*, 2(4), 289-294.

Poli, P., Hersbach, H., Dee, D. P., Berrisford, P., Simmons, A. J., Vitart, F., ... & Fisher, M. (2016). ERA-20C: An atmospheric reanalysis of the twentieth century. *Journal of Climate*, 29(11), 4083-4097.

Powell, M. D., & Reinhold, T. A. (2007). Tropical cyclone destructive potential by integrated kinetic energy. *Bulletin of the American Meteorological Society*, 88(4), 513-526.

Powell, M. D., Vickery, P. J., & Reinhold, T. A. (2003). Reduced drag coefficient for high wind speeds in tropical cyclones. *Nature*, 422(6929), 279-283.

Radu, R., Toumi, R., & Phau, J. (2014). Influence of atmospheric and sea surface temperature on the size of hurricane Catarina. *Quarterly Journal of the Royal Meteorological Society*, 140(682), 1778-1784.

Raymond, D. J. (1992). Nonlinear balance and potential-vorticity thinking at large Rossby number. *Quarterly Journal of the Royal Meteorological Society*, 118(507), 987-1015.

Ren, H., Dudhia, J., & Li, H. (2022). The size characteristics and physical explanation for the radius of maximum wind of hurricanes. *Atmospheric Research*, 106313.

Rogers, E., Black, T., Ferrier, B., Lin, Y., Parrish, D., & DiMego, G. (2001). Changes to the NCEP Meso Eta Analysis and Forecast System: Increase in resolution, new cloud microphysics, modified precipitation assimilation, modified 3DVAR analysis. *NWS Technical Procedures Bulletin*, 488, 15.

Sampson, C. R., & Knaff, J. A. (2015). A consensus forecast for tropical cyclone gale wind radii. *Weather and Forecasting*, 30(5), 1397-1403.

Sanderson, B. M., Shell, K. M., & Ingram, W. (2010). Climate feedbacks determined using radiative kernels in a multi-thousand member ensemble of AOGCMs. *Climate dynamics*, 35(7), 1219-1236.

Schubert, W. H., & Hack, J. J. (1982). Inertial stability and tropical cyclone development. *Journal of the Atmospheric Sciences*, 39(8), 1687-1697.

Shapiro, L. J., & Willoughby, H. E. (1982). The response of balanced hurricanes to local sources of heat and momentum. *Journal of the Atmospheric Sciences*, 39(2), 378-394.

Shen, W., Tuleya, R. E., & Ginis, I. (2000). A sensitivity study of the thermodynamic environment on GFDL model hurricane intensity: Implications for global warming. *Journal of Climate*, 13(1), 109-121.

Simpson, R. H., & Saffir, H. (1974). The hurricane disaster potential scale. *Weatherwise*, 27(8), 169.

Skamarock, W. C., Klemp, J. B., Dudhia, J., Gill, D. O., Barker, D., Duda, M. G., ... Powers, J. G. (2008). A Description of the Advanced Research WRF Version 3 (No. NCAR/TN-475+STR). University Corporation for Atmospheric Research. doi:10.5065/D68S4MVH

Srinivas, D., & Bhaskar Rao, D. V. (2014). Implications of vortex initialization and model spin-up in tropical cyclone prediction using Advanced Research Weather Research and Forecasting Model. *Natural hazards*, 73(2), 1043-1062.

Stephens, G. L. (1990). On the relationship between water vapor over the oceans and sea surface temperature. *Journal of Climate*, 3(6), 634-645.

Stern, D. P., & Nolan, D. S. (2009). Reexamining the vertical structure of tangential winds in tropical cyclones: Observations and theory. *Journal of the atmospheric sciences*, 66(12), 3579-3600.

Taylor, K. E., Stouffer, R. J., & Meehl, G. A. (2012). An overview of CMIP5 and the experiment design. *Bulletin of the American meteorological Society*, 93(4), 485-498.

Tory, K. J., Kepert, J. D., Sippel, J. A., & Nguyen, C. M. (2012). On the use of potential vorticity tendency equations for diagnosing atmospheric dynamics in numerical models. *Journal of the atmospheric sciences*, 69(3), 942-960.

Tsai, H. C., & Elsberry, R. L. (2014). Applications of situation-dependent intensity and intensity spread predictions based on a weighted analog technique. *Asia-Pacific Journal of Atmospheric Sciences*, 50(4), 507-518.

Tuleya, R. E., Bender, M., Knutson, T. R., Sirutis, J. J., Thomas, B., & Ginis, I. (2016). Impact of upper-tropospheric temperature anomalies and vertical wind shear on tropical cyclone evolution using an idealized version of the operational GFDL hurricane model. *Journal of the Atmospheric Sciences*, 73(10), 3803-3820.

Wallace, J. M., & Hobbs, P. V. (2006). *Atmospheric science: an introductory survey* (Vol. 92). Elsevier.

Walsh, K. J., Camargo, S. J., Vecchi, G. A., Daloz, A. S., Elsner, J., Emanuel, K., ... & Henderson, N. (2015). Hurricanes and climate: The US CLIVAR working group on hurricanes. *Bulletin of the American Meteorological Society*, 96(6), 997-1017.

Walters, M. K. (2000). Comments on “The differentiation between grid spacing and resolution and their application to numerical modeling”. *Bulletin of the American Meteorological Society*, 81(10), 2475-2477.

Wang, C. C., Lin, B. X., Chen, C. T., & Lo, S. H. (2015). Quantifying the effects of long-term climate change on tropical cyclone rainfall using a cloud-resolving model: Examples of two landfall typhoons in Taiwan. *Journal of Climate*, 28(1), 66-85.

Wang, C., Wang, W., Wang, D., & Wang, Q. (2006). Interannual variability of the South China sea associated with El Niño. *Journal of Geophysical Research: Oceans*, 111(C3).

Wang, Y. (2002). Vortex Rossby waves in a numerically simulated tropical cyclone. Part I: Overall structure, potential vorticity, and kinetic energy budgets. *Journal of the atmospheric sciences*, 59(7), 1213-1238.

Wang, Y. (2008). Rapid filamentation zone in a numerically simulated tropical cyclone. *Journal of the atmospheric sciences*, 65(4), 1158-1181.

Wang, Y. (2008). Structure and formation of an annular hurricane simulated in a fully compressible, nonhydrostatic model—TCM4. *Journal of the atmospheric sciences*, 65(5), 1505-1527.

Wang, Y. (2009). How do outer spiral rainbands affect tropical cyclone structure and intensity?. *Journal of the Atmospheric Sciences*, 66(5), 1250-1273.

Wang, Y. Q., & Wu, C. C. (2004). Current understanding of tropical cyclone structure and intensity

changes—a review. *Meteorology and Atmospheric Physics*, 87(4), 257-278.

Weatherford, C. L., & Gray, W. M. (1988). Typhoon structure as revealed by aircraft reconnaissance.

Part II: Structural variability. *Mon. Wea. Rev*, 116(5), 1044-1056.

Wehner, M., Reed, K. A., Stone, D., Collins, W. D., & Bacmeister, J. (2015). Resolution dependence

of future tropical cyclone projections of CAM5. 1 in the US CLIVAR Hurricane Working

Group idealized configurations. *Journal of Climate*, 28(10), 3905-3925.

Wilks, D. S. (2011). Statistical methods in the atmospheric sciences (Vol. 100). Academic press.

Willoughby, H. E. (1990). Gradient balance in tropical cyclones. *Journal of the Atmospheric*

Sciences, 47(2), 265-274.

Willoughby, H. E. (1990). Temporal changes of the primary circulation in tropical cyclones. *Journal*

of Atmospheric Sciences, 47(2), 242-264.

Willoughby, H. E. (1998). Tropical cyclone eye thermodynamics. *Monthly weather review*, 126(12),

3053-3067.

Willoughby, H. E., Clos, J. A., & Shoreibah, M. G. (1982). Concentric eye walls, secondary wind

maxima, and the evolution of the hurricane vortex. *Journal of Atmospheric Sciences*, 39(2),

395-411.

Wong, M. L., & Chan, J. C. (2004). Tropical cyclone intensity in vertical wind shear. *Journal of the*

atmospheric sciences, 61(15), 1859-1876.

Wu, L., Su, H., Fovell, R. G., Wang, B., Shen, J. T., Kahn, B. H., ... & Jiang, J. H. (2012). Relationship

of environmental relative humidity with North Atlantic tropical cyclone intensity and

intensification rate. *Geophysical research letters*, 39(20).

- Xu, J., & Wang, Y. (2010a). Sensitivity of tropical cyclone inner-core size and intensity to the radial distribution of surface entropy flux. *Journal of the atmospheric sciences*, 67(6), 1831-1852.
- Xu, J., & Wang, Y. (2010b). Sensitivity of the simulated tropical cyclone inner-core size to the initial vortex size. *Monthly Weather Review*, 138(11), 4135-4157.
- Yamada, Y., Satoh, M., Sugi, M., Kodama, C., Noda, A. T., Nakano, M., & Nasuno, T. (2017). Response of tropical cyclone activity and structure to global warming in a high-resolution global nonhydrostatic model. *Journal of Climate*, 30(23), 9703-9724.
- Ying, Y., & Zhang, Q. (2012). A modeling study on tropical cyclone structural changes in response to ambient moisture variations. *Journal of the Meteorological Society of Japan. Ser. II*, 90(5), 755-770.
- Zhan, R., Wang, Y., & Ying, M. (2012). Seasonal forecasts of tropical cyclone activity over the western North Pacific: A review. *Tropical Cyclone Research and Review*, 1(3), 307-324.
- Zhao, H., & Wang, C. (2019). On the relationship between ENSO and tropical cyclones in the western North Pacific during the boreal summer. *Climate Dynamics*, 52(1), 275-288.

APPENDIX I

Selected CMIP5 Models

APPENDIX Table 1. 31 CMIP5 Models used in RCP8.5 PGW Experiments

Model Name	Modelling Center	Institution
ACCESS1.0	CSIRO-BOM	Commonwealth Scientific and Industrial Research Organisation, Australia (CSIRO) and Bureau of Meteorology, Australia (BOM)
ACCESS1.3	CSIRO-BOM	Commonwealth Scientific and Industrial Research Organisation, Australia (CSIRO) and Bureau of Meteorology, Australia (BOM)
BCC-CSM1.1	BCC	Beijing Climate Center, China Meteorological Administration
BNU-ESM	GCESS	College of Global Change and Earth System Science, Beijing Normal University
CanESM2	CCCma	Canadian Centre for Climate Modelling and Analysis
CCSM4	NCAR	National Center for Atmospheric Research
CESM1-BGC	NSF-DOE-NCAR	National Science Foundation, Department of Energy, National Center for Atmospheric Research
CESM1-CAM5	NSF-DOE-NCAR	National Science Foundation, Department of Energy, National Center for Atmospheric Research
CMCC-CM	CMCC	Centro Euro-Mediterraneo per i Cambiamenti Climatici
CNRM-CM5	CNRM-CERFACS	Centre National de Recherches Meteorologiques / Centre European de Recherche et Formation Avancees en Calcul Scientifique
CSIRO-Mk3-6-0	CSIRO-QCCCE	Commonwealth Scientific and Industrial Research Organisation in collaboration with the Queensland Climate Change Centre of Excellence
FGOALS-g2	LASG-CESS	LASG, Institute of Atmospheric Physics, Chinese Academy of Sciences; and CESS, Tsinghua University
FGOALS-s2	LASG-IAP	LASG, Institute of Atmospheric Physics, Chinese Academy of Sciences
GFDL-CM3	NOAA GFDL	Geophysical Fluid Dynamics Laboratory
GFDL-ESM2G	NOAA GFDL	Geophysical Fluid Dynamics Laboratory
GISS-E2-H	NASA GISS	NASA Goddard Institute for Space Studies
GISS-E2-R	NASA GISS	NASA Goddard Institute for Space Studies
HadGEM2-A	MOHC	Met Office Hadley Centre
HadGEM2-ES	MOHC, INPE	Met Office Hadley Centre and Instituto Nacional de Pesquisas Espaciais
INM-CM4	INM	Institute for Numerical Mathematics
IPSL-CM5A-LR	IPSL	Institut Pierre-Simon Laplace
IPSL-CM5A-MR	IPSL	Institut Pierre-Simon Laplace
IPSL-CM5B-LR	IPSL	Institut Pierre-Simon Laplace

MIROC-ESM	MIROC	Japan Agency for Marine-Earth Science and Technology, Atmosphere and Ocean Research Institute (The University of Tokyo), and National Institute for Environmental Studies
MIROC-ESM-CHEM	MIROC	Japan Agency for Marine-Earth Science and Technology, Atmosphere and Ocean Research Institute (The University of Tokyo), and National Institute for Environmental Studies
MIROC5	MIROC	Atmosphere and Ocean Research Institute (The University of Tokyo), National Institute for Environmental Studies, and Japan Agency for Marine-Earth Science and Technology
MPI-ESM-LR	MPI-M	Max Planck Institute for Meteorology (MPI-M)
MPI-ESM-MR	MPI-M	Max Planck Institute for Meteorology (MPI-M)
MRI-CGCM3	MRI	Meteorological Research Institute
NorESM1-M	NCC	Norwegian Climate Centre
NorESM1-ME	NCC	Norwegian Climate Centre

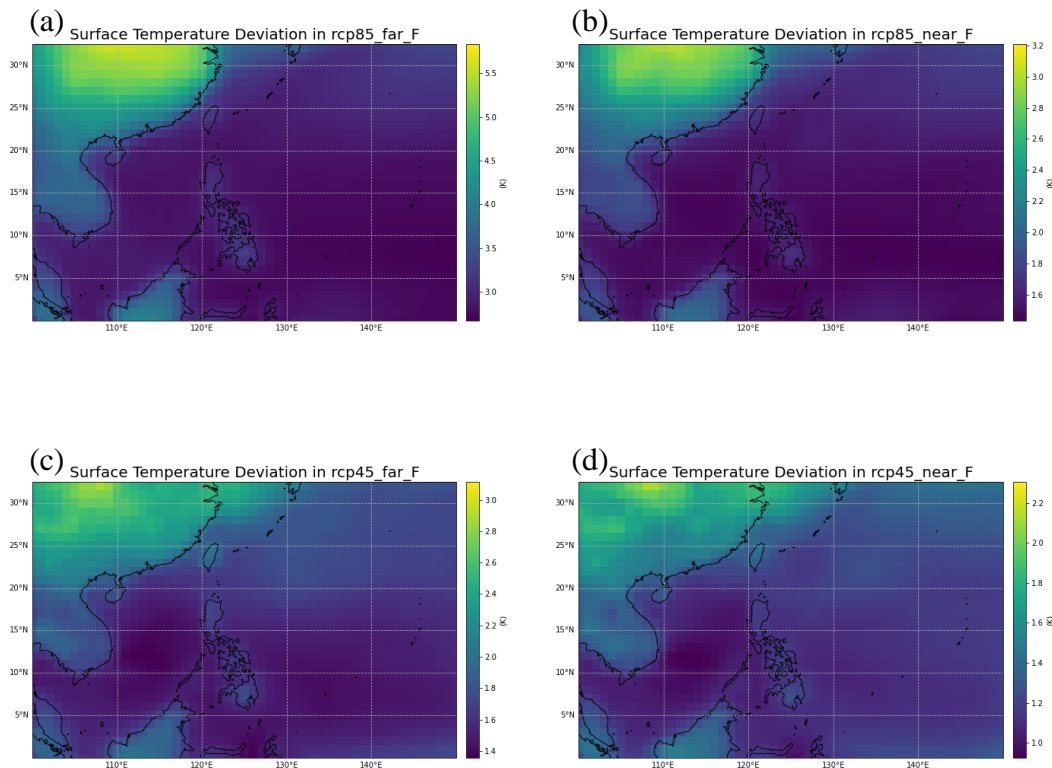
APPENDIX Table 2. 5 CMIP5 Models used in RCP4.5 PGW Experiments

Model Name	Modelling Center	Institution
CESM1-CAM5	NSF-DOE-NCAR	National Science Foundation, Department of Energy, National Center for Atmospheric Research
CCSM4	NCAR	National Center for Atmospheric Research
GFDL-CM3	NOAA GFDL	Geophysical Fluid Dynamics Laboratory
GFDL-ESM2M	NOAA GFDL	Geophysical Fluid Dynamics Laboratory
MRI-CGCM3	MRI	Meteorological Research Institute

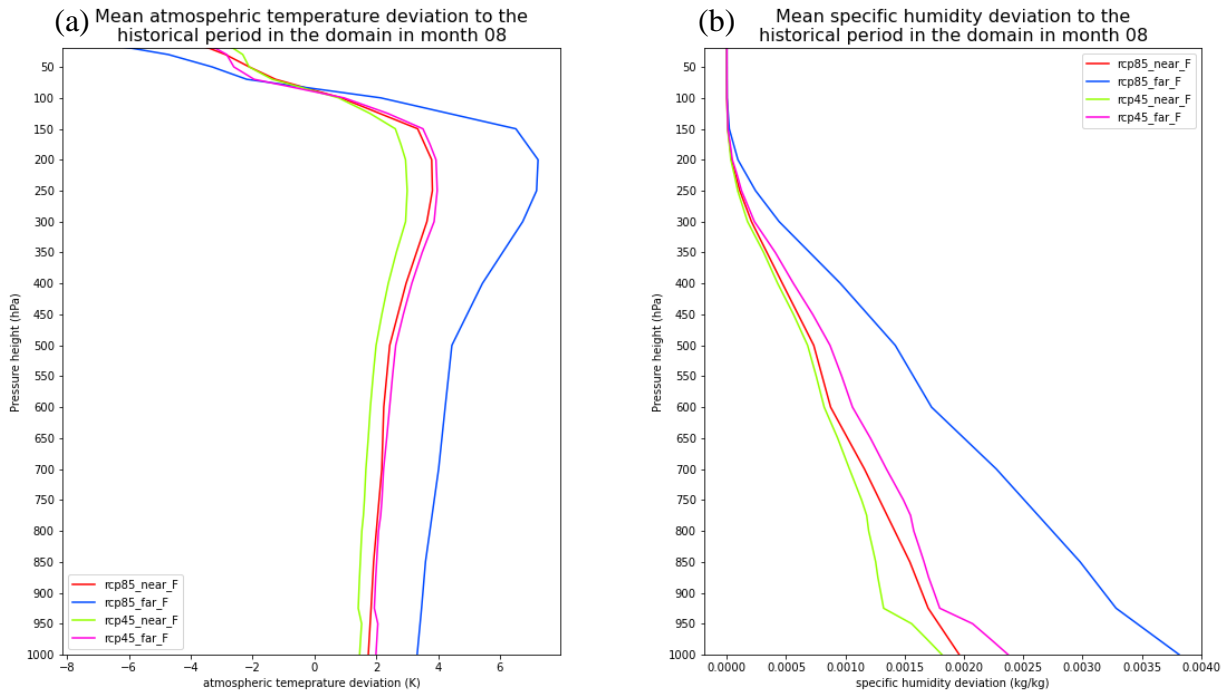
APPENDIX II

Superimposed PGW signals

An example of the deviation of the surface temperature, atmospheric temperature profile and the specific humidity profile in August in the near future and the far future projected in the RCP8.5 and RCP4.5 emission scenarios were shown in APPENXIX Figure 1 and 2 respectively. One can see an increase in surface SST and land surface temperature in all future climate scenarios. Moreover, the increased SST scaled to the increase in greenhouse gases concentration, which is consistent to previous studies (Knutti, R & Sedláček, J., 2013). Moreover, the atmosphere was observed to be stabilized by a larger increase in atmospheric temperature in the upper troposphere than the lower



APPENDIX Figure 1 Changes in SST (K) and land surface temperature (K) in August in (a) RCP8.5 Far Future, (b) RCP8.5 Near Future, (c) RCP4.5 Far Future, (d) RCP4.5 Near Future



APPENDIX Figure 2 Change in (a) atmospheric temperature profile (K), (b) specific humidity profile (kg / kg) averaged in the WRF outer domain in August for different emission scenarios

troposphere. A larger increase in atmospheric moisture content nearer to the surface were observed in this study, which is also similar to previous studies (Held & Soden, 2006; Hill & Lackmann, 2011).

APPENDIX III

Ertel Potential Vorticity (EPV) Diagnostics

Various researchers had considered the dynamics of TCs in terms of the Ertel Potential Vorticity (EPV). Wang and Zhang had developed a PV inversion algorithm, which can recover most of the circulation features associated with the TC, including the tangential circulation, boundary layer convergence in radial inflow, outward tilting of the RMW across height and the temperature feather in the eye of the TC (Wang & Zhang, 2003). The effects of diabatic heating, frictional dissipation contributing to the changes of EPV associated with the TC can be related by the flux form of the EPV budget equation in pressure coordinate:

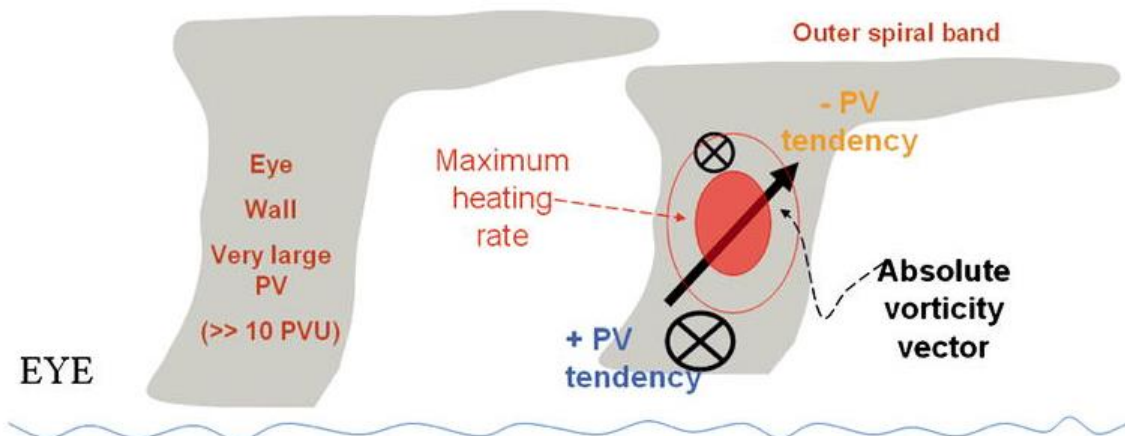
$$\frac{\partial P}{\partial t} = -\nabla_p \cdot (P \vec{V}_h) - \frac{\partial}{\partial p}(P\omega) - g\nabla_3 \cdot \vec{Y} \quad [1]$$

where P is the EPV:

$$P = g(f\hat{k} + \nabla_3 \times \vec{V}_h) \cdot \nabla_3 \theta \quad [2]$$

and \vec{Y} is the non-advection PV flux:

$$\vec{Y} = -\frac{d\theta}{dt}(f\hat{k} + \nabla_3 \times \vec{V}_h) + \nabla_3 \theta \times \vec{F} \quad [3]$$



APPENDIX Figure 3 Idealized schematic diagram of the PV point-of-view of a TC (figure from Figure 2 in Hill and Lackmann (2009))

noted that $f\hat{k} + \nabla_3 \times \vec{V}_h$ is the absolute vorticity vector (Raymond, 1992; Lackmann, 2002; Hill & Lackmann, 2009).

The EPV budget equation can be understood by APPENDIX Figure 3, which shows an idealized schematic of the TC in the EPV point-of-view (figure from Hill and Lackmann (2009)). A large central EPV tower can be found near to the eye of the TC. At the eyewall, as the tangential circulation decrease in its magnitude along the height, this results in an outward tilted absolute vorticity vector at the eyewall. At the outer spiral rainbands, the absolute vorticity vector also tilts outward according to the vertical gradient of tangential wind magnitude. From equation [1] and [3], the local EPV tendency depends on the gradient of the heating rate projecting onto the absolute vorticity vector, therefore positive EPV tendency can be found below the heating source while negative EPV tendency can be found above the heating source. If the frictional dissipation term, which is the last term in [3] was neglected, the non-advective EPV flux act likes transporting the EPV at the top of the rainbands downward to the lower troposphere, following the direction of the outward tilted absolute vorticity vector.

Moreover, taking the volume integral to the EPV budget equation remove the advective flux term, which is the first and the second term in [1], given that the volume enclosed is large enough and the advective flux of EPV at the lower and upper boundary of the volume is small, and the contribution of the source term and the sink term to the volume integrated EPV tendency can then be identified. The magnitude of the diabatic EPV production depends on the magnitude of the heating rate gradient, magnitude of the absolute vorticity vector and the tilt of the absolute vorticity vector. However, it should be reminded that cautions should be taken when viewing the vertical EPV advection term and the diabatic EPV tendency term. Tori et.al. (2012) had identified a large cancellation problem between the adiabatic vertical EPV advection term and the diabatic term (their figure 3), which numerical error may be comparable to the local EPV tendency term (Tori, et.al., 2012). Despite the possible limitation of the equation [1-3], it was still be chosen as the method to

diagnose the influence of historical environmental RH to the outer core size change of TCs in future climate in the PGW experiments due to its simplicity in relating the source term to the local EPV tendency.

APPENDIX IV

Absolute Angular Momentum (AAM) Budget Analysis

The azimuthally averaged AAM budget equation was used to diagnose the influence of historical outer wind speed to the difference in the percentage change of TC outer core size among each TC to the same PGW forcing. The AAM is defined as:

$$AAM = v_\theta r + \frac{fr^2}{2} \quad [4]$$

which the first term at the RHS is the relative angular momentum of the TC circulation and the second term is the earth angular momentum projecting onto the TC rotational axis. From the tangential momentum equation:

$$\frac{\partial v_\theta}{\partial t} + v_r \frac{\partial v_\theta}{\partial r} + \frac{v_\theta}{r} \frac{\partial v_\theta}{\partial \theta} + w \frac{\partial v_\theta}{\partial z} = -\frac{1}{r\rho} \frac{\partial p}{\partial \theta} - v_r \left(f + \frac{v_\theta}{r} \right) + F_\theta \quad [5]$$

where v_r is the radial wind, v_θ is the tangential wind, w is the vertical wind, ρ is the air density, p is the pressure, f is the Coriolis parameter and F_θ is the friction/diffusion term in tangential direction (Chan & Chan, 2015). By multiplying equation [5] by r , separate the quantities to the azimuthally mean term and perturbation term, and taking the azimuthally averaged to the equation, the azimuthally averaged AAM budget equation is:

$$\frac{\partial \bar{AAM}}{\partial t} = -r \bar{v}_r \bar{\zeta}_a - r \bar{v}'_r \bar{\zeta}'_a - \bar{w} \frac{\partial \bar{AAM}}{\partial z} - \bar{w}' \frac{\partial \bar{AAM}}{\partial z} - \frac{1}{\rho'} \frac{\partial p'}{\partial \theta} + r \bar{F}_\theta \quad [6]$$

where $\bar{\zeta}_a = \bar{f} + \frac{1}{r} \frac{\partial(r \bar{v}_\theta)}{\partial r}$ is the azimuthally mean vertical component of the absolute vorticity. The terms at the RHS are the radial flux of the vertical component of absolute vorticity (radial advection of AAM), eddy radial flux of vertical component of absolute vorticity, vertical advection of AAM, eddy vertical advection of AAM, eddy pressure gradient term and the frictional dissipation rate of the azimuthally averaged AAM respectively (Chan & Chan 2014, 2015). The bar denotes the azimuthal average and the prime term denote the perturbation from the symmetric term. From the study of Chan

and Chan (2014, 2015), as well as this study, the dominant terms in the RHS at the lowest model level are the radial advection of azimuthally averaged vertical component of the absolute vorticity and the frictional dissipation term (Chan & Chan 2014, 2015). Moreover, the radial influx of vertical absolute vorticity in the boundary layer causes an increase in local AAM. Therefore, the radial advection of AAM was investigated in this study. Moreover, as various research found that the radial AM fluxes contribute to the change in outer core size of the TC, the absolute angular momentum flux (AAMF) was investigated (Merrill, 1984; Chan & Chan, 2012).

Consider the radial component of the AAMF across a circle with radius r centered at the center of the TC at the lowest model level, the azimuthally averaged AAMF is defined as:

$$\begin{aligned} \overline{AAMF} &= \frac{\int_0^{2\pi} \left(v_\theta r + \frac{fr^2}{2} \right) v_r r d\theta}{\int_0^{2\pi} r d\theta} \\ &= r \bar{v}_r \bar{v}_\theta + r \bar{v}'_r \bar{v}'_\theta + \frac{f_0 r^2 \bar{v}_r}{2} + \frac{r^2 \bar{f} \bar{v}'_r}{2} \end{aligned} \quad [7]$$

which the terms at the RHS are the symmetric relative angular momentum flux (SRAMF), asymmetric (eddy) relative angular momentum flux (ARAMF), symmetric Coriolis torque (SCT) and the asymmetric (eddy) Coriolis torque respectively. f_0 denotes the Coriolis parameter at the center of the TC. From Chan and Chan (2014, 2015), the eddy term is small compared to the SRAMF and the SCT, therefore, in this project, the differences in SRAMF and the SCT for different TCs in the warming runs relative to the control run were investigated.

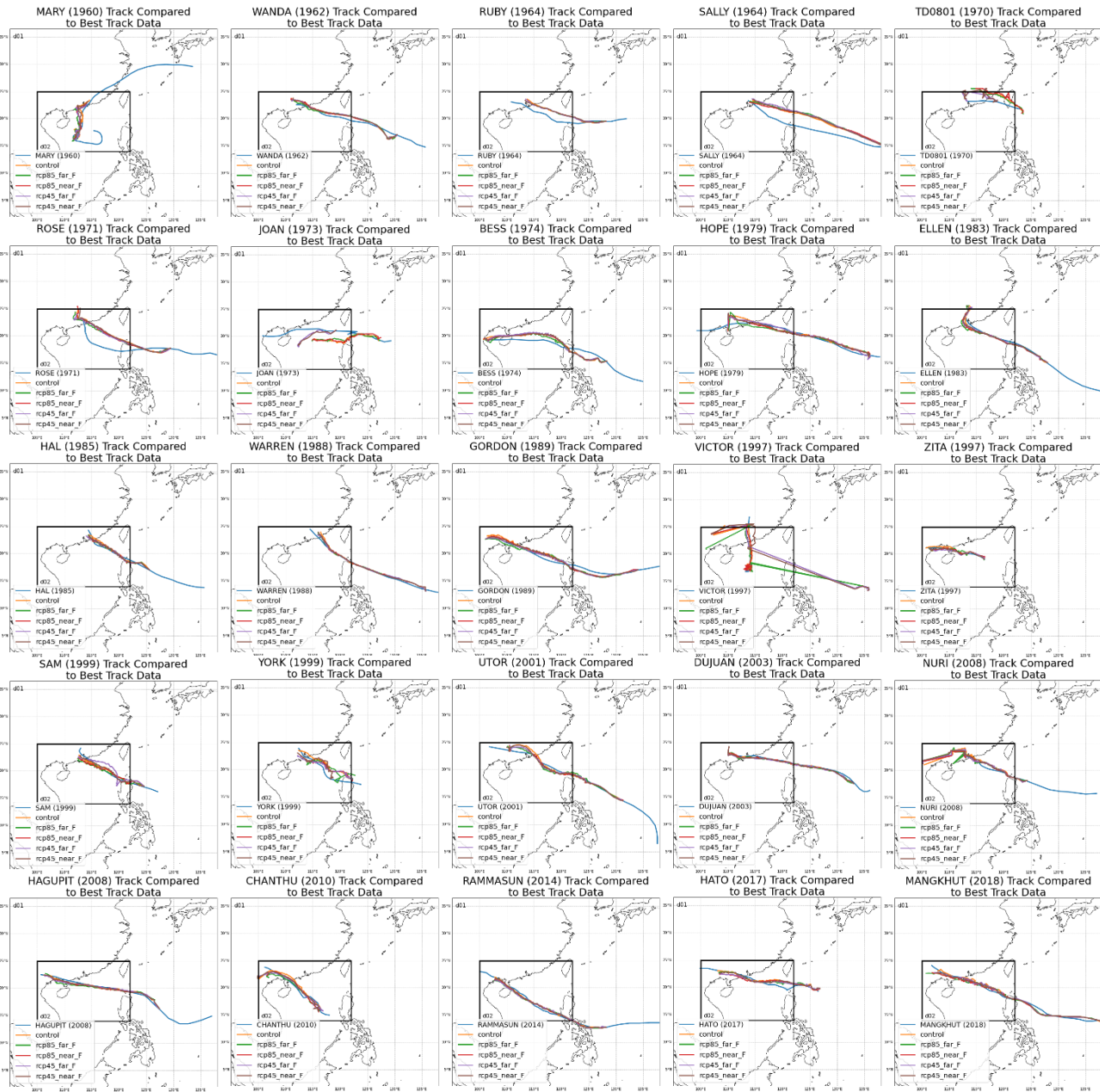
APPENDIX V

TCs Model Results Verification

In this research, a total of 25 TCs that had entered the SCS in the past were selected to be modelled by WRF version 3.7. Initial and boundary conditions using the historical atmospheric and oceanic condition associated with these TCs were referred as the control run. Moreover, changes in the thermodynamical variables in the near and far future era relative to the 1975-1999 period, following the RCP8.5 and RCP4.5 emission scenario, were superimposed to the historical environment to form a total of 4 warming experiments. Therefore, there were 125 TC simulations in total in this research.

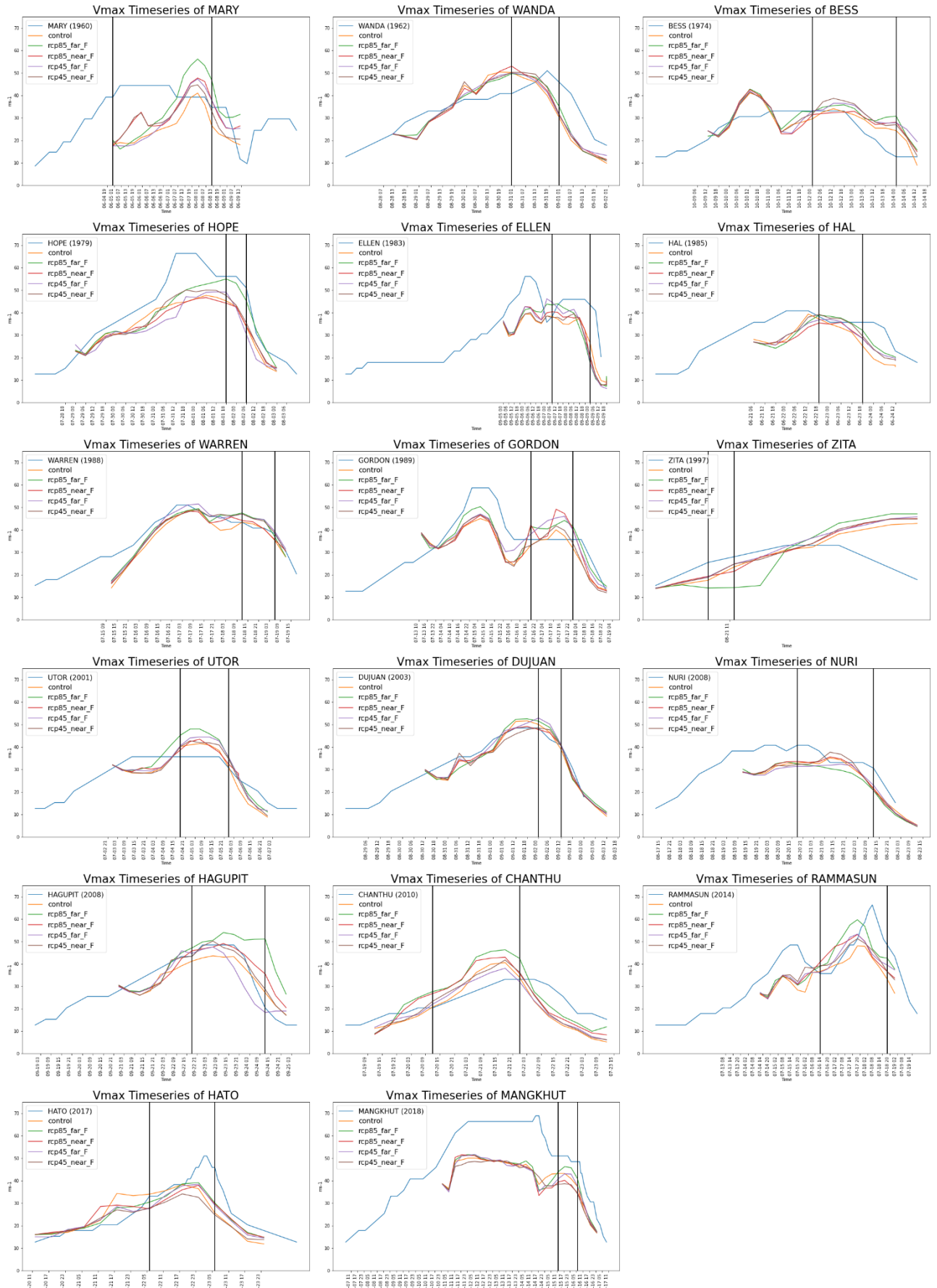
Results of the simulated TCs were compared to the best-tracked data obtained from the Hong Kong Observatory except for TC Mary (1960) because the Hong Kong Observatory data started at 1961. For TC Mary (1960), the best-track data from the China Meteorological Administration (CMA) were obtained from the International Best Track Archive for Climate Stewardship program (IBTrACS) (Knapp et.al., 2010). Both the intensity and the track of the TC were obtained to verify the model ability to capture the track and the intensity of the TCs. Moreover, the IBTrACS RMW and R17 data obtained from the USA agencies were used to verify the model ability to capture the RMW and the R17 of the TCs (Knapp et.al., 2010). As the RMW and the R17 data were only documented by the best-tracked dataset since 2002, only the size of the TCs after 2002 were compared to the best-tracked data. The 4 quadrant R17 obtained from the best-tracked data were averaged to produce the azimuthally averaged R17.

APPENDIX Figure 4 shown the modelled TC tracks for both the control run and the warming runs compared to the best-tracked data. Model ability of capturing the TC tracks relative to the best-track data varies across different TCs. TC Ruby (1964), TC Joan (1973) and TC York (1999) could



APPENDIX Figure 4 Simulated TC tracks in (orange) control run, (green) RCP8.5 Far Future, (red) RCP8.5 Near Future, (purple) RCP4.5 Far Future, (brown) RCP4.5 Near Future compared to the (blue) best-tracked data. TCs were ordered in chronological order from top-left to lower-right. (Same as Figure 4.1)

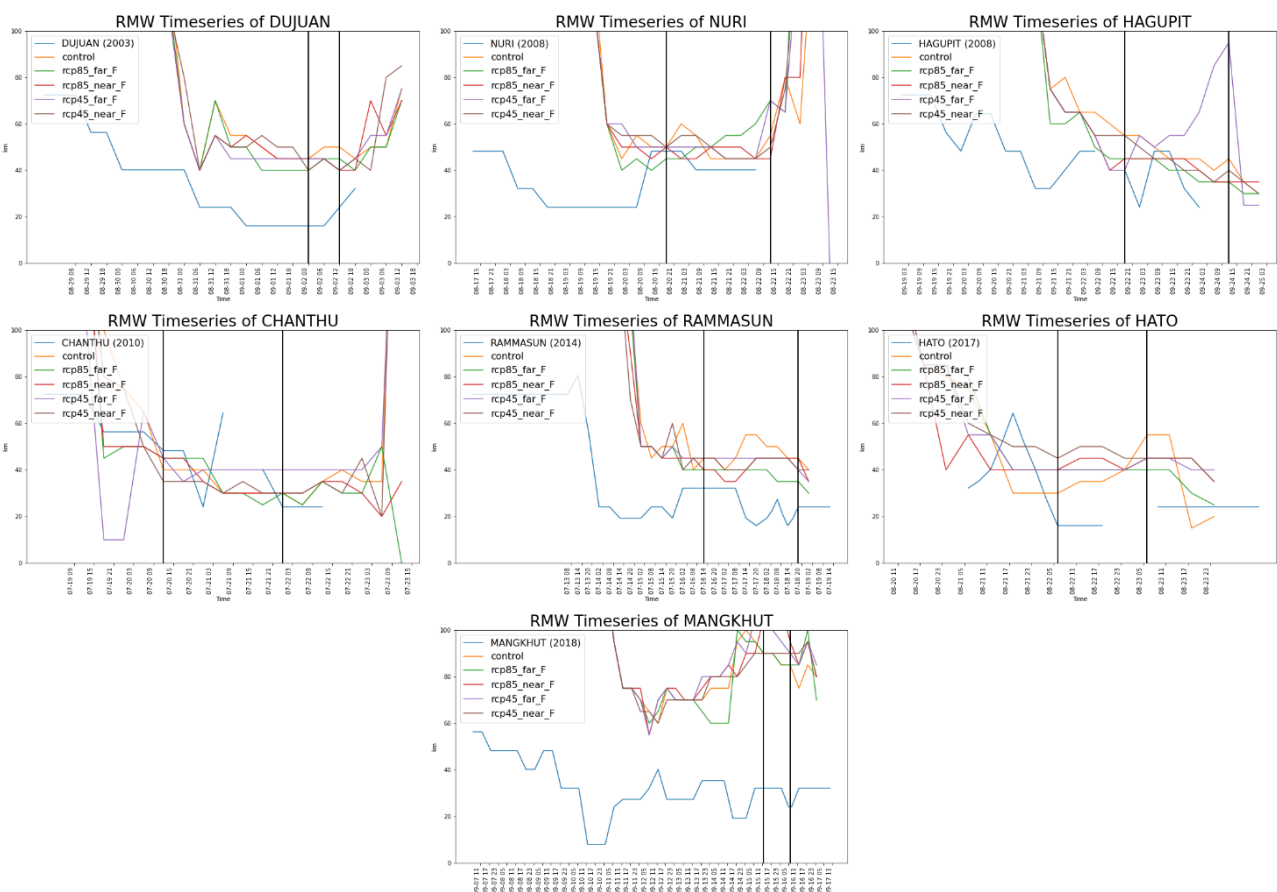
not make their landfall at the South China coast in either one of the 5 experiments. Moreover, the tracks of TC Sally (1964), TD 0801 (1970), TC Rose (1971), TC Victor (1997) and TC Sam (1999) in one or more experiments were very different compared to the best-tracked data. These deficiencies in model ability to capture the historical track of these TCs may be resulted from the physical schemes chosen, the resolution of the initial and boundary conditions, model ability to resolve the steering wind, or were case dependent. To minimize the complexity brought by the difference in the tracks, and therefore, the background environment, for these TCs compared to the historical best-tracked



APPENDIX Figure 5 Simulated TC azimuthally averaged 10m Vmax ($m s^{-1}$) timeseries in (orange) control run, (green) RCP8.5 Far Future, (red) RCP8.5 Near Future, (purple) RCP4.5 Far Future, (brown) RCP4.5 Near Future compared to the (blue) best-tracked data. TCs were ordered in chronological order from top-left to lower-right. 2 Vertical Black lines marked the time when the TC with a minimum of TS intensity entered the SCS and landfall at the South China coast.

warming experiments compared to the best-tracked data. The TCs' tracks in the warmed environment did not change much compared to the control run. Therefore, the change in the TC intensity and size in a warmed climate were resulted from the historical environment that the TC was embedded in, and the imposed warmed signal.

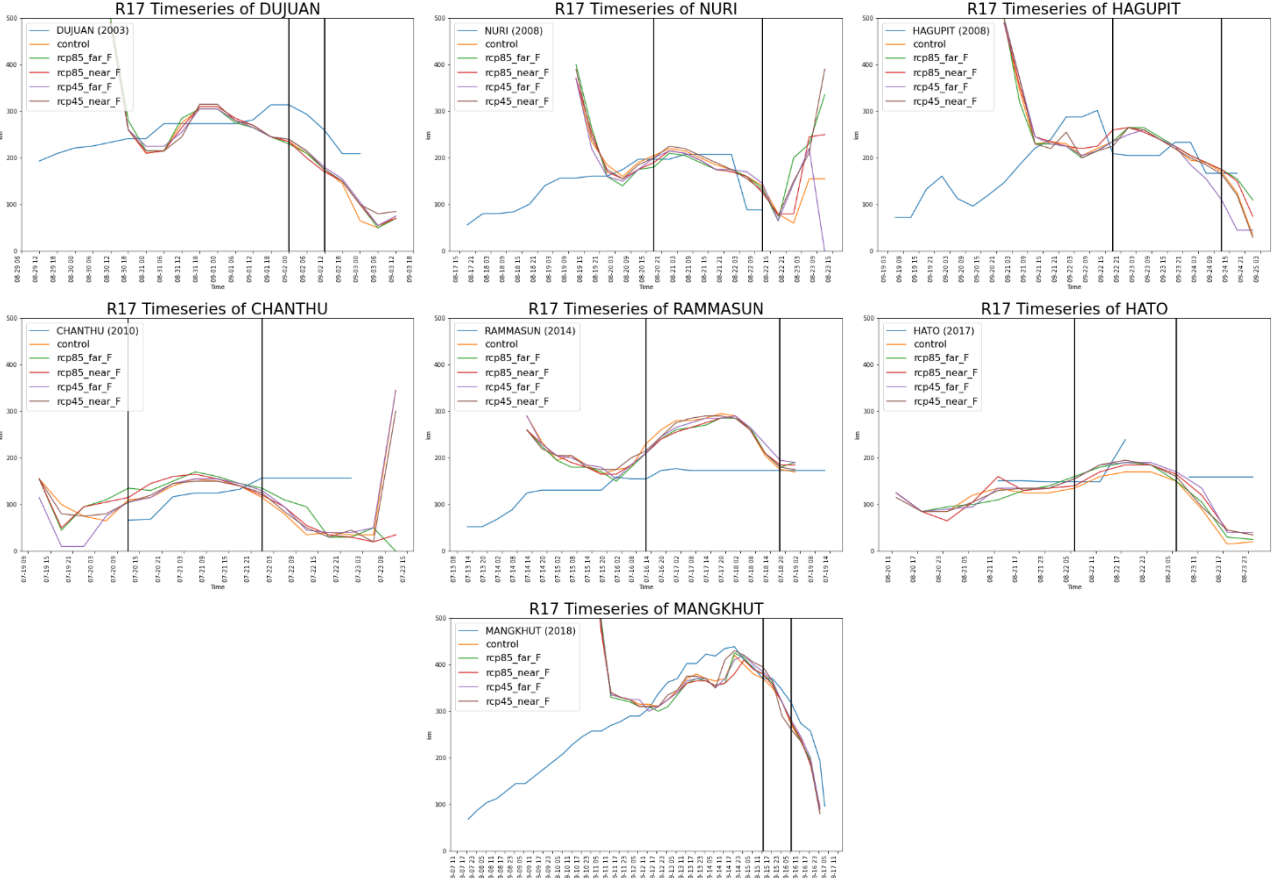
APPENDIX Figure 5 showed the modelled 10 m Vmax timeseries in m s^{-1} compared to the best-tracked data for the remaining 17 TCs. From the Figure, the model ability to capture the intensity of the TCs in the SCS varies by cases. The majority of the simulated TCs in the control run underestimated their intensity in the SCS compared to the best-tracked data, especially for the more intense TCs like TC Hope (1979) and TC Rammamun (2014). Reason for an underestimation of TC intensity in the model was due to a horizontal resolution of 3 km in the inner domain, which was not fine enough to resolve the internal processes which could affect the TC intensity (Gentry & Lackmann,



APPENDIX Figure 6 Simulated TC RMW (km) timeseries in (orange) control run, (green) RCP8.5 Far Future, (red) RCP8.5 Near Future, (purple) RCP4.5 Far Future, (brown) RCP4.5 Near Future compared to the (blue) best-tracked data for the TCs since 2002. TCs were ordered in chronological order from top-left to lower-right. 2 Vertical Black lines marked the time when the TC with a minimum of TS intensity entered the SCS and landfall at the South China coast.

2010). However, as they had also reported the TC intensity do not converge even for a horizontal resolution as fine as 1 km, 3 km resolution were still be chosen as the inner domain resolution in order to balance the computer resources and some ability of modeling the TC intensity. TC Hal (1985), TC Warren (1988) and TC Dujuan (2001) captured well the intensity of the TC in the SCS compared to the best-track data. However, there was only one timestep for TC Zita (1997) reaching a minimum of TS intensity in the SCS, therefore TC Zita (1997) were also discarded in the MLR analysis.

APPENDIX Figure 6 compared the modelled TCs' RMW to the best-track data for the TCs after 2002. Nearly all modelled TCs had a RMW larger than the best-track data. This is because of the horizontal resolution of the model was not fine enough to resolve the eyewall processes that influences the size of the RMW. According to Walter (2000), wave having a wavelength larger than $10\Delta x$, where Δx is the grid size, could be adequately resolved by the numerical model. Therefore, as the inner domain horizontal resolution was 3 km in this study, only the process with a scale of 30 km were resolved. Therefore, most of the eyewall processes that influences the size of the RMW were



APPENDIX Figure 7 Same as APPENDIX Figure 6, but the R17 (km) were shown

not resolved. Moreover, Gentry and Lackmann (2010) had found that finer the horizontal resolution, smaller the RMW of the TC were modelled, and the RMW did not converge for a horizontal resolution as fine as 1 km. Therefore, the limitation of the horizontal resolution in this study caused an overestimation of the RMW for the TCs selected compared to the best tracked data.

APPENDIX Figure 7 showed the modelled R17 of the TCs since 2002 and the associated best-track data. Most of the simulated TCs' R17 were comparable to the best-track data. However, overestimation or underestimation were also found for some of the TCs (TC Rammamun (2014) and TC Dujuan (2001)). The inaccuracy of the simulated TCs' R17 may be attributed to the sensitivity of the PBL scheme and microphysics scheme chosen, which caused uncertainties in frictional dissipation in the PBL and the latent heating at the inner core and the spiral rainbands (Hill & Lackmann, 2011; Krishnamurti, et.al., 2013; Chan & Chan, 2016). Limitations from the spatial resolution may cause errors of EPV production, therefore causing errors of simulated TCs R17. However, further research are needed to examine the ability of numerical models in simulating the climatology of the outer core size of TCs compared to the observations.

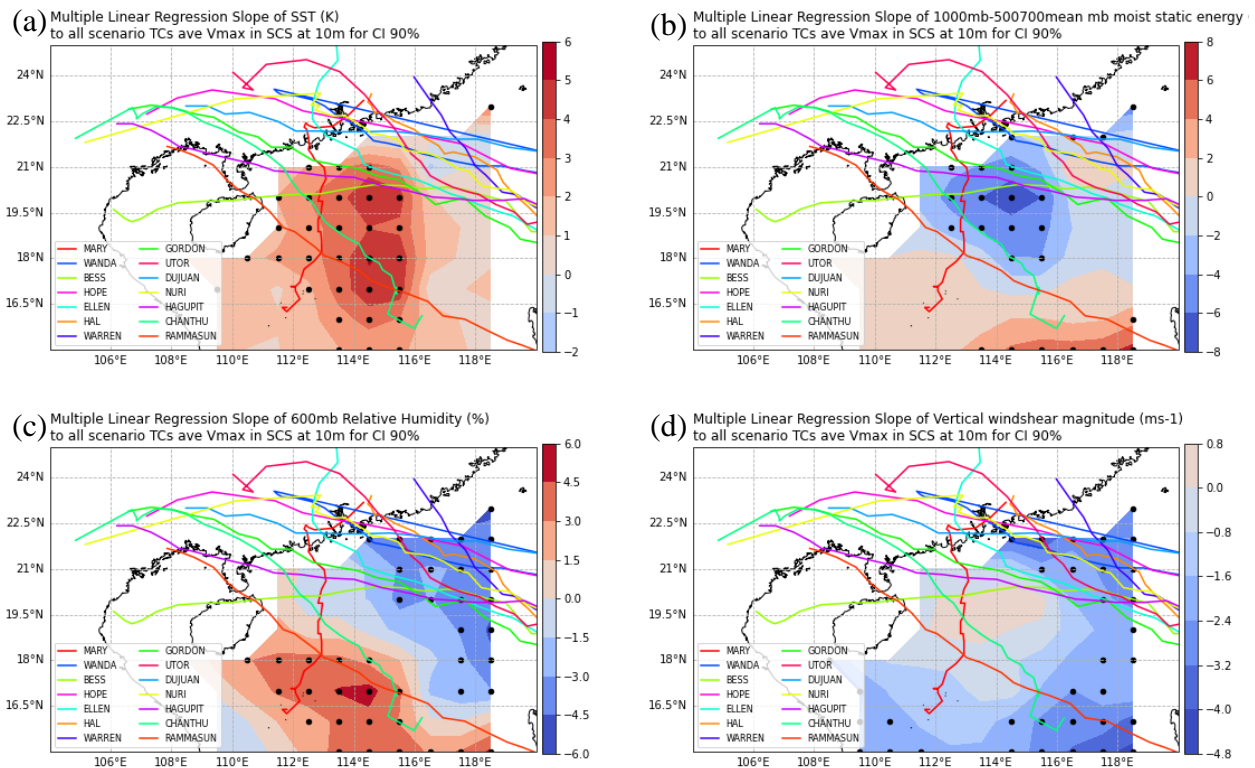
The selection criteria of the TC used are 1. Simulated tracks of the TCs in all warming experiments compared to the best track data. 2. Number of timesteps that the TC exceeding TS intensity found in the SCS. 3. TCs were not observed to have any very uncommon features in their lifetime. Based on criteria 1, TC Ruby (1964), TC Sally (1964), TC TD0801 (1970), TC Rose (1971), TC Joan (1973), TC Victor (1997), TC Sam (1999), TC York (1999) were dropped out. Moreover, based on criteria 2, TC Zita (1997) were dropped because there was only one timestep for TC Zita (1997) exceeding TS intensity in the SCS. Apart from that, TC Hato (2017) and TC Mangkhut (2018) were dropped out due to their unusual behavior of rapid intensification and RMW expansion after landfalling at the Philippines respectively, according the criteria 3 (Choy, et.al., 2020a). Yet, the results of the change in mean Vmax and R17 were only -1.2% and +0.4% for a 2°C warming if TC Hato (2017) and TC Mangkhut (2018) were included. The MLR relationship of the historical

environment to the difference in TC intensity and size changes did not change much if TC Hato (2017) and TC Mangkhut (2018) were also included (not shown). Therefore, these 2 TCs were left for future studies and discarded based on criteria 3, and a total of 14 TCs (70 simulations for control run and 4 warming experiments) were selected in this research, and were shown by the bold text in Table 3.1.

APPENDIX VI

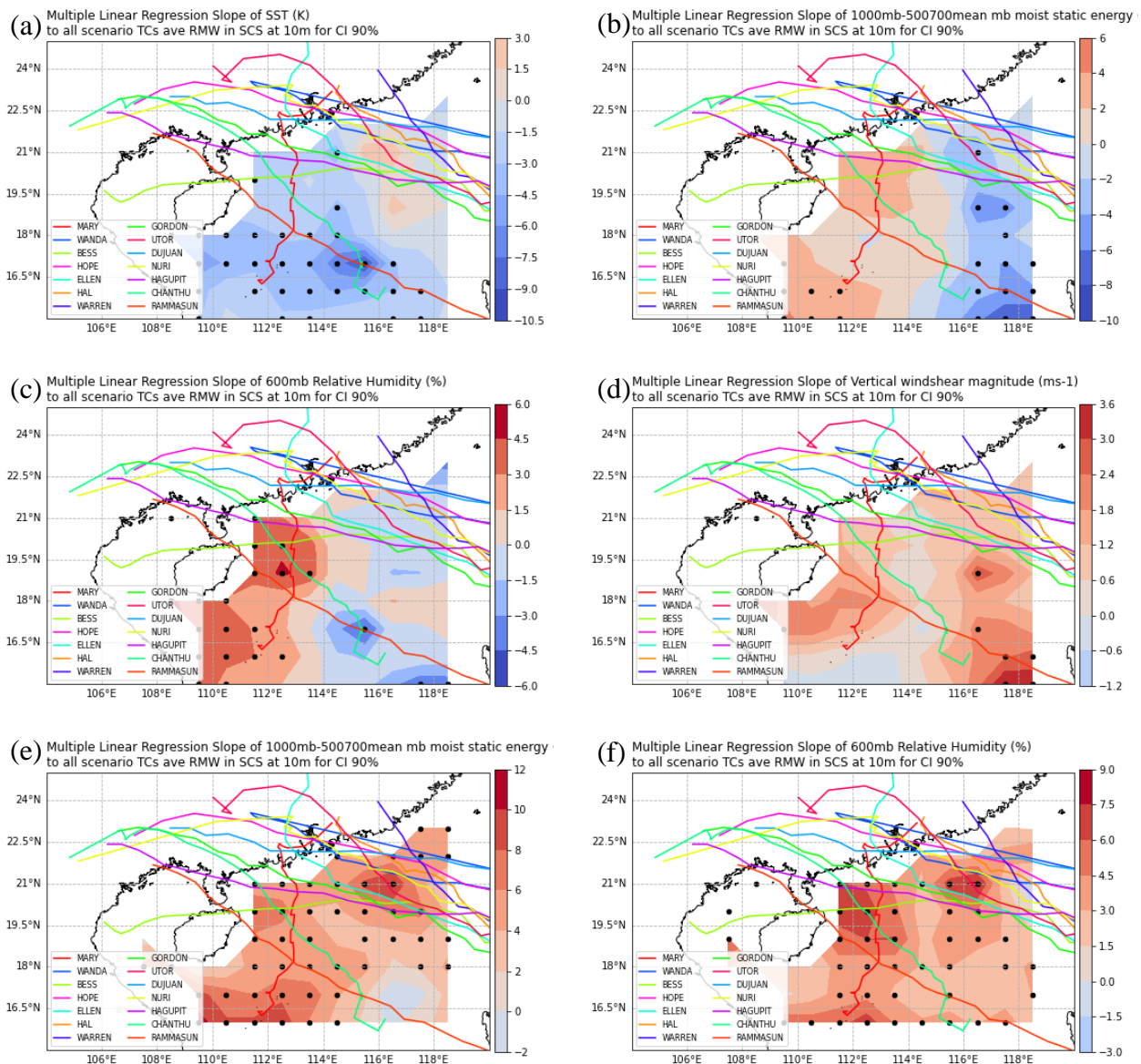
Statistical Significance on MLR Slope Map

Details of the statistical tests for the MLR slope retrieved from the MLR analysis were presented in this section. The null hypothesis for the MLR slope retrieved in each $1^\circ \times 1^\circ$ grids for each historical environmental variable was that the slope is equal to 0. If the p-value for the slope is smaller than a certain confidence interval, the null hypothesis will be rejected and the slope at that grid is significant different to 0 in a certain confidence interval. We had assumed that the each of the TC was independent in each warming experiment, therefore a total of 54 sample size was used for the significance test. The mean percentage change of Vmax, RMW and R17 in the SCS for all warming experiments for these 14 TCs were regressed to their associated historical environmental variables, and the MLR slopes were plotted. Grids that had a slope significantly different to 0 were



APPENDIX Figure 8 MLR slope map of (a) detrended SST, (b) 1000 mb - 500 to 700 mb mean moist static energy, (c) 600 mb RH, (d) vertical wind shear within 500 km of the storm center retrieved from the control simulation, regressing to the variation in the percentage change of Vmax for different TCs, assuming all TCs in all warming experiments were independent with each other. Red color means positive relation between the historical environmental variables to the difference in the change in mean Vmax among each TC. Units of the colorbar were % of Vmax change per 1 unit of standardized environmental parameters. Overlaid were the TC tracks in the control run. Black dots showed the grids with a slope significantly different to 0 in 90% CI.

indicated by black dots. Noted that there were minor differences of the MLR slope map here and that in section 5.2 because all TCs in all warming experiments were assumed to be independent with each other before carrying out the MLR analysis here, while the slope retrieved in section 5.2 were averaged across all warming experiments later. However, the differences were minor, and did not affect the results.



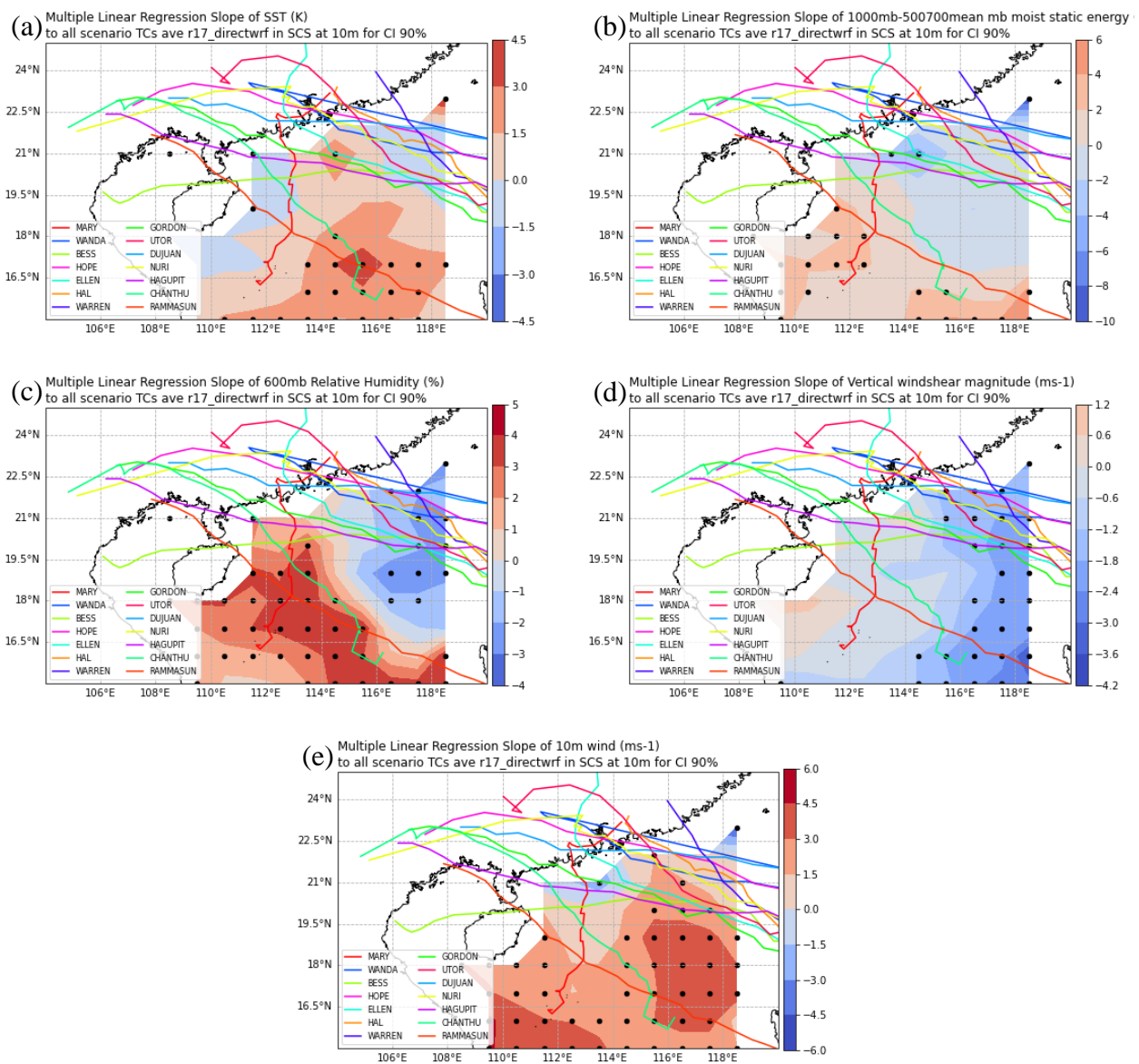
APPENDIX Figure 9 MLR slope map of (a) detrended SST, (b) 1000 mb - 500 to 700 mb mean moist static energy, (c) 600 mb RH, (d) vertical wind shear within 500 km of the storm center retrieved from the control simulation, (e) Historical 1000 mb – 500 to 700 mb mean moist static energy, (f) historical 600 mb RH retrieved from the control simulation by WRF, regressing to the variation in the percentage change of RMW for different TCs, assuming all TCs in all warming experiments were independent with each other. Red color means positive relation between the historical environmental variables to the difference in the change in mean RMW among each TC. Units of the colorbar were % of RMW change per 1 unit of standardized environmental parameters. Overlaid were the TC tracks in the control run. Black dots showed the grids with a slope significantly different to 0 in 90% CI

APPENDIX Figure 8 showed the MLR slope map of the historical environmental condition retrieved from the ERA-20C and ERA5 reanalysis data, regressing to the change in mean Vmax in the SCS. The pattern of the MLR slopes for each historical environmental variables were very similar to that in Figure 5.3. From the Figure, most of the grids of the historical detrended SST regressing to the change in Vmax for different TCs had passed the significance test in 90% CI, which means that the positive relation between the detrended SST and the change in Vmax were significantly different to 0. Moreover, the negative relation between the historical vertical wind shear and the change in Vmax in the SCS for different TCs was significantly different to 0. Therefore, it could be concluded that historical detrended SST and the historical vertical wind shear were related to the spread in the change in Vmax in a warmed climate.

APPENDIX Figure 9a – 9d showed the MLR slope map of the historical environment, retrieved from the ERA-20C and ERA5 data, regressing to the percentage change in RMW in the SCS for different TCs. Compared to the Figures for Vmax, fewer grids showed a significantly different to 0 slope for the percentage change in RMW for different TCs regressing to the historical environmental conditions in the SCS. From the figures, the MLR slope for the detrended SST regressed to the percentage change in RMW in the SCS was significantly different to 0 in 90% CI. Although the pattern of the MLR slope for the percentage change in RMW were slightly different to the percentage change in Vmax for different TCs, there should be some relationship between the variation in the percentage change in Vmax to the variation in RMW. Moreover, APPENDIX Figure 9e – 9f showed the MLR slope map of the atmospheric instability and mid-tropospheric RH retrieved from the control simulation and regressed to the variation in the percentage change of RMW. From the Figure, the positive slope between the historical atmospheric instability and the mid-tropospheric RH to the RMW percentage change variation were significantly different to 0 in 90% CI, as shown by the wide coverage of the black dots. Therefore, there were high confident that the variation in the percentage change of RMW among each TC in the SCS in a warmed climate were related to the

historical atmospheric instability and mid-tropospheric RH, which should be further confirmed by high-resolution model experiments in the future.

APPENDIX Figure 10 showed the MLR slope map of the historical environmental conditions regressing to the difference in the percentage change of R17 for different TCs. From the Figure, it can be seen that both the positive slope of the mid-tropospheric RH (APPENDIX Figure 10c) and the outer wind speed (APPENDIX Figure 10e) to the variance of R17 percentage change for different



APPENDIX Figure 10 MLR slope map of (a) detrended SST, (b) 1000 mb - 500 to 700 mb mean moist static energy, (c) 600 mb RH, (d) vertical wind shear within 500 km of the storm center, (e) outer wind speed ($m s^{-1}$) retrieved from the control simulation, regressing to the variation in percentage change in R17 of different TCs, assuming all TCs in all warming experiments were independent with each other. Red color means positive relation between the historical environmental variables to the difference in the change in mean R17 among each TC. Units of the colorbar were % of R17 change per 1 unit of standardized environmental parameters. Overlaid were the TC tracks in the control run. Black dots showed the grids with a slope significantly different to 0 in 90% CI.

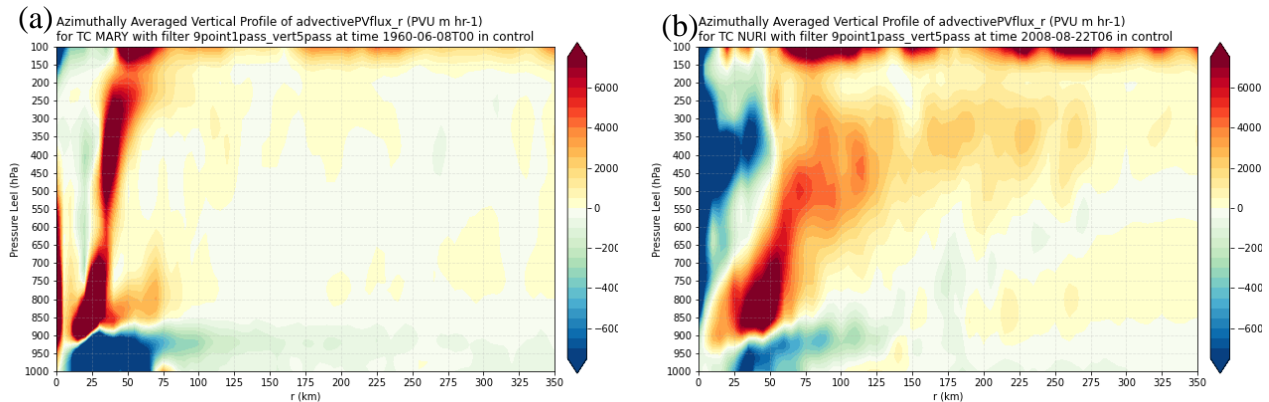
TCs were significantly different to 0 in 90% CI. There were more grids for the mid-tropospheric RH and the outer wind speed passing the statistical significance test compared to other historical environmental variables. Therefore, there should be high confidence that the variance of R17 percentage change in the SCS in a warmed environment for different TCs were related to the historical mid-tropospheric RH and outer wind speed associated with these TCs.

APPENDIX VII

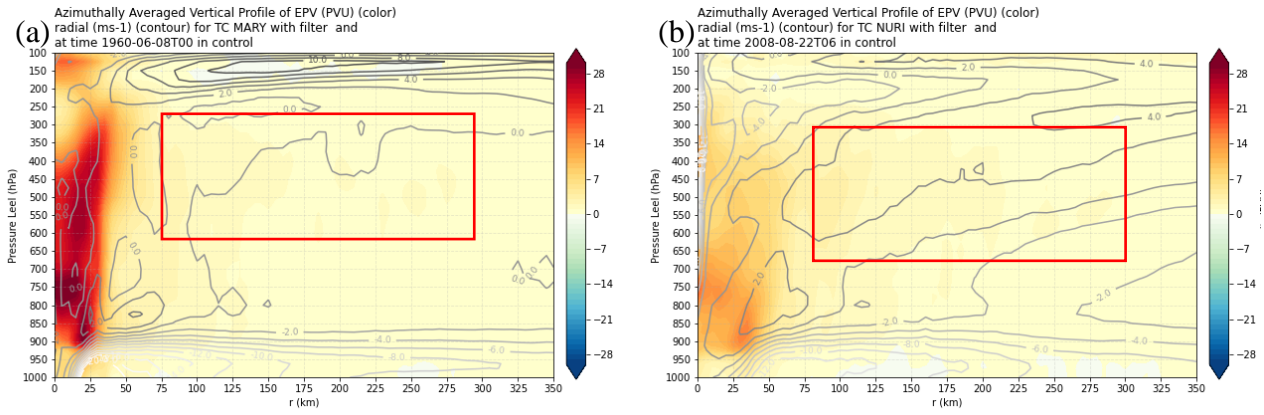
Difference in Volume Averaging of TC Mary and TC Nuri

Reasons for using a different radius of volume in the volume averaging for TC Mary and TC Nuri were presented in this sub-section. The main reason was because TC Mary and TC Nuri had a different circulation pattern, especially at the upper troposphere.

As the volume averaged horizontal divergence of the advective EPV flux reduced to the radial influx of the advective EPV flux by the Gauss divergence theorem, the azimuthally averaged vertical profile of the horizontal advective EPV flux for Mary at model timestep 1960-06-08-00 and for TC Nuri at the model timestep of 2008-08-22-06 in control run were shown in APPENDIX Figure 11. Compared APPENDIX Figure 11a and b, it can be seen that the radial advective EPV outflux for TC Mary at the upper troposphere remains near to the eyewall of the TC while that for Nuri extended to a radius more than 350 km from the TC center at the upper troposphere. Therefore, a 150 km radius for TC Mary was enough to enclose the whole radial circulation while more than 350 km radius for the volume should be used for TC Nuri. Moreover, timeseries of the radial advective flux showed a loosening upper core structure of TC Nuri, which means that TC Nuri was weakening at model timestep 2008-08-22-06.



APPENDIX Figure 11 Azimuthally averaged vertical profile of radial advective PV flux (unit: PVU m hr-1) for (a) Mary in control run at 1960-06-08-00, (b) Nuri in control run at 2008-08-22-06. Positive means outward



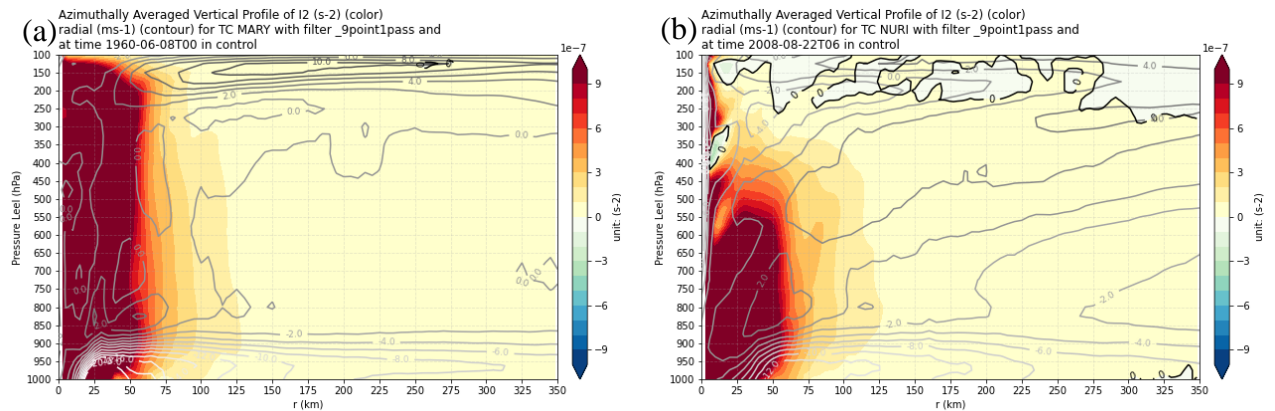
APPENDIX Figure 12 Azimuthally averaged vertical profile of (color) EPV (unit: PVU) and (contour) radial wind (unit: $m s^{-1}$) for (a) Mary in control run at 1960-06-08-00, (b) Nuri in control run at 2008-08-22-06. Positive contour means outward

APPENDIX Figure 12a and b showed the azimuthally averaged vertical profile of EPV and radial wind for TC Mary at model timestep 1960-06-08-00 and TC Nuri at model timestep 2008-08-22-06 in the control run respectively. From the figures, the EPV of TC Mary were more concentrated near to the center of the TC while that for TC Nuri dispersed to a wider radius from the TC center. Moreover, a slightly stronger EPV were found between 250-650 hPa, which extended outward to a larger radius from the TC center (red rectangles). Moreover, the radial outflow associated with TC Mary were located at a higher vertical level at 150 hPa and 100 hPa in the control run. But the radial outflow associated with TC Nuri were located at 400 hPa and 350 hPa in the control run. Therefore, more outward radial advective EPV flux for TC Nuri were because of a lower altitude of radial wind for TC Nuri compared to TC Mary. When the radial wind was located at a lower vertical level, it could transport the EPV to a distance very far away from the TC center, resulting in a loose EPV structure at the mid-upper troposphere.

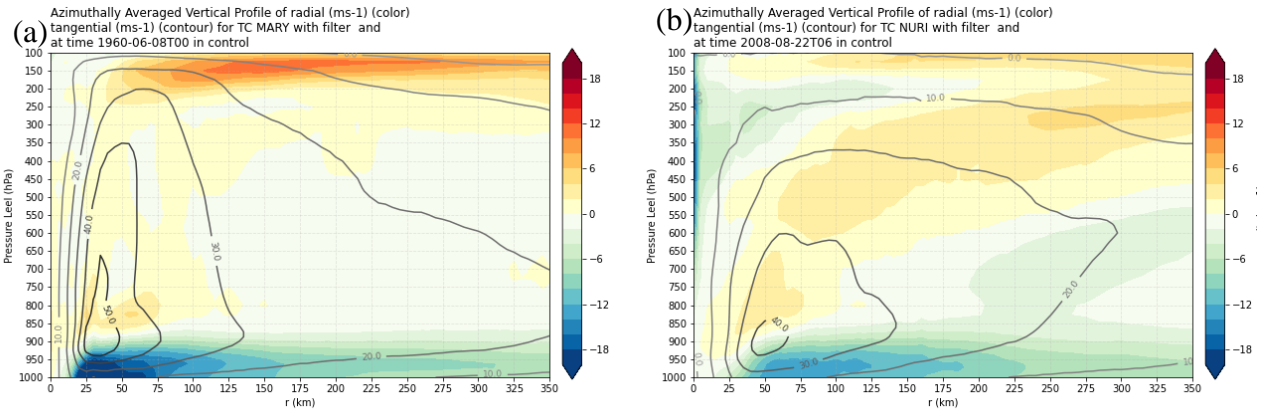
To examine why the azimuthally averaged radial wind was located at a lower vertical level for TC Nuri compare for TC Mary, the inertial stability associated with the 2 TCs were analysed. The inertial stability of a TC describes the resistance to radial movement of an air parcel. If the inertial stability is largely positive, an initially small radial disturbance of an air parcel will be restricted to return to its original position. However, if the inertial stability is small, or even negative, a small radial motion of the air parcel will cause the air parcel to keep moving radially until it reaches a

location with high inertial stability. Typically, the inertial stability of a TC is $100f$ in the eye and $10f$ across the RMW of a TC (Kepert, 2010). Equation 2 in section 2.1.2 shows the relationship of inertial stability to the tangential wind speed and the Coriolis parameter. Larger tangential wind speed leads to a larger resistance to radial motion of a TC, thus the structure is more organized.

APPENDIX Figure 13a and b showed the azimuthally averaged vertical profile of the inertial stability for TC Mary at model time 1960-06-08-00 and TC Nuri at model time 2008-08-22-06 in control run respectively. From the Figure, it can be seen that the inertial stability for TC Mary were stable throughout the whole TC. Therefore, the radial outflow for TC Mary were located just below the tropopause. However, TC Nuri started to become inertially unstable at 350 hPa and above. The inertially unstable atmosphere caused the air parcel to move outward at a lower vertical level than TC Mary, resulting in a radial outflow layer at a much lower vertical level, and a looser structure for TC Nuri. The higher inertial stability for TC Mary than TC Nuri also explained the more symmetrical horizontal circulation of TC Mary as shown in Figure 6.8 and 6.9. Moreover, the more organized structure for TC Mary in the RCP8.5 Far Future experiment than the control run can be explained by the larger inertial stability for TC Mary in the warming run (not shown), which tends to organize the TC structure to follow the typical structure of a TC.



APPENDIX Figure 13 Azimuthally averaged vertical profile of (color) Inertial Stability (unit: 10^{-7} s^{-2}) (red means positive), and (contour) radial wind (unit: m s^{-1}) (outward means positive) for (a) Mary in control run at 1960-06-08-00,(b) Nuri in control run at 2008-08-22-06



APPENDIX Figure 14 Azimuthally averaged vertical profile of (color) radial wind (unit: $m s^{-1}$) (red means outward), and (contour) tangential wind (unit: $m s^{-1}$) for (a) Mary in control run at 1960-06-08-00,(b) Nuri in control run at 2008-08-22-06

APPENDIX Figure 14 showed the radial wind and the tangential wind speed of TC Mary and TC Nuri in the control run. TC Mary had a much larger maximum tangential wind speed, reaching near $60 m s^{-1}$, than TC Nuri, which is around $40 m s^{-1}$ most of the time. Moreover, stronger tangential wind speed had extended to a higher pressure level for TC Mary compared to TC Nuri, which the $30 m s^{-1}$ tangential wind was confined at the lower troposphere. The weaker tangential wind speed for TC Nuri resulted in an inertially more unstable circulation system compared to TC Mary. Moreover, as TC Nuri was weakening from 2008-08-21-18 to 2008-08-22-12 (not shown), the inertial stability was reduced, and the radial structure became looser with time, resulting in a loosening radial advective #PV flux structure. To conclude, TC Nuri had a weaker tangential circulation than TC Mary. Therefore, TC Nuri was more inertially unstable, and air parcel escape the eyewall at a lower vertical level. As the radial outflow layer of TC Nuri was located at a lower vertical level, it transported the EPV to a farther distance, and therefore a larger radius of the volume should be used for TC Nuri than TC Mary in order to enclose the whole circulation system.